Instabilities of a Compressible Mixing Layer

by

Jeun-Len Wu

Dissertation submitted to the Faculty of the

Virginia Polytechnic Institute and State University

in partial fulfillment of the requirements for the degree of

Doctor of Philosophy

in

Engineering Mechanics

APPROVED :

Saad A. Ragab, Chairman

Ali H. Nayfeh

D. T. Mook

J. N. Reddy

S. L. Hendricks

W. F. Ng

November, 1989

Blacksburg, Virginia

Instabilities of a Compressible Mixing Layer

by

Jeun-Len Wu

Saad A. Ragab, Chairman

Engineering Mechanics

(ABSTRACT)

Instability waves in a free shear layer formed by two parallel compressible streams are analyzed using the linear spatial stability theory. Both viscous and inviscid disturbances are considered. The basic state is obtained by solving the compressible laminar boundary-layer equations or is specified by the hyperbolic tangent velocity profile. The effects of viscosity, Mach number, the velocity and temperature ratios on the growth rate are determined.

Unlike the boundary layer flow, viscosity has a stabilizing effect on the mixing layer flow. Increasing the temperature ratio produces a strong stabilizing effect on the growth of the mixing flow; this stabilization does not, however, persist at higher Mach numbers. Whereas the maximum growth rate of the incompressible mixing layer varies linearly with the velocity ratio, the maximum growth rate of the compressible mixing flow varies nonlinearly with the velocity ratio. The numerical results substantiate the fact that the convective Mach number is the appropriate parameter for correlating the compressibility effects on the spreading rate of the mixing layer. The ratio of the spreading rate of a compressible layer to that of an incompressible layer at the same velocity and density ratios depends primarily on the convective Mach number. Three-dimensional waves become important when the convective Mach number is greater than 0.6. The influence of nonparallelism on the

spatial growth rate of two-dimensional disturbances is evaluated and is found to be negligible.

Linear subharmonic instabilities of a compressible mixing layer, which is spatially periodic in a translating frame of reference, are analyzed by using Floquet theory. The basic state is obtained by the linear superposition of a steady mean flow, which is given by a solution to the compressible boundary-layer equations or by a hyperbolic tangent velocity profile approximation, and the neutral primary wave of that mean flow.

The results show that the growth rates of two-dimensional subharmonic instabilities (pairing mode) increase with increasing amplitude of the periodicity but decrease with increasing the convective Mach number. In the incompressible flow case, the most amplified subharmonic wave is a two-dimensional mode, which is in agreement with the published results. For subsonic convective Mach numbers, the presence of the periodicity enhances the growth rates of three-dimensional subharmonic waves over a wide range of spanwise wavenumber which shows a preferred band over which the growth rate is maximum. However, when the convective Mach number is greater than one, the interaction between the subharmonic wave and the primary wave marginally increases the maximum growth rate of the subharmonic. Nevertheless, that interaction dramatically increases the range of amplified spanwise wave numbers.

Fourth-order compact finite-difference codes are developed for solving the compressible boundary-layer equations and investigating their primary and subharmonic instabilities. The codes proved to be very accurate and versatile.

Acknowledgements

I wish to express my gratitude and appreciation to my adviser Dr. Saad A. Ragab for his advice, guidance, patience, understanding, and encouragement during the course of this research project. Without his help and support, it is doubtful that this work could have ever been completed. I also enjoy his pleasant friendship outside the research arena. I am very thankful to Professor A. H. Nayfeh, who perused this dissertation and made many useful suggestions. I also appreciate his contribution to my education. Thanks are also due to Dr. D. T. Mook, Dr. J. N. Reddy, Dr. S. L. Hendricks, and Dr. W. F. Ng for their contributions to my education and serving on the examining committee.

Special thanks are due to my mother and my sisters and for their encouragement and constant support. I wish to express my deep appreciation to my wife for her love, patience, understanding and encouragement.

This research has been supported by the Office of Naval Research under Contracts No. 00014-87-k-0168 and N00014-89-J-1544. I thank who has been the scientific officer of the contracts, for his encouragement. I thank Ohio State University, for providing Figure 2.2. Also thank Georgia Institute of Technology, for providing a copy of his direct simulation code.

Table of Contents

List of Tables

1.0 Introduction

1.1 Motivation

The scramjet engine cycle in which the combustion of liquid fuels takes place at supersonic speeds is recognized as an efficient propulsive cycle for missiles and airplanes cruising at hypersonic speed (Ferri 1964, Billing 1984, Waltrup 1986). Since early experimentation in the 1950's that demonstrates the feasibility of combustion of liquid fuels in a supersonic airstream, efforts have resulted in a hybrid engine cycle called the Dual-Combustion Ramjet (DCR) (Billing and Waltrup 1980). A schematic is shown in Fig. 1.1. In this cycle, roughly 25% of the supersonic inlet flow is decelerated to subsonic (or sonic) speed and directed into a "dump combustor" or gas generator. Then all of the fuel is injected into the high-temperature subsonic stream which results in a very fuel-rich mixture, and hence ignition and combustion can be maintained. However, the combustion process of the unreacted fuel has to be completed in a supersonic combustor downstream of the gas generator after mixing with the supersonic airstream previously diverted by the inlet.

The propulsive efficiency of the DCR cycle will be affected by the quality of mixing taking place in the shear layer that is formed by the subsonic (or sonic) stream issuing from the gas generator and the supersonic stream surrounding it. Waltrup (1986) pointed out that "Our current understanding of the mechanisms governing and/or controlling the mixing and combustion processes when two sonic or

supersonic streams merge to form a free shear layer ... is very limited". Thus, there is a need to investigate the structure, growth, and means of controlling supersonic turbulent mixing layers in nonreactive and reactive flows.

1.2 Basic Features of Mixing Layers

It has been experimentally established that the spreading rates (and presumably entrainment and mixing) of supersonic turbulent mixing layers are substantially lower than those of incompressible mixing layers (Ikawa and Kubota 1975, Chinzei et al. 1986). Moreover, the basic structures of incompressible mixing layers are well defined. Linear instability waves prevail in the initial stage of development, followed by the formation of large-scale coherent vortical motions, and finally, the pairing or amalgamation of these vortices (Ho and Huerre 1984). Thus, the mixing process is governed by the coherent structures that are predominantly spanwise vortices; however, spanwise waviness and small-scale streamwise vortices have also been experimentally observed (Breidenthal 1981, Jimenez 1983).

In supersonic mixing layers, the structure is much less understood. Ikawa and Kubota (1975) investigated a single-stream supersonic mixing layer. From the measured energy spectra, they have found that the coherent structures (spectral peaks) disappear with increasing the Reynolds number and with the boundary-layer trip roughness, which implies a fully developed layer at the trailing edge of the plate. They have concluded that the structure of fully developed supersonic turbulent free mixing layers consists of a randomly fluctuating field with no concentration of high-intensity large-scale wave motions in a preferred frequency range. Recently,

however, Chinzei et al. (1986) have conducted experiments on two-stream supersonic layers and presented, among other results, spark Schlieren photographs of flow fields that show the presence of large-scale structures similar to, but weaker and displaced somewhat farther downstream of the splitter plate than, those observed by Brown and Roshko (1974) for a low-speed case. The presence of large-scale structures in supersonic mixing layers also has been reported by the most recent experimental work on the subject by Papamoschou and Roshko (1986). This result is very significant because it suggests the possibility of exciting the layer so that these structures might be enhanced and appear sooner than in the natural cases. This point has been advocated by Ho and Huang (1982), who showed that the spreading of a mixing layer can be greatly manipulated by exciting the layer near a subharmonic of the most amplified frequency.

1.3 *Stability of Free-Shear Layers*

Linear stability analysis of free-shear layers is a very simple and inexpensive method that provides valuable information about the range of amplified frequencies, the most amplified frequency, the maximum growth rate, and the streamwise as well as the transverse extent of disturbances. The analysis also helps in investigating the effects of key parameters such as Mach number, Reynolds number, velocity ratio, temperature ratio, and chemical composition of the two streams on the previously mentioned stability characteristics. A stability analysis can also provide meaningful initial and boundary conditions for more elaborate computational efforts, which aim

at analyzing the nonlinear development of disturbances and/or controlling the shear layer by active or passive means.

The linear stability equations are derived from the compressible Navier-Stokes equations (see Lees and Lin 1946, Mack 1969) under the assumptions of a quasi-parallel steady mean flow and infinitesimally small disturbances. By invoking the normal mode solutions to the system of equations, we express the disturbances in a form containing exponential time and space factors such as $e^{i(\alpha x-\omega t)}$. The vanishing of the disturbances at the boundaries results in a characteristic value problem with α or ω as the eigenvalue. Usually, if ω is specified, then α is required; this kind of problem is called spatial stability analysis. On the other hand, if α is specified, then ω is required; this kind of problem is called temporal stability analysis. Whether the mean flow is stable or not depends on the imaginary part of the characteristic value. For spatial stability analysis, if the imaginary part of α is negative, then the motion is said to be unstable and the disturbances grow in space. For temporal stability analysis, if the imaginary part of ω is positive, then the flow is unstable and the disturbances grow in time. Whether the spatial theory or temporal theory is applicable has been addressed by Huerre and Monkewitz (1985). If the flow is convectively unstable, then the spatial theory is the relevant theory. If the flow is absolutely unstable, then the temporal theory should be used.

In contrast to the incompressible stability problem, the compressible problem is more complex because of the coupling between the velocity and temperature fields. Furthermore, viscous and thermal transport coefficients depend on the instantaneous local temperature. Fortunately, in the study of Lees and Lin (1946), it has been shown that compressible free shear flows are unstable with respect to inviscid disturbances because of the existence of a point of inflection in the density vorticity product. This point is called a generalized inflection point by Mack (1969) and was found to play the

same role in the compressible theory as the inflection point of the velocity profile in the incompressible case. Therefore, inviscid stability theory, which is much simpler than its viscous counterpart, has been used by many investigators to study the instability of compressible shear flows. For example, Lessen et al. (1965, 1966) considered the inviscid temporal stability of a laminar mixing layer. They obtained the mean flow by solving the compressible boundary-layer equations and found that the flow is more unstable with respect to waves propagating at an angle to the mean flow. Blumen et al. (1975) also considered the inviscid temporal stability of the hyperbolic tangent profile. They concluded that the flow is unstable to two-dimensional disturbances at all values of the Mach number as a result of the existence of an unstable second mode. Gropengiesser (1970) was the first to consider the spatial stability of supersonic free-shear layers. He approximated the mean-flow velocity by a generalized hyperbolic-tangent profile. Assuming a parallel mean flow and inviscid disturbances, he investigated the effects of the Mach number and temperature ratio on the stability of a single stream layer. He also obtained some results for oblique waves.

The effect of walls on the stability of supersonic mixing layers was studied by Tam and Hu (1988) and Greenough et al. (1989). They found two general types of instability: Kelvin-Helmhotz modes and supersonic wall modes. The existence of the wall modes is reminiscent of Mack's (1969, 1984) finding concerning the compressible boundary layers which indicates that there will be unstable modes as long as there is a region of supersonic relative flow.

Direct simulations of compressible mixing layers have been performed using finite-difference representations. Lele (1989) have simulated a developing mixing layer using a compact finite-difference scheme with spectral-like accuracy. Time advancement is carried out by a compact storage third-order Runge-Kutta scheme

(Wray 1987). Simulations have been conducted for both spatially-evolving and temporally-evolving mixing layers in two- and three-dimensions. The Reynolds number $R = \rho_1 (U_1 - U_2) \delta_\omega / \mu$ is in the range 100-500, where the subscripts 1 and 2 refer to the high speed and low speed streams, respectively, and δ_ω is the initial vorticity thickness. He has addressed that the initial evolution of the disturbances corresponded to the predictions of the linear stability analysis. As the disturbances become nonlinear the harmonics of the linearly unstable disturbances begin to amplify. With significant vorticity clumping the growth rates become larger than the laminar instability estimates, and the nonlinear process generates a broadband spectrum. Tang et al. (1989) have also presented direct simulations of two-dimensional spatially-evolving mixing layers using a modified MacCormack scheme that is second order in time and fourth order in space. They have found that the shear layer growth rate decrease with increasing values of the theoretical convective Mach number of the shear layer. Sandham and Reynolds (1989) also presented direct numerical simulation of temporally developing mixing layers.

In this study, the influences of the velocity ratio, temperature ratio, and Mach number on the stability characteristic of unbounded compressible mixing layers are investigated in more detail. Two different mean flows are used in this work. The first is a solution to the compressible laminar boundary-layer equations. The second is a hyperbolic-tangent velocity profile, and by appealing to the Crocco-Busemann integral of the energy equation, we obtain the temperature profile from the velocity profile. The second mean flow has been extensively used by many investigators in stability studies of turbulent incompressible and compressible flows.

Although the instability mechanism is essentially inviscid, viscous disturbances are investigated in order to determine the effect of viscosity on the growth rates for low-Reynolds-number applications and to justify the inviscid results as the limit of

Infinite Reynolds numbers. It should be also recognized that the flow is really not parallel. Thus, the variation of the shear-layer thickness and the flow profiles in the streamwise direction must be considered. Ragab and Wu (1989) among others used the method of multiple-scales to study the nonparallel effects on the stability of axisymmetric turbulent mixing layers. They found that nonparallelism of the mean flow can have significant contributions to the growth rates of both axisymmetric and azimuthal modes. Here, we investigate the nonparallel effects on two-dimensional compressible laminar mixing layers using the viscous theory of El-Hady and Nayfeh (1980).

1.4 The Convective Mach Number

A parameter called the convective Mach number M^+ was proposed by Bogdanoff (1983) and Papamoschou and Roshko (1986) to explain compressibility effects on the growth rate of supersonic mixing layers. This parameter is defined as the average of the Mach numbers of the two streams in a frame of reference moving with the large-scale structures, and it represents the combined effects of velocity ratio, temperature ratio, and Mach number on the growth of mixing layers. This parameter was used by Papamoschou and Roshko to correlate their experimental data and to explain the dramatic reduction of the growth rate as a result of compressibility. Bogdanoff, and Papamoschou and Roshko presented limited theoretical results from the linear stability analysis in support of M^+ as a compressibility parameter. In this work, we present a more comprehensive substantiation of M^+ based on the spatial linear stability analysis of different mean flows. It is important to note here that the

theoretical results used by Bogdanoff, and Papamoschou and Roshko are for a single stream and for two-dimensional disturbances. The present theoretical work includes three-dimensional disturbances over wide ranges of velocity ratios, temperature ratios, and Mach numbers.

1.5 Subharmonic Instabilities

In the initial region of a mixing layer, the most amplified instability wave grows exponentially according to linear theory. Farther downstream, such a wave saturates due to nonlinear effects resulting in an almost spatially and temporally periodic vortical structure. This new state is subject to secondary instabilities of the subharmonic or fundamental type. The two-dimensional subharmonic instability is responsible for vortex pairing and hence an increase in the spreading rate of the shear layer. The three-dimensional counterpart is called helical pairing and is responsible for the development of streamwise vorticity and three-dimensionality in shear layers (Pierrehumbert and Widnall 1982, Ho and Huerre 1984, Santos 1987). To study the processes of mixing enhancement and to have a better understanding of the transition phenomenon to turbulence, we undertake in this work a study of the subharmonic instability of a compressible mixing layer, which is periodic in space and time.

Oscillations having a frequency equal to one-half the frequency of the fundamental oscillations of free-shear layers have been observed experimentally (see Sato 1959, Browand 1966, Freymuth 1966, and Ho and Huang 1982). Kelly (1967) has shown that these oscillations are a result of a secondary instability of spatially

and temporally periodic basic state composed of the mean flow and a finite amplitude fundamental wave. For the hyperbolic-tangent profile, Kelly found that the subharmonic growth rate may exceed the growth rate of the fundamental wave if the amplitude of the streamwise component of the periodic flow is about 12% of the mean velocity difference across the shear layer. Kelly's temporal analysis and weakly nonlinear method of handling the mode interactions has been adapted to spatially developing instability waves by Monkewitz (1988) who has also established conditions for resonant interaction between a fundamental-subharmonic pair and derived corresponding amplitude equations.

The phenomenon of vortex pairing in free shear layers and the development of three-dimensional disturbances have been recently investigated by Pierrehumbert and Widnall (1982), Santos and Herbert (1986), and Santos (1987). The basic state in Pierrehumbert and Widnall's work is given by an exact solution to the Euler equations which was found by Stuart (1967). They have confirmed that the most unstable subharmonic mode is two-dimensional (vortex-pairing) and have found that the fundamental mode is inherently three-dimensional (translative instability). On the other hand, the basic state in the work of Santos and Herbert work is given by the shape function approximation which is composed of the hyperbolic-tangent profile and a primary wave which is a solution to the Rayleigh equation. Santos' results show reasonable agreement with those obtained by Pierrehumbert and Widnall. This agreement gives a credibility to the shape-function assumption. More recently, using temporal linear stability analysis and nonlinear flow simulation, Klaassen and Peltier (1989) have found out that vortex pairing is the most rapidly amplified mode in a continuous spectrum of vortex merging instabilities. A distinct feature of their work is that the periodic basic state is determined numerically by solving the nonlinear

Navier-Stokes equations, and hence the nonlinear development of the primary wave is correctly accounted for.

The approach followed here is based on the Floquet analysis of the periodic basic state consisting of the mean flow and a finite amplitude instability wave. This method was developed by Herbert (1981-1988) and has been remarkably successful in calculating secondary instabilities in channel flows and boundary-layer flows. The effects of the temperature ratio, velocity ratio, Reynolds number, Mach number, and the amplitude of the primary wave on the growth rate of the subharmonic instabilities are investigated. We believe that the present work is the first attempt to extend to compressible flow the work of Santos (1987). However, we must also note that the subharmonic instability in compressible Boundary layers have been addressed by Nayfeh (1988) and El-Hady (1988, 1989).

1.6 Objectives :

In summary, the objectives of this study are

- To investigate the effects of different flow parameters such as velocity ratio, temperature ratio, Mach number, and Reynolds number on the development of instability waves in compressible mixing layers.

- To study the nonparallel effects on the stability of compressible mixing layers.

- To substantiate the convective Mach number as a compressibility parameter that unifies the effects of velocity ratio, temperature ratio, and Mach number.

- To Study the interaction of a primary wave with its subharmonic in compressible mixing layers.

- To develop versatile numerical methods for the eigenvalue problems pertinent to the primary and subharmonic instabilities of viscous compressible bounded and free-shear layers.

2.0 The Mean Flow

2.1 *Introduction*

In the theory of hydrodynamic stability, one is concerned with the stability of a mean flow that is a solution to the Navier-Stokes equations. For thin shear layers (free or bounded) a high Reynolds number approximation to the mean flow can be obtained by solving the boundary-layer equations. Therefore, in a mixing layer formed by two parallel streams of the same gas, the mean flow is determined by solving the compressible boundary-layer equations for steady laminar flow. The main parameters of the mixing layer are the velocity and temperature ratios of the two streams and the Mach number of one of the streams. The mean pressure is assumed to be uniform throughout the flow.

In the literature of instabilities of both compressible and incompressible mixing layers, the hyperbolic-tangent velocity profile has been used extensively. In addition to its simple analytical form, the hyperbolic-tangent profile is a good approximation to experimental mean velocity profiles in turbulent mixing layers. For example, Samimy and Elliott (1989) made measurements in a compressible turbulent mixing layer and were able to collapse their mean velocity data as well as data from other experiments on a single curve given by

$$u \equiv \frac{u^* - U_2^*}{U_1^* - U_2^*} = \frac{1}{2}\left[1 + \tanh 2.4 \frac{y^* - y_m^*}{\delta_\omega^*}\right] \tag{2.1}$$

where u^* is the streamwise velocity profile, and U_1^* and U_2^* are its value in the farfield of the upper and lower streams, respectively, δ_ω^* is the local vorticity thickness, and y_m^* is the transverse coordinate at which $u = 1/2$. Samimy and Elliott obtained (2.1) by a least square fit to the experimental data, and a comparison between the prediction of (2.1) and the data is shown in Fig. 2.1. For stability analysis the mean temperature profile is also needed. If the velocity profile is known, for example (2.1), an approximation to the temperature profile is obtained from Busemann-Crocco energy integral (Michalke, 1984).

Although there may not be a *direct* relationship between the growth rates of instability waves of the mean flow of a turbulent mixing layer and its spreading rate, the present results and those of other investigators suggest that flow parameters such as the velocity ratio, temperature ratio, and Mach number have the same *qualitative effects* on both measures of growth. This makes the stability analysis of mean turbulent profiles worth the study.

In Section 2.2, the compressible boundary-layer equations are presented. A *compact fourth-order finite-difference method* is developed in Section 2.3. The mean flow profiles of laminar mixing layers for selected values of Mach number and temperature ratio are summarized in Section 2.4 along with their approximations by hyperbolic-tangent profiles.

2.2 *The Compressible Boundary-layer Equations*

We introduce Cartesian coordinates (x^*, y^*) in the streamwise and transverse directions, respectively. We let u^* and v^* denote the corresponding velocity components, and p^*, T^*, and ρ^* denote the static pressure, temperature, and density, respectively.

The two-dimensional compressible boundary-layer equations (Schilichting, 1979) are

Continuity Equation :

$$\frac{\partial}{\partial x^*}(\rho^* u^*) + \frac{\partial}{\partial y^*}(\rho^* v^*) = 0 \tag{2.2}$$

X-Momentum Equation :

$$\rho^* u^* \frac{\partial u^*}{\partial x^*} + \rho^* v^* \frac{\partial u^*}{\partial y^*} = -\frac{dp^*}{dx^*} + \frac{\partial}{\partial y^*}\left(\mu^* \frac{\partial u^*}{\partial y^*}\right) \tag{2.3}$$

Energy Equation :

$$C_p^* \rho^* u^* \frac{\partial T^*}{\partial x^*} + C_p^* \rho^* v^* \frac{\partial T^*}{\partial y^*} = u^* \frac{dp^*}{dx^*} + \frac{\partial}{\partial y^*}\left(k^* \frac{\partial T^*}{\partial y^*}\right) + \mu^* \left(\frac{\partial u^*}{\partial y^*}\right)^2 \tag{2.4}$$

where μ^* and k^* are the coefficients of shear viscosity and thermal conductivity, respectively, and C_p^* is the specific heat at constant pressure.

The domain of the solution is $0 \le x^* < \infty$ and $-\infty < y^* < \infty$, see Fig. 2.1. Letting the subscripts 1 and 2 denote the upper and lower freestream conditions, we specify the initial conditions at $x^* = 0$ by

$$u^* = U_1^* \ , \ T^* = T_1^* \ \text{for} \ y^* > 0 \tag{2.5}$$

$$u^* = U_2^* \ , \ T^* = T_2^* \ \text{for} \ y^* < 0 \tag{2.6}$$

and the matching conditions by

$$u^* = U_1^* \ , \ T^* = T_1^* \ \text{as} \ y^* \to \infty \, , \ x^* > 0 \tag{2.7}$$

$$u^* = U_2^* \ , \ T^* = T_2^* \ \text{as} \ y^* \to -\infty \, , \ x^* > 0 \tag{2.8}$$

A third boundary condition must be specified on the transverse velocity component v^*. A practical approximation is to assume that the dividing streamline coincides with x^*-axis, hence the result :

$$v^* = 0 \quad \text{at} \ y^* = 0 \ , \ x^* \geq 0 \tag{2.9}$$

Ting (1959) showed that an approximate boundary condition on the transverse component can be obtained by considering the second-order terms in the asymptotic expansion of the boundary-layer theory. Ting's boundary condition is tantamount to equating the static pressures on the upper and lower sides of the displacement surface of the mixing layer. Klemp and Acrivos (1972) showed that Ting's boundary condition is incomplete when both streams are subsonic. Thus, one should use Ting's condition only if at least one of the streams is supersonic. However, different boundary conditions on the v^* component produce the same u^* and T^* profiles shifted only by different amounts in the transverse direction. This shift does not affect the parallel stability computations, however, it may have some effects on the nonparallel stability. For simplicity, the boundary condition given by (2.9) is used in the present work.

Next, we introduce the following nondimensional variables :

$$(x, y) = \frac{(x^*, y^*)}{L^*} \tag{2.10}$$

$$(u, v) = \frac{(u^*, v^*)}{U_1^*} \tag{2.11}$$

$$T = \frac{T^*}{T_1^*} \tag{2.12}$$

$$\rho = \frac{\rho^*}{\rho_1^*} \tag{2.13}$$

$$p = \frac{p^*}{\rho_1^* U_1^{*2}} \tag{2.14}$$

$$\mu = \frac{\mu^*}{\mu_1^*} \tag{2.15}$$

where L^* is a reference length that need not be specified at this point of analysis. The velocity U_1^*, temperature T_1^*, density ρ_1^*, and viscosity μ_1^* of the upper stream are used as reference values.

Substituting (2.10)-(2.15) into (2.2)-(2.4), we obtain the compressible boundary-layer equations in nondimensional form

$$\frac{\partial}{\partial x}(\rho u) + \frac{\partial}{\partial y}(\rho v) = 0 \tag{2.16}$$

$$\rho u \frac{\partial u}{\partial x} + \rho v \frac{\partial u}{\partial y} = -\frac{dp}{dx} + \frac{1}{Re_L} \frac{\partial}{\partial y}\left(\mu \frac{\partial u}{\partial y}\right) \tag{2.17}$$

$$\rho u \frac{\partial T}{\partial x} + \rho v \frac{\partial T}{\partial y} = Ec\, u \frac{dp}{dx} + \frac{1}{Re_L Pr} \frac{\partial}{\partial y} \left(\mu \frac{\partial T}{\partial y} \right) + Ec \frac{\mu}{Re_L} \left(\frac{\partial u}{\partial y} \right)^2 \quad (2.18)$$

where

$$Ec = \frac{U_1^{*2}}{C_p^* T_1^*} \quad (2.19)$$

$$Re_L = \frac{\rho_1^* U_1^* L^*}{\mu_1^*} \quad (2.20)$$

$$Pr = \frac{\mu_1^* C_p^*}{k_1^*} \quad (2.21)$$

These are the Eckert, Reynolds, and Prandtl numbers, respectively.

The initial conditions at $x = 0$ now become

$$u = 1 \ , \ T = 1 \ \text{ for } y > 0 \quad (2.22)$$

$$u = U_2 \ , \ T = T_2 \ \text{ for } y < 0 \quad (2.23)$$

and the boundary conditions become

$$u = 1, \quad T = 1 \ , \text{as } y \to \infty \ , \ x > 0 \quad (2.24)$$

$$u = U_2, \quad T = T_2 \ , \text{as } y \to -\infty \ , \ x > 0 \quad (2.25)$$

$$v = 0 \quad \text{at } y = 0 \ , \ x > 0 \quad (2.26)$$

We note that C_p^* and the Prandtl number Pr are assumed to be constant, and hence we replaced the nondimensional thermal conductivity k^*/k_1^* by the nondimensional viscosity μ^*/μ_1^*.

Unless otherwise specified, the Prandtl number Pr is assumed to be 0.72, the specific heat ratio $\gamma_e = 1.4$, and the viscosity-temperature relation is given by the Sutherland formula

$$\frac{\mu^*}{\mu_1^*} = \left(\frac{T^*}{T_1^*}\right)^{3/2} \frac{T_1^* + T_a^*}{T^* + T_a^*} \tag{2.27}$$

where $T_a^* = 110.4^\circ K$ for air and $T_1^* = 273^\circ K$.

Levy-Lees Transformation

The use of a similarity type transformation simplifies the application of the boundary and initial conditions in compressible boundary-layer computations. It also alleviates (or eliminates) the growth of the boundary layer thickness in terms of the transformed variables. Although the present problem admits a self-similar solution, we present here the general case of nonsimilar flows and allow U_1, ρ_1, and T_1 to be functions of x, but rename them by U_e, ρ_e, and T_e, respectively. We note also that the present analysis applies to nonsimilar compressible boundary layers without modifications. We use the Levy-Lees transformation (Blottner, 1975) that is given by

$$\xi(x) = \int_0^x \rho_e \mu_e U_e dx \tag{2.28}$$

$$\eta(x,y) = \frac{\rho_e U_e}{\sqrt{2\xi}} \int_0^y \frac{\rho}{\rho_e} dy \tag{2.29}$$

The velocity and temperature profiles are normalized with $U_\bullet$ and $T_\bullet$, respectively,

$$F(\xi, \eta) = \frac{u(x, y)}{U_e(x)} \tag{2.30}$$

$$Q(\xi, \eta) = \frac{T(x, y)}{T_e(x)} \tag{2.31}$$

Changing variables in (2.16)-(2.18), we obtain

Continuity Equation :

$$2\xi \frac{\partial F}{\partial \xi} + \frac{\partial V}{\partial \eta} + F = 0 \tag{2.32}$$

X-Momentum Equation :

$$2\xi F \frac{\partial F}{\partial \xi} + V \frac{\partial F}{\partial \eta} - \frac{\partial}{\partial \eta}\left(\theta \frac{\partial F}{\partial \eta}\right) + \beta(F^2 - Q) = 0 \tag{2.33}$$

Energy Equation :

$$2\xi F \frac{\partial Q}{\partial \xi} + V \frac{\partial Q}{\partial \eta} - \frac{1}{Pr} \frac{\partial}{\partial \eta}\left(\theta \frac{\partial Q}{\partial \eta}\right) - Ec\,\theta \left(\frac{\partial F}{\partial \eta}\right)^2 = 0 \tag{2.34}$$

where

$$V(\xi, \eta) = \frac{\sqrt{2\xi}}{\rho_e \mu_e U_e}\left(\rho v \sqrt{Re_L} + \sqrt{2\xi} \frac{\partial \eta}{\partial x} F\right) \tag{2.35}$$

$$Ec = (\gamma_g - 1)M_1^2 \frac{U_e^2}{T_e} \tag{2.36}$$

$$\theta = \frac{\rho\mu}{\rho_e\mu_e} \tag{2.37}$$

$$\beta = \frac{2\xi}{U_e}\frac{dU_e}{d\xi} \tag{2.38}$$

where M_1 is the Mach number in the freestream and β is called the pressure gradient parameter; in general, it is a function of x (or ξ). In our study, $\beta = 0$. Because there is no pressure variation across the shear layer, the equation of state gives

$$\rho T = \rho_e T_e \tag{2.39}$$

and hence (2.37) can be written as

$$\theta = Q^{1/2}\frac{1 + T_a/T_e}{Q + T_a/T_e} \tag{2.40}$$

The boundary conditions (2.24)-(2.26) become

$$F = 1\,,\ Q = 1 \ \text{ as } \eta \to \infty. \tag{2.41}$$

$$F = \phi_2\,,\ Q = \psi_2 \text{ as } \eta \to -\infty \tag{2.42}$$

$$V = 0 \text{ at } \eta = 0 \tag{2.43}$$

where $\phi_2 = U_2/U_e$ and $\psi_2 = T_2/T_e$.

2.3 A Finite-Difference Method for Compressible Shear Layers

In this section, we present a finite-difference method for solving the steady two-dimensional compressible boundary-layer equations. The method is implicit, fourth-order accurate in the step size in the η -direction, and second-order accurate in the step size in the ξ -direction. The method provides highly accurate velocity and temperature profiles as well as their partial derivatives with respect to x and y that are needed for viscous stability analyses.

The present method is an extension of the Keller box scheme (Keller, 1978) which is first presented by Wornom (1977a, 1977b) for incompressible flows. Malik (1988) also used the same method to solve the self-similar compressible equations, but no details were provided. Here, we describe the method in full details for *nonsimilar* compressible bounded- and free-shear layers.

We introduce the new variables

$$Z_1 = V \tag{2.44}$$

$$Z_2 = F \tag{2.45}$$

$$Z_3 = \frac{\partial F}{\partial \eta} \tag{2.46}$$

$$Z_4 = Q \tag{2.47}$$

$$Z_5 = \frac{\partial Q}{\partial \eta} \tag{2.48}$$

and reduce the governing equations to a system of first-order equations for Z_m(m = 1,.., 5). After straightforward algebraic manipulations, we obtain from (2.32)-(2.34)

$$\frac{\partial Z_m}{\partial \eta} = g_m, \quad m = 1, .., 5. \tag{2.49}$$

where

$$g_1 = -Z_2 - 2\xi Z_{2,\xi} \tag{2.50}$$

$$g_2 = Z_3 \tag{2.51}$$

$$g_3 = \frac{1}{\theta}[(Z_1 - \theta' Z_5) Z_3 + 2\xi Z_2 Z_{2,\xi} + \beta(Z_2^2 - Z_4)] \tag{2.52}$$

$$g_4 = Z_5 \tag{2.53}$$

$$g_5 = \frac{Pr}{\theta}[(Z_1 - \frac{\theta'}{Pr} Z_5) Z_5 + 2\xi Z_2 Z_{4,\xi} - Ec\,\theta Z_3^2] \tag{2.54}$$

where $Z_{m,\xi} = \frac{\partial Z_m}{\partial \xi}$ and

$$\theta' = \frac{d\theta}{dZ_4} \tag{2.55}$$

The method can be applied directly to the system (2.49). However, we find that the algebra is somewhat easier if we recast the left-hand side of the system in terms of the new variables G_m that are related to Z_m by

$$G_1 = Z_1 \tag{2.56}$$

$$G_2 = Z_2 \tag{2.57}$$

$$G_3 = \theta Z_3 - Z_1 Z_2 \tag{2.58}$$

$$G_4 = Z_4 \tag{2.59}$$

$$G_5 = \frac{\theta Z_5}{Pr} - Z_1 Z_4 \tag{2.60}$$

Hence, the system of the equations (2.49) are written

$$G'_m = \Lambda_m, \quad m = 1, .., 5 \tag{2.61}$$

where

$$\Lambda_1 = -2\xi Z_{2,\xi} - Z_2 \tag{2.62}$$

$$\Lambda_2 = Z_3 \tag{2.63}$$

$$\Lambda_3 = 4\xi Z_2 Z_{2,\xi} + (1+\beta) Z_2^2 - \beta Z_4 \tag{2.64}$$

$$\Lambda_4 = Z_5 \tag{2.65}$$

$$\Lambda_5 = 2\xi (Z_2 Z_4)_{,\xi} + Z_2 Z_4 - Ec\, \theta Z_3^2 \tag{2.66}$$

To solve the system (2.61) using finite differences, we establish a Cartesian grid in the domain of interest in the $\xi - \eta$ plane. The grid points are denoted by ξ_i (i = 1, ..., M) and η_j (j = 1, ..., N), where M and N are the total number of points in the ξ – and η – directions, respectively. The grid need not be uniform in either direction.

The present higher-order method is based on the following **Euler-Maclurin** formula for a smooth function f(η) (see Keller, 1978) :

$$\int_{\eta_{j-1}}^{\eta_j} f d\eta = \frac{h_j}{2}(f_j + f_{j-1}) - \frac{h_j^2}{12}(f'_j - f'_{j-1}) + \frac{h_j^4}{720}(f'''_j - f'''_{j-1}) + O(h_j^7) \tag{2.67}$$

where a prime denotes differentiation with respect to η and

$$h_j = \eta_j - \eta_{j-1} \tag{2.68}$$

Letting $f = G'$ and noting that $G_j^{iv} - G_{j-1}^{iv} = O(h_j)$, we obtain from (2.67) that

$$(G_j - G_{j-1}) - \frac{h_j}{2}(G'_j + G'_{j-1}) + \frac{h_j^2}{12}(G''_j - G''_{j-1}) + O(h_j^5) = 0 \tag{2.69}$$

where $G'_j = \dfrac{\partial G_j}{\partial \eta}$ and $G_j'' = \dfrac{\partial^2 G_j}{\partial \eta^2}$.

Now, the function G in (2.69) is replaced by the vector G_m and G'_m by Λ_m. The second derivatives G''_m are obtained by differentiating (2.61) with respect to η and then using (2.49) again to eliminate Z'_m. The result is

$$G''_m = \Gamma_m, \quad m = 1, .., 5. \tag{2.70}$$

where

$$\Gamma_1 = -2\xi Z_{3,\xi} - Z_3 \tag{2.71}$$

$$\Gamma_2 = \frac{1}{\theta}[(Z_1 - \theta' Z_5) Z_3 + 2\xi Z_2 Z_{2,\xi} + \beta(Z_2^2 - Z_4)] \tag{2.72}$$

$$\Gamma_3 = 4\xi(Z_3 Z_{2,\xi} + Z_2 Z_{3,\xi}) + 2(1+\beta) Z_2 Z_3 - \beta Z_5 \tag{2.73}$$

$$\Gamma_4 = \frac{Pr}{\theta}\left[\left(Z_1 - \frac{\theta'}{Pr} Z_5\right) Z_5 + 2\xi Z_2 Z_{4,\xi} - Ec\,\theta Z_3^2\right] \tag{2.74}$$

$$\begin{aligned}\Gamma_5 = {} & 2\xi\left(Z_3 Z_4 + Z_2 Z_5\right)_{,\xi} + Z_3 Z_4 + Z_2 Z_5 + Ec\,\theta' Z_5 Z_3^2 \\ & - 2\,Ec\,Z_3\left[Z_1 Z_3 + 2\xi Z_2 Z_{2,\xi} + \beta\left(Z_2^2 - Z_4\right)\right]\end{aligned} \tag{2.75}$$

At the grid point (ξ_i, η_j), the ξ – derivatives $Z_{2,\xi}$, $Z_{3,\xi}$, $Z_{4,\xi}$, and $Z_{5,\xi}$ are replaced by the three-point backward formulae

$$\left(Z_{2,\xi}\right)_j^i = a_{0i} Z_{2j}^i + a_{1i} Z_{2j}^{i-1} + a_{2i} Z_{2j}^{i-2} \tag{2.76}$$

$$\left(Z_{3,\xi}\right)_j^i = a_{0i} Z_{3j}^i + a_{1i} Z_{3j}^{i-1} + a_{2i} Z_{3j}^{i-2} \tag{2.77}$$

$$\left(Z_{4,\xi}\right)_j^i = a_{0i} Z_{4j}^i + a_{1i} Z_{4j}^{i-1} + a_{2i} Z_{4j}^{i-2} \tag{2.78}$$

$$\left(Z_{5,\xi}\right)_j^i = a_{0i} Z_{5j}^i + a_{1i} Z_{5j}^{i-1} + a_{2i} Z_{5j}^{i-2} \tag{2.79}$$

where

$$a_{0i} = \frac{2\xi_i - \xi_{i-1} - \xi_{i-2}}{\left(\xi_i - \xi_{i-1}\right)\left(\xi_i - \xi_{i-2}\right)} \tag{2.80}$$

$$a_{1i} = -\frac{\xi_i - \xi_{i-2}}{\left(\xi_i - \xi_{i-1}\right)\left(\xi_{i-1} - \xi_{i-2}\right)} \tag{2.81}$$

$$a_{2i} = \frac{\xi_i - \xi_{i-1}}{\left(\xi_i - \xi_{i-2}\right)\left(\xi_{i-1} - \xi_{i-2}\right)} \tag{2.82}$$

Expressions (2.76)-(2.79) imply that the vector $Z_m(j)$, $m = 1, \ldots, 5$ is known at all values of j at the two stations ξ_{i-1} and ξ_{i-2}. In a marching scheme, these values are available

if $i \geq 3$. At $i=1$, $\xi_1 = 0$ and hence $\xi_1 Z_{2,\xi}$, $\xi_1 Z_{3,\xi}$, $\xi_1 Z_{4,\xi}$, and $\xi_1 Z_{5,\xi}$ are equal to zero. Thus we may take

$$a_{01} = 0,\ a_{11} = 0, \text{ and } a_{21} = 0 \quad \text{for } i = 1 \tag{2.83}$$

This substitution also takes care of the initial conditions because the resulting equations are self-similar. At $i=2$, we drop the accuracy to first-order in $\Delta\xi$ and use the two-point backward differencing formula

$$a_{02} = \frac{1}{\xi_2 - \xi_1} = -a_{12}, \quad a_{22} = 0 \quad \text{for } i = 2 \tag{2.84}$$

We may compensate for the loss of accuracy due to this approximation by using a very small $\Delta\xi$ in the initial region. A more accurate approach is to use a Crank-Nicholsen differencing at the expense of a somewhat more complex equations.

With G_m, G'_m, and G''_m given by (2.56)-(2.60), (2.61) and (2.70), and $Z_{2,\xi}$, $Z_{3,\xi}$, $Z_{4,\xi}$, and $Z_{5,\xi}$ given by (2.76)-(2.79), application of (2.69) at the grid points $j=2,\ldots, N$ results in a system of (5N-5) nonlinear equations in the 5N unknowns $Z_m(j)$, $m=1, .., 5$ and $j=1, .., N$ at the ξ_i. This system is closed by writing the boundary and matching conditions. Letting $j=N$ denote the condition as $\eta \to \infty$, we set

$$Z_2 = 1, \quad Z_4 = 1 \quad \text{at } j=N \tag{2.85}$$

For boundary-layer applications, we let $j=1$ denote the wall boundary condition, and hence

$$Z_1 = 0 \quad \text{at } j = 1 \ (\text{no suction or blowing}) \tag{2.86}$$

$$Z_2 = 0 \quad \text{at } j = 1 \ (\text{no} - \text{slip}) \tag{2.87}$$

$$Z_4 = Q_w \quad \text{at } j = 1 \quad (\text{specified wall temperature}) \tag{2.88}$$

or

$$Z_5 = q_w \quad \text{at } j = 1 \quad (\text{specified rate of heat transfer})$$

For free shear-layer applications, we let $j=1$ denote the condition as $\eta \to -\infty$. Then from (2.42) we have

$$Z_2 = \phi_2 , \quad Z_4 = \psi_2 \quad \text{at } j=1 \tag{2.89}$$

The boundary condition (2.43) now reads

$$Z_1 = 0 \quad \text{at } \eta = 0 \tag{2.90}$$

This condition is satisfied iteratively. First a value of Z_1 is estimated at $j=1$, and the system of equations is solved yielding a value for Z_1 at $\eta = 0$. The estimated value of Z_1 is then updated through a Newton-Raphson procedure to make the computed Z_1 vanish at $\eta = 0$.

The nonlinear algebraic system can be solved by a Newton iterative method starting from a reasonable initial estimate of all the variables. An equivalent procedure is to linearize (also called quasi-linearization) the expressions of G_m ,G'_m, and G''_m before substitution into (2.69), and thus the resulting algebraic system will be linear. The second approach is followed here. In a certain iteration, the current values of Z_m are written as

$$Z_m = \bar{Z}_m + \delta Z_m , \quad m = 1, .., 5. \tag{2.91}$$

where a bar indicates a value known from the previous iteration or an initial estimate and δZ_m is a small variation to Z_m. Substituting (2.91) into (2.56)-(2.60), we obtain

$$G_m = \overline{G}_m + C_{mk}\,\delta Z_k, \quad m = 1, .., 5, \quad k = 1, .., 5. \tag{2.92}$$

where the Jacobian matrix C_{mk}, after dropping the bar for simplicity, is

$$C_{mk} = \frac{\partial G_m}{\partial Z_k} \rightarrow \begin{bmatrix} 1 & 0 & 0 & 0 & 0 \\ 0 & 1 & 0 & 0 & 0 \\ -Z_2 & -Z_1 & \theta & \theta' Z_3 & 0 \\ 0 & 0 & 0 & 1 & 0 \\ -Z_4 & 0 & 0 & -Z_1 + \dfrac{\theta' Z_5}{Pr} & \dfrac{\theta}{Pr} \end{bmatrix} \tag{2.93}$$

Similarly, (2.61) becomes

$$G'_m = \overline{\Lambda}_m + A_{mk}\,\delta Z_k, \quad m = 1, .., 5, \quad k = 1, .., 5. \tag{2.94}$$

where

$$A_{mk} = \frac{\partial \Lambda_m}{\partial Z_k} \rightarrow \begin{bmatrix} 0 & -1 - 2\xi_i a_{0i} & 0 & 0 & 0 \\ 0 & 0 & 1 & 0 & 0 \\ 0 & A_{32} & 0 & -\beta & 0 \\ 0 & 0 & 0 & 0 & 1 \\ 0 & A_{52} & -2Ec\theta Z_3 & A_{54} & 0 \end{bmatrix} \tag{2.95}$$

where

$$A_{32} = 2(1 + \beta + 2\xi_i a_{0i}) Z_2 + 4\xi_i Z_{2,\xi}$$

$$A_{52} = (1 + 2\xi_i a_{0i})Z_4 + 2\xi_i Z_{4,\xi}$$

$$A_{54} = (1 + 2\xi_i a_{0i})Z_2 + 2\xi_i Z_{2,\xi} - Ec\,\theta' Z_3^2$$

and (2.70) becomes

$$G''_m = \overline{\Gamma}_m + B_{mk}\,\delta Z_k, \quad m = 1, .., 5, \quad k = 1, .., 5. \tag{2.96}$$

$$B_{mk} = \frac{\partial \Gamma_m}{\partial Z_k} \rightarrow \begin{bmatrix} 0 & 0 & -2\,\xi_i a_{0i} - 1 & 0 & 0 \\ \dfrac{Z_3}{\theta} & B_{22} & \dfrac{Z_1 - \theta' Z_5}{\theta} & B_{24} & \dfrac{-\theta' Z_3}{\theta} \\ 0 & B_{32} & B_{33} & 0 & -\beta \\ \dfrac{PrZ_5}{\theta} & \dfrac{2\xi_i Z_{4,\xi} Pr}{\theta} & -2Ec\,PrZ_3 & B_{44} & \dfrac{-2\theta' Z_5}{\theta} \\ -2Ec\,Z_3^2 & B_{52} & B_{53} & B_{54} & B_{55} \end{bmatrix} \tag{2.97}$$

where

$$B_{22} = \frac{2\xi_i}{\theta}(Z_{2,\xi} + Z_2 a_{0i}) + \frac{2\beta Z_2}{\theta}$$

$$B_{24} = \frac{-1}{\theta}(\theta'' Z_5 Z_3 + \beta + \theta' \Gamma_2)$$

$$B_{32} = 4\xi_i (Z_3 a_{0i} + Z_{3,\xi}) + 2(1 + \beta)Z_3$$

$$B_{33} = 4\xi_i (Z_2 a_{0i} + Z_{2,\xi}) + 2(1 + \beta)Z_2$$

$$B_{44} = \frac{-Pr}{\theta}\left(\frac{\theta''}{Pr} Z_5^2 - 2\xi_i Z_2 a_{0i} + Ec\theta' Z_3^2 + \frac{\theta' \Gamma_4}{Pr}\right)$$

$$B_{52} = 2\xi_i Z_{5,\xi} + (1 + 2\xi_i a_{0i})Z_5 - 4EcZ_3[\xi_i Z_{2,\xi} + (\xi_i a_{0i} + \beta)Z_2]$$

$$B_{53} = 2\xi_i Z_{4,\xi} + (1 + 2\xi_i a_{0i})Z_4 + 2Ec\theta' Z_5 Z_3 - 2Ec[2Z_1 Z_3 + 2\xi_i Z_2 Z_{2,\xi} + \beta(Z_2^2 - Z_4)]$$

$$B_{54} = 2\xi_i Z_{3,\xi} + (1 + 2\xi_i a_{0i})Z_3 + Ec\theta'' Z_5 Z_3^2 + 2EcZ_3\beta$$

$$B_{55} = 2\xi_i Z_{2,\xi} + (1 + 2\xi_i a_{0i})Z_2 + Ec\theta' Z_3^2$$

Substituting (2.92), (2.94), and (2.96) into (2.69) at the grid point (i,j), we obtain the following system of equations :

$$[\mathbf{D}]_j \delta Z_{j-1} + [\mathbf{E}]_j \delta Z_j = [\mathbf{H}]_j , \quad 2 \le j \le N \tag{2.98}$$

where

$$D_{mk} = -C_{mk}^- - \frac{h_j}{2} A_{mk}^- - \frac{h_j^2}{12} B_{mk}^- \tag{2.99}$$

$$E_{mk} = C_{mk} - \frac{h_j}{2} A_{mk} + \frac{h_j^2}{12} B_{mk} \tag{2.100}$$

$$H_m = -G_m + \frac{h_j}{2}\Lambda_m - \frac{h_j^2}{12}\Gamma_m + G_m^- + \frac{h_j}{2}\Lambda_m^- + \frac{h_j^2}{12}\Gamma_m^- \tag{2.101}$$

where m, k = 1 ,..., 5 and the superscript − means that the entries are evaluated at j-1.

Since $Z_1(1)$, $Z_2(1)$, $Z_4(1)$, $Z_2(N)$, and $Z_4(N)$ are fixed by the boundary conditions, we have

$$\delta Z_1(1) = 0 \tag{2.102}$$

$$\delta Z_2(1) = 0 \tag{2.103}$$

$$\delta Z_4(1) = 0 \tag{2.104}$$

$$\delta Z_2(N) = 0 \tag{2.105}$$

$$\delta Z_4(N) = 0 \tag{2.106}$$

The insulated wall case is treated by replacing (2.104) by $\delta Z_5(1) = 0$.

Now, the system (2.98) and the five boundary conditions (2.102)-(2.106) give a linear system to be solved for $\delta Z_m(j)$, $m = 1, ..., 5$ and $j = 1, ..., N$. The composite system is restructured as a block tridiagonal system using a procedure similar to that of Cebeci and Smith (1974) for the incompressible case.

The boundary conditions (2.102)-(2.106) and the system (2.98) at $j=2$ are rewritten in matrix form as

$$\begin{bmatrix} \mathbf{B}_1 & \mathbf{C}_1 & \mathbf{0} \\ \mathbf{A}_2 & \mathbf{B}_2 & \mathbf{C}_2 \end{bmatrix} \begin{bmatrix} \underset{\sim}{W}_1 \\ \underset{\sim}{W}_2 \\ \underset{\sim}{W}_3 \end{bmatrix} = \begin{bmatrix} \underset{\sim}{H}_1 \\ \underset{\sim}{H}_2 \end{bmatrix} \tag{2.107}$$

where

$$\underset{\sim}{W}_1 = \begin{bmatrix} \delta Z_2(0) \\ \delta Z_4(0) \\ \delta Z_1(1) \\ \delta Z_2(1) \\ \delta Z_4(1) \end{bmatrix} \tag{2.108}$$

$$\underline{W}_2 = \begin{bmatrix} \delta Z_3(1) \\ \delta Z_5(1) \\ \delta Z_1(2) \\ \delta Z_3(2) \\ \delta Z_5(2) \end{bmatrix} \tag{2.109}$$

$$\mathbf{B}_1 = \begin{bmatrix} 1 & 0 & 0 & 0 & 0 \\ 0 & 1 & 0 & 0 & 0 \\ 0 & 0 & 1 & 0 & 0 \\ 0 & 0 & 0 & 1 & 0 \\ 0 & 0 & 0 & 0 & 1 \end{bmatrix} \tag{2.110}$$

$$\mathbf{C}_1 = [\,\mathbf{0}\,]_{5\times5}$$

$$\mathbf{A}_2 = \begin{bmatrix} 0 & 0 & D_{11} & D_{12} & D_{14} \\ 0 & 0 & D_{21} & D_{22} & D_{24} \\ 0 & 0 & D_{31} & D_{32} & D_{34} \\ 0 & 0 & D_{41} & D_{42} & D_{44} \\ 0 & 0 & D_{51} & D_{52} & D_{54} \end{bmatrix} \tag{2.111}$$

$$\mathbf{B}_2 = \begin{bmatrix} D_{13} & D_{15} & E_{11} & E_{13} & E_{15} \\ D_{23} & D_{25} & E_{21} & E_{23} & E_{25} \\ D_{33} & D_{35} & E_{31} & E_{33} & E_{35} \\ D_{43} & D_{45} & E_{41} & E_{43} & E_{45} \\ D_{53} & D_{55} & E_{51} & E_{53} & E_{55} \end{bmatrix} \tag{2.112}$$

$$C_2 = \begin{bmatrix} E_{12} & E_{14} & 0 & 0 & 0 \\ E_{22} & E_{24} & 0 & 0 & 0 \\ E_{32} & E_{34} & 0 & 0 & 0 \\ E_{42} & E_{44} & 0 & 0 & 0 \\ E_{52} & E_{54} & 0 & 0 & 0 \end{bmatrix} \tag{2.113}$$

$$\underset{\sim}{H}_1 = [0]_{5\times 1}$$

$$\underset{\sim}{H}_2 = \begin{bmatrix} H_1(2) \\ H_2(2) \\ H_3(2) \\ H_4(2) \\ H_5(2) \end{bmatrix} \tag{2.114}$$

where $\delta Z_2(0)$ and $\delta Z_4(0)$ are dummy variables that have no significance to the problem.

For $3 \leq j \leq N$, (2.98) is rearranged in the form

$$A_j \underset{\sim}{W}_{j-1} + B_j \underset{\sim}{W}_j + C_j \underset{\sim}{W}_{j+1} = \underset{\sim}{H}_j \tag{2.115}$$

where

$$\underset{\sim}{W}_j = \begin{bmatrix} \delta Z_2(j-1) \\ \delta Z_4(j-1) \\ \delta Z_1(j) \\ \delta Z_3(j) \\ \delta Z_5(j) \end{bmatrix} \tag{2.116}$$

$$\mathbf{A}_j = \begin{bmatrix} 0 & 0 & D_{11} & D_{13} & D_{15} \\ 0 & 0 & D_{21} & D_{23} & D_{25} \\ 0 & 0 & D_{31} & D_{33} & D_{35} \\ 0 & 0 & D_{41} & D_{43} & D_{45} \\ 0 & 0 & D_{51} & D_{53} & D_{55} \end{bmatrix} \tag{2.117}$$

$$\mathbf{B}_j = \begin{bmatrix} D_{12} & D_{14} & E_{11} & E_{13} & E_{15} \\ D_{22} & D_{24} & E_{21} & E_{23} & E_{25} \\ D_{32} & D_{34} & E_{31} & E_{33} & E_{35} \\ D_{42} & D_{44} & E_{41} & E_{43} & E_{45} \\ D_{52} & D_{54} & E_{51} & E_{53} & E_{55} \end{bmatrix} \tag{2.118}$$

$$\mathbf{C}_j = \begin{bmatrix} E_{12} & E_{14} & 0 & 0 & 0 \\ E_{22} & E_{24} & 0 & 0 & 0 \\ E_{32} & E_{34} & 0 & 0 & 0 \\ E_{42} & E_{44} & 0 & 0 & 0 \\ E_{52} & E_{54} & 0 & 0 & 0 \end{bmatrix} \tag{2.119}$$

$$\underset{\sim}{H}_j = \begin{bmatrix} H_1(j) \\ H_2(j) \\ H_3(j) \\ H_4(j) \\ H_5(j) \end{bmatrix} \tag{2.120}$$

Equations (2.107)-(2.120) are combined into the general block tridiagonal system

$$\begin{bmatrix} B_1 & C_1 & 0 & 0 & 0 & 0 & 0 & 0 \\ A_2 & B_2 & C_2 & 0 & 0 & 0 & 0 & 0 \\ 0 & A_3 & B_3 & C_3 & 0 & 0 & 0 & 0 \\ 0 & 0 & -- & -- & -- & 0 & 0 & 0 \\ 0 & 0 & 0 & -- & -- & 0 & 0 & 0 \\ 0 & 0 & 0 & A_j & B_j & C_j & 0 & 0 \\ 0 & 0 & 0 & 0 & 0 & -- & -- & 0 \\ 0 & 0 & 0 & 0 & 0 & A_{N-1} & B_{N-1} & C_{N-1} \\ 0 & 0 & 0 & 0 & 0 & 0 & A_N & B_N \end{bmatrix} \begin{bmatrix} \underset{\sim}{W}_1 \\ \underset{\sim}{W}_2 \\ \underset{\sim}{W}_3 \\ : \\ : \\ \underset{\sim}{W}_j \\ : \\ \underset{\sim}{W}_{N-1} \\ \underset{\sim}{W}_N \end{bmatrix} = \begin{bmatrix} \underset{\sim}{H}_1 \\ \underset{\sim}{H}_2 \\ \underset{\sim}{H}_3 \\ : \\ : \\ \underset{\sim}{H}_j \\ : \\ \underset{\sim}{H}_{N-1} \\ \underset{\sim}{H}_N \end{bmatrix} \tag{2.121}$$

We note that the boundary conditions at $j=N$ need no special treatment because $C_N \underset{\sim}{W}_{N+1}$ vanishes.

A standard procedure for solving (2.121) is as follows:

First, we compute

$$Q_1 = B_1 \tag{2.122}$$

$$R_1 = Q_1^{-1} C_1 \tag{2.123}$$

$$\underset{\sim}{S}_1 = Q_1^{-1} \underset{\sim}{H}_1 \tag{2.124}$$

Next, for $j = 2, ..., N$ we compute

$$Q_j = B_j - A_j R_{j-1} \tag{2.125}$$

$$R_j = Q_j^{-1} C_j \tag{2.126}$$

$$\underset{\sim}{S}_j = Q_j^{-1}(\underset{\sim}{H}_j - A_j \underset{\sim}{S}_{j-1}) \tag{2.127}$$

Then,

$$\underset{\sim}{W}_N = \underset{\sim}{S}_N \tag{2.128}$$

and for j = N-1, ..., 1, we compute

$$\underset{\sim}{W}_j = \underset{\sim}{S}_j - \mathbf{R}_j \underset{\sim}{W}_{j+1} \tag{2.129}$$

We note that the above algorithm can be simplified by taking advantage of the special format of the matrices $\mathbf{A}_j$ and $\mathbf{C}_j$; this has not been done in the computer program that we developed, however.

2.4 *Numerical Results*

Step Size Study

The method presented in Section 2.3 is programmed for self-similar shear layers. Here we present results for a mixing layer and a zero pressure gradient insulated wall boundary layer.

To verify the fourth-order accuracy of the code, we conduct a step size study. We want to verify that the truncation error is $O(h^4)$. To this end, we assume a uniform grid and obtain solutions using different values of h. The solutions obtained on the finest grid (h = 0.01 for the Blasius boundary layer case and h = 0.03125 for the mixing-layer case) are considered to give the exact solutions against which coarser grid results are calibrated.

Let G^h denote Z_3 at $\eta = 0$ obtained on a grid of step size h, and G^* denote the corresponding value obtained on the finest grid. For the Blasius flow at $M_\infty = 4.5$, Fig. 2.3 shows the variation of $|G^h - G^*|$ with the step size h on a log-log scale. The relationship is linear with a slope of 4, and hence the fourth-order accuracy of the method is verified. Fig. 2.3 also includes results for the second-order scheme obtained by dropping the $O(h^2)$ term in (2.69). As anticipated the slope is 2, and the second-order accuracy is verified.

The case of a mixing layer at $M_1 = 5$, $T_2 = 2$, and $U_2 = 0$ is shown in Fig. 2.4. Once again the results verify the fourth-order accuracy of the code.

Laminar Mixing Layer Profiles

Next, we discuss the mean-flow profiles for a single stream mixing layer ($U_2 = 0$). The Prandtl number is assumed to be 0.72 and the viscosity-temperature relation is specified by the Sutherland formula (2.27) with $T^*_\infty = 273°K$ at all Mach numbers and temperature ratios. For the three temperature ratios $T_2 = 0.5$, 1.0 and 2.0, the velocity profiles are shown in Figs. 2.5-2.7. The y coordinate is scaled by $\delta^* = \sqrt{\nu^*_1 x^*/U^*_1}$, which is the scaling that we usually use for stability analysis. We note that δ^* is independent of the flow parameters, such as the Mach number, temperature ratio, etc. We note that the profiles are not symmetric with respect to $y = 0$ and that diffusion is more pronounced in the lower stream than in the upper stream. Moreover, the shear-layer thickness increases with increasing the Mach number and temperature ratio. These characteristics can also be observed in Figs. 2.8-2.10, which depict the vorticity profiles dU/dy. The maximum vorticity decreases very rapidly as the Mach number is increased, especially when the Mach number is low and the stagnant stream is colder than the moving stream; i.e. $T_2 < 1$. However, the area

under the vorticity DU-y curve is the same for all flow conditions because this area is equal to $U_1 - U_2 = 1$. The temperature profiles are shown in Figs. 2.11-2.13. The rise in the temperature profiles near the center increases with increasing Mach number due to the viscous dissipation which scales with $(\gamma_g - 1)M_1^2$, where $\gamma_g = 1.4$. Once again, we note the deeper penetration of temperature changes in the lower stream as the Mach number is increased. It is also interesting to note that in the limit $x \to 0$, the temperature profile has a spike at $y = 0$.

The quantity D(DU/T) is of importance in compressible inviscid stability theory. It was shown by Lees and Lin (1946) that the vanishing of this quantity somewhere in the shear layer is a necessary and sufficient condition for the existence of a neutral subsonic wave. The phase speed of this wave is given by the mean flow velocity at the point where D(DU/T) vanishes. This point is called a generalized inflection point by Mack (1969). Furthermore, Jackson and Grosch (1989) investigated the effects of Pr and viscosity on the roots of D(DU/T) and found that it is possible to have three roots depending on the Mach number and temperature ratio. The profiles D(DU/T) are shown in Figs. 2.14-2.16 for the three temperature ratios $T_2 = 0.5$, 1.0 and 2.0. We note that there is only one generalized inflection point.

Hyperbolic-Tangent Approximation

In Chapter 5 and 7 we present stability characteristics for the hyperbolic-tangent velocity profile. Here we discuss that profile as an approximation to the laminar mixing-layer profile. As we mentioned in Section (2.1), the hyperbolic-tangent profile is also a good approximation to measured turbulent velocity profiles, but with a length scale different from the laminar case. Let $y = y^*/\delta^*$, where $\delta^* = \sqrt{\nu_1^* x^*/U_1^*}$, the laminar mixing-layer profiles shown in Figs. 2.18-2.21 are approximated by

$$U = \frac{1}{2}\left[1 + U_2 + (1 - U_2)\tanh ay\right] \tag{2.130}$$

where "a" is a parameter that depends on the Mach number, velocity ratio and temperature ratio. We determine "a" such that the maximum vorticity of the hyperbolic-tangent profile is equal to the maximum vorticity in the exact solution to the compressible boundary-layer equations. Thus, we have

$$a = 2\left(dU/dy\right)_{max} \tag{2.131}$$

where $(dU/dy)_{max}$ is determined numerically for each Mach number, velocity ratio, and temperature ratio. The variation of "a" with M_1 is shown in Fig. 2.17 for different T_2 and $U_2 = 0$.

The velocity vorticity, and temperature profiles are shown in Figs. 2.18-2.20, respectively. Although the maximum values of vorticity are the same as those of the exact solution, the profiles shown in Fig. 2.20 are symmetric, which differ from the exact profiles shown in Fig. 2.8. The temperature profiles are obtained from Busemann-Crocco integral. Finally, the function D(DU/T) is shown in Fig. 2.21, and we note that there is only one generalized inflection point.

Because the vorticity thickness δ^*_ω is defined by

$$\delta^*_\omega = \frac{U^*_1 - U^*_2}{(dU^*/dy^*)_{max}} \tag{2.132}$$

or

$$\frac{\delta^*_\omega}{\delta^*} = \frac{1 - U_2}{(dU/dy)_{max}}$$

the parameter "a" is given by

$$a^{-1} = \frac{1}{2} \frac{\delta^*_\omega}{\delta^*} \tag{2.133}$$

This relation helps in transforming data based on δ^* as the reference length to data based on the vorticity thickness as the reference length. For a direct evaluation of the effects of approximating the actual velocity profile by a hyperbolic-tangent profile on the stability characteristics, we prefer to work with the form (2.130) rather than the classical form, which incorporates the factor (tanh y). The latter makes the reference length a function of the flow parameters, such as the Mach number, velocity ratio, and temperature ratio.

3.0 Linear Instability

3.1 Introduction

In this chapter, we investigate the propagation of small disturbances in compressible mixing layers using linear stability theory. Linear stability analysis of free shear layers is a very simple and inexpensive method that provides valuable information about the range of amplified frequencies, the most amplified frequency, the maximum growth rate, and the streamwise as well as the transverse extent of disturbances. The analysis also helps in investigating the effects of key parameters such as the Mach number, Reynolds number, velocity ratio, temperature ratio, and chemical composition of the two streams, on the previously mentioned stability characteristics. Stability analysis can also provide meaningful initial and boundary conditions for more elaborate computational efforts, which aim at analyzing the nonlinear development of disturbances and/or controlling the shear layer by active or passive means.

In Section 3.2, a linear stability theory of slightly nonparallel free-shear layers is presented. The method of multiple scales is used to account for the nonparallel effects. The theory has been developed and documented in the works of Nayfeh and co-workers (Nayfeh 1980, Nayfeh and Reed 1982). For completeness and further reference, the theory is reproduced here. To the best of our knowledge, the present effort is the first application of the viscous theory to compressible shear layers.

In Section 3.3, the boundary conditions appropriate for unbounded mixing layers are presented. In Section 3.4, the nonparallel correction is presented. Finally, in Section 3.5, the inviscid theory of quasi-parallel flows is presented.

3.2 Equations of Linear Stability Theory of Slightly Nonparallel Shear Layers

The presentation in this section follows closely that given by Reed (1981).

To study the linear instabilities of a steady basic state, we superimpose a small time-dependent disturbance on each variable of the basic state. Thus, the total flow is the sum of the basic state and disturbance; that is,

$$\overline{q}(x, y, z, t) = Q_b(x, y, z) + q(x, y, z, t) \tag{3.1}$$

where $\overline{q}$ denotes a total-flow quantity (the velocity components $\overline{u}$, $\overline{v}$, $\overline{w}$, temperature $\overline{T}$, pressure $\overline{p}$, density $\overline{\rho}$, and viscosity $\overline{\mu}$), $Q_b(x, y, z)$ denotes a basic-state quantity ($U_b, V_b, W_b, T_b, P_b, \rho_b$), and q is an unsteady disturbance quantity including u, v, w, p, T, ρ, and μ.

Substituting (3.1) into the nondimensional form of the Navier-Stokes equations given in Appendix A, subtracting the basic-state quantities, and linearizing the resulting equations by neglecting the quadratic and higher-order terms of the disturbances, we obtain the *disturbance equations* in the form,

Continuity Equation :

$$\frac{\partial \rho}{\partial t} + \frac{\partial}{\partial x}(\rho_b u + \rho U_b) + \frac{\partial}{\partial y}(\rho_b v + \rho V_b) + \frac{\partial}{\partial z}(\rho_b w + \rho W_b) = 0. \qquad (3.2)$$

X - Momentum Equation :

$$\begin{aligned}
&\rho_b\left(\frac{\partial u}{\partial t} + U_b\frac{\partial u}{\partial x} + u\frac{\partial U_b}{\partial x} + V_b\frac{\partial u}{\partial y} + v\frac{\partial U_b}{\partial y} + W_b\frac{\partial u}{\partial z} + w\frac{\partial U_b}{\partial z}\right) \\
&\quad + \rho\left(U_b\frac{\partial U_b}{\partial x} + V_b\frac{\partial U_b}{\partial y} + W_b\frac{\partial U_b}{\partial z}\right) \\
&= -\frac{\partial p}{\partial x} + \frac{1}{R}\left\{\frac{\partial}{\partial x}\left[\mu_b\left(r\frac{\partial u}{\partial x} + m\frac{\partial v}{\partial y} + m\frac{\partial w}{\partial z}\right) + \mu\left(r\frac{\partial U_b}{\partial x}\right.\right.\right. \qquad (3.3) \\
&\left. + m\frac{\partial V_b}{\partial y} + m\frac{\partial W_b}{\partial z}\right)\Big] + \frac{\partial}{\partial y}\left[\mu_b\left(\frac{\partial u}{\partial y} + \frac{\partial v}{\partial x}\right) + \mu\left(\frac{\partial U_b}{\partial y} + \frac{\partial V_b}{\partial x}\right)\right] \\
&\quad \left.\left. + \frac{\partial}{\partial z}\left[\mu_b\left(\frac{\partial w}{\partial x} + \frac{\partial u}{\partial z}\right) + \mu\left(\frac{\partial W_b}{\partial x} + \frac{\partial U_b}{\partial z}\right)\right]\right\}
\end{aligned}$$

Y - Momentum Equation :

$$\begin{aligned}
&\rho_b\left(\frac{\partial v}{\partial t} + U_b\frac{\partial v}{\partial x} + u\frac{\partial V_b}{\partial x} + V_b\frac{\partial v}{\partial y} + v\frac{\partial V_b}{\partial y} + W_b\frac{\partial v}{\partial z} + w\frac{\partial V_b}{\partial z}\right) \\
&\quad + \rho\left(U_b\frac{\partial V_b}{\partial x} + V_b\frac{\partial V_b}{\partial y} + W_b\frac{\partial V_b}{\partial z}\right) \\
&= -\frac{\partial p}{\partial y} + \frac{1}{R}\left\{\frac{\partial}{\partial x}\left[\mu_b\left(\frac{\partial u}{\partial y} + \frac{\partial v}{\partial x}\right) + \mu\left(\frac{\partial U_b}{\partial y} + \frac{\partial V_b}{\partial x}\right)\right]\right. \qquad (3.4) \\
&\quad + \frac{\partial}{\partial y}\left[\mu_b\left(m\frac{\partial u}{\partial x} + r\frac{\partial v}{\partial y} + m\frac{\partial w}{\partial z}\right) + \mu\left(m\frac{\partial U_b}{\partial x} + r\frac{\partial V_b}{\partial y} + m\frac{\partial W_b}{\partial z}\right)\right] \\
&\quad \left. + \frac{\partial}{\partial z}\left[\mu_b\left(\frac{\partial v}{\partial z} + \frac{\partial w}{\partial y}\right) + \mu\left(\frac{\partial V_b}{\partial z} + \frac{\partial W_b}{\partial y}\right)\right]\right\}
\end{aligned}$$

Z - Momentum Equation :

$$\rho_b\left(\frac{\partial w}{\partial t}+U_b\frac{\partial w}{\partial x}+u\frac{\partial W_b}{\partial x}+V_b\frac{\partial w}{\partial y}+v\frac{\partial W_b}{\partial y}+W_b\frac{\partial w}{\partial z}+w\frac{\partial W_b}{\partial z}\right)$$
$$+\rho\left(U_b\frac{\partial W_b}{\partial x}+V_b\frac{\partial W_b}{\partial y}+W_b\frac{\partial W_b}{\partial z}\right)$$
$$=-\frac{\partial p}{\partial z}+\frac{1}{R}\left\{\frac{\partial}{\partial x}\left[\mu_b\left(\frac{\partial w}{\partial x}+\frac{\partial u}{\partial z}\right)+\mu\left(\frac{\partial W_b}{\partial x}+\frac{\partial U_b}{\partial z}\right)\right]\right. \tag{3.5}$$
$$+\frac{\partial}{\partial y}\left[\mu_b\left(\frac{\partial v}{\partial z}+\frac{\partial w}{\partial y}\right)+\mu\left(\frac{\partial V_b}{\partial z}+\frac{\partial W_b}{\partial y}\right)\right]$$
$$\left.+\frac{\partial}{\partial z}\left[\mu_b\left(m\frac{\partial u}{\partial x}+m\frac{\partial v}{\partial y}+r\frac{\partial w}{\partial z}\right)+\mu\left(m\frac{\partial U_b}{\partial x}+m\frac{\partial V_b}{\partial y}+r\frac{\partial W_b}{\partial z}\right)\right]\right\}$$

Energy Equation :

$$\rho_b\left(\frac{\partial T}{\partial t}+U_b\frac{\partial T}{\partial x}+u\frac{\partial T_b}{\partial x}+V_b\frac{\partial T}{\partial y}+v\frac{\partial T_b}{\partial y}+W_b\frac{\partial T}{\partial z}+w\frac{\partial T_b}{\partial z}\right)$$
$$+\rho\left(U_b\frac{\partial T_b}{\partial x}+V_b\frac{\partial T_b}{\partial y}+W_b\frac{\partial T_b}{\partial z}\right)=(\gamma_g-1)M_1^2\left(\frac{\partial p}{\partial t}\right.$$
$$\left.+U_b\frac{\partial p}{\partial x}+u\frac{\partial p_b}{\partial x}+V_b\frac{\partial p}{\partial y}+v\frac{\partial p_b}{\partial y}+W_b\frac{\partial p}{\partial z}+w\frac{\partial p_b}{\partial z}+\frac{1}{R}\Phi\right) \tag{3.6}$$
$$+\frac{1}{RP_r}\left[\frac{\partial}{\partial x}\left(\mu_b\frac{\partial T}{\partial x}+\mu\frac{\partial T_b}{\partial x}\right)+\frac{\partial}{\partial y}\left(\mu_b\frac{\partial T}{\partial y}+\mu\frac{\partial T_b}{\partial y}\right)+\frac{\partial}{\partial z}\left(\mu_b\frac{\partial T}{\partial z}+\mu\frac{\partial T_b}{\partial z}\right)\right]$$

Equation of State :

$$\frac{p}{p_b}=\frac{T}{T_b}+\frac{\rho}{\rho_b} \tag{3.7}$$

where Φ is the perturbation dissipation function defined by

$$\Phi = \mu_b\{2r\left(\frac{\partial U_b}{\partial x}\frac{\partial u}{\partial x} + \frac{\partial V_b}{\partial y}\frac{\partial v}{\partial y} + \frac{\partial W_b}{\partial z}\frac{\partial w}{\partial z}\right)$$
$$+ 2m\left[\frac{\partial U_b}{\partial x}\left(\frac{\partial v}{\partial y}+\frac{\partial w}{\partial z}\right) + \frac{\partial V_b}{\partial y}\left(\frac{\partial u}{\partial x}+\frac{\partial w}{\partial z}\right)+\frac{\partial W_b}{\partial z}\left(\frac{\partial u}{\partial x}+\frac{\partial v}{\partial y}\right)\right]$$
$$+ 2\left(\frac{\partial u}{\partial y}+\frac{\partial v}{\partial x}\right)\left(\frac{\partial U_b}{\partial y}+\frac{\partial V_b}{\partial x}\right)+2\left(\frac{\partial u}{\partial z}+\frac{\partial w}{\partial x}\right)\left(\frac{\partial U_b}{\partial z}+\frac{\partial W_b}{\partial x}\right)$$
$$+ 2\left(\frac{\partial v}{\partial z}+\frac{\partial w}{\partial y}\right)\left(\frac{\partial V_b}{\partial z}+\frac{\partial W_b}{\partial y}\right)\}$$
$$+ \mu\{r\left[\left(\frac{\partial U_b}{\partial x}\right)^2 + \left(\frac{\partial V_b}{\partial y}\right)^2 + \left(\frac{\partial W_b}{\partial z}\right)^2\right] + 2m\left(\frac{\partial U_b}{\partial x}\frac{\partial V_b}{\partial y}\right.$$
$$+ \left.\frac{\partial U_b}{\partial x}\frac{\partial W_b}{\partial z}+\frac{\partial V_b}{\partial y}\frac{\partial W_b}{\partial z}\right)+\left(\frac{\partial U_b}{\partial y}+\frac{\partial V_b}{\partial x}\right)^2$$
$$+ \left(\frac{\partial U_b}{\partial z}+\frac{\partial W_b}{\partial x}\right)^2+\left(\frac{\partial V_b}{\partial z}+\frac{\partial W_b}{\partial y}\right)^2\}$$

The constants m and r are given by

$$m = \frac{\lambda}{\mu}\ , \quad r = 2 + m \tag{3.8}$$

In equations (3.2)-(3.7), the reference velocity, density, temperature, and viscosity coefficient are U_1^*, ρ_1^*, T_1^*, and μ_1^*, respectively. These are the corresponding values in the farfield of the upper stream. The reference length δ_o^* is a viscous length scale; here we take

$$\delta_o^* = \sqrt{\frac{\mu_1^* x_o^*}{\rho_1^* U_1^*}} \tag{3.9}$$

where x_o^* is a fixed value of the x^*–coordinate measured from the initial station of mixing; see Fig. 3.1 for definition. Accordingly, the Reynolds number R is defined by

$$R = \frac{\rho_1^* U_1^* \delta_o^*}{\mu_1^*} \tag{3.10}$$

In this work, we consider the three-dimensional instabilities of a steady two-dimensional mixing layer ($W_b = 0$ and $\partial Q_b/\partial z = 0$). We obtain the basic state by solving the two-dimensional compressible boundary-layer equations and denote it by Q_b. We will confine our analysis to mean flows that are only slightly nonparallel; that is, the normal velocity component V_b is small compared to U_b, and the variations of the flow variables with y are much larger than those with respect to x; that is, $\partial U_b/\partial x << \partial U_b/\partial y$. This in turn implies that all the mean-flow variables must be weak functions of the streamwise coordinate compared with the normal coordinate. In other words, we describe the relatively slow variations of the mean-flow quantities in the streamwise direction by the slow scale $x_1 = \varepsilon x$. Here $\varepsilon = 1/R$, and the mean-flow variables are defined by

$$U_b = U_o(x_1, y) \tag{3.11}$$

$$V_b = \varepsilon V_o^*(x_1, y), \qquad V_o^* = O(1) \tag{3.12}$$

$$W_b = 0 \tag{3.13}$$

$$\rho_b = \rho_o(x_1, y) \tag{3.14}$$

$$T_b = T_o(x_1, y) \tag{3.15}$$

The method of multiple scales

Using the method of multiple scales (Nayfeh 1981), we expand each disturbance quantity in a power series in ε and write the propagating wave form

$$q(x,y,z,t;\varepsilon) = [q_{10}(x_1, y) + \varepsilon\, q_{11}(x_1, y) + \ldots.]\, e^{i\theta} \tag{3.16}$$

where

$$\theta = \int \alpha(x_1)\, dx + \beta z - \omega t \tag{3.17}$$

Here α and β are dimensionless components of the local wavenumber in the streamwise and spanwise directions, respectively, and ω is the dimensionless frequency of the disturbance. In general, ω, α, and β are complex numbers. For temporal stability, α and β are real, but ω is complex. For spatial stability, ω is real, but α and β are complex. Here we study only the case of β real. In the quasiparallel theory, the negative of the imaginary part $-\alpha_i$ of α, gives the spatial growth rate, while ω_i gives the temporal growth rate.

Substituting (3.11)-(3.17) into the disturbance equations (3.2)-(3.7) and equating coefficients of like powers of ε, we obtain the zeroth- and first- order problems, describing the disturbances.

The Quasiparallel Problem O (ε^0)

We find the equations governing the zeroth-order to be

Continuity :

$$\begin{aligned} L_1(u_{10}, v_{10}, w_{10}, p_{10}, T_{10}) = &- i\rho_o(\omega - \alpha U_o)\left(\frac{p_{10}}{P_o} - \frac{T_{10}}{T_o}\right) \\ &+ i\rho_o(\alpha u_{10} + \beta w_{10}) + D(\rho_o v_{10}) = 0 \end{aligned} \tag{3.18}$$

X Momentum :

$$L_2(u_{10}, v_{10}, w_{10}, p_{10}, T_{10}) = -i\rho_o(\omega - \alpha U_o)u_{10} + \rho_o v_{10} DU_o + i\alpha p_{10}$$
$$-\frac{1}{R}\{-\mu_o(r\alpha^2 + \beta^2)u_{10} + D(\mu_o Du_{10}) + i\alpha\mu_o(1+m)Dv_{10} + i\alpha v_{10}D\mu_o \quad (3.19)$$
$$-\alpha\beta\mu_o(1+m)w_{10} + D(\frac{d\mu_o}{dT}T_{10})DU_o + \frac{d\mu_o}{dT}T_{10}D^2U_o\} = 0$$

Y-Momentum :

$$L_3(u_{10}, v_{10}, w_{10}, p_{10}, T_{10}) = -i\rho_o(\omega - \alpha U_o)v_{10} + Dp_{10}$$
$$-\frac{1}{R}\{i\mu_o(1+m)(\alpha Du_{10} + \beta Dw_{10}) + im(\alpha u_{10} + \beta w_{10})D\mu_o - (\alpha^2 + \beta^2)\mu_o v_{10} \quad (3.20)$$
$$-(\alpha^2 + \beta^2)\mu_o v_{10} + D(\mu_o rDv_{10}) + i\alpha DU_o\frac{d\mu_o}{dT}T_{10}\} = 0$$

Z-Momentum :

$$L_4(u_{10}, v_{10}, w_{10}, p_{10}, T_{10}) = -i\rho_o(\omega - \alpha U_o)w_{10} + i\beta p_{10} - \frac{1}{R}\{-\alpha\beta\mu_o(1+m)u_{10} \quad (3.21)$$
$$+ i\beta\mu_o(1+m)Dv_{10} + i\beta v_{10}D\mu_o - \mu_o(\alpha^2 + r\beta^2)w_{10} + D(\mu_o Dw_{10})\} = 0$$

Energy Equation :

$$L_5(u_{10}, v_{10}, w_{10}, p_{10}, T_{10}) = -i\rho_o(\omega - \alpha U_o)T_{10} + \rho_o v_{10}DT_o + i(\gamma_g - 1)M_1^2 p_{10}(\omega - \alpha U_o)$$
$$-\frac{(\gamma_g - 1)M_1^2}{R}\{2\mu_o DU_o Du_{10} + 2i\mu_o\alpha DU_o v_{10} + \frac{d\mu_o}{dT}(DU_o)^2 T_{10}\} \quad (3.22)$$
$$-\frac{1}{RP_r}\{2D\mu_o DT_{10} + \mu_o D^2T_{10} - (\alpha^2 + \beta^2)\mu_o T_{10} + D^2\mu_o T_{10}\} = 0$$

Equation of State :

$$\gamma_g M_1^2 p_{10} = \frac{T_{10}}{T_o} + \frac{\rho_{10}}{\rho_o} \quad (3.23)$$

The symbol D stands for $\frac{d}{dy}$. This system is subject to the boundary conditions

$$u0,\ v0,\ p0,\ w_{10},\ t0 \to 0 \quad \text{as} \quad y \to \pm\infty \tag{3.24}$$

Introducing the new variables,

$$[Z_{10},\ Z_{20},\ Z_{30},\ Z_{40},\ Z_{50},\ Z_{60},\ Z_{70},\ Z_{80}] = [u_{10},\ Du_{10},\ v_{10},\ p_{10},\ T_{10},\ DT_{10},\ w_{10},\ Dw_{10}] \tag{3.25}$$

we find that the zeroth-order equations can be written as a system of eight linear first-order ordinary-differential equations of the form

$$D\,Z_{n0} - \sum_{m=1}^{8} F_{nm}\,Z_{m0} = 0 \quad , \quad n = 1, \ldots, 8. \tag{3.26}$$

The F_{nm} are the elements of an 8 × 8 variable-coefficient matrix whose nonzero elements are given in Appendix B. The boundary conditions become

$$Z_{n0} \to 0 \quad \text{as} \quad y \to \pm\infty \ , \quad n = 1, \ldots, 8. \tag{3.27}$$

For a specified mean flow, the eigenvalue problem (3.26) and (3.27) has nontrivial solutions only if α, β, ω, and R satisfy a relation which is called the *dispersion relation* expressed as

$$\omega = \omega\,(\alpha, \beta, R) \tag{3.28}$$

Given R, for temporal stability, we specify real values for α and β and then determine ω as a complex eigenvalue; whereas for spatial stability we specify real values for ω and β and then determine α as a complex eigenvalue.

Once the correct eigenvalue is determined, we recover the eigenfunctions ζ_m, m = 1, ...,8.. Then, recognizing that the F_{nm} are only slowly-varying functions of x, we write the solution of (3.26) and (3.27) as

$$Z_{m0} = A(x_1)\,\zeta_m(y; x_1)\ , \qquad m = 1, \ldots 8. \tag{3.29}$$

The amplitude function A is determined by imposing the solvability condition on the next first-order problem. Substituting (3.29) into (3.26) and (3.27), we express the system of equations in terms of the eignfunctions ζ_n as

$$D\zeta_n - \sum_{m=1}^{8} F_{nm}\,\zeta_m = 0\ , \qquad n = 1, \ldots 8. \tag{3.30}$$

$$\zeta_n \to 0 \quad \text{as } y \to \pm\infty \tag{3.31}$$

3.3 *Transformation of Boundary Conditions At Infinity*

Because the mean flow becomes uniform outside some region $y_{min} \le y \le y_{max}$, the elements of the matrix F_{nm} become constant, and therefore a closed form solution for the system (3.30) can be obtained. This solution is then used to replace the asymptotic boundary conditions (3.31) by equivalent conditions at finite values of y. This results in a more efficient numerical procedure, because the system (3.30) is numerically integrated only over the interval $y_{min} \le y \le y_{max}$ when the matrix **F** varies with y.

The constant-coefficient system is written as

$$D\zeta_n - \sum_{m=1}^{8} C_{nm}\,\zeta_m = 0\ , \qquad n = 1, \ldots, 8. \tag{3.32}$$

where the matrix **C** is given in Appendix C. We write the solution to (3.32) in the form

$$\underset{\sim}{\zeta} = \underset{\sim}{a}\, e^{\lambda y} \tag{3.33}$$

where

$$\underset{\sim}{\zeta} = \{ \zeta_1, \zeta_2, ..., \zeta_8 \} ,$$

λ is a constant scalar, and $\underset{\sim}{a}$ is a constant eight-component vector. Substituting (3.33) into (3.32) and rearranging, we obtain

$$(\mathbf{C} - \lambda \mathbf{I})\, \underset{\sim}{a} = 0 \tag{3.34}$$

For a nontrivial solution for $\underset{\sim}{a}$, the determinant of the coefficient matrix (3.34) must vanish; that is,

$$| \mathbf{C} - \lambda \mathbf{I} | = 0 \tag{3.35}$$

Hence, we can determine eight values for λ; they are given in Appendix D.1. It is possible to arrange the eigenvalues such that λ_1, λ_2, λ_3 and λ_4 have positive real parts and λ_5, λ_6, λ_7 and λ_8 have negative real parts. Therefore, we can write the general solution of (3.32) in the matrix form

$$\underset{\sim}{\zeta} = \mathbf{Q}\, \underset{\sim}{\eta} \tag{3.36}$$

where **Q** is given in Appendix D.2; it is an 8 × 8 matrix whose columns are the corresponding eigenvectors. And $\underset{\sim}{\eta}$ is given by

$$\underset{\sim}{\eta} = \{ c_1 e^{\lambda_1 y}, c_2 e^{\lambda_2 y}, ..., c_8 e^{\lambda_8 y} \}^T \tag{3.37}$$

where $c_1, c_2, \ldots, c_8$ are constant. In order to obtain decaying solutions outside the shear layer, we demand from (3.37) that

$$\eta_1, \eta_2, \eta_3, \text{ and } \eta_4 = 0 \quad \text{for } y \geq y_{max} \tag{3.38}$$

$$\eta_5, \eta_6, \eta_7, \text{ and } \eta_8 = 0 \quad \text{for } y \leq y_{min} \tag{3.39}$$

Now, multiplying both sides of (3.36) by the inverse $\mathbf{Q}^{-1}$ of $\mathbf{Q}$, we express $\underset{\sim}{\eta}$ as

$$\underset{\sim}{\eta} = \mathbf{Q}^{-1} \underset{\sim}{\zeta} \tag{3.40}$$

By applying (3.38) and (3.39) to (3.40), we obtain the boundary conditions in a matrix form as

$$\mathbf{A} \underset{\sim}{\zeta} = 0 \quad \text{at } y = y_{max} \tag{3.41}$$

$$\mathbf{B} \underset{\sim}{\zeta} = 0 \quad \text{at } y = y_{min} \tag{3.42}$$

where the matrix **A** is the first four rows of $\mathbf{Q}^{-1}$ and the matrix **B** is the last four rows of $\mathbf{Q}^{-1}$.

The Adjoint Problem

The matrices **A** and **B** in the boundary conditions (3.41) and (3.42) are determined by direct evaluation of $\mathbf{Q}^{-1}$. For a larger system of equations (the case of viscous compressible three-dimensional theory), it may be difficult to find $\mathbf{Q}^{-1}$ analytically; in which case $\mathbf{Q}^{-1}$ is to be found numerically and that may be expensive. It turns out that the matrices **A** and **B** can be expressed in terms of the $\mathbf{Q}^*$ matrix of the adjoint problem. Finding $\mathbf{Q}^*$ requires the determination of the eigenvectors of the adjoint

system and hence is equivalent to finding the inverse of a matrix, but the algebra is much less involved. The solution to the adjoint problem is also needed in formulating the solvability condition of the first-order problem.

We multiply (3.30) by the functions $\underset{\sim}{\zeta}^{*T}(y)$, which is called an adjoint solution to be specified later, and obtain

$$\underset{\sim}{\zeta}^{*T} D \underset{\sim}{\zeta} - \underset{\sim}{\zeta}^{*T} \mathbf{F} \underset{\sim}{\zeta} = 0 \tag{3.43}$$

Integrating (3.43) from $y = y_{min}$ to $y = y_{max}$ yields

$$\int_{y_{min}}^{y_{max}} \{ \underset{\sim}{\zeta}^{*T} D \underset{\sim}{\zeta} - \underset{\sim}{\zeta}^{*T} \mathbf{F} \underset{\sim}{\zeta} \} \, dy = 0 \tag{3.44}$$

Next, integrating (3.44) by parts, we obtain

$$\underset{\sim}{\zeta}^{*T} \underset{\sim}{\zeta} \Big|_{y_{min}}^{y_{max}} - \int_{y_{min}}^{y_{max}} [D \underset{\sim}{\zeta}^{*T} + \underset{\sim}{\zeta}^{*T} \mathbf{F}] \underset{\sim}{\zeta} \, dy = 0 \tag{3.45}$$

The equation governing the adjoint function $\underset{\sim}{\zeta}^{*}$ is defined by setting the integrand of the second term of (3.45) equal to zero; that is,

$$D \underset{\sim}{\zeta}^{*T} + \underset{\sim}{\zeta}^{*T} \mathbf{F} = 0 \tag{3.46}$$

Taking the transpose of (3.46), we obtain

$$D \underset{\sim}{\zeta}^{*} + \mathbf{F}^{T} \underset{\sim}{\zeta}^{*} = 0 \tag{3.47}$$

which is called the *adjoint equation* of (3.30). Now, (3.45) gives

$$\underset{\sim}{\zeta}^{*T}\underset{\sim}{\zeta}|_{y_{min}} - \underset{\sim}{\zeta}^{*T}\underset{\sim}{\zeta}|_{y_{max}} = 0 \tag{3.48}$$

Furthermore, because the boundary conditions on $\underset{\sim}{\zeta}$ at $y = y_{max}$ and $y = y_{min}$ are disjoint, we choose

$$\underset{\sim}{\zeta}^{*T}\underset{\sim}{\zeta} = 0 \qquad \text{at } y = y_{max} \tag{3.49}$$

$$\underset{\sim}{\zeta}^{*T}\underset{\sim}{\zeta} = 0 \qquad \text{at } y = y_{min} \tag{3.50}$$

We also demand that the adjoint solution decay outside the shear layer

$$\underset{\sim}{\zeta}^{*} = 0 \qquad \text{as } y \to \infty \tag{3.51}$$

$$\underset{\sim}{\zeta}^{*} = 0 \qquad \text{as } y \to -\infty \tag{3.52}$$

Outside the shear layer, (3.47) can be written as

$$D\underset{\sim}{\zeta}^{*} + \mathbf{C}^{T}\underset{\sim}{\zeta}^{*} = 0 \tag{3.53}$$

Following similar procedures of getting the general solution of (3.30), we obtain the general solution of (3.53) as

$$\underset{\sim}{\zeta}^{*} = \mathbf{Q}^{*}\underset{\sim}{\eta}^{*} \tag{3.54}$$

where $\mathbf{Q}^{*}$, given in Appendix D.3, is an 8 × 8 matrix whose columns are the eigenvectors of $-\mathbf{C}^{T}$, and η^{*} is given by

$$\eta^{*} = \{k_1 e^{\hat{\lambda_1} y}, k_2 e^{\hat{\lambda_2} y}, \ldots, k_8 e^{\hat{\lambda_8} y}\}^{T} \tag{3.55}$$

where $k_1, k_2, \ldots,$ and k_8 are constants and $\lambda_1^*, \lambda_2^*, \ldots,$ and λ_8^* are the eigenvalues of the adjoint system which are the same as those of the original system (3.32). In order that $\underset{\sim}{\zeta}^*$ decay at infinity, we require that

$$\eta_1^* = \eta_2^* = \eta_3^* = \eta_4^* = 0 \quad \text{at } y = y_{max} \tag{3.56}$$

$$\eta_5^* = \eta_6^* = \eta_7^* = \eta_8^* = 0 \quad \text{at } y = y_{min} \tag{3.57}$$

Next, substituting (3.54) into (3.49) and (3.50), we obtain

$$\underset{\sim}{\eta}^{*T}\mathbf{Q}^{*T}\underset{\sim}{\zeta} = 0 \quad \text{at } y = y_{max} \tag{3.58}$$

$$\underset{\sim}{\eta}^{*T}\mathbf{Q}^{*T}\underset{\sim}{\zeta} = 0 \quad \text{at } y = y_{min} \tag{3.59}$$

Letting

$$\underset{\sim}{\eta} = \mathbf{Q}^{*T}\underset{\sim}{\zeta} \tag{3.60}$$

in (3.49) and (3.50), we obtain

$$\eta_1^*\eta_1 + \eta_2^*\eta_2 + \eta_3^*\eta_3 + \eta_4^*\eta_4 + \eta_5^*\eta_5 + \eta_6^*\eta_6 + \eta_7^*\eta_7 + \eta_8^*\eta_8 = 0 \text{ at } y = y_{max} \tag{3.61}$$

$$\eta_1^*\eta_1 + \eta_2^*\eta_2 + \eta_3^*\eta_3 + \eta_4^*\eta_4 + \eta_5^*\eta_5 + \eta_6^*\eta_6 + \eta_7^*\eta_7 + \eta_8^*\eta_8 = 0 \text{ at } y = y_{min} \tag{3.62}$$

Substituting (3.56) into (3.61) and (3.57) into (3.62), we obtain

$$\eta_5^*\eta_5 + \eta_6^*\eta_6 + \eta_7^*\eta_7 + \eta_8^*\eta_8 = 0 \quad \text{at } y = y_{max} \tag{3.63}$$

$$\eta_1^*\eta_1 + \eta_2^*\eta_2 + \eta_3^*\eta_3 + \eta_4^*\eta_4 = 0 \quad \text{at } y = y_{min} \tag{3.64}$$

To satisfy (3.63) and (3.64), we choose

$$\eta_5 = \eta_6 = \eta_7 = \eta_8 = 0 \qquad \text{at } y = y_{max} \tag{3.65}$$

$$\eta_1 = \eta_2 = \eta_3 = \eta_4 = 0 \qquad \text{at } y = y_{min} \tag{3.66}$$

Substituting (3.65) and (3.66) into (3.60), we write the boundary conditions of the original system in the form

$$\mathbf{A}\underset{\sim}{\zeta} = 0 \qquad \text{at } y = y_{max} \tag{3.67}$$

$$\mathbf{B}\underset{\sim}{\zeta} = 0 \qquad \text{at } y = y_{min} \tag{3.68}$$

where the matrix **A** is the last four rows of $\mathbf{Q}^{*T}$, and the matrix **B** is the first four rows of $\mathbf{Q}^{*T}$.

Similarly, we can write the boundary conditions on the adjoint problem in the form

$$\mathbf{A}^{*}\underset{\sim}{\zeta}^{*} = 0 \qquad \text{at } y = y_{max} \tag{3.69}$$

$$\mathbf{B}^{*}\underset{\sim}{\zeta}^{*} = 0 \qquad \text{at } y = y_{min} \tag{3.70}$$

where the matrix $\mathbf{A}^{*}$ is the last four rows of $\mathbf{Q}^{T}$, and the matrix $\mathbf{B}^{*}$ is the first four rows of $\mathbf{Q}^{T}$.

3.4 Nonparallel Correction

Here, we only consider the nonparallel effect on two-dimensional disturbances. Substituting (3.16) into (3.2)-(3.7), we find that the first-order problem can be written as a first-order system of six ordinary-differential equations of the form

$$DZ_{n1} - \sum_{m=1}^{6} F_{nm} Z_{m1} = E_n \frac{dA}{dx_1} + G_n A \ , \quad n = 1, ..., 6 \tag{3.71}$$

where $[Z_{11}, Z_{21}, Z_{31}, Z_{41}, Z_{51}, Z_{61}] = [u_1, Du_1, v_1, p_1, T_1, DT_1]$ and the F_{nm} are the same as in (3.26). The function E_n and G_n given in Appendix E are determined in terms of the zeroth-order eigenfunctions ζ_n, α, ω, and the mean-flow quantities.

The system is subject to the boundary conditions

$$Z_{n1} \to 0 \ , \quad n = 1, 2, ..., 6 \quad \text{as } y \to \pm\infty \tag{3.72}$$

Because the homogeneous part of (3.71) is the same as (3.26) and because the latter has a nontrivial solution, the system (3.71) will have a nontrivial solution only if a solvability condition is satisfied. The solvability condition is (see Nayfeh 1981)

$$\int_{-\infty}^{\infty} \sum_{n=1}^{6} [E_n \frac{dA}{dx_1} + G_n A] \zeta_n^* dy = 0 \tag{3.73}$$

where the ζ_n^* are the eigensolutions of the adjoint homogeneous problem, which has been defined by (3.47). This condition implies that

$$H_0 \frac{dA}{dx_1} + H_1 A = 0 \tag{3.74}$$

where

$$H_0 = \int_{-\infty}^{\infty} \sum_{n=1}^{6} E_n \zeta_n^* \, dy \tag{3.75}$$

$$H_1 = \int_{-\infty}^{\infty} \sum_{n=1}^{6} G_n \zeta_n^* \, dy \tag{3.76}$$

The solution to (3.74) is

$$A = A_0 e^{-\int \frac{H_1}{H_0} dx_1} = A_0 e^{-\varepsilon \int \frac{H_1}{H_0} dx} \tag{3.77}$$

where A_0 is a constant.

Therefore, by substituting (3.77) and (3.29) into (3.16), we obtain the disturbance solution to first-order as

$$q_n = A_0 \zeta_n(x_1, y) e^{i\theta} , \quad n = 1, 2, ..., 6. \tag{3.78}$$

where q_n stands for the disturbance quantities u, Du, v, p, T, and DT and θ is given by

$$\theta = \int_{x_0}^{x} (\alpha + i\varepsilon \frac{H_1}{H_0}) \, dx - \omega t \tag{3.79}$$

It is well known (Saric and Nayfeh 1982) that the growth rate and wavenumber of a nonparallel flow are not uniquely defined. The growth rate of the nonparallel flow depends on the streamwise coordinate x as well as on the transverse coordinate y; whereas the growth rate of a parallel flow is independent of y. Moreover, different

physical quantities (pressure, velocity, density) may have different growth rates. Here we define a complex wavenumber $\hat{\alpha}$ for the diturbance q_n by

$$i\,\hat{\alpha}(x,y,\zeta_n) = \frac{1}{q_n}\frac{\partial q_n}{\partial x} \tag{3.80}$$

Using (3.78), we write (3.80) as

$$i\,\hat{\alpha}(x,y,\zeta_n) = i(\alpha + \varepsilon\,\alpha_1) \tag{3.81}$$

where

$$\alpha_1 = i\,\frac{H_1}{H_o} - \frac{1}{\zeta_n}\frac{\partial \zeta_n}{\partial x_1} \tag{3.82}$$

The growth rate of the quasi-parallel stability is $-\alpha_i$ and the correction due to the nonparallel effects is $-\varepsilon\,\alpha_{1i}$, where α_{1i} is the imaginary part of α_1.

3.5 *Compressible Inviscid Instabilities*

Because the mean flow of a mixing layer always possesses a generalized inflection point where D(DU/T) = 0 at some point in the layer, the instability is basically inviscid in nature, and viscosity has a stabilizing effect on the flow. That is to say, the growth rates of amplified disturbances decrease with decreasing Reynolds number. Numerical results in Chapter 5 justify this statement for Mach numbers less than 6. Therefore, a simplified model of the stability theory is obtained by neglecting the viscous terms in the disturbance equations. Equivalently, one can obtain the

disturbance equations by linearizing the Euler equations about the given basic state. Limiting the analysis to quasi-parallel flows, we obtain

Continuity Equation :

$$\frac{\partial \rho}{\partial t} + \rho_o \frac{\partial u}{\partial x} + U_o \frac{\partial \rho}{\partial x} + \frac{d\rho_o}{dy} \rho + \rho_o \frac{\partial v}{\partial y} + \rho_o \frac{\partial w}{\partial z} = 0 \qquad (3.83)$$

X - Momentum :

$$\rho_o \left(\frac{\partial u}{\partial t} + U_o \frac{\partial u}{\partial x} + \frac{dU_o}{dy} v \right) = - \frac{\partial p}{\partial x} \qquad (3.84)$$

Y - Momentum :

$$\rho_o \left(\frac{\partial v}{\partial t} + U_o \frac{\partial v}{\partial x} \right) = - \frac{\partial p}{\partial y} \qquad (3.85)$$

Z - Momentum :

$$\rho_o \left(\frac{\partial w}{\partial t} + U_o \frac{\partial w}{\partial x} \right) = - \frac{\partial p}{\partial z} \qquad (3.86)$$

Energy Equation :

$$\rho_o \left(\frac{\partial T}{\partial t} + U_o \frac{\partial w}{\partial x} + \frac{dT_o}{dy} v \right) = (\gamma_g - 1) M_1^2 \left(\frac{\partial p}{\partial t} + U_o \frac{\partial p}{\partial x} \right) \qquad (3.87)$$

Equation of state :

$$\gamma_g M_1^2 p = \frac{T}{T_o} + T_o \rho \qquad (3.88)$$

The boundary conditions are

$$u, v, T \to 0 \quad \text{as} \quad y \to \pm \infty \tag{3.89}$$

Using normal mode analysis, we assume the disturbance variables in the form

$$u(x, y, z, t) = \hat{u}(y)\, e^{i(\alpha x + \beta z - \omega t)} \tag{3.90}$$

$$v(x, y, z, t) = \hat{v}(y)\, e^{i(\alpha x + \beta z - \omega t)} \tag{3.91}$$

$$w(x, y, z, t) = \hat{w}(y)\, e^{i(\alpha x + \beta z - \omega t)} \tag{3.92}$$

$$p(x, y, z, t) = \hat{p}(y)\, e^{i(\alpha x + \beta z - \omega t)} \tag{3.93}$$

$$T(x, y, z, t) = \hat{T}(y)\, e^{i(\alpha x + \beta z - \omega t)} \tag{3.94}$$

$$\rho(x, y, z, t) = \hat{\rho}(y)\, e^{i(\alpha x + \beta z - \omega t)} \tag{3.95}$$

Substituting (3.90)-(3.94) into (3.83)-(3.87), and dropping the hat for simplicity, we obtain the system of equations

$$\frac{dv}{dy} = \frac{i\Omega}{\rho_o}\rho - \frac{1}{\rho_o}\frac{d\rho_o}{dy}v - i(\alpha u + \beta w) \tag{3.96}$$

$$i\Omega\rho_o u = \rho_o \frac{dU_o}{dy} v + i\alpha p \tag{3.97}$$

$$\frac{dp}{dy} = i\rho_o \Omega v \tag{3.98}$$

$$i\rho_o \Omega w = i\beta p \tag{3.99}$$

$$i\rho_o \Omega T = \rho_o \frac{dT_o}{dy} v + i(\gamma_g - 1) M_1^2 \Omega p \tag{3.100}$$

where $\Omega = \omega - \alpha U_o$.

Substituting (3.100) into (3.88) and using $\rho_o T_o = 1$, we express the disturbance ρ as

$$\rho = \frac{\gamma_g M_1^2}{T_o} p - \frac{1}{i \Omega T_o^2} \left[\frac{dT_o}{dy} v + i (\gamma_g - 1) M_1^2 T_o \Omega p \right] \tag{3.101}$$

Using (3.97), (3.99), (3.100) and (3.101), we eliminate ρ, u, w and T from (3.96), and obtain

$$\frac{dv}{dy} = \frac{1}{\Omega} \frac{d\Omega}{dy} v - \frac{i}{\rho_o \Omega} (\alpha^2 + \beta^2 - \frac{\Omega^2 M^2}{T_o}) p \tag{3.102}$$

Because there are only two first-order differential equations (3.102) and (3.98) to be solved rather than eight, the inviscid analysis is much simpler than the viscous theory.

Outside the shear layer, the mean flow approaches a uniform state, (3.102) and (3.98) become

$$\frac{d}{dy} \begin{bmatrix} v \\ p \end{bmatrix} = \begin{bmatrix} 0 & \frac{-i}{\rho_o \Omega} (\alpha^2 + \beta^2 - \frac{\Omega^2 M_1^2}{T_o}) \\ i \rho_o \Omega & 0 \end{bmatrix} \begin{bmatrix} v \\ p \end{bmatrix} \tag{3.103}$$

where ρ_o, T_o, and Ω are evalutated using the free-stream values. Substituting

$$\begin{bmatrix} v \\ p \end{bmatrix} = \begin{bmatrix} k_1 \\ k_2 \end{bmatrix} e^{\lambda y} \tag{3.104}$$

into (3.103), we obtain

$$\begin{bmatrix} -\lambda & \frac{-i}{\rho_o \Omega} (\alpha^2 + \beta^2 - \frac{\Omega^2 M^2}{T_o}) \\ i \rho_o \Omega & -\lambda \end{bmatrix} \begin{bmatrix} k_1 \\ k_2 \end{bmatrix} e^{\lambda y} = 0 \tag{3.105}$$

For nontrivial solutions of k_1 and k_2, the determinant of the coefficient matrix of (3.105) must be zero. Hence,

$$\begin{vmatrix} -\lambda & \frac{-i}{\rho_o\Omega}(\alpha^2+\beta^2-\frac{\Omega^2M^2}{T_o}) \\ i\rho_o\Omega & -\lambda \end{vmatrix} = 0 \qquad (3.106)$$

The eigenvalues are

$$\lambda_1 = \sqrt{\alpha^2+\beta^2-\frac{\Omega^2M^2}{T_o}} \quad \text{and} \quad \lambda_2 = -\sqrt{\alpha^2+\beta^2-\frac{\Omega^2M^2}{T_o}} \qquad (3.107)$$

and the corresponding eigenvectors are given by

$$\eta_1 = \begin{bmatrix} \frac{-i\lambda_1}{\rho_o\Omega} \\ 1 \end{bmatrix} \quad \text{and} \quad \eta_2 = \begin{bmatrix} \frac{-i\lambda_2}{\rho_o\Omega} \\ 1 \end{bmatrix} \qquad (3.108)$$

Therefore, the general solution of (3.103) is

$$\begin{bmatrix} v \\ p \end{bmatrix} = c_1e^{\lambda_1 y}\eta_1 + c_2e^{\lambda_2 y}\eta_2 = \begin{bmatrix} \frac{-i\lambda_1}{\rho_o\Omega} & \frac{-i\lambda_2}{\rho_o\Omega} \\ 1 & 1 \end{bmatrix} \begin{bmatrix} c_1e^{\lambda_1} \\ c_2e^{\lambda_2} \end{bmatrix} \qquad (3.109)$$

where c_1 and c_2 are constant. They can be expressed in terms of v and p as

$$\begin{bmatrix} c_1e^{\lambda_1 y} \\ c_2e^{\lambda_2 y} \end{bmatrix} = \frac{i\rho_o\Omega}{2\lambda_1} \begin{bmatrix} 1 & \frac{i\lambda_2}{\rho_o\Omega} \\ -1 & \frac{-i\lambda_1}{\rho_o\Omega} \end{bmatrix} \begin{bmatrix} v \\ p \end{bmatrix} \qquad (3.110)$$

From (3.110), we can decide the asymptotic boundary conditions by investigating whether $c_1e^{\lambda_1 y}$ or $c_2e^{\lambda_2 y}$ tends to zero as y goes to infinity. Since $\text{Real}(\lambda_1) > 0$, c_1 must

be zero at $y = y_{max}$ In order to satisfy the decaying condition of the disturbance. Thus, the boundary condition at $y = y_{max}$ is given by

$$i\rho_o\Omega v + \sqrt{\alpha^2 + \beta^2 - \frac{\Omega^2 M^2}{T_o}}\, p = 0 \qquad (3.111)$$

Similarly, since $\text{Real}(\lambda_2) < 0$, c_2 must be zero at $y = y_{min}$. Hence, the boundary condition at $y = y_{min}$ is given by

$$i\rho_o\Omega v - \sqrt{\alpha^2 + \beta^2 - \frac{\Omega^2 M^2}{T_o}}\, p = 0 \qquad (3.112)$$

We determine v and p by solving (3.98) and (3.102) with the boundary conditions (3.111) and (3.112).

4.0 Numerical Methods

4.1 Introduction

In this chapter, we present numerical methods for solving the eigenvalue problem that is given by the system

$$\frac{d\zeta_n}{dy} = \sum_{m=1}^{8} F_{nm}(y; \alpha, \omega, R)\,\zeta_m , \quad n = 1, \ldots, 8 \tag{4.1}$$

where

$$\begin{bmatrix} \zeta_1 \\ \zeta_2 \\ \zeta_3 \\ \zeta_4 \\ \zeta_5 \\ \zeta_6 \\ \zeta_7 \\ \zeta_8 \end{bmatrix} = \begin{bmatrix} u \\ du/dy \\ v \\ p \\ T \\ dT/dy \\ w \\ dw/dy \end{bmatrix} \tag{4.2}$$

and F_{nm} is given in Appendix B. The system (4.1) is subject to the boundary conditions

$$\sum_{m=1}^{8} A_{nm}\,\zeta_m = 0\,, \quad n = 1\,,\ldots,\,4 \;\text{ at } y = y_{max} \tag{4.3}$$

$$\sum_{m=1}^{8} B_{nm}\,\zeta_m = 0\,, \quad n = 1\,,\ldots,\,4 \;\text{ at } y = y_{min} \tag{4.4}$$

where A_{nm} and B_{nm} are specified by (3.67) and (3.68), respectively.

We have developed three different computer codes for solving the eigenvalue problem (4.1), (4.3), and (4.4). All three codes, however, search for one eigenvalue at a time starting from an estimated value. The first two codes rely on the use of "canned" routines for the integration of the differential system (4.1). These codes are briefly described in Section 4.2. In Section 4.3, we present in details a fourth-order compact finite-difference method that is used in the third code.

4.2 Using SUPORT and DB2PFD

In the first code, we employ an initial value integrator and a shooting technique. First, we find four linearly independent solutions that satisfy the boundary conditions (4.3). In this step, the integration starts from $y = y_{max}$ and marches toward $y = 0$. Second, we find four other linearly independent solutions that satisfy the boundary conditions (4.4). The integration starts at $y = y_{min}$ and marches toward $y = 0$. Equating the linear superposition of the four solutions in the first step to those in the second step at $y = 0$ for all eight variables (ζ_m, $m = 1, \ldots, 8$), we obtain an algebraic

homogeneous system for the eight coefficients of the linear superpositions. A nontrivial solution is obtained if the determinant of the system vanishes. We use a Newton-Raphson procedure to iterate on the eigenvalue until the determinant vanishes. In each iteration, we have to repeat the two steps of integration and the evaluation of an 8×8 complex determinant.

The problem of parasitic error that destroys the linear independence of the four solutions is treated by using a Gram-Schmidt orthonormalization procedure at selected integration steps. A well-known computer code called SUPORT has been developed by Scott and Watts (1977) where this procedure is automated. This code has been used by many investigators for incompressible and compressible stability problems.

The main advantage of this method is the relatively small computer storage requirement. The method is also easy to program provided that a code such as SUPORT is available. The disadvantages of this method are that it requires an accurate estimate of the eigenvalue, and that it always takes a long time to converge, especially when the system is very stiff (as we shall see in Section 4.4).

In the second code, we use an IMSL subroutine called DB2PFD. This subroutine solves a two-point boundary-value problem governed by a system of differential equations that may be nonlinear. It uses a variable-order, variable-step size finite-difference method with deferred correction (Pereyra, 1978). To avoid obtaining a trivial solution, we augment the system (4.1) by an additional equation for the unknown eigenvalue that is given by

$$\frac{d\alpha}{dy} = 0 \ , \tag{4.5a}$$

for spatial stability, or

$$\frac{d\omega}{dy} = 0 \ , \qquad (4.5b)$$

for temporal stability. After (4.5a) or (4.5b) is added, the augmented system of equations becomes nonlinear. Because we are solving an eigenvalue problem, the eigenfunctions are determined to within a multiplying constant. Therefore, we specify one more boundary condition by letting anyone of the disturbances ζ_n equal to a nonzero value at y_{min} or y_{max}.

Compared to the first code, the convergence of this code is much faster. The disadvantage of this code is that we should have an accurate initial estimate of the eigenfunctions $\zeta_n(j)$, $j = 1, .., N$; otherwise convergence is not always guaranteed.

4.3 *Fourth-Order Compact Finite-Difference Method*

In the third code, we use a fourth-order compact finite-difference method based on the Euler-Maclurin formula. This method has been applied to boundary-layer stability problems by Malik (1988) in which the domain of integration is semi-infinite. Here we present the method in details and extend its application to free shear layers where the domain of integration is infinite. We have also used this method in the secondary stability calculations presented in Chapter 7.

To solve (4.1), (4.3) and (4.4) using finite differences, we establish a grid in the y-direction which covers the range $y_{min} \le y \le y_{max}$. The grid points are denoted by y_j, $j = 1, ..., N$, where N is the total number of points in the y-direction, $y(1) = y_{min}$, and $y(N) = y_{max}$. The grid need not be uniform. The Euler-Maclurin formula is

$$(G_j - G_{j-1}) - \frac{h_j}{2}(G'_j + G'_{j-1}) + \frac{h_j^2}{12}(G''_j - G''_{j-1}) + O(h_j^5) = 0 \quad (4.6)$$

where $G'_j = \frac{dG_j}{dy}$, $G''_j = \frac{dG'_j}{dy}$ and $h_j = y_j - y_{j-1}$.

Now, the function G is replaced by the vector $\underset{\sim}{\zeta}$; hence, (4.6) is written as

$$\underset{\sim}{\zeta}_j - \underset{\sim}{\zeta}_{j-1} - \frac{h_j}{2}(\underset{\sim}{\zeta}'_j + \underset{\sim}{\zeta}'_{j-1}) + \frac{h_j^2}{12}(\underset{\sim}{\zeta}''_j - \underset{\sim}{\zeta}''_{j-1}) = 0 \quad (4.7)$$

In order to obtain $\underset{\sim}{\zeta}''$, we take the derivative of (4.1) with respect to y and then use (4.1) again to eliminate $\underset{\sim}{\zeta}'$ in favor of $\underset{\sim}{\zeta}$. The result is

$$\zeta''_n = \sum_{m=1}^{8} S_{nm}\,\zeta_m\,, \quad n = 1,\ldots, 8 \quad (4.8)$$

where

$$S_{nm} = \frac{dF_{nm}}{dy} + \sum_{k=1}^{8} F_{nk}\,F_{km}\,, \quad n, m = 1, \ldots, 8 \quad (4.9)$$

With $\underset{\sim}{\zeta}$, $\underset{\sim}{\zeta}'$ and $\underset{\sim}{\zeta}''$ given by (4.2), (4.1) and (4.8), application of (4.7) at the grid points j=2, ..., N results in a system of (8N-8) linear equations in the 8N unknowns $\underset{\sim}{\zeta}(j)$, j = 1, ..., N. The system is closed by writing the boundary conditions (4.3) and (4.4) in the form

$$\sum_{m=1}^{8} A_{nm}\,\zeta_m(1) = 0\,, \quad n = 1, .., 4 \quad (4.10)$$

$$\sum_{m=1}^{8} B_{nm}\,\zeta_m(N) = 0\,, \quad n = 1, .., 4 \tag{4.11}$$

We consider α as a variable in the system of equations. By starting from a reasonable initial estimate of all variables including α, we solve the nonlinear system by a Newton iterative method. Hence, at a certain iteration, the current values of ζ_n are written as

$$\zeta_n = \zeta_{n0} + \delta\zeta_n\,, \quad n = 1, ..., 8 \tag{4.12}$$

and

$$\alpha = \alpha_0 + \delta\alpha \tag{4.13}$$

where ζ_{n0} and α_0 indicate the known values from the previous iteration or the estimated values, and $\delta\zeta_n$ and $\delta\alpha$ are small variations to ζ_n and α. Substituting (4.12) and (4.13) into (4.1), we obtain

$$\begin{aligned} \zeta_n' &= \zeta_{n0}' + \delta\zeta_n' \\ &= \sum_{m=1}^{8} [\,F_{nm}(\alpha_0 + \delta\alpha)\,]\,(\zeta_{m0} + \delta\zeta_m) \end{aligned} \tag{4.14}$$

Using a Taylor series expansion, we write $F_{nm}(\alpha_0 + \delta\alpha)$ as

$$F_{nm}(\alpha_0 + \delta\alpha) = F_{nm}(\alpha_0) + \frac{\partial F_{nm}}{\partial\alpha}\,\delta\alpha + O[(\delta\alpha)^2] \tag{4.15}$$

Substituting (4.15) into (4.14) and keeping linear terms in the δ 's, we obtain

$$\zeta_n' = \zeta_{n0}' + \delta\zeta_n'$$
$$= \sum_{m=1}^{8} F_{nm}(\alpha_0)\,\zeta_{m0} + \sum_{m=1}^{8} \left[F_{nm}(\alpha_0)\,\delta\zeta_m + \frac{\partial F_{nm}}{\partial \alpha}\zeta_{m0}\,\delta\alpha \right] \tag{4.16}$$

Similarly, (4.8) is written as

$$\zeta_n'' = \zeta_{n0}'' + \delta\zeta_n''$$
$$= \sum_{m=1}^{8} S_{nm}(\alpha_0)\,\zeta_{m0} + \sum_{m=1}^{8} \left[S_{nm}(\alpha_0)\,\delta\zeta_m + \frac{\partial S_{nm}}{\partial \alpha}\zeta_{m0}\,\delta\alpha \right] \tag{4.17}$$

Substituting (4.12), (4.16), and (4.17) into (4.7), we obtain

$$\begin{aligned}
&(\zeta_{n0})_j - (\zeta_{n0})_{j-1} + (\delta\zeta_n)_j - (\delta\zeta_n)_{j-1} - \frac{h_j}{2}\Big\{\Big[\sum_{m=1}^{8} F_{nm}(\alpha_0)\,\zeta_{m0} + \sum_{m=1}^{8}\Big(F_{nm}(\alpha_0)\,\delta\zeta_m \\
&+ \frac{\partial F_{nm}}{\partial \alpha}\zeta_{m0}\,\delta\alpha\Big)\Big]_j + \Big[\sum_{m=1}^{8} F_{nm}(\alpha_0)\,\zeta_{m0} + \sum_{m=1}^{8}\Big(F_{nm}(\alpha_0)\,\delta\zeta_m + \frac{\partial F_{nm}}{\partial \alpha}\zeta_{m0}\,\delta\alpha\Big)\Big]_{j-1}\Big\} \\
&+ \frac{h_j^2}{12}\Big\{\Big[\sum_{m=1}^{8} S_{nm}(\alpha_0)\,\zeta_{m0} + \sum_{m=1}^{8}\Big(S_{nm}(\alpha_0)\,\delta\zeta_m + \frac{\partial S_{nm}}{\partial \alpha}\zeta_{m0}\,\delta\alpha\Big)\Big]_j \\
&- \Big[\sum_{m=1}^{8} S_{nm}(\alpha_0)\,\zeta_{m0} + \sum_{m=1}^{8}\Big(S_{nm}(\alpha_0)\,\delta\zeta_m + \frac{\partial S_{nm}}{\partial \alpha}\zeta_{m0}\,\delta\alpha\Big)\Big]_{j-1}\Big\} = 0
\end{aligned} \tag{4.18}$$

If we define

$$\begin{aligned}
(H_n)_j = -\Big\{&(\zeta_{n0})_j - (\zeta_{n0})_{j-1} - \frac{h_j}{2}\Big[\Big(\sum_{m=1}^{8} F_{nm}(\alpha_0)\,\zeta_{m0}\Big)_j + \Big(\sum_{m=1}^{8} F_{nm}(\alpha_0)\,\zeta_{m0}\Big)_{j-1}\Big] \\
&+ \frac{h_j^2}{12}\Big[\Big(\sum_{m=1}^{8} S_{nm}(\alpha_0)\,\zeta_{m0}\Big)_j - \Big(\sum_{m=1}^{8} S_{nm}(\alpha_0)\,\zeta_{m0}\Big)_{j-1}\Big]\Big\}
\end{aligned} \tag{4.19}$$

Then we obtain from (4.18) the equations for the small variations $\delta\zeta_n$ and $\delta\alpha$,

$$
\begin{aligned}
&(\delta\zeta_n)_j - (\delta\zeta_n)_{j-1} - \frac{h_j}{2}\{[\sum_{m=1}^{8} F_{nm}(\alpha_0)\,\delta\zeta_m + (\sum_{m=1}^{8} \frac{\partial F_{nm}}{\partial\alpha}\,\zeta_{m0})\,\delta\alpha]_j \\
&+ [\sum_{m=1}^{8} F_{nm}(\alpha_0)\,\delta\zeta_m + (\sum_{m=1}^{8} \frac{\partial F_{nm}}{\partial\alpha}\,\zeta_{m0})\,\delta\alpha]_{j-1}\} \\
&+ \frac{h_j^2}{12}\{[\sum_{m=1}^{8} S_{nm}(\alpha_0)\,\delta\zeta_m + (\sum_{m=1}^{8} \frac{\partial S_{nm}}{\partial\alpha}\,\zeta_{m0})\,\delta\alpha]_j \\
&- [\sum_{m=1}^{8} S_{nm}(\alpha_0)\,\delta\zeta_m + (\sum_{m=1}^{8} \frac{\partial S_{nm}}{\partial\alpha}\,\zeta_{m0})\,\delta\alpha]_{j-1}\} = (H_n)_j\ , \quad n=1, \ldots, 8
\end{aligned}
\tag{4.20}
$$

Now, we let

$$\zeta_9 = \alpha \tag{4.21}$$

Since α is not a function of y, we add one more equation to the system by taking the derivative of (4.21) with respect to y

$$\frac{d\zeta_9}{dy} = 0 \tag{4.22}$$

We then rewrite $\delta\zeta_n'$ as

$$\delta\zeta_n' = \sum_{m=1}^{9} \tilde{F}_{nm}(\alpha_0)\,\delta\zeta_m\ , \quad n = 1, \ldots, 9 \tag{4.23}$$

where

$$\tilde{F}_{nm}(\alpha_0) = F_{nm}(\alpha_0)\ , \quad n, m = 1, \ldots, 8 \tag{4.24}$$

$$\tilde{F}_{n9} = \sum_{m=1}^{8} \frac{\partial F_{nm}}{\partial \alpha} \zeta_{m0} \quad , \quad n = 1, \ldots, 8 \tag{4.25}$$

$$\tilde{F}_{9n} = 0 \quad , \quad n = 1, \ldots, 9 \tag{4.26}$$

Similarly,

$$\delta\zeta_n'' = \sum_{m=1}^{9} \tilde{S}_{nm} \delta\zeta_m \quad , \quad n = 1, \ldots, 9 \tag{4.27}$$

where

$$\tilde{S}_{nm} = S_{nm} \quad , \quad n,m = 1, \ldots, 8 \tag{4.28}$$

$$\tilde{S}_{n9} = \sum_{m=1}^{8} \frac{\partial S_{nm}}{\partial \alpha} \zeta_{m0} \quad , \quad n = 1, \ldots, 8 \tag{4.29}$$

$$\tilde{S}_{9n} = 0 \quad , \quad n = 1, \ldots, 9 \tag{4.30}$$

Using (4.21)-(4.30), we write the augmented equations that correspond to (4.20) as

$$\begin{aligned} &(\delta\zeta_n)_j - (\delta\zeta_n)_{j-1} - \frac{h_j}{2}\{[\sum_{m=1}^{9}\tilde{F}_{nm}(\alpha_0)\,\delta\zeta_m]_j + [\sum_{m=1}^{9}\tilde{F}_{nm}(\alpha_0)\,\delta\zeta_m]_{j-1}\} \\ &+ \frac{h_j^2}{12}\{[(\sum_{m=1}^{9}\tilde{S}_{nm}(\alpha_0)\,\delta\zeta_m)_j - (\sum_{m=1}^{9}\tilde{S}_{nm}(\alpha_0)\,\delta\zeta_m)_{j-1}]\} \\ &= (H_n)_j \quad , \qquad \text{for } 2 \le j \le N \end{aligned} \tag{4.31}$$

Rearranging, we write (4.31) in the matrix form

$$[\mathbf{D}]_j \{\delta\zeta\}_{j-1} + [\mathbf{E}]_j \{\delta\zeta\}_j = \{\mathbf{H}\}_j \quad \text{for } 2 \le j \le N \tag{4.32}$$

where $[\mathbf{D}]$ and $[\mathbf{E}]$ are 9×9 matrices defined by

$$[\mathbf{D}]_j = -[\mathbf{I}] - \frac{h_j}{2}[\tilde{\mathbf{F}}]_{j-1} - \frac{h_j^2}{12}[\tilde{\mathbf{S}}]_{j-1} \tag{4.33}$$

$$[\mathbf{E}]_j = [\mathbf{I}] - \frac{h_j}{2}[\tilde{\mathbf{F}}]_j + \frac{h_j^2}{12}[\tilde{\mathbf{S}}]_j \tag{4.34}$$

and $[\mathbf{I}]$ is the identity matrix.

Introducing the variations (4.12) and (4.13) into the boundary condition (4.10), we obtain

$$\sum_{m=1}^{8} [A_{nm}(\alpha_0) + \frac{\partial A_{nm}}{\partial \alpha}\delta\alpha](\zeta_{m0} + \delta\zeta_m) = 0 \tag{4.35}$$

Hence

$$\sum_{m=1}^{8} [A_{nm}(\alpha_0)\zeta_{m0} + \frac{\partial A_{nm}}{\partial \alpha}\zeta_{m0}\delta\alpha + A_{nm}(\alpha_0)\delta\zeta_m] + O(\delta^2) = 0 \tag{4.36}$$

Neglecting the quadratic terms in (4.36) and including α as the ninth variable, we rewrite the boundary condition (4.36) as

$$\sum_{m=1}^{9} \tilde{A}_{nm}(\alpha_0)\delta\zeta_m(1) = -\sum_{m=1}^{8} A_{nm}(\alpha_0)\zeta_{m0}(1) \quad , \quad \text{for } n = 1, .., 4 \tag{4.37}$$

where

$$\tilde{A}_{nm} = A_{nm} \ , \quad \text{for } n = 1, .. ,4, \ m = 1, .., 8 \tag{4.38}$$

and

$$\tilde{A}_{n9} = \sum_{m=1}^{8} \frac{\partial A_{nm}}{\partial \alpha} \zeta_{m0}(1) \ , \quad \text{for } n = 1, .., 4 \tag{4.39}$$

Similarly, the boundary condition (4.11) can be rewritten as

$$\sum_{m=1}^{9} \tilde{B}_{nm}(\alpha_0)\, \delta\zeta_m(N) = -\sum_{m=1}^{8} B_{nm}(\alpha_0)\, \zeta_{m0}(N) \ , \quad \text{for } n = 1, .., 4 \tag{4.40}$$

where

$$\tilde{B}_{nm} = B_{nm} \ , \quad \text{for } n = 1, .. ,4, \ m = 1, .., 8 \tag{4.41}$$

and

$$\tilde{B}_{n9} = \sum_{m=1}^{8} \frac{\partial B_{nm}}{\partial \alpha} \zeta_{m0}(N) \ , \quad \text{for } n = 1, .., 4 \tag{4.42}$$

One more boundary condition must be specified. We fix any of the variables ζ_n except α , of course, at y = y(1) or y = y(N), meaning that the corresponding perturbation to that variable is zero.

Now, the system (4.32) for $2 \leq j \leq N$, and the nine boundary conditions give a linear system to be solved for $\delta\zeta_n(j)$, j = 1, ..., N. This system is restructured as a block tridiagonal system for which an efficient method for solution is available.

For computational reasons, it was necessary to rearrange the solution vector $(\zeta_1, \zeta_2, ..., \zeta_9)$ into the order ζ_6, ζ_2, ζ_8, ζ_3, ζ_4, ζ_5, ζ_1, ζ_7, and ζ_9. Therefore, the columns of the coefficient matrices [**D**], [**E**] , [$\tilde{\mathbf{A}}$] and [$\tilde{\mathbf{B}}$] must be rearranged accordingly. However, this rearrangement of the variables is not unique.

The boundary conditions (4.37) at j = 1 are rewritten in the matrix form

$$\mathbf{B}_1 \underline{W}_1 + \mathbf{C}_1 \underline{W}_2 = \underline{H}_1 \tag{4.43}$$

The vectors $\underline{W}_1$, $\underline{W}_2$, and $\underline{H}_1$ are defined as

$$\underline{W}_1 = \{ \delta\zeta_6(0), \delta\zeta_2(0), \delta\zeta_8(0), \delta\zeta_3(0), \delta\zeta_4(1), \delta\zeta_5(1), \delta\zeta_1(1), \delta\zeta_7(1), \delta\zeta_9(1) \}^T \tag{4.44}$$

$$\underline{W}_2 = \{ \delta\zeta_6(1), \delta\zeta_2(1), \delta\zeta_8(1), \delta\zeta_3(1), \delta\zeta_4(2), \delta\zeta_5(2), \delta\zeta_1(2), \delta\zeta_7(2), \delta\zeta_9(2) \}^T \tag{4.45}$$

$$\underline{H}_1 = - \begin{bmatrix} [0]_{5\times1} \\ \sum_{m=1}^{8} A_{1m}(\alpha_0)\, \zeta_{m0}(1) \\ \sum_{m=1}^{8} A_{2m}(\alpha_0)\, \zeta_{m0}(1) \\ \sum_{m=1}^{8} A_{3m}(\alpha_0)\, \zeta_{m0}(1) \\ \sum_{m=1}^{8} A_{4m}(\alpha_0)\, \zeta_{m0}(1) \end{bmatrix} \tag{4.46}$$

where $\delta\zeta_6(0)$, $\delta\zeta_2(0)$, $\delta\zeta_8(0)$ and $\delta\zeta_3(0)$ are dummy variables that have no significance to the problem, and hence the first four equations mean $\delta\zeta_6(0) = 0$, $\delta\zeta_2(0) = 0$, $\delta\zeta_8(0) = 0$ and $\delta\zeta_3(0) = 0$ and the matrices [$\mathbf{B}_1$] and [$\mathbf{C}_1$] are defined by

$$\mathbf{B}_1 = \begin{bmatrix} [\mathbf{I}]_{4\times4} & [\mathbf{0}]_{4\times5} \\ [\mathbf{0}]_{1\times4} & [\underset{\sim}{\mathbf{B}}]_{1\times5} \\ [\mathbf{0}]_{4\times4} & [\hat{\mathbf{B}}]_{4\times5} \end{bmatrix} \tag{4.47}$$

$$\mathbf{C}_1 = \begin{bmatrix} [\mathbf{0}]_{5\times4} & [\mathbf{0}]_{5\times5} \\ [\hat{\mathbf{C}}]_{4\times4} & [\mathbf{0}]_{4\times5} \end{bmatrix} \tag{4.48}$$

where

$$[\hat{\mathbf{B}}]_{4\times5} = \text{the last five columns of } [\tilde{\mathbf{A}}] \tag{4.49}$$

$$[\underset{\sim}{\mathbf{B}}]_{1\times5} = [1, 0, 0, 0, 0] \tag{4.50}$$

$$[\hat{\mathbf{C}}]_{4\times4} = \text{the first four columns of } [\tilde{\mathbf{A}}] \tag{4.51}$$

For $2 \leq j \leq N$, the system of the equations (4.30) is rearranged in the form

$$\mathbf{A}_j \underset{\sim}{W}_{j-1} + \mathbf{B}_j \underset{\sim}{W}_j + \mathbf{C}_j \underset{\sim}{W}_{j+1} = \underset{\sim}{H}_j \tag{4.52}$$

where the vectors $\underset{\sim}{W}_j$ and $\underset{\sim}{H}_j$ are defined by

$$\begin{aligned} \underset{\sim}{W}_j = \{ &\delta\zeta_6(j-1), \delta\zeta_2(j-1), \delta\zeta_8(j-1), \delta\zeta_3(j-1), \delta\zeta_4(j), \\ &\delta\zeta_5(j), \delta\zeta_1(j), \delta\zeta_7(j), \delta\zeta_9(j) \}^T \end{aligned} \tag{4.53}$$

$$\underset{\sim}{H}_j = \{ H_1(j), H_2(j), H_3(j), H_4(j), H_5(j), H_6(j), H_7(j), H_8(j), H_9(j) \}^T \tag{4.54}$$

And the matrices $\mathbf{A}_j$, $\mathbf{B}_j$ and $\mathbf{C}_j$ at y(j) are defined by

$$\mathbf{A}_j = \begin{bmatrix} [\mathbf{0}]_{9\times4} & [\hat{\mathbf{A}}]_{9\times5} \end{bmatrix} \tag{4.55}$$

$$\mathbf{B}_j = \left[\; [\bar{\mathbf{B}}]_{9\times4} \;\; [\hat{\mathbf{B}}]_{9\times5} \; \right] \tag{4.56}$$

$$\mathbf{C}_j = \left[\; [\bar{\mathbf{C}}]_{9\times4} \;\; [\mathbf{0}]_{9\times5} \; \right] \tag{4.57}$$

where

$$[\hat{\mathbf{A}}]_{9\times5} = \text{the last five columns of } [\mathbf{D}]_j \tag{4.58}$$

$$[\bar{\mathbf{B}}]_{9\times4} = \text{the first four columns of } [\mathbf{D}]_j \tag{4.59}$$

$$[\hat{\mathbf{B}}]_{9\times5} = \text{the last five columns of } [\mathbf{E}]_j \tag{4.60}$$

$$[\bar{\mathbf{C}}]_{9\times4} = \text{the first four columns of } [\mathbf{E}]_j \tag{4.61}$$

Regarding the boundary condition (4.40) at y = y(N), we include a dummy computational point j = N+1 and express the boundary condition as

$$\mathbf{A}_{N+1}\,\underset{\sim}{W}_N + \mathbf{B}_{N+1}\,\underset{\sim}{W}_{N+1} = \underset{\sim}{H}_{N+1} \tag{4.62}$$

where the vectors $\underset{\sim}{W}_N$, $\underset{\sim}{W}_{N+1}$ and $\underset{\sim}{H}_{N+1}$ are defined by

$$\begin{aligned}\underset{\sim}{W}_N = \{ &\delta\zeta_6(N-1), \delta\zeta_2(N-1), \delta\zeta_8(N-1), \delta\zeta_3(N-1), \delta\zeta_4(N), \\ &\delta\zeta_5(N), \delta\zeta_1(N), \delta\zeta_7(N), \delta\zeta_9(N) \}^T\end{aligned} \tag{4.63}$$

$$\begin{aligned}\underset{\sim}{W}_{N+1} = \{ &\delta\zeta_6(N), \delta\zeta_2(N), \delta\zeta_8(N), \delta\zeta_3(N), \delta\zeta_4(N+1), \\ &\delta\zeta_5(N+1), \delta\zeta_1(N+1), \delta\zeta_7(N+1), \delta\zeta_9(N+1) \}^T\end{aligned} \tag{4.64}$$

$$\underset{\sim}{H}_{N+1} = -\begin{bmatrix} \sum_{m=1}^{9} B_{1m}(\alpha_0)\,\zeta_{m0}(N) \\ \sum_{m=1}^{9} B_{2m}(\alpha_0)\,\zeta_{m0}(N) \\ \sum_{m=1}^{9} B_{3m}(\alpha_0)\,\zeta_{m0}(N) \\ \sum_{m=1}^{9} B_{4m}(\alpha_0)\,\zeta_{m0}(N) \\ [0]_{5\times 1} \end{bmatrix} \tag{4.65}$$

Here, $\delta\zeta_4(N+1)$, $\delta\zeta_5(N+1)$, $\delta\zeta_1(N+1)$, $\delta\zeta_7(N+1)$ and $\delta\zeta_9(N+1)$ are dummy variables, and the last five equations mean that $\delta\zeta_4(N+1)=0$, $\delta\zeta_5(N+1)=0$, $\delta\zeta_1(N+1)=0$, $\delta\zeta_7(N+1)=0$, and $\delta\zeta_8(N+1)=0$. The matrices $\mathbf{A}_{N+1}$ and $\mathbf{B}_{N+1}$ are defined by

$$\mathbf{A}_{N+1} = \begin{bmatrix} [0]_{4\times 4} & [\hat{\mathbf{A}}]_{4\times 5} \\ [0]_{5\times 4} & [0]_{5\times 5} \end{bmatrix} \tag{4.66}$$

$$\mathbf{B}_{N+1} = \begin{bmatrix} [\hat{\mathbf{B}}]_{4\times 4} & [0]_{4\times 5} \\ [0]_{5\times 4} & [I]_{5\times 5} \end{bmatrix} \tag{4.67}$$

where

$$[\hat{\mathbf{A}}]_{4\times 5} = \text{the last five columns of } [\tilde{\mathbf{B}}] \tag{4.68}$$

$$[\hat{\mathbf{B}}]_{4\times 4} = \text{the first four columns of } [\tilde{\mathbf{B}}] \tag{4.69}$$

Equations (4.43)-(4.69) are combined into the general block tridiagonal system

$$
\begin{bmatrix}
B_1 & C_1 & 0 & 0 & 0 & 0 & 0 & 0 \\
A_2 & B_2 & C_2 & 0 & 0 & 0 & 0 & 0 \\
0 & A_3 & B_3 & C_3 & 0 & 0 & 0 & 0 \\
0 & 0 & -- & -- & -- & 0 & 0 & 0 \\
0 & 0 & 0 & -- & -- & 0 & 0 & 0 \\
0 & 0 & 0 & A_j & B_j & C_j & 0 & 0 \\
0 & 0 & 0 & 0 & 0 & -- & -- & 0 \\
0 & 0 & 0 & 0 & 0 & A_N & B_N & C_N \\
0 & 0 & 0 & 0 & 0 & 0 & A_{N+1} & B_{N+1}
\end{bmatrix}
\begin{bmatrix} \underset{\sim}{W}_1 \\ \underset{\sim}{W}_2 \\ \underset{\sim}{W}_3 \\ : \\ : \\ \underset{\sim}{W}_j \\ : \\ \underset{\sim}{W}_N \\ \underset{\sim}{W}_{N+1} \end{bmatrix}
=
\begin{bmatrix} \underset{\sim}{H}_1 \\ \underset{\sim}{H}_2 \\ \underset{\sim}{H}_3 \\ : \\ : \\ \underset{\sim}{H}_j \\ : \\ \underset{\sim}{H}_N \\ \underset{\sim}{H}_{N+1} \end{bmatrix}
\qquad (4.70)
$$

The procedure of solving (4.70) is the same as that we presented in Section (2.3) for the mean-flow calculations. The solution $\underset{\sim}{W}$ gives us corrections $\delta\zeta_n$ (n = 1, 2, ..., 8) and $\delta\alpha$. The coefficients in (4.70) are then updated, and the process is repeated until the correction $\delta\alpha$ is below a certain tolerance.

A second-order accurate method is obtained from the above formulation by neglecting the $O(h_j^2)$ terms in (4.33) and (4.34).

4.4 Comparison of Different Methods

We choose two cases to compare the results obtained from the different numerical approaches. The computations are performed on an IBM 3090 computer using double precision arithmetics. Here, we use the notation "SUPORT" to represent

the results from the first method, "DB2PFD" from the second method, and "2nd" and "4th" to stand for the second- and fourth- order methods.

The flow conditions for the first case are

Mach number	$M = 6.0$
Temperature ratio	$T_2 = 2.0$
Velocity ratio	$U_2 = 0.0$
Reynolds number	$R = 1000$
Number of points	$N = 301$ (for DB2PFD and 4th)
Frequency	$\omega = 0.1$
Estimated value of α	$\alpha_0 = 0.11300 - i\,0.001160$

The converged eigenvalues and the CPU times are shown in Table 1.

We note that the differences among the α's are very small. This establishes the reliability of our numerical calculations. Concerning the CPU time, however, Suport and DB2PFD consume much more time than the 4th-order method.

The flow conditions for the second case are

Mach number	$M = 2.0$
Temperature ratio	$T_2 = 2.0$
Velocity ratio	$U_2 = 0.0$
Reynolds number	$R = 5000$
Frequency	$\omega = 0.10$
Estimated value of α	$\alpha_0 = 0.14400 - i\,0.008500$

Because R is so large that the instability can be considered inviscid, α can be easily obtained from the inviscid code. The result is

$$\alpha = 0.1447844 - i\,0.008584644$$

SUPPORT took a 217 sec CPU to get the value

$$\alpha = 0.1447831 - i\,0.008493894$$

Because R is very large, the system is very stiff, and DB2PFD code could not converge to a value of α, even when N is increased to 601. Tables 2 and 3 list the converged values of α obtained from the 2nd- and 4th-order methods for various values of N. Obviously, the CPU times taken by the 4th- and 2nd-order codes are not sensitive to the high Reynolds number. Furthermore, the results in Table 3 show that the converged values of α do not change when $N \geq 201$.

Three large Reynolds numbers are chosen, and the 4th-order code is used to obtain the eigenvalues, which are expected to be close to the inviscid solution, see Table 4.

Table 1. Comparison among SUPORT, DB2PFD, and 4th-order method.

CODE	real part	Imaginary part	CPU TIME
SUPORT	0.11258858	- 0.00075378	127 sec
DB2PFD	0.11258858	- 0.00075375	75 sec
4TH	0.11258900	- 0.00075357	16 sec

Table 2. **Second-order** ($M = 2, R = 5000, T_2 = 2,$ and $U_2 = 0$)

N	real part	imaginary part	CPU TIME
101	0.14482427	- 0.00849691	7 sec
201	0.14481926	- 0.00850180	11 sec
301	0.14481834	- 0.00850271	22 sec
401	0.14481801	- 0.00850303	22 sec
501	0.14481786	- 0.00850318	26 sec
601	0.14481778	- 0.00850325	34 sec
701	0.14481773	- 0.00850330	39 sec
801	0.14481770	- 0.00850333	45 sec

Table 3. Fourth-order ($M = 2, R = 5000, T_2 = 2$, and $U_2 = 0$)

N	real part	Imaginary part	CPU TIME
101	0.144817597	- 0.00850344	7 sec
201	0.144817596	- 0.00850343	10 sec
301	0.144817596	- 0.00850343	16 sec
401	0.144817596	- 0.00850343	21 sec

Table 4. Fourth-order ($M = 2, N = 301, T_2 = 2$, and $U_2 = 0$)

R	real part	imaginary part	CPU TIME
50000	0.144786657	- 0.00857795	19 sec
70000	0.144785657	- 0.00858032	17 sec
100000	0.144784913	- 0.00858210	17 sec
Inviscid	0.1447844	- 0.0085846	7 sec

5.0 Primary Instability Results

5.1 *Introduction*

The linear stability problem of a supersonic free shear layer has been studied by several investigators. Lessen et al. (1965, 1966) considered the inviscid temporal stability of a laminar mixing layer. They obtained the mean flow by solving the compressible boundary-layer equations and found that the flow is more unstable with respect to waves propagating at an angle to the mean flow. Blumen et al. (1975) also considered the inviscid temporal stability of the hyperbolic tangent profile. They concluded that the flow is unstable to two-dimensional disturbances at all values of the Mach number as a result of the existence of an unstable second mode. Gropengiesser (1970) was the first to consider the spatial stability of supersonic free shear layers. Assuming a parallel mean flow and inviscid disturbances, he investigated the effects of the Mach number and temperature ratio on the stability of a single stream layer. He also obtained some results for oblique waves.

There are many parameters that affect the stability of the compressible shear layers formed by two parallel supersonic streams. They include the Mach number, velocity ratio, temperature ratio, streamwise variations of the basic state (nonparallel effects), Reynolds number (viscous effects), etc. Moreover, attention must be paid to oblique waves and the possibility of different modes of instability. Nonparallel and viscous effects may be dismissed as unimportant for supersonic layers with a

generalized inflection point. However, we want to study these effects to establish their orders of magnitudes, especially the nonparallel effects that were found to significantly affect the growth rate of turbulent free shear layers (Cringhton and Gaster 1976, Ragab and Wu 1989).

Bogdanoff (1983) suggested a Mach number M^+ as a parameter which may correlate the compressibility effects in turbulent free shear layers. He assumed the presence of large scale structures that travel at a mean speed U_w. To estimate U_w, he used the argument that the total drag force on the large scale structure is zero, and therefore he equated the dynamic pressures of the freestreams relative to the large structures; that is the dynamic pressures based on the Mach numbers $(U_1 - U_w)/a_1$ and $(U_w - U_2)/a_2$ are equal. Finally, he defined M^+ as the geometric average of the Mach numbers of the large structures relative to the two freestreams. After justifiable approximations, Bogdanoff gave the expression

$$M^+ = M_1(1 - \lambda_u)/(1 + \lambda_\rho^{-1/2})\lambda_\gamma^{1/4} \tag{5.1}$$

where $\lambda_u = U_2/U_1$, $\lambda_\rho = \rho_2/\rho_1$, $\lambda_\gamma = \gamma_2/\gamma_1$, and γ_1 and γ_2 are the specific heat ratios in the two streams.

Papamoschou and Roshko (1986) used the argument that in a coordinate system convecting with the large scale structures, a saddle point is present between the structures, which is a common stagnation point of the two streams. Equating the stagnation pressures of the two streams in the moving coordinate system, they obtained an estimate of the velocity by which the structure is convecting, which is the same estimate as the one obtained by Bogdanoff because the static pressure is constant. They also gave M^+ as the parameter which correlates the compressibility of the shear layer and called it the convective Mach number, a terminology that we will use in the following discussion.

Bogdanoff and Papamoschou and Roshko presented limited theoretical results from linear stability analysis in support of M^+ as a compressibility parameter. In Section 5.8, we present more comprehensive substantiation of M^+ based on spatial linear stability analysis of the Blasius-profile for wide ranges of velocity ratio, temperature ratio and Mach number. However, we limit our analysis to the case $\gamma_1 = \gamma_2$

In addition to investigating the viscous and nonparallel effects, we have two basic objectives to be accomplished in this Chapter. The first is to study in detail the influences of the velocity ratio and temperature ratio on the stability characteristics of the shear layer. The second is to substantiate the convective Mach number that has been proposed by Bogdanoff and Papamoschou and Roshko as a parameter that correlates the compressibility effects in mixing layers.

5.2 *Effect of The Reynolds Number*

The instability of a free shear layer with a generalized inflection point is primarily inviscid (Lees and Lin 1946, Mack 1969), and viscous stresses have a stabilizing effect. For a complete understanding of the instability, growing ,neutral, as well as damped disturbances must be computed. Using the inviscid theory in computing neutral or damped disturbances requires deforming the integration contour around the singularity point of the inviscid equation (Mack 1969). One can avoid the numerical difficulties associated with this deformation by using the complete viscous disturbance equations. This method involves higher computing costs, but the process is straightforward and the results are reliable. To the best of our knowledge,

the present work is the first study of the viscous effects on amplified disturbances in compressible mixing layers.

First, we present results for laminar mixing layers. The growth rates $-\alpha_i$ of two-dimensional waves are depicted in Fig. 5.1a and 5.1b as functions of the frequency ω for different Reynolds numbers R. The flow conditions for Fig. 5.1a are $M_1 = 2.0, U_2 = 0.0,$ and $T_2 = 1.0$ and for Fig. 5.1b they are $M_1 = 3.0, U_2 = 0.6, T_2 = 2.0$. The Results show that the shear layer is unstable at all Reynolds numbers down to $R = 50$, and for $R > 1000$ the growth rate approaches the values predicted by the inviscid stability theory. However, the amplified frequency domain becomes narrower as R is decreased. The phase speed ω/α_r is found to be almost independent of the Reynolds number.

Next, we consider the hyperbolic-tangent velocity profile $U(y) = 0.5 (1 + \tanh y)$ at $M_1 = 2.0$ and $T_2 = 1.0$. The growth rate versus frequency is shown in Fig. 5.2a. The three Reynolds numbers 500, 2000, and 5000 are considered in this case. There are two modes shown in Fig. 5.2a. The mode with higher growth rate shows that viscosity reduces the growth rate. The other mode is less sensitive to the Reynolds number. The phase speeds of the two modes are shown in Fig. 5.2b.

5.3 Comparison with Gropengiesser's Results

Gropengiesser (1970) presented the most compressive computations of the spatial inviscid stability for a single-stream ($U_2 = 0.0$) free-shear layer. We compared our computation with Gropengiesser's. We reproduced a large portion of Gropengiesser's computations. In computing the basic state, we assumed that the

Prandtl number Pr = 1.0 and used a linear viscosity-temperature relation ($\mu = T$). In Fig. 5.3, we compare our results with Gropengiesser's for the case $M_1 = 0.0$, $U_2 = 0.0$, and different temperature ratios. Full agreement is obtained.

5.4 *Effect of the Mach Number*

The variation of the growth rate with Mach number M_1 at the frequency $\omega_1 = 0.1$ is shown in Fig. 5.4. The results shown in Fig. 5.4 are obtained at the flow conditions $R = 1000$, $U_2 = 0.4$ and $T_2 = 0.6$. We observe in Fig. 5.4 that the growth rate is reduced rapidly as the Mach number M_1 is increased to $M_1 = 2.68$. If the Mach number is further increased, the original mode denoted by the first mode becomes damped. However, at the same time, two different modes with small but positive growth rates appear as shown in Fig. 5.4. The modes are called the second and third mode.

The convective Mach number based on the phase speed C_{ph} of the disturbance for each stream is given by

$$M_{c_1} = \frac{U_1 - C_{ph}}{a_1} , \qquad M_{c_2} = \frac{C_{ph} - U_2}{a_2}$$

where a_1 and a_2 are the speeds of sound in the upper and lower streams, respectively. The disturbances are classified into subsonic, sonic, and supersonic disturbances according to whether M_{c_1} (or M_{c_2}) is less than, equal to, or greater than 1 (Lees and Lin 1946). M_{c_1} and M_{c_2} are plotted versus Mach number in Fig. 5.5a and Fig. 5.5b, respectively, at the same flow conditions as those of Fig. 5.4. Both upper and lower

streams have subsonic disturbances when $M_1 \leq 2.68$ ($M^+ \simeq 0.906$) . Once the Mach number M_1 exceeds 2.68, the first and second modes produce supersonic disturbances in the upper stream and subsonic disturbances in the lower stream. However, the third mode produces a subsonic disturbance in the upper stream and a supersonic disturbance in lower stream. The second and third modes are called slow and fast modes by Jackson and Grosch (1988). In the following work, we adopt their terminology for classifying these higher modes.

The distributions of the amplitude of the u-component of the velocity disturbances for the three different modes at $M_1 = 2.9$ are plotted in Fig. 5.6.

5.5 *Effect of the Velocity Ratio*

Using linear spatial stability theory and assuming incompressible flow, Monkewitz and Huerre (1982) showed that the maximum growth rate is approximately proportional to the velocity ratio λ defined by $\lambda = (1 - U_2)/(1 + U_2)$. Hence, the maximum growth rate for two streams ($U_2 \neq 0$) can be obtained from the growth rate of a single stream ($U_2 = 0, \lambda = 1$) by multiplying the latter by λ, and there is no need to solve the eigenvalue problem for different velocity ratios. Similar conclusions will be presented in Section 5.6 for compressible shear layers with variable temperature distributions, except that the variation of the maximum growth rate with λ is nonlinear.

Because of the terms $u\partial u/\partial x$ and $u\partial T/\partial x$, the velocity ratio U_2 or λ directly affects the velocity and temperature profiles obtained by solving the shear-layer equations. Furthermore in the spatial stability theory, the average velocity $(1 + U_2)/2$ can not be

absorbed In the phase speed, except for neutral waves. In this Section we investigate the effect of U_2 while keeping T_2 and M_1 fixed.

Numerical results have been obtained for a fixed $T_2 = 2.0$ and for different Mach numbers M_1 ranging from 0.0 to 6.0. The variations of the growth rate $-\alpha_i$ with frequency ω are shown in Fig. 5.7a, Fig. 5.8a, and Fig. 5.9a, and the corresponding variations of the phase speed are shown in Fig. 5.7b, Fig. 5.8b, and Fig. 5.9b, for $U_2 = 0.0, 0.3$, and 0.6, respectively. One observes that there is a slight increase in the range of amplified frequency as U_2 increases. Moreover, increasing the Mach number has a significant effect on the growth rate for $U_2 = 0.0$, but it becomes less effective as U_2 increases. Comparison among Fig. 5.7b, Fig. 5.8b and Fig. 5.9b also shows that increasing U_2 results in less dispersion.

In Fig. 5.7a, Fig. 5.8a and Fig. 5.9a, we note that, for all the Mach numbers and velocity ratios considered, the most amplified frequency falls in the range $\omega = 0.05$ to 0.15. We computed the growth rate and the phase speed at the three frequencies $\omega = 0.05, 0.1$ and 0.15 and plotted the results against the velocity ratio $\lambda = (1 - U_2)/(1 + U_2)$. The growth rates are shown in Fig. 5.10a, Fig. 5.11a, and Fig. 5.12a, while the phase speeds are shown in Fig. 5.10b, Fig. 5.11b, and Fig. 5.12b. In Fig. 5.10a, Fig. 11a and Fig. 5.12a the growth rate is normalized with respect to its value at $M_1 = 0.0$ and $\lambda = 1.0\,(U_2 = 0.0)$. It follows from Fig. 5.10a that only the incompressible case shows nearly linear variation of $-\alpha_i$ with λ. At higher Mach numbers the variation is evidently nonlinear. The effects of velocity ratios on oblique waves are given in Section 5.7.

5.6 *Effect of the Temperature Ratio*

Next, we fix the velocity ratio at $U_2 = 0.0$ and study the effect of cooling/heating on the stability of the mixing layer. At the Mach number $M_1 = 0.0$, we have already seen in Fig. 5.3 that heating the stagnant stream (or cooling the faster stream) has a strong stabilizing effect. However, this stabilization does not persist at higher Mach number. The variation of the growth rate $-\alpha_i$ with frequency ω is shown in Figs. 5.13a-13c for $M_1 = 1.0$, 1.5 and 2.0, respectively. We observe from Fig. 5.13b that the effect of heating/cooling on the maximum growth rate starts to reverse, and at $M_1 = 2.0$, heating is destabilizing at all frequencies.

The maximum growth rate $-\alpha_{imax}$ ($-\alpha_i$ maximized over all frequencies) is shown in Fig. 5.14 against the Mach number M_1 for $T_2 = 0.5$, 1.0, and 2.0. It is evident that for $M_1 \leq 1.5$ heating is stabilizing, but for $M_1 > 1.5$ heating is destabilizing.

The previous results concern the first mode of instability (fast mode). However as we increase the Mach number M_1 (for fixed U_2 and T_2), there is always a possibility of a second mode becoming amplified. For complete presentations on higher modes in shear layers, we refer the reader to the recent contributions by Mack (1989) and Jackson and Grosch (1988). Figure 5.15 shows that at $M_1 = 2.0$, the second mode is stabilized by heating. When $T_2 = 0.5$ the maximum growth rate of the second mode exceeds that of the first mode, but when $T_2 = 1.0$ and $T_2 = 2.0$, the first mode is the most amplified mode.

5.7 Three-Dimensional Waves

It is well known that oblique waves have higher growth rates than two-dimensional waves at high Mach numbers. In Fig. 5.16, the growth rate of oblique waves ($\beta \neq 0$) is depicted against the wave propagation angle $\theta = \tan^{-1}(\beta/\alpha_r)$, for different Mach numbers and at the respective most amplified frequency. The flow parameters are $U_2 = 0.0$ and $T_2 = 1.0$. These results are obtained as followed. The spanwise wavenumber β is assumed to be real and the streamwise wavenumber α is complex. For a fixed Mach number M_1, we scan the $\omega - \beta$ plane to find the maximum growth rate $-\alpha_{i_{max}}$. This is accomplished by fixing ω and increasing β from zero to a value at which the disturbance becomes neutral, and recording the maximum growth rate for that frequency. Next we increment the frequency and repeat the β calculations and record the new maximum growth rate. After scanning the frequency domain, we compare all the recorded maxima and choose the frequency that gives the largest value among them. The results presented in Fig. 5.16 correspond to the maximum amplified frequency for the given Mach number M_1, and θ is computed from $\theta = \tan^{-1}(\beta/\alpha)$.

In Section 5.5, we showed that the growth rates of two-dimensional waves at high Mach number vary nonlinearly with the velocity ratio λ at a certain frequency and temperature ratio. Fig. 5.17 shows the relationship between the maximum growth rates (maximized over all frequencies and propagation angles) and the velocity ratio λ for six different Mach numbers $M_1 = 0.0,\ 1.0,\ 1.448,\ 3.0,\ 4.0$ and 5.0 at the Reynolds number $R = 2000$. In Fig. 5.17 the solid lines represent two-dimensional waves, and the dashed lines represent three-dimensional waves. As expected, for incompressible flow the results show that the maximum growth rate varies nearly

linearly with the velocity ratio λ. As the Mach number increases, the linear relationship ceases, and each curve has a maximum value at $\lambda = 1.0$ when M_1 is less than 1.448 (i.e., $M^+ = 0.6$). If the convective Mach number $M^+ > 0.6$ at $\lambda = 1.0$, the maximum growth rate shifts to a smaller λ. Moreover, the maximum growth rate will not occur for two-dimensional waves but for oblique waves. However, the maximum growth rate is insensitive to the velocity ratio once M^+ is greater than 0.6.

The phase speed of the most amplified fast and slow two-dimensional modes as well as the most amplified three-dimensional waves are depicted against the velocity ratio in Fig. 5.18. The corresponding propagation angles of the three-dimensional waves are shown in Fig. 5.19. For the combination of Mach numbers, phase speeds, and propagation angles involved, there is only one amplified oblique wave.

We have attempted to compare between the present theoretical results and the experimental results of Chinzei et al. (1986), who experimentally investigated the effect of the velocity ratio on the growth rate. In the experimental work, the Mach number of the faster stream was kept constant at $M_1 = 2.3$, and the total stagnation temperatures of the two streams were kept equal. Accordingly, the static temperature ratio T_2 decreased as the velocity ratio U_2 was increased. Moreover, the boundary layer on the splitter plate as well as the mixing layer itself were completely turbulent. In Fig. 5.20, the maximum growth rate of three-dimensional and two-dimensional waves for the hyperbolic-tangent velocity profile are presented. The data are normalized with respect to the growth rate at $\lambda = 1$. There is a qualitative agreement between the three-dimensional stability results and the experimental data. Moreover, oblique waves are more amplified than two-dimensional waves when the velocity ratio U_2 is less than 0.33, where $T_2 = 1.708$, and $M^+ = 0.635$.

5.8 *Correlation with the Convective Mach Number*

To isolate the compressibility effect on the spreading rates of shear layers, Papamoschou and Roshko pointed out that the spreading rate σ for certain values of Mach number M_1, velocity ratio U_2, and density ratio ρ_2, must be normalized with respect to the spreading rate at Mach number M_1, but at the same velocity ratio U_2 and density ratio ρ_2. They gave the following expression for the spreading rate ratio R_σ :

$$R_\sigma = \frac{\sigma(M_1, U_2, \rho_2)}{\sigma(0, U_2, \rho_2)} = F(M^+). \tag{5.2}$$

In general, available experimental data on compressible shear layers do not necessarily include data at zero Mach number for the same velocity and temperature ratios. Therefore, a model is needed to estimate the incompressible growth rate over a range of velocity and temperature ratios. Such a model is given by Papamoschou and Roshko by the following formula:

$$\sigma(0, U_2, \rho_2) = \sigma_0 \frac{(1 - U_2)(1 + \rho_2^{1/2})}{(1 + U_2\rho_2^{1/2})} \tag{5.3}$$

where σ_0 is a constant. When normalizing data based on the visual shear-layer thickness they suggested the value $\sigma_0 = 0.17$. However, when normalizing data based on the vorticity thickness Papamoschou (1986) suggested a value of 0.085.

In our study, we assume that the maximum growth rate of instability waves $-\alpha_{imax}$ (maximized over all frequencies) correlates with the spreading rate of the

shear layer. Thus, in the present comparison between theory and experiments, we define the growth rate ratio R_σ as

$$R_\sigma = \frac{-\alpha_{i\max}(M_1, U_2, \rho_2)}{-\alpha_{i\max}(0, U_2, \rho_2)} \tag{5.4}$$

Before discussing the correlation with the convective Mach number M^+, we compare between the results predicted by linear stability theory and the model given by (5.3) for incompressible flow. In Fig. 5.21, we depict the ratio $-\alpha_{i\max}(0, U_2, \rho_2)/-\alpha_{i\max}(0, U_2, 1)$ against $T_2 = \rho_2^{-1}$ for the two velocity ratios $U_2 = 0.0$ and $U_2 = 0.6$. The agreement is only qualitative, and the linear stability results show great sensitivity to the density ratio in comparison with the model suggested by Papamoschou and Roshko.

Assuming two-dimensional disturbances and using the laminar mean flow profiles, we computed the growth rate ratio R_σ, as defined by (5.4) for the combinations of velocity ratio U_2 and temperature ratio T_2 (density ratio $\rho_2 = T_2^{-1}$) given by $(U_2, T_2) = (0.0, 1.0), (0.0, 2.0), (0.3, 1.0), (0.3, 2.0), (0.6, 1.0), (0.6, 2.0)$, and $(0.4, 0.6)$. For each combination, the Mach number M_1 is varied from 0.0 to a value of 4.0 when $U_2 = 0.0$ and to a value of 6.0 when $U_2 \geq 0.3$. The ratio R_σ is depicted in Fig. 5.22 against the convective Mach number M^+ defined by (5.1). It is evident from Fig. 5.22 that the $R_\sigma - M^+$ relation is practically independent of the specific values of M_1, U_2, and T_2. However, there is a slight variation with these values when the convective Mach number is greater than one. Also shown in Fig. 5.22 are the $R_\sigma - M^+$ results obtained for the hyperbolic tangent profile for $U_2 = 0.3$ and $T_2 = 2.0$. The R_σ values are slightly higher than the value for the Blasius-Lock profile.

The experimental data for turbulent shear layers, obtained by Papamoschou and Roshko based on the visual shear layer thickness and those by other investigators

(also taken from Papamoschou 1986), are depicted in Fig. 5.22 along with the present laminar stability results. The data of Chinzei et al. (1986) are normalized with respect to the incompressible growth rate according to (5.3), with $\sigma_0 = 0.085$. Increasing the convective Mach number affects the growth rate ratio of instability waves in laminar flows in a strikingly similar way as it influences the ratio of the spreading rate of turbulent shear layers. This is only true, however, for convective Mach number less than 0.8. For higher Mach numbers, the experimental data levels off at about 0.25, while the laminar stability ratio continues to decrease.

The growth rate ratio R_σ based on the maximum growth rate of oblique waves is also shown in Fig. 5.22. The oblique wave results show better agreement with the experimental data of Papamoschou and Roshko for convective Mach numbers less than 1.3. However, the theoretical ratio R_σ continues to decrease with increasing M^+, but the experimental data levels off at about 0.25.

Figure 5.22 should not be read as a comparison between the linear stability analysis of laminar flow and turbulent experimental data. Our intention is to demonstrate that the convective Mach number, introduced by Bogdanoff and Papamoschou and Roshko, is a viable compressibility parameter of mixing layers.

The calculations of normalized growth with convective Mach number are also obtained for the hyperbolic-tangent velocity profile at a Reynolds number of 2000, and the results are shown in Fig. 5.23. Comparison between Fig. 5.22 for a laminar shear mean flow and Fig. 5.23 for the hyperbolic profile shows that the relationship between R_σ and M^+ is insensitive to the details of the mean-flow profiles.

Zhuang et al. (1988) conducted a similar study and correlated their stability calculations with a convective Mach Mach number M_{c_1}, based on the phase speed. They showed a similar collapse of the data as in Fig. 5.22. The Mach numbers $M_{c_1} = M_1(1 - \omega/\alpha_r)$, $M_{c_2} = M_1(\omega/\alpha_r - U_2)/\sqrt{T_2}$ and their average $M_{av} = (M_{c_1} + M_{c_2})/2$

are shown against M^+ [defined by (5.1)] in Fig. 5.24a, Fig. 5.24b and Fig. 5.24c for the temperature ratios $T_2 = 0.6$, 1.0, and 2.0, respectively, and for $U_2 = 0.0$. We note that for $M^+ < 1.0$, the four Mach numbers are close to each other, but for $M^+ > 1$, M_{c_2} remains constant, while M_{c_1} and M_{av} "almost" linearly depend on M^+.

5.9 *Nonparallel effects*

The streamwise variation of the basic state (nonparallel effects) has a significant effect on the growth rate of turbulent free shear layers. This result has been demonstrated by many investigators (see Ragab and Wu 1989, Cringhton and Gaster 1976). Here we study the nonparallel effects on the laminar mixing layer.

It was mentioned in Chapter 3 that the nonparallel correction to the growth rate depends on the disturbance quantity being investigated through the term $(1/\zeta_n)\,\partial\zeta_n/\partial x_1$, and on the transverse location y. The nonparallel correction to the wavenumber α is given by Eq.(3.82). The correction to the growth rate is $-\varepsilon\alpha_{1i}$, where $\varepsilon = 1/R$; the variation of α_{1i} with y is shown in Fig. 5.25 for the v-component. The flow parameters are $U_2 = 0.6$, $T_2 = 1.0$, $M_1 = 2.0$, and the Reynolds number takes the three values 500, 1000, and 3000. In Fig. 5.25 the curve marked inviscid ($R = \infty$) is computed using the simplified nonparallel inviscid model of Ragab and Wu (1988). The present viscous nonparallel calculations approach the results of the inviscid model as $R \to \infty$. However, the numerical values depicted in Fig. 5.25 imply that the nonparallel corrections for laminar shear layers at high Reynolds numbers are small.

The variation of the growth rates of parallel and nonparallel flows with the physical frequency $F = \omega^* \nu^*/U_\infty^{*2}$ at $R = 1000$ are plotted in Fig. 5.26. Two nonparallel

corrections corresponding to pressure- and mass-disturbances at y = 0 are expressed by α_{lp} and α_{lm}, respectively [see (3.82)]. Figure 5.26 shows that the nonparallel effects are negligible in this case. However, for the same flow conditions but R = 100, the results in Fig. 5.27 show that the nonparallel correction $-\alpha_{lp}$ can be appreciable in comparison to the parallel growth rate. Moreover, the amplified frequency domain is enlarged when the nonparallel effects are included.

For a higher Mach number, the nonparallel effects at a Reynolds number of 1000 are shown in Fig. 5.28. In comparison with the low Mach number case of Fig. 5.26, we conclude that the nonparallel effects are more important at high Mach numbers than at low Mach numbers.

6.0 Subharmonic Instabilities

6.1 Introduction

Oscillations having a frequency equal to one-half the frequency of the fundamental oscillations of the free-shear layers have been observed experimentally (Sato 1959, Browand 1966, Freymuth 1966). Ho and Huang (1982) have used the technique of forcing the subharmonic wave to study the enhancement of vortices merging. They have concluded that the presence of the subharmonic is necessary in vortex merging. These investigations have been conducted for incompressible shear layers. Corresponding investigations for compressible shear layers have not been conducted yet.

To motivate the present study, we present in Fig. 6.1a the vorticity contours of a spatially developing mixing layer obtained by solving the full unsteady Navier-Stokes equations. The computer code was provided by Dr. Sankar of Georgia Institute of Technology (see Tang et al., 1989). The initial flow is specified by a linear superposition of a hyperbolic tangent velocity profile and its most amplified wave. The flow is forced at the inflow boundary by the most amplified wave. The flow conditions are $M_1 = 2.0$, $R = 100$, $U_2 = 0.6$, and $T_2 = 1.0$. We note in Fig. 6.1a that the shear layer develops a well defined periodic state far downstream. When we added the subharmonic wave of the most amplified wave at the inflow boundary, the shear layer develops the expected pairing mode as shown in Fig. 6.1b.

Our objective is to study the effects of various flow parameters on the pairing mode and development of three-dimensionality in compressible mixing layer. We use a simplified model of the problem. Here, we construct a periodic 2D flow by linearly superposing a mean flow and a finite amplitude wave. The shape function of the wave is taken to be the eigenfunction of the neutral wave of the mean flow. The vorticity contours of such a periodic basic state are shown in Fig. 6.2. Also shown in that figure is the superposition of the basic state and the computed subharmonic wave. Evident in Fig. 6.2 is the initial phase of the pairing phenomenon; however, the complete roll up and merging of the vortices are beyond the present linear analysis.

The mathematical formulation of the secondary subharmonic problem is described in Section 6.2. The boundary conditions of the problem are discussed in Section 6.3. In Section 6.4, the numerical approach is presented. The results are presented in Chapter 7.

6.2 *Mathematical Formulation*

The total flow $q = (u, v, w, p, T, \rho, \mu)$ is decomposed into three components as $q = q_o + q_1 + q_2$. Here, q_o denotes the mean flow, which is assumed to be steady and locally parallel, that is $q_o = q_o(y)$. Two types of mean flows are considered in this study. The first is obtained by solving the two-dimensional compressible boundary-layer equations. The second is the hyperbolic-tangent velocity profile, and the temperature profile is determined from the Crocco-Busemann integral.

Before we discuss the flow component given by q_1, which is called the primary wave, we review the very much related work by Pierrehumbert and Widnall (1982) and by Santos and Herbert (1986, see Santos 1987 for more details). Pierrehumbert and Widnall considered the primary instability of Stuart vortices using Floquet analysis. The basic state is spatially periodic and is given by an exact solution known as Stuart vortices to the incompressible Euler equations. The solution represents an infinite row of continuously distributed vortices. Pierrehumbert and Widnall considered temporal linear inviscid stability and demonstrated that the subharmonic wave (an instability wave whose wavelength is double that of the periodicity of the basic state) is the most unstable wave in the two-dimensional limit (pairing mode). They also identified the 3D fundamental mode (a wave with wavelength that is equal to that of the vortices) and found it to be most unstable for spanwise wavelengths approximately 2/3 of the space between vortex centers.

Santos (1987) expanded the streamfunction of the Stuart vortices, which is given by

$$\psi = \ln(\cosh y - d\cos x) \tag{6.1}$$

where d is a constant signifying the strength of the vortices, in a Taylor series for small d and obtained

$$\psi = \ln(\cosh y) - d\,\frac{\cos x}{\cosh y} + O(d^2) \tag{6.2}$$

He then realized that the first term in the expansion is precisely the streamfunction of the hyperbolic-tangent velocity profile $u = \tanh y$ and that the second term coincides with the neutral solution of the Rayleigh equation for that profile. The corresponding neutral wavenumber is $\alpha = 1$ and the eigenfunction is sech y. The

parameter d plays the role of an amplitude which can be related to the maximum root-mean-square of the streamwise velocity perturbation.

Santos studied the secondary instability of a basic state that is obtained by a superposition of the mean flow q_o, given by the hyperbolic tangent velocity profile, and the neutral inviscid instability wave with a specified amplitude. He obtained the growth rates of the subharmonic, fundamental, and combination modes. His results are in agreement with those of Pierrehumbert and Widnall.

The Stuart vortices are an exact solution to the incompressible Euler equations, but their counterpart for compressible flows is unknown to us. Therefore, we follow Santos and Herbert in using an approximate solution which is periodic in space and time. That approximation is obtained by a linear superposition of the mean flow q_o and a solution to the viscous compressible stability problem for that mean flow. For a given set of flow parameters (Mach number, Reynolds number, temperature ratio, and velocity ratio), we determine the eigenfunctions of the 2D neutral wave solution to the compressible Orr-Sommerfeld equations. These functions are normalized such that the maximum root-mean-square of the streamwise velocity component u_1 has a specified value, which is denoted by A_{rms}. We note that the wavelengths of these periodic structures depend on the specific values of the flow parameters. For example, as we vary the Mach number, say, we also vary the wavelength of the periodic part of the flow. In this dissertation, we use the words "primary wave" and "periodicity" interchangeably.

The basic state is now given by $q_o + q_1$, where q_1 is the neutral wave solution. This state is periodic in space and time, and in a frame of reference moving with the phase speed it becomes spatially periodic. We use Floquet analysis to determine its stability with respect to disturbances which have double the wavelength of the periodic part q_1 . That is to say, we investigate the subharmonic instability of that

basic flow which corresponds to principal parameter resonance in the Floquet analysis (see Nayfeh 1988). The total-flow variables are written as

$$u(x,y,z,t) = u_o(y) + u_1E + \bar{u}_1E^{-1} + \Theta\,[u_2(y)E^{1/2} + \tilde{u}_2(y)E^{-1/2}]\cos(\beta z) \tag{6.3}$$

$$v(x,y,z,t) = v_1E + \bar{v}_1E^{-1} + \Theta\,[v_2(y)E^{1/2} + \tilde{v}_2(y)E^{-1/2}]\cos(\beta z) \tag{6.4}$$

$$w(x,y,z,t) = \Theta\,[w_2(y)E^{1/2} + \tilde{w}_2(y)E^{-1/2}]\sin(\beta z) \tag{6.5}$$

$$T(x,y,z,t) = T_o(y) + T_1E + \bar{T}_1E^{-1} + \Theta\,[T_2(y)E^{1/2} + \tilde{T}_2(y)E^{-1/2}]\cos(\beta z) \tag{6.6}$$

$$p(x,y,z,t) = p_o + p_1E + \bar{p}_1E^{-1} + \Theta\,[p_2(y)E^{1/2} + \tilde{p}_2(y)E^{-1/2}]\cos(\beta z) \tag{6.7}$$

$$\rho(x,y,z,t) = \rho_o(y) + \rho_1E + \bar{\rho}_1E^{-1} + \Theta\,[\rho_2(y)E^{1/2} + \tilde{\rho}_2(y)E^{-1/2}]\cos(\beta z) \tag{6.8}$$

$$\mu(x,y,z,t) = \mu_o(y) + \mu_1E + \bar{\mu}_1E^{-1} + \Theta\,[\mu_2(y)E^{1/2} + \tilde{\mu}_2(y)E^{-1/2}]\cos(\beta z) \tag{6.9}$$

where an over bar indicates the complex conjugate, and

$$E = \exp\,[\,i\,(\alpha_r x - \omega_r t)\,] \tag{6.10}$$

$$\Theta = \exp\,(\sigma t + \gamma x) \tag{6.11}$$

Here, α_r and ω_r are the wavenumber and frequency of the 2D neutral primary wave, $\sigma\,(= \sigma_r + i\sigma_i)$ and $\gamma\,(= \gamma_r + i\gamma_i)$ are called the characteristic exponents of the Floquet analysis. We note that the subharmonic waves are three-dimensional with a spanwise wavenumber β. We also note that in (6.3)-(6.9) only two terms ($q_2E^{1/2}$ and $\tilde{q}_2E^{-1/2}$) of a Fourier series expansion of the periodic eigenfunction of the Floquet analysis are retained. For temporal stability, we set $\gamma = 0$; then σ_r gives the growth rate, and σ_i represents a frequency shift from $\omega_r/2$. For spatial stability, we

set $\sigma = 0$; then γ_r gives the growth rate and γ_i represents a wavenumber shift from $\alpha_r/2$. For synchronized primary and subharmonic waves we have $\sigma_i = 0$ and $\gamma_i = 0$, and only for this case q_2 and $\tilde{q}_2$ can be assumed to be a complex conjugate pair.

The viscosity perturbations in (6.9) can be related to the temperature perturbations of (6.6) by using the viscosity-temperature relation. In this study, the Sutherland viscosity-temperature equation is used with $T_\infty = 273°K$ at all Mach numbers. The ratio of the bulk viscosity to the kinetic viscosity is taken to be 0.6; however, the bulk viscosity has negligible effects at low Mach numbers.

Substituting (6.3)-(6.9) into the disturbance equations (3.2)-(3.7), neglecting nonlinear terms in the primary wave (i.e., terms of order q_1^2 and higher) and then equating the coefficients of $E^{1/2}$ on both sides of the equations, we obtain the governing equations for q_2.

Continuity Equation :

$$\begin{aligned}
&\rho_o \frac{dv_2}{dy} + \rho_1 \frac{d\tilde{v}_2}{dy} + v_1 \frac{d\tilde{\rho}_2}{dy} \\
&= -\{\rho_o(\gamma + \frac{i\alpha}{2})u_2 + \frac{d\rho_o}{dy} v_2 + [(\sigma - \frac{i\omega}{2}) + u_o(\gamma + \frac{i\alpha}{2})]\rho_2 + \rho_o \beta w_2 \qquad (6.12) \\
&+ \rho_1(\gamma + \frac{i\alpha}{2})\tilde{u}_2 + \frac{d\rho_1}{dy}\tilde{v}_2 + [(\gamma + \frac{i\alpha}{2})u_1 + \frac{dv_1}{dy}]\tilde{\rho}_2 + \rho_1 \beta \tilde{w}_2\}
\end{aligned}$$

X-Momentum Equation :

$$\mu_o \frac{d^2u_2}{dy^2} = R\rho_o[(\sigma - \frac{i\omega}{2}) + u_o(\gamma + \frac{i\alpha}{2})]u_2 + R\{\rho_o(\gamma + \frac{i\alpha}{2})u_1$$

$$+ \rho_1[(\sigma + \frac{i\omega}{2}) + u_o(\gamma - \frac{i\alpha}{2})]\tilde{u}_2 + R\{\rho_o v_1 \frac{d\tilde{u}_2}{dy} + \rho_o \frac{du_o}{dy} v_2$$

$$+ (\rho_o \frac{du_1}{dy} + \rho_1 \frac{du_o}{dy})\tilde{v}_2 + (\gamma + \frac{i\alpha}{2})p_2 - [i(\omega - \alpha u_o)u_1 - v_1 \frac{du_o}{dy}]\tilde{\rho}_2\} \quad (6.13)$$

$$- \mu_o[(2+m)(\gamma + \frac{i\alpha}{2})^2 - \beta^2]u_2 - \frac{d\mu_o}{dy}\frac{du_2}{dy} - (\gamma + \frac{i\alpha}{2})\frac{d\mu_o}{dy} v_2$$

$$- \mu_o(1+m)(\gamma + \frac{i\alpha}{2})\frac{dv_2}{dy} - \frac{d}{dy}(\mu_2 \frac{du_o}{dy}) - (1+m)\mu_o\beta(\gamma + \frac{i\alpha}{2})w_2 - K_{12}$$

where

$$K_{12} = \mu_1\{\frac{d^2\tilde{u}_2}{dy^2} + [(2+m)(\gamma^2 + \frac{\alpha^2}{4}) - \beta^2]\tilde{u}_2\} + \frac{d\mu_1}{dy}\frac{d\tilde{u}_2}{dy} + (\gamma - \frac{i\alpha}{2})\frac{d\mu_1}{dy}\tilde{v}_2$$

$$+ \mu_1[m(\gamma + \frac{i\alpha}{2}) + (\gamma - \frac{i\alpha}{2})]\frac{d\tilde{v}_2}{dy} + (\gamma + \frac{i\alpha}{2})[i\alpha(2+m)u_1 + m\frac{dv_1}{dy}]\tilde{\mu}_2$$

$$+ \frac{d}{dy}[\tilde{\mu}_2(\frac{du_1}{dy} + i\alpha v_1)] + \beta\mu_1[m(\gamma + \frac{i\alpha}{2}) + (\gamma - \frac{i\alpha}{2})]\tilde{w}_2$$

Y-Momentum Equation :

$$\frac{dp_2}{dy} = -i\alpha\rho_o v_1\tilde{u}_2 - \rho_o[(\sigma - \frac{i\omega}{2}) + u_o(\gamma + \frac{i\alpha}{2})]v_2$$

$$- \{\rho_o u_1(\gamma - \frac{i\alpha}{2}) + \rho_o\frac{dv_1}{dy} + \rho_1[(\sigma + \frac{i\omega}{2}) + u_o(\gamma - \frac{i\alpha}{2})]\}\tilde{v}_2$$

$$- \rho_o v_1\frac{d\tilde{v}_2}{dy} + i(\omega - \alpha u_o)v_1\tilde{\rho}_2 + \frac{1}{R}\{m(\gamma + \frac{i\alpha}{2})\frac{d\mu_o}{dy}u_2 \quad (6.14)$$

$$+ \mu_o(1+m)(\gamma + \frac{i\alpha}{2})\frac{du_2}{dy} + \mu_o[(\gamma + \frac{i\alpha}{2})^2 - \beta^2]v_2 + (2+m)\frac{d}{dy}(\mu_o\frac{dv_2}{dy})$$

$$+ (\gamma + \frac{i\alpha}{2})\frac{du_o}{dy}\mu_2 + m\beta\frac{d\mu_o}{dy}w_2 + \mu_o\beta(1+m)\frac{dw_2}{dy}\} + L_{12}$$

where

$$L_{12} = \frac{1}{R}\{m(\gamma - \frac{i\alpha}{2})\frac{d\mu_1}{dy}\tilde{u}_2 + \mu_1[(\gamma + \frac{i\alpha}{2}) + m(\gamma - \frac{i\alpha}{2})]\frac{d\tilde{u}_2}{dy}$$
$$+ \mu_1(\gamma^2 + \frac{\alpha^2}{4} - \beta^2)\tilde{v}_2 + (2+m)\frac{d}{dy}(\mu_1\frac{d\tilde{v}_2}{dy}) + (\gamma + \frac{i\alpha}{2})(\frac{du_1}{dy} + i\alpha v_1)\tilde{\mu}_2$$
$$+ \frac{d}{dy}\{[i\alpha m u_1 + (2+m)\frac{dv_1}{dy}]\tilde{\mu}_2\} + m\beta\frac{d\mu_1}{dy}\tilde{w}_2 + \mu_1\beta(1+m)\frac{d\tilde{w}_2}{dy}\}$$

Z-Momentum Equation :

$$\mu_o\frac{d^2w_2}{dy^2} = -R\beta p_2 + R\rho_o[(\sigma - \frac{i\omega}{2}) + u_o(\gamma + \frac{i\alpha}{2})]w_2$$
$$+ R\{\rho_o(\gamma - \frac{i\alpha}{2})u_1 + \rho_1[(\sigma + \frac{i\omega}{2}) + u_o(\gamma - \frac{i\alpha}{2})]\}\tilde{w}_2 + R\rho_o v_1\frac{d\tilde{w}_2}{dy} \quad (6.15)$$
$$+ \mu_o\beta(1+m)(\gamma + \frac{i\alpha}{2})u_2 + \beta\frac{d\mu_o}{dy}v_2 + \mu_o\beta(1+m)\frac{dv_2}{dy}$$
$$- \mu_o[(\gamma + \frac{i\alpha}{2})^2 - (m+2)\beta^2]w_2 - \frac{d\mu_o}{dy}\frac{dw_2}{dy} + M_{12}$$

where

$$M_{12} = \beta\mu_1[(\gamma + \frac{i\alpha}{2}) + m(\gamma - \frac{i\alpha}{2})]\tilde{u}_2 + \beta\frac{d\mu_1}{dy}\tilde{v}_2 + \beta(1+m)\mu_1\frac{d\tilde{v}_2}{dy}$$
$$- \mu_1\frac{d^2\tilde{w}_2}{dy^2} + m\beta(i\alpha u_1 + \frac{dv_1}{dy})\tilde{\mu}_2 - \mu_1[\gamma^2 + \frac{\alpha^2}{4} - (2+m)\beta^2]\tilde{w}_2 - \frac{d\mu_1}{dy}\frac{d\tilde{w}_2}{dy}$$

Energy Equation :

$$\mu_o \frac{d^2T_2}{dy^2} = RPr\{ i\alpha[\rho_o T_1 - (\gamma_g - 1)M^2 p_1]\tilde{u}_2 + \rho_o \frac{dT_o}{dy} v_2$$
$$+ [(\rho_o \frac{dT_1}{dy} + \rho_1 \frac{dT_o}{dy}) - (\gamma_g - 1)M^2 \frac{dp_1}{dy}]\tilde{v}_2 \}$$
$$- R(\gamma_g - 1)M^2 Pr\{ [(\sigma - \frac{i\omega}{2}) + u_o(\gamma + \frac{i\alpha}{2})]p_2 + (\gamma - \frac{i\alpha}{2})u_1\tilde{p}_2$$
$$+ v_1 \frac{d\tilde{p}_2}{dy} \} + RPr\rho_o[(\sigma - \frac{i\omega}{2}) + u_o(\gamma + \frac{i\alpha}{2})]T_2$$
$$+ RPr\{ \rho_o(\gamma - \frac{i\alpha}{2})u_1 + \rho_1[(\sigma + \frac{i\omega}{2}) + u_o(\gamma - \frac{i\alpha}{2})]\}\tilde{T}_2 \qquad (6.16)$$
$$+ RPr\rho_o v_1 \frac{d\tilde{T}_2}{dy} + RPr[-i(\omega - \alpha u_o)T_1 + \frac{dT_o}{dy} v_1]\tilde{\rho}_2$$
$$- (\gamma_g - 1)M^2 Pr\{2\mu_o \frac{du_o}{dy}[\frac{du_2}{dy} + (\gamma + \frac{i\alpha}{2})v_2] + (\frac{du_o}{dy})^2 \mu_2\}$$
$$- \mu_o[(\gamma + \frac{i\alpha}{2})^2 - \beta^2]T_2 - \frac{d}{dy}(\frac{dT_o}{dy}\mu_2) - \frac{d\mu_o}{dy}\frac{dT_2}{dy} + N_{12}$$

where

$$N_{12} = -\mu_1 \frac{d^2\tilde{T}_2}{dy^2} - 2(\gamma_g - 1)M^2 Pr\{\mu_o(\gamma - \frac{i\alpha}{2})(i\alpha r u_1 + m\frac{dv_1}{dy})\tilde{u}_2$$
$$+ [\mu_o(\frac{du_1}{dy} + i\alpha v_1) + \mu_1 \frac{du_o}{dy}]\frac{d\tilde{u}_2}{dy} + (\gamma - \frac{i\alpha}{2})[\mu_o(\frac{du_1}{dy} + i\alpha v_1) + \frac{du_o}{dy}\mu_1]\tilde{v}_2$$
$$+ \mu_o[(2 + m)\frac{dv_1}{dy} + i\alpha m u_1]\frac{d\tilde{v}_2}{dy} + \frac{du_o}{dy}(\frac{du_1}{dy} + i\alpha v_1)\tilde{\mu}_2\}$$
$$- [\mu_1(\gamma^2 + \frac{\alpha^2}{4} - \beta^2) + i\alpha(\gamma + \frac{i\alpha}{2})\mu_1]\tilde{T}_2 - \frac{d}{dy}(\tilde{\mu}_2 \frac{dT_1}{dy})$$
$$- \frac{d\mu_1}{dy}\frac{d\tilde{T}_2}{dy} - 2m\beta\mu_o(\gamma_g - 1)M^2 Pr(i\alpha u_1 + \frac{dv_1}{dy})\tilde{w}_2$$

Equation of State :

$$\gamma_g M^2 p_2 = \rho_o T_2 + T_o \rho_2 + \rho_1 \tilde{T}_2 + T_1 \tilde{\rho}_2 \qquad (6.17)$$

Whereas by equating the coefficients of $E^{-1/2}$, we get the equations for the component $\tilde{q}_2$ as follows,

Continuity Equation :

$$\begin{aligned}
&\rho_o \frac{d\tilde{v}_2}{dy} + \bar{\rho}_1 \frac{dv_2}{dy} + \bar{v}_1 \frac{d\rho_2}{dy} \\
&= -\{\rho_o(\gamma - \frac{i\alpha}{2})\tilde{u}_2 + \frac{d\rho_o}{dy}\tilde{v}_2 + [(\sigma + \frac{i\omega}{2}) + u_o(\gamma - \frac{i\alpha}{2})]\tilde{\rho}_2 + \rho_o\beta\tilde{w}_2 \qquad (6.18)\\
&+ \bar{\rho}_1(\gamma - \frac{i\alpha}{2})u_2 + \frac{d\bar{\rho}_1}{dy}v_2 + [(\gamma - \frac{i\alpha}{2})\bar{u}_1 + \frac{d\bar{v}_1}{dy}]\rho_2 + \bar{\rho}_1\beta w_2\}
\end{aligned}$$

X-Momentum Equation :

$$\begin{aligned}
\mu_o \frac{d^2\tilde{u}_2}{dy^2} &= R\rho_o[(\sigma + \frac{i\omega}{2}) + u_o(\gamma - \frac{i\alpha}{2})]\tilde{u}_2 + R\{\rho_o(\gamma - \frac{i\alpha}{2})\bar{u}_1 \\
&+ \bar{\rho}_1[(\sigma - \frac{i\omega}{2}) + u_o(\gamma + \frac{i\alpha}{2})]\}u_2 + R\{\rho_o\bar{v}_1\frac{du_2}{dy} + \rho_o\frac{du_o}{dy}\tilde{v}_2 \\
&+ (\rho_o\frac{d\bar{u}_1}{dy} + \bar{\rho}_1\frac{du_o}{dy})v_2 + (\gamma - \frac{i\alpha}{2})\tilde{p}_2 + [i(\omega - \alpha u_o)\bar{u}_1 + \bar{v}_1\frac{du_o}{dy}]\rho_2\} \qquad (6.19)\\
&- \mu_o[(2+m)(\gamma - \frac{i\alpha}{2})^2 - \beta^2]\tilde{u}_2 - \frac{d\mu_o}{dy}\frac{d\tilde{u}_2}{dy} - (\gamma - \frac{i\alpha}{2})\frac{d\mu_o}{dy}\tilde{v}_2 \\
&- \mu_o(1+m)(\gamma - \frac{i\alpha}{2})\frac{d\tilde{v}_2}{dy} - \frac{d}{dy}(\tilde{\mu}_2\frac{du_o}{dy}) - (1+m)\mu_o\beta(\gamma - \frac{i\alpha}{2})\tilde{w}_2 - \tilde{K}_{12}
\end{aligned}$$

where

$$\begin{aligned}
\tilde{K}_{12} &= \bar{\mu}_1\{\frac{d^2u_2}{dy^2} + [(2+m)(\gamma^2 + \frac{\alpha^2}{4}) - \beta^2]u_2\} + \frac{d\bar{\mu}_1}{dy}\frac{du_2}{dy} + (\gamma + \frac{i\alpha}{2})\frac{d\bar{\mu}_1}{dy}v_2 \\
&+ \bar{\mu}_1[m(\gamma - \frac{i\alpha}{2}) + (\gamma + \frac{i\alpha}{2})]\frac{dv_2}{dy} + (\gamma - \frac{i\alpha}{2})[-i\alpha(2+m)\bar{u}_1 + m\frac{d\bar{v}_1}{dy}]\mu_2 \\
&+ \frac{d}{dy}[\mu_2(\frac{d\bar{u}_1}{dy} - i\alpha\bar{v}_1)] + \beta\bar{\mu}_1[m(\gamma - \frac{i\alpha}{2}) + (\gamma + \frac{i\alpha}{2})]w_2
\end{aligned}$$

Y-Momentum Equation :

$$\frac{d\tilde{p}_2}{dy} = i\alpha\rho_o\bar{v}_1u_2 - \rho_o[(\sigma + \frac{i\omega}{2}) + u_o(\gamma - \frac{i\alpha}{2})]\tilde{v}_2$$
$$- \{\rho_o\bar{u}_1(\gamma + \frac{i\alpha}{2}) + \rho_o\frac{d\bar{v}_1}{dy} + \bar{\rho}_1[(\sigma - \frac{i\omega}{2}) + u_o(\gamma + \frac{i\alpha}{2})]\}v_2$$
$$- \rho_o\bar{v}_1\frac{dv_2}{dy} - i(\omega - \alpha u_o)\bar{v}_1\rho_2 + \frac{1}{R}\{m(\gamma - \frac{i\alpha}{2})\frac{d\mu_o}{dy}\tilde{u}_2 \qquad (6.20)$$
$$+ \mu_o(1+m)(\gamma - \frac{i\alpha}{2})\frac{d\tilde{u}_2}{dy} + \mu_o[(\gamma - \frac{i\alpha}{2})^2 - \beta^2]\tilde{v}_2 + (2+m)\frac{d}{dy}(\mu_o\frac{d\tilde{v}_2}{dy})$$
$$+ (\gamma - \frac{i\alpha}{2})\frac{du_o}{dy}\tilde{\mu}_2 + m\beta\frac{d\mu_o}{dy}\tilde{w}_2 + \mu_o\beta(1+m)\frac{d\tilde{w}_2}{dy}\} + \tilde{L}_{12}$$

where

$$L_{12} = \frac{1}{R}\{m(\gamma + \frac{i\alpha}{2})\frac{d\bar{\mu}_1}{dy}u_2 + \bar{\mu}_1[(\gamma - \frac{i\alpha}{2}) + m(\gamma + \frac{i\alpha}{2})]\frac{du_2}{dy}$$
$$+ \bar{\mu}_1(\gamma^2 + \frac{\alpha^2}{4} - \beta^2)v_2 + (2+m)\frac{d}{dy}(\bar{\mu}_1\frac{dv_2}{dy}) + (\gamma - \frac{i\alpha}{2})(\frac{d\bar{u}_1}{dy} - i\alpha\bar{v}_1)\mu_2$$
$$+ \frac{d}{dy}\{[-i\alpha m\bar{u}_1 + (2+m)\frac{d\bar{v}_1}{dy}]\mu_2\} + m\beta\frac{d\bar{\mu}_1}{dy}w_2 + \bar{\mu}_1\beta(1+m)\frac{dw_2}{dy}\}$$

Z-Momentum Equation :

$$\mu_o\frac{d^2\tilde{w}_2}{dy^2} = -R\beta\tilde{p}_2 + R\rho_o[(\sigma + \frac{i\omega}{2}) + u_o(\gamma - \frac{i\alpha}{2})]\tilde{w}_2$$
$$+ R\{\rho_o(\gamma + \frac{i\alpha}{2})\bar{u}_1 + \bar{\rho}_1[(\sigma - \frac{i\omega}{2}) + u_o(\gamma + \frac{i\alpha}{2})]\}w_2 + R\rho_o\bar{v}_1\frac{dw_2}{dy} \qquad (6.21)$$
$$+ \mu_o\beta(1+m)(\gamma - \frac{i\alpha}{2})\tilde{u}_2 + \beta\frac{d\mu_o}{dy}\tilde{v}_2 + \mu_o\beta(1+m)\frac{d\tilde{v}_2}{dy}$$
$$- \mu_o[(\gamma - \frac{i\alpha}{2})^2 - (m+2)\beta^2]\tilde{w}_2 - \frac{d\mu_o}{dy}\frac{d\tilde{w}_2}{dy} + \tilde{M}_{12}$$

where

$$\tilde{M}_{12} = \beta\bar{\mu}_1[(\gamma - \frac{i\alpha}{2}) + m(\gamma + \frac{i\alpha}{2})]u_2 + \beta\frac{d\bar{\mu}_1}{dy}v_2 + \beta(1+m)\bar{\mu}_1\frac{dv_2}{dy}$$
$$-\bar{\mu}_1\frac{d^2w_2}{dy^2} + m\beta(-i\alpha\bar{u}_1 + \frac{d\bar{v}_1}{dy})\mu_2 - \mu_1[\gamma^2 + \frac{\alpha^2}{4} - (2+m)\beta^2]w_2 - \frac{d\bar{\mu}_1}{dy}\frac{dw_2}{dy}$$

Energy Equation :

$$\begin{aligned}
\mu_o\frac{d^2\tilde{T}_2}{dy^2} &= RPr\{ -i\alpha[\rho_o\bar{T}_1 - (\gamma_g - 1)M^2\bar{p}_1]u_2 + \rho_o\frac{dT_o}{dy}\tilde{v}_2 \\
&+ [(\rho_o\frac{d\bar{T}_1}{dy} + \bar{\rho}_1\frac{dT_o}{dy}) - (\gamma_g - 1)M^2\frac{d\bar{p}_1}{dy}]v_2\} \\
&- R(\gamma_g - 1)M^2Pr\{[(\sigma + \frac{i\omega}{2}) + u_o(\gamma - \frac{i\alpha}{2})]\tilde{p}_2 + (\gamma + \frac{i\alpha}{2})\bar{u}_1p_2 \\
&+ \bar{v}_1\frac{dp_2}{dy}\} + RPr\rho_o[(\sigma + \frac{i\omega}{2}) + u_o(\gamma - \frac{i\alpha}{2})]\tilde{T}_2 \\
&+ RPr\{\rho_o(\gamma + \frac{i\alpha}{2})\bar{u}_1 + \bar{\rho}_1[(\sigma - \frac{i\omega}{2}) + u_o(\gamma + \frac{i\alpha}{2})]\}T_2 \\
&+ RPr\rho_o\bar{v}_1\frac{dT_2}{dy} + RPr[i(\omega - \alpha u_o)\bar{T}_1 + \frac{dT_o}{dy}\bar{v}_1]\rho_2 \\
&- (\gamma_g - 1)M^2Pr\{2\mu_o\frac{du_o}{dy}[\frac{d\tilde{u}_2}{dy} + (\gamma - \frac{i\alpha}{2})\tilde{v}_2] + (\frac{du_o}{dy})^2\tilde{\mu}_2\} \\
&- \mu_o[(\gamma - \frac{i\alpha}{2})^2 - \beta^2]\tilde{T}_2 - \frac{d}{dy}(\frac{dT_o}{dy}\tilde{\mu}_2) - \frac{d\mu_o}{dy}\frac{d\tilde{T}_2}{dy} + \tilde{N}_{12}
\end{aligned} \tag{6.22}$$

where

$$\tilde{N}_{12} = -\bar{\mu}_1 \frac{d^2T_2}{dy^2} - 2(\gamma_g - 1)M^2 Pr\{\mu_o(\gamma + \frac{i\alpha}{2})(-i\alpha r\bar{u}_1 + m\frac{d\bar{v}_1}{dy})u_2$$

$$+ [\mu_o(\frac{d\bar{u}_1}{dy} - i\alpha\bar{v}_1) + \bar{\mu}_1\frac{du_o}{dy}]\frac{du_2}{dy} + (\gamma + \frac{i\alpha}{2})[\mu_o(\frac{d\bar{u}_1}{dy} - i\alpha\bar{v}_1) + \frac{du_o}{dy}\bar{\mu}_1]v_2$$

$$+ \mu_o[(2+m)\frac{d\bar{v}_1}{dy} - i\alpha m\bar{u}_1]\frac{dv_2}{dy} + \frac{du_o}{dy}(\frac{d\bar{u}_1}{dy} - i\alpha\bar{v}_1)\mu_2\}$$

$$- [\bar{\mu}_1(\gamma^2 + \frac{\alpha^2}{4} - \beta^2) - i\alpha(\gamma - \frac{i\alpha}{2})\bar{\mu}_1]T_2 - \frac{d}{dy}(\frac{d\bar{T}_1}{dy}\mu_2)$$

$$- \frac{d\bar{\mu}_1}{dy}\frac{dT_2}{dy} - 2m\beta\mu_o(\gamma_g - 1)M^2 Pr(-i\alpha\bar{u}_1 + \frac{d\bar{v}_1}{dy})w_2$$

Equation of State :

$$\gamma_g M^2\tilde{p}_2 = \rho_o\tilde{T}_2 + T_o\tilde{\rho}_2 + \bar{\rho}_1 T_2 + \bar{T}_1\rho_2 \tag{6.23}$$

We note that (6.18)-(6.23) are the complex conjugate of (6.12)-(6.17) only if σ and γ are real.

We demand that the disturbances (u_2, v_2, w_2, T_2) and $(\tilde{u}_2, \tilde{v}_2, \tilde{w}_2, \tilde{T}_2)$ decay as $y \to \pm\infty$. Hence the system is subject to the boundary conditions

$$u_2, v_2, w_2, T_2 \to 0 \quad \text{as} \quad y \to \pm\infty \tag{6.24}$$

$$\tilde{u}_2, \tilde{v}_2, \tilde{w}_2, \tilde{T}_2 \to 0 \quad \text{as} \quad y \to \pm\infty \tag{6.25}$$

and we have an eigenvalue problem for σ or γ. To solve this problem, we reduce the governing equations to a first-order system of ordinary-differential equations in the sixteen variables $(u_2, Du_2, v_2, p_2, T_2, DT_2, w_2, Dw_2)$ and $(\tilde{u}_2, D\tilde{u}_2, \tilde{v}_2, \tilde{p}_2, \tilde{T}_2, D\tilde{T}_2, \tilde{w}_2, D\tilde{w}_2)$ where $D = d/dy$. We note that, in the course of the analysis we neglect terms $O(q_1\tilde{q}_2/R$ or $\bar{q}_1 q_2/R)$, which is justified on the basis that q_1 and $\bar{q}_1$ are very small compared to the mean flow and the Reynolds number is very high. This

approximation also includes neglecting the terms K_{12}, L_{12}, M_{12} and N_{12} in equations (6.12)-(6.17), and $\tilde{K}_{12}$, $\tilde{L}_{12}$, $\tilde{M}_{12}$ and $\tilde{N}_{12}$ in equations (6.18)-(6.23).

Our approach of reducing the system (6.12)-(6.17) to a first-order system is based on approximating $\frac{d\tilde{v}_2}{dy}$, $\frac{d\tilde{p}_2}{dy}$, and $\tilde{\rho}_2$ by their respective expressions in the absence of the primary wave. These approximate expressions are used only when $\frac{d\tilde{v}_2}{dy}$, $\frac{d\tilde{p}_2}{dy}$ and $\tilde{\rho}_2$ are multiplied by a primary-wave quantity q_1 or divided by the Reynolds number R. Thus, the neglected terms continue to be $O(q_1^2)$ or q_1q_2/R and that is consistent with the order of the theory presented here. The approximate expressions of ρ_2, $\frac{dv_2}{dy}$, $\frac{d^2v_2}{dy^2}$, $\frac{dp_2}{dy}$ and $\frac{d\rho_2}{dy}$ are given by

$$\rho_2 \cong \frac{\gamma_g M^2}{T_o} p_2 - \frac{T_2}{T_o^2} \tag{6.26}$$

$$\frac{dv_2}{dy} \cong B_1u_2 + B_3v_2 + B_4p_2 + B_5T_2 + B_7w_2 \tag{6.27}$$

$$\begin{aligned}\frac{d^2v_2}{dy^2} \cong\ & G_1u_2 + G_2\frac{du_2}{dy} + G_3v_2 + G_4p_2 + G_5T_2 + G_6\frac{dT_2}{dy} \\ & + G_7w_2 + G_8\frac{dw_2}{dy} + B_4\frac{dp_2}{dy}\end{aligned} \tag{6.28}$$

$$\frac{dp_2}{dy} \cong -\rho_o[(\sigma - \frac{i\omega}{2}) + u_o(\gamma + \frac{i\alpha}{2})]v_2 \tag{6.29}$$

$$\begin{aligned}\frac{d\rho_2}{dy} \cong\ & -\frac{\gamma_g M^2}{T_o^2}[(\sigma - \frac{i\omega}{2}) + u_o(\gamma + \frac{i\alpha}{2})]v_2 - \frac{\gamma_g M^2}{T_o^2}\frac{dT_o}{dy}p_2 \\ & -\frac{1}{T_o^2}\frac{dT_2}{dy} + \frac{2}{T_o^3}\frac{dT_o}{dy}T_2\end{aligned} \tag{6.30}$$

where B_1, B_3, B_4, B_5, B_7, G_1, G_2, G_3, G_4, G_5, G_6, G_7 and G_8 are given in the Appendix F. Similar expressions can be written for $\tilde{q}_2$. Substituting (6.26)-(6.30) into (6.12)-(6.17) and adopting the convention

$$[Z_1, Z_2, Z_3, Z_4, Z_5, Z_6, Z_7, Z_8] = [u_2, \frac{du_2}{dy}, v_2, p_2, T_2, \frac{dT_2}{dy}, w_2, \frac{dw_2}{dy}] \quad (6.31)$$

and

$$[\tilde{Z}_1, \tilde{Z}_2, \tilde{Z}_3, \tilde{Z}_4, \tilde{Z}_5, \tilde{Z}_6, \tilde{Z}_7, \tilde{Z}_8] = [\tilde{u}_2, \frac{d\tilde{u}_2}{dy}, \tilde{v}_2, \tilde{p}_2, \tilde{T}_2, \frac{d\tilde{T}_2}{dy}, \tilde{w}_2, \frac{d\tilde{w}_2}{dy}] \quad (6.32)$$

we obtain eight first-order ordinary-differential equations in the form

$$DZ_n = \sum_{m=1}^{8} F_{nm} Z_m + \sum_{m=1}^{8} E_{nm} \tilde{Z}_m , \quad n = 1, .., 8 \quad (6.33)$$

where F_{nm} and E_{nm} are 8×8 variable-coefficient matrices whose nonzero elements are given in Appendix F. Note that the second term on the right-hand side of (6.33) is the contribution of the periodic primary wave which will produce the parametric effects on the system. Moreover, as the amplitude of the primary wave goes to zero, the second term on the right-hand side of (6.33) vanishes, and (6.33) is nothing but the usual three-dimensional linear instability equations presented in Chapter 3.

Similarly, we reduce (6.18)-(6.23) to the following eight first-order differential equations :

$$D\tilde{Z}_n = \sum_{m=1}^{8} \tilde{E}_{nm} Z_m + \sum_{m=1}^{8} \tilde{F}_{nm} \tilde{Z}_m , \quad n = 1, .., 8 \quad (6.34)$$

where $\tilde{F}_{nm}$ and $\tilde{E}_{nm}$ are obtained by taking the complex conjugate of F_{nm} and E_{nm} except for σ and γ.

The boundary conditions (6.24) and (6.25) become

$$Z_n \to 0 \qquad \text{as} \quad y \to \pm\infty, \quad n = 1, ..., 8 \tag{6.35}$$

$$\tilde{Z}_n \to 0 \qquad \text{as} \quad y \to \pm\infty, \quad n = 1, ..., 8 \tag{6.36}$$

Letting $Z_9 = \tilde{Z}_1, Z_{10} = \tilde{Z}_2, \ldots Z_{15} = \tilde{Z}_7$, and $Z_{16} = \tilde{Z}_8$, we combine the system of equations (6.33) and (6.34) into a system of sixteen first-order ordinary differential equations having the form

$$DZ_n = \sum_{m=1}^{16} K_{nm} Z_m \quad , \quad n = 1, ..., 16 \tag{6.37}$$

where [K] is a 16 x 16 matrix expressed by

$$[K] = \begin{bmatrix} F & E \\ \tilde{E} & \tilde{F} \end{bmatrix} \tag{6.38}$$

And the boundary conditions (6.35) and (6.36) become

$$Z_n \to 0 \qquad \text{as} \quad y \to \pm\infty, \quad n = 1, ..., 16 \tag{6.39}$$

In general we solve the system (6.37) and (6.39) for the complex variables Z_m ($m = 1, ..., 16$). However, if we are interested only in real value of σ or γ, we can solve only the eight equations (6.33) after taking $\tilde{Z}_m$ to be the complex conjugates of Z_m. In this case the system of equations must be solved in real form for the real and imaginary parts of Z_m.

6.3 *Matrix Form of Boundary Conditions At Infinity*

For computational purposes, we need to replace the asymptotic boundary conditions (6.39) by equivalent conditions at finite values of y. Because the mean-flow quantities q_o are uniform outside some region, $y_{min} \leq y \leq y_{max}$, and because the primary wave also decays exponentially as $y \rightarrow \pm \infty$, the matrix K takes a constant value K_o. Outside this region, we replace the system (6.37) by the constant-coefficient system

$$D \underset{\sim}{Z} = K_0 \underset{\sim}{Z} \tag{6.40}$$

and the elements of E_{nm} and $\tilde{E}_{nm}$ are zero so that the 16 × 16 constant matrix $\mathbf{K_0}$ is obtained from (6.38) as

$$[\,K_0\,] = \begin{bmatrix} \mathbf{C} & \mathbf{0} \\ \mathbf{0} & \tilde{\mathbf{C}} \end{bmatrix} \tag{6.41}$$

where **C**, given in the Appendix G, is an 8 × 8 matrix whose elements are obtained by eliminating the derivatives of the mean flow and primary wave from the matrix F. Also, $\tilde{\mathbf{C}}$ is an 8 × 8 matrix whose elements are obtained by taking the complex conjugate of the corresponding elements of **C** except for σ and γ. By following similar procedures as in section (3.3), we obtain the eigenvalues of **C** and $\tilde{\mathbf{C}}$, given in Appendix D.1. The adjoint problem of (6.40) is solved, and the matrices $\mathbf{Q}^*$ and $\tilde{\mathbf{Q}}^*$ are given in Appendix D.3; they correspond to **C** and $\tilde{\mathbf{C}}$, respectively. Then, the boundary conditions (6.39) at y = ∞ are replaced with the matrix form given by

$$[\,\mathbf{A}\,]\underset{\sim}{Z} = 0 \qquad \text{at } y = y_{max} \tag{6.42}$$

where

$$[\mathbf{A}]_{8\times16} = \begin{bmatrix} \mathbf{A}_1 & \mathbf{0} \\ \mathbf{0} & \tilde{\mathbf{A}}_1 \end{bmatrix} \tag{6.43}$$

and the matrices $\mathbf{A}_1$ and $\tilde{\mathbf{A}}_1$ are the last four rows of $\mathbf{Q}^{*T}$ and $\tilde{\mathbf{Q}}^{*T}$, respectively. Similarly, the boundary conditions (6.39) at $y = -\infty$ are replaced with the matrix form

$$[\mathbf{B}]\underset{\sim}{Z} = 0 \qquad \text{at } y = y_{min} \tag{6.44}$$

where

$$[\mathbf{B}]_{8\times16} = \begin{bmatrix} \mathbf{B}_1 & \mathbf{0} \\ \mathbf{0} & \tilde{\mathbf{B}}_1 \end{bmatrix} \tag{6.45}$$

and the matrices $\mathbf{B}_1$ and $\tilde{\mathbf{B}}_1$ are the first four rows of $\mathbf{Q}^{*T}$ and $\tilde{\mathbf{Q}}^{*T}$, respectively.

6.4 *Numerical Approach*

Three codes are developed to solve the system of equations (6.37) with the boundary conditions (6.42) and (6.44). The first two codes use SUPORT and DB2PFD, respectively, and the third code is developed by using the Euler-Maclurin formula including the second-order terms only. The reason we dropped the fourth-order term in the Euler-maclurin formula is that the second-order scheme is found to be accurate

enough, and thus we can avoid the complexity of taking the derivatives of (6.33) and (6.34).

A Cartesian grid in the y-direction is used. The grid points are the same as those used for calculating the primary wave. Because the form of equations (6.37) and boundary conditions (6.42) and (6.44) are the same as that of equations (4.1), (4.3), and (4.4), the numerical approaches for solving the subharmonic system are similar to those for solving the primary system discussed in Chapter 4. The only difference between them is that we need to solve sixteen equations in the case of subharmonic waves instead of eight equations in the case of primary waves. Hence, the details are not discussed here.

7.0 Subharmonic Instability Results

7.1 Introduction

The theory presented in Chapter 6 is used to investigate the instability characteristics of a spatially and temporal periodic mixing layer. The theory also helps in studying the effects of compressibility on the pairing of vortical structures and the development of three-dimensionality in mixing layers.

There are many parameters that influence the growth of the subharmonic instability of a periodic basic state. Some of the parameters are characteristics of the basic state. These parameters include the velocity ratio, temperature ratio, Mach number, and wavelength and amplitude of the periodic component of the flow. We may also add the Reynolds number and the type of mean-flow profile, which might be a hyperbolic-tangent velocity profile or a solution to the compressible boundary-layer equations. In addition to these parameters, there are other considerations such as the possibility of the existence of more than one mode of primary instability (periodicity), the spatial dimensionality of the subharmonic wave (two- and three-dimensional waves), and the type of stability analysis: spatial or temporal.

There are two mean flows used in this study. The first mean flow is obtained by solving the compressible boundary-layer equations discussed in Chapter two. In this Chapter, we refer to this mean flow as "SHEAR". The second type of mean flows is

the hyperbolic-tangent velocity profile, which has been used by many authors as a good approximation to the Lock profile. However, using the form $u_o = A + B \tanh y$, where A and B are constants, implies that the reference length is a function of the Mach number, temperature ratio, etc.. We prefer to use a reference length that is independent of the flow parameters. Thus we use

$$\delta^* = \sqrt{\mu_1^* x_o^* / \rho_1^* u_1^*} \tag{7.1}$$

as a reference length, and write the velocity profile in the form

$$u_o = \frac{1}{2} [1 + U_2 + (1 - U_2) \tanh ay] \tag{7.2}$$

where $a = 2 (du_o/dy)_{max}$, which is determined from the solution to the compressible boundary-layer equations. The parameter "a" is shown in Fig. 2.17 as a function of the Mach number at different values of T_2 (see Section 2.4). Only when using (7.2), we determine the temperature profile from the Crocco-Busemann integral. We refer to this mean flow as "TANH". The stability characteristics of any tanh profile of the form $u_o = A + B \tanh (cy)$ can be related to those of (7.2) by a simple transformation.

The periodic part of the basic state is specified by a two-dimensional neutral wave of the respective mean flow. The amplitude of that wave is specified by the maximum root-mean-square of the streamwise velocity disturbance, which is denoted by A_{rms}. After obtaining the eigenfunctions of the primary neutral wave we normalize the u_1-eigenfunction such that $|u_{1max}| = A_{rms}/\sqrt{2}$. This normalization fixes the amplitudes of the rest of the disturbance quantities such as v_1, T_1, etc.

Most of the subharmonic results in this Chapter are obtained for the TANH profile. We first compare its primary stability characteristics with those of the SHEAR profile that are presented in Chapter 5. We depict in Fig. 7.1 and Fig. 7.2 the temporal growth

rates for the TANH and SHEAR profiles, respectively. Because we used the same reference length, the two figures can be directly compared. We note that the growth rates of the two profiles are practically equal up to a Mach number M_1 of 1.6. The deviation in the growth rate for $M_1 > 1.6$ is attributed to the large asymmetry in the velocity of the SHEAR profiles as compared to the TANH profiles. The variation of the phase speed ω_r/α with ω_r is shown in Fig. 7.3 for the SHEAR profile, while it is constant and equal to 0.5 for the TANH profile. The spatial growth rates $-\alpha_i$ are shown in Fig. 7.4 and Fig. 7.5 for the TANH and SHEAR profiles, respectively. The results are qualitatively the same except that the range of amplified frequency is larger in the case of the SHEAR profile than in the case of the TANH profile. The corresponding variations of the phase speeds with ω are shown in Fig. 7.6 and Fig. 7.7.

The wavenumber α_r and frequency ω_r of the neutral wave of the TANH profile are shown in Fig. 7.8 as a function of Mach number M_1 at fixed $T_2 = 1$ and $U_2 = 0$. We note that α_r decreases with Mach number, and hence the wavelength $2\pi/\alpha_r$ of the periodic component of the basic state increases with Mach number. We also note that amplified waves have larger wavelengths than neutral waves. Fig. 7.9 and Fig. 7.10 show the variation of α_r and ω_r with the velocity ratio U_2 and temperature ratio T_2, respectively.

7.2 Comparison with Santos' Results for an Incompressible Mixing Layer

In Santos' work (1987), the mean flow is specified by the hyperbolic-tangent velocity profile $u_o = \tanh y$ and the primary wave, u_1, is given by the inviscid neutral solution to the Rayleigh equation, which is exactly given by $u_1 = c \tanh y \operatorname{sech} y$, where c is a constant. The maximum root-mean-square of $(u_1 E + \bar{u}_1 E^{-1})$, which we call A_{rms} is related to the maximum of u_1 by $A_{rms} = \sqrt{2}\, u_{1max}$. We specify a value for A_{rms}, then we find u_{1max} and hence the constant c.

The temporal growth rate σ_r is depicted in Fig. 7.11 as a function of the spanwise wavenumber β for three values of $A_{rms} =$ 0.00, 0.0356, and 0.0916 at a Reynolds number R = 200. The imaginary part $\sigma_i = 0$, and therefore the primary and subharmonic waves are synchronized. The present computations are in full agreement with those of Santos. It is evident that the pairing mode ($\beta = 0$) is the most amplified in the case of incompressible flow.

7.3 The Subharmonic Wave at $A_{rms} = 0.0$

If the frequency and wavenumber of the neutral primary wave are denoted by ω_r and α_r, respectively, then the subharmonic wave at $A_{rms} = 0.0$ must reproduce a "primary" wave at $\omega_r/2$ when spatial stability is used or at $\alpha_r/2$ when temporal stability is used. This property of the subharmonic equations is used as a necessary check

on the subharmonic code. Using the temporal stability, we set $\gamma = 0$ and determine σ as the eigenvalue at $A_{rms} = 0$. This value of σ must be related to the eigenvalue $\overline{\omega}$ of the primary code at $\alpha_r/2$ by

$$\sigma = -i\left(\overline{\omega} - \frac{\omega_r}{2}\right) \tag{7.3}$$

and hence

$$\sigma_r = \overline{\omega}_i$$

$$\sigma_i = -\overline{\omega}_r + \frac{\omega_r}{2}$$

Similarly, using the spatial stability, we set $\sigma = 0$ and determine γ as the eigenvalue at $A_{rms} = 0$. This value of γ must be related to the eigenvalue $\overline{\alpha}$ of the primary code at $\omega_r/2$ by

$$\gamma = i\left(\overline{\alpha} - \frac{\alpha_r}{2}\right) \tag{7.4}$$

and hence

$$\gamma_r = -\overline{\alpha}_i$$

$$\gamma_i = \overline{\alpha}_r - \frac{\alpha_r}{2}$$

7.4 Temporal Stability

First we investigate the temporal subharmonic stability problem ($\gamma = 0, \sigma \neq 0$) . All the results presented in this Section are for the TANH profile.

7.4.1 Subsonic Convective Mach Number Range

Two-Dimensional Waves $\beta = 0$.

The temporal growth rates σ_r of the synchronized subharmonic mode ($\sigma_i = 0$) are shown in Fig. 7.12 as functions of A_{rms} for various Mach numbers. In Fig. 7.12 we identify two modes of instability. The mode with the higher growth rate is called the pairing mode, and that with the lower growth rate is called the draining mode. In the pairing mode, the two adjacent vortices are displaced in opposite directions, and hence both vortices are merged together (Pierrehumbert and Widnall 1982). In the draining mode, as classified by Klassen and Peltier (1989), two adjacent vortices are deformed; one vortex becomes smaller, while the other vortex becomes larger. Both pairing and draining modes represent interactions that lead to the merging of vortices through distinctly different routes. Figure 7.13 displays the vorticity contours of the basic state which is the sum of the mean flow TANH and a primary wave with an $A_{rms} = 0.04$. The flow variables are $M_1 = 1.4, U_2 = 0.0, T_2 = 1.0$, and $R = 500$. The vorticity contours of the pairing mode and the draining mode are shown in Fig. 7.14 and Fig. 7.15, respectively. The amplitude of the subharmonic wave is arbitrarily

chosen at $B_{rms} = 0.2$. The clockwise rotation of the vortices in Fig. 7.14 indicates the beginning of the pairing phase.

The results in Fig. 7.12 show that as A_{rms} increases, the growth rate of the pairing mode increases, but the growth rate of the draining mode decreases abruptly and diminishes at a certain A_{rms}. The rate of increase of the growth rate of the pairing mode is slowed down as the Mach number is increased. Furthermore, at a given amplitude, compressibility slows down the pairing mode. Finally, we note that the range of amplitudes covered in Fig. 7.12 is somewhat larger than what may be consistent with linear analysis or superposition which are the basis of the present theory. Because of the smaller growth rate of the draining mode, in the following work we will study the pairing mode only.

The effect of the temperature ratio T_2 on the growth rate of the pairing mode is shown in Fig. 7.16 at $M_1 = 1.4$. We observe that cooling or heating reduces the growth rate of the subharmonic wave, and that the maximum growth rate is obtained when T_2 is slightly above 1.

Three-Dimensional Waves $\beta \neq 0$.

Next, we consider 3D subharmonic waves, which are called helical pairing modes. The variations of the growth rates with the amplitude A_{rms} are shown in Fig. 7.17 for various values of Reynolds numbers. The flow variables are $M_1 = 1.4, U_2 = 0.0, T_2 = 1.0$ and $\beta = 0.12$. Figure 7.17 illustrates that as R is increased, the growth rate σ_r at a fixed A_{rms} approaches a limiting value. For Reynolds numbers greater than 500 the viscous effects are negligible. Therefore, most of the subharmonic instability results in this work are obtained at a Reynolds number R = 500.

We have seen that the presence of a periodic component with a moderate amplitude has little effect on the growth rate of the two-dimensional subharmonic mode at high Mach numbers. This is not the case with the three-dimensional mode. In Fig. 7.18, the growth rates are shown as functions of β at $M_1 = 1.4$ and various values of A_{rms}. The results show that the presence of the periodic part dramatically enhances the growth rate of the subharmonic over a wide range of β. The short-wave cut-off first increases to $\beta = 1$ at $A_{rms} = 0.005$, and thereafter decreases again as A_{rms} is further increased. This phenomenon was found in the case of incompressible flow by Pierrehumbert and Widnall (1982). Furthermore, unlike the incompressible case discussed in Section 7.2, the three-dimensional mode is more amplified than the pairing mode. We note that in Fig. 7.18 the most amplified subharmonic wave has a spanwise wavenumber β close to 0.12. This value of β makes the wavelength in the spanwise direction twice that of the primary 2D wave whose wavenumber is $\alpha \cong 0.2446$.

Variation of the temporal growth rate of the three-dimensional *primary* waves is shown in Fig. 7.19 against β. The results are obtained from the 3D primary wave code at $M_1 = 1.4$ and $M_1 = 2.5$, and the other flow variables are $T_2 = 1.0$, $U_2 = 0.0$, and $R = 500$. The curve in Fig. 7.19 obtained at $M_1 = 1.4$ is identical to the curve in Fig. 7.18 when $A_{rms} = 0.0$ obtained from the subharmonic code. This result verifies (7.3) and provides the necessary check on the subharmonic code.

The growth rates of the 3D subharmonic mode are plotted in Fig. 7.20 against A_{rms} for $M = 1.4$ and various values of β. The curve with $\beta = 0.12$ is most amplified over a wide range of amplitudes $0 < A_{rms} < 0.1$. The shorter waves corresponding to $\beta = 0.24$ are also more amplified than the two-dimensional mode over a smaller range of A_{rms}. The amplified domains of these three-dimensional modes with respect

to A_{rms} are decreased as β is increased. Figure 7.20 also demonstrates the short-wave cut-off features of 3D subharmonic waves.

To demonstrate that the trend shown in Fig. 7.20 holds for other subsonic convective Mach numbers, we depict in Fig. 7.21 the variation of the growth rate with A_{rms} for several values of β. The flow variables are $M_1 = 4.0$, $U_2 = 0.6$, and $T_2 = 1.0$ which give a convective Mach number of 0.8. The wavenumber α_r and frequency ω_r of the primary wave are 0.0986 and 0.0789, respectively. We note in Fig. 7.21 that the β corresponding to the maximum growth rate shifts to a smaller value in comparison with the case of Fig. 7.20 which corresponds to a convective Mach number of 0.7.

To obtain an overall picture of the Mach number effects, we plot in Fig. 7.22 the variation of the growth rate with β for several Mach numbers and for a fixed amplitude $A_{rms} = 0.04$. There is a short-wave cut-off wavenumber, which is approximately equal to 0.45, for all Mach numbers. Furthermore, the most amplified subharmonic wave is two dimensional for $M_1 < 0.8$, but it appears at $\beta \cong 0.12$ at higher Mach numbers. The decreasing σ_r with Mach number is better observed in Fig. 7.23 in which we depict the growth rate against Mach number for $A_{rms} = 0.04$ and $\beta = 0.00, 0.12, 0.24,$ and 0.36. Because the convective Mach number M^+ is $M_1/2$, the maximum M^+ is 0.975; i.e., subsonic. The fact that the growth rates remain positive at $M^+ = 0.975$ indicates that the subharmonic is still active, and pairing ($\beta = 0$) and helical pairing ($\beta \neq 0$) continue to grow but at a much lower rate when compared with the incompressible case. The supersonic convective Mach number range will be discussed in Section 7.4.2.

The variation of the growth rate of the subharmonic wave with the velocity ratio U_2 is presented in Fig. 7.24 for several values of A_{rms} . The other flow variables are $M_1 = 1.4$, $T_2 = 1.0$, R. = 500 and $\beta = 0.12$. The results show that the growth rate σ_r monotonically decreases with increasing velocity ratio U_2.

The variation of the growth rate of 2D subharmonic waves with the temperature ratio T_2 is depicted in Fig. 7.16. The corresponding variation for 3D waves is shown in Fig. 7.25 at $\beta = 0.12$. The other flow variables are $M_1 = 1.4, U_2 = 0.0$, and $R = 500$. In Fig. 7.16, we find that the pairing mode $\beta = 0.0$ is most amplified for a temperature ratio close to one, and that heating or cooling has a stabilizing effect. However, the three-dimensional mode shown in Fig. 7.25 is more amplified when the slow stream is cooler than the faster stream.

To investigate the effect of the wavelength of the periodic part of the flow (primary wave) on the growth rate of the subharmonic wave, we consider basic states composed of the TANH mean flow and a growing primary wave. These growing waves have wavelengths larger than the neutral wave. The temporal growth rates of the subharmonic waves (tuned mode $\sigma_1 = 0$) are shown in Fig. 7.26 against A_{rms} for different primary wavenumbers α_r. In these calculation we ignored the growth of the primary wave. We note in Fig. 7.26 that the subharmonic wave attains a maximum growth rate when the primary wave is given by the neutral wave at $\alpha_r = 0.244$.

7.4.2 Supersonic Convective Mach number Range

The supersonic range of convective Mach number is more involved than the subsonic range because of the existence of more than one neutral mode. For example, at a convective Mach number of 1.25, there are two neutral modes. The u-component eigenfunctions of the fast and slow modes are shown in Fig. 7.27 and Fig. 7.28, respectively. The vorticity contours of the two basic states are shown in Fig. 7.29 and Fig. 7.30 at $A_{rms} = 0.04$. The fast mode is supersonic relative to the

stagnant flow on bottom and subsonic relative to the moving stream on top. More activity is evident in the top stream where the relative flow is subsonic. If we rotate one of the vorticity-contours figures 180 degrees, we obtain the other figure.

The growth rates of the *primary* wave of the two modes and their phase speeds are shown in Fig. 7.31 and Fig. 7.32, respectively. We note that the slow mode has smaller phase velocity than the fast mode. However, the growth rates of the two modes are equal when $T_2 = 1$. The slow mode is more amplified than the fast mode when $T_2 < 1$. Whereas, the fast mode is more amplified than the slow mode when $T_2 > 1$.

For $T_2 = 1$, we find that the growth rate of subharmonic waves is independent of which of the two modes is used as the neutral primary wave. Two subharmonic modes are found; the first is synchronized ($\sigma_i = 0.0$), and the second is detuned ($\sigma_i \neq 0.0$). The variation of the growth rate of the synchronized mode with A_{rms} is shown in Fig. 7.33. We note that for a fixed value of A_{rms}, the growth rate increases as the spanwise wavenumber increases up to $\beta = 0.12$, and then it falls again for further increase in β. Moreover, as $A_{rms} \rightarrow 0$, the synchronized mode is damped at all spanwise wavenumbers. We also note that the synchronized 2D mode is damped if $A_{rms} < 0.047$. The variation of the growth rate of the synchronized mode with β for various values of A_{rms} is shown in Fig. 7.34. The maximum growth rate shifts to smaller β as A_{rms} is increased. When A_{rms} is small enough, the amplified synchronized subharmonic mode only appears as a short wave in the spanwise direction.

The growth rate and frequency detuning σ_i of the detuned mode are shown in Fig. 7.35 and Fig. 7.36, respectively. We note that the maximum growth rate is marginally increased by the presence of the periodic component of the basic state. However, the range of amplified spanwise wavenumber increases dramatically by the interaction between the primary and subharmonic waves, and hence the interaction

enhances the development of 3D waves of short wavelengthes. Comparing Fig. 7.35 for the detuned mode and Fig. 7.34 for the synchronized mode, we find that the detuned mode is the most amplified of the two. In the meantime, the growth rate at $A_{rms} = 0.0$ in Fig. 7.35 is exactly the same as that shown in Fig. 7.19 which is obtained from the 3D primary code. Thus, (7.3) is also verified for the case of supersonic convective Mach numbers.

We note that detuned modes must exist in pairs with eigenvalues $(\sigma_r \pm i\sigma_i)$. This condition has been verified numerically in the present work; that is, if we find an eigenvalue σ, then its complex conjugate must be also an eigenvalue.

Next, we investigate the effect of the temperature ratio. The variations of the temporal growth rate σ_r of the synchronized subharmonic mode against spanwise wavenumber β for three different temperature ratios $T_2 = 0.5$, 1.0, and 2.0 are plotted in Fig. 7.37. The solid and dashed lines represent the growth rates σ_r obtained by using the fast and slow primary waves, respectively. The results in Fig. 7.37 show that for a cooler lower stream, the maximum growth rate of the subharmonic wave interacting with the slow primary wave is larger than that when interacting with the fast primary wave. However, for a hotter lower stream, the trend is reversed. This dependence on T_2 of the subharmonic wave is similar to that of the primary wave discussed in Fig. 7.31.

Next, we consider the detuned mode. The growth rate σ_r and the frequency detuning σ_i are shown in Fig. 7.38 and Fig. 7.39, respectively, for the fast primary mode, and in Fig. 7.40 and Fig. 7.41 for the slow primary mode. In Fig. 7.38 and Fig. 7.40, we note that cooling is more destabilizing in the case of the slow mode than the fast mode while heating produces the opposite trend. The curves in Fig. 7.38 marked $T_2 = 1$ are identical to the corresponding curves in Fig. 7.40. For a temperature ratio of 0.5, the frequency detuning σ_i shown in Fig. 7.39 is roughly 0.01. This value should

be compared to the frequencies of the fast and slow modes which are 0.03 and 0.06, respectively.

7.5 *Spatial Stability*

Here, we investigate the subharmonic spatial stability problem ($\sigma = 0, \gamma \neq 0$). Once more all the results presented in this Section are for TANH profile.

7.5.1 Subsonic Convective Mach Number Range

Two-Dimensional Waves $\beta = 0$.

The spatial growth rate γ_r of the 2D subharmonic wave ($\beta = 0$) is shown in Fig. 7.42. As in the temporal stability case, we identify two modes of instability, the pairing mode with the larger growth rate, and the draining mode with the smaller growth rate. We note that for very small amplitudes ($A_{rms} \rightarrow 0$), the subharmonic wave is detuned. This is because the phase speed in the spatial theory is a function of frequency as shown in Fig. 7.6. As shown in Fig. 7.42, the detuned mode branches into synchronized pairing and draining modes after a small amplitude that depends on the Mach number. For larger amplitudes, the modes remain synchronized at all Mach numbers.

We also observe in Fig. 7.42 that the pairing mode for $M_1 \leq 0.8$ shows an unexpected cusp in the growth rate for $A_{rms} > 0.09$. To the right of the cusp, the mode

is detuned ($\gamma_i \neq 0$). We investigate the region around the cusp in more details. In Fig. 7.43 we depict the growth rate against amplitude for $M_1 = 0.4$. We find multiple synchronized modes with very large growth rates within a narrow range of amplitudes, $0.083 \leq A_{rms} \leq 0.107$. As we shall see shortly, the eigenfunctions oscillates very rapidly in the direction normal to the mixing layer as γ_r becomes large. We could not find a turning point of that branch of tuned modes. Furthermore, we find that at the points where the slope of the $\gamma_r - A_{rms}$ curve is vertical, there is a branch of detuned mode springing off that point (only one branch is shown).

In Fig. 7.43 we see that there are four synchronized modes at $A_{rms} = 0.09$. The growth rates of these modes are $\gamma_r = 0.192$, 0.331, 0.701, and 2.579; the corresponding eigenfunctions of the u-component are shown in Figs. 7.44-7.47. We note that the modes having large growth rates oscillate and decay very rapidly in the y-direction. We have not investigated these modes any further because we felt that the amplitudes involved ($A_{rms} > 0.08$) require considerations of nonlinear interactions, which is beyond the scope of this dissertation.

Three-Dimensional Waves $\beta \neq 0$.

We investigated the effects of the Reynolds number on the spatial subharmonic stability. The growth rate is shown in Fig. 7.48 for the Reynolds numbers R = 200, 500, 2000, and 5000. we observe in Fig. 7.48 that viscous effects are stabilizing, and that for $R > 500$ these effect may be neglected.

The variation of the growth rate with the spanwise wavenumber β is shown in Fig. 7.49 at $M_1 = 1.4$ and for several amplitudes. The imaginary part of γ is zero for nonzero A_{rms} , and hence synchronized modes are obtained. The curves shown in Fig. 7.49 are similar to those in Fig. 7.18 of the temporal stability analysis. Therefore,

no further investigation of the spatial theory will be discussed. However, we note that the modified Gaster's transformation $\gamma_r \cong \sigma_r/C_{ph}$ proposed by Bertolloti (1985) is approximately valid for synchronized subharmonic waves. The growth rate γ_r predicted by the spatial theory and σ_r/C_{ph} are plotted in Fig. 7.50 at $A_{rms} = 0.01$ and 0.04. We noted that the modified transformation reproduces the computed spatial growth rate with acceptable accuracy only when the growth rate is small.

7.5.2 Supersonic Convective Mach number Range

The results of the spatial stability in the supersonic convective Mach numbers are qualitatively the same as those of the temporal stability. For example, the variations of the growth rate with the spanwise wavenumber of synchronized modes are shown in Fig. 7.51 and 7.52, for the fast and slow primary waves, respectively. These figures should be compared with Fig. 7.34 of the temporal stability analysis which is the same for both fast and slow modes at $T_2 = 1$. Here again, the modified Gaster transformation σ_r/C_{ph} and γ_r are plotted in Fig. 7.57 and Fig. 7.58 for the fast and slow primary wave, respectively. The modified Gaster's transformation shows an excellent agreement to the computed γ_r except for some points that have larger values of σ_r. The growth rates of the detuned spatial stability modes are shown in Fig. 7.53 and Fig. 7.55. They show similar trend to those of the temporal stability detuned mode shown by Fig. 7.35. The corresponding wavenumber detuning γ_i are shown in Fig. 7.54 and Fig. 7.56.

7.6 SHEAR Profiles Case

In this Section, we investigate the subharmonic stability characteristics of the mean flow which is obtained by solving the compressible boundary-layer equations. We refer to this mean flow as the "SHEAR" profile. Because the results for this profile are found to be qualitatively similar to those of the TANH profile profile, we present here a sample of the results.

The growth rates σ_r and γ_r of synchronized subharmonic waves are shown in Fig. 7.59 against the Mach number M_1. The spanwise wavenumber β is 0.12, and the velocity and temperature ratios are 0.0 and 1.0, respectively. The amplitude of the primary wave A_{rms} is 0.04. Also shown in Fig. 7.59 is the spatial growth rate according to the modified Gaster's transformation σ_r/C_{ph}. The growth rate decreases with increasing the Mach number, and the transformed spatial growth rate is in fair agreement with the computed one.

The temporal and spatial growth rates of 3D subharmonic waves at $\beta = 0.12$ are shown in Fig(7.60) versus A_{rms}. Two modes of instability waves are found; one mode is a detuned mode, while the other is a synchronized mode. The detuned mode ($\gamma_i \neq 0$, $\sigma_i \neq 0$) remains amplified in the limit $A_{rms} \rightarrow 0$, whereas the synchronized mode becomes damped. The growth rate of the detuned mode at $A_{rms} = 0$ is exactly equal to the growth rate of the 3D primary subharmonic wave. For this case of subsonic convective Mach number ($M^+ = 0.7$) we note that for large primary amplitude the synchronized mode is more amplified than the detuned mode. Finally, the frequency detuning σ_i and wavenumber detuning γ_i are shown in Fig. 7.61. They monotonically increase with A_{rms} These values should be compared with the frequency and

wavenumber of the neutral primary wave, which are $\omega_r \cong 0.150$ and $\alpha_r \cong 0.250$, respectively.

8.0 Summary and Conclusions

Two main subjects related to the development of instability waves in compressible mixing layers are investigated in this work. The first subject is the development of a primary instability wave, and the second subject is the interaction of a primary wave with its subharmonic.

8.1 Primary Instabilities

By using the linear stability theory, the effects of the velocity ratio, temperature ratio, and Mach number on the growth rate are computed. The basic state is obtained by solving the compressible boundary-layer equations or specified by the hyperbolic-tangent velocity profile. Both viscous and inviscid disturbances are considered. The effect of the variation of the mean flow in the streamwise direction is investigated by using the method of multiple scales. We conclude

- The maximum growth rate of a compressible shear layer depends on the velocity ratio $\lambda = (U_1 - U_2)/(U_1 + U_2)$ in a somewhat complex manner; whereas the maximum growth rate of an incompressible layer varies linearly with λ. Moreover, for a given Mach number, temperature ratio, and frequency, the

growth rate shows a maximum value at a particular velocity ratio. The maximum growth rate (maximized over all frequencies and propagation angles) is insensitive to the velocity ratio if the convective Mach number is greater than 0.6.

- If the disturbances are subsonic in both upper and lower streams (the upper stream is the faster stream), then cooling the lower stream produces a higher maximum growth rate. Once the Mach number is high enough to produce more than one amplified mode, the effect of cooling/heating on the growth rate depends on the mode under consideration. For the slow mode, which has a supersonic disturbance in the upper stream and subsonic disturbance in the lower stream, cooling the lower stream produces a higher maximum growth rate. However, for the fast mode, which has a supersonic disturbance in the lower stream and subsonic disturbance in the upper stream, cooling the lower stream stabilizes the flow. It can also be concluded that the mode with a subsonic disturbance in the cooler stream has the higher maximum growth rate.

- The present results substantiate the convective Mach number introduced by Bogdanoff, and Papamoschou and Roshko, as a parameter that correlates the compressibility effects on the spreading rate of mixing layers. The ratio of the spreading rate of a compressible mixing layer to that of an incompressible layer at the same velocity ratio and density ratio depends primarily on the convective Mach number.

- If the convective Mach number is greater than 0.6, oblique waves are more amplified than two-dimensional waves.

- Viscosity has a stabilizing effect at Mach numbers as high as 6.

- Nonparallel correction to the growth rate is negligible at low Mach numbers. At high Mach numbers, nonparallel effect is more evident.

8.2 *Subharmonic Instabilities*

The second part of this work is concerned with the Floquet analysis of a periodic mixing layer in order to study the interaction between a primary wave and its subharmonic wave in a compressible mixing layer. Several conclusions are obtained :

- Increasing the amplitude of the periodicity (primary wave) enhances the growth rate of two-dimensional subharmonic waves, especially at low convective Mach numbers where the pairing mode is the most amplified. As the Mach number increases, increasing the amplitude of the periodicity becomes less effective in enhancing the two-dimensional subharmonic mode.

- At a relatively small amplitude of the periodicity (about $A_{rms} = 0.02$) and convective Mach numbers above 0.4, the three-dimensional subharmonic wave is dramatically amplified over a wide range of spanwise wavenumber, which shows the broad band character of the subharmonic.

- Viscosity effect on the growth rate of the subharmonic waves is similar to that on the primary waves; that is, viscosity has a stabilizing effect.

- The results of the spatial subharmonic analysis have similar trend as those of the temporal analysis. Moreover, the modified Gaster's transformation is approximately applicable for small growth rates.

- The fourth-order compact finite-difference method presented in detail in this work is found to be accurate and versatile for both primary and subharmonic stability analyses.

References

Bertolloti, F. P., 1985 *"Temporal and Spatial Growth of Subharmonic Disturbances in Falkner-Skan Flows,"* MS. Thesis Va. Polytech. Inst. State Univ., Blacksburg.

Billing, F. S., 1984 *"Ramjets with Supersonic Combustion,"* AGARD Lecture Series No. 136, pp. 8-1 to 8-29.

Billing, F. S., Waltrup, P. J., and Stockbridge, R. D., 1980 *"The Integral Rocket Dual Combustion Ramjet: A New Propulsion Concept,"* J. of Spacecraft and Rockets, Vol. 17, No. 5, pp. 416-424.

Blottner, F. G., 1975 *"Computational Techniques for Boundary Layers,"* AGARD Lecture Series NO. 73, pp. 1-51.

Blumen, W., Drain, P. G., and Billings, D. F., 1975 *"Shear Layer Instability of an Inviscid Compressible Fluid,"* J. Fluid Mech., Vol. 71, Part 2, pp. 305-316.

Bogdanoff, D. W., 1983 *"Compressibility effects in turbulent shear layers, "* AIAA J., Vol. 21, NO. 6, pp. 926-927.

Breidenthal, R., 1981 *"Structure in Turbulent Mixing Layers and Wakes Using Chemical Reaction,"* J. Fluid Mech., Vol. 109, pp. 1-24.

Browand, F. k., 1966 *"An Experimental Investigation of the Instability of an Incompressible Separated Shear Layer,"* J. Fluid Mech. vol. 26, pp. 281-307.

Brown, G. L. and Roshko, A., 1974 *"On Density Effects and Large Structure in Turbulent Mixing Layer,"* J. Fluid Mech., Vol. 83, Pt. 4, pp. 641-671.

Cebeci, T. and Smith, A. M. O., 1974 *"Analysis of Turbulent Boundary Layer,"* Academic Press New York San Francisco London.

Chinzei, N., Masuya, G., Komuro, T., Murakami, A., and Kudou, D., 1986 *"Spreading of Two-Stream Supersonic Turbulent Mixing Layers,"* Phys. of Fluids, Vol. 29, No. 5, pp. 1345-1347.

Cringhton, D. G. and Gaster, M., 1976 *"Stability of Slowing Diverging Jet Flow,"* J. Fluid Mech., Vol. 77, pp. 397-413.

El-Hady N. M. and Nayfeh, A. H., 1980 *"Nonparallel Stability of Compressible Boundary-Layer Flows,"* AIAA Paper No. 80-0277.

El-Hady N. M., 1988 *"Secondary Instability of Compressible Boundary Layer to Subharmonic Three-Dimensional Disturbances,"* NASA Contractor Report No. 4144.

El-Hady N. M., 1989 *"Secondary Instability of Compressible Boundary Layer to Subharmonic Three-Dimensional Disturbances,"* AIAA Paper No. 89-0035.

Ferri, A., 1964 *"Supersonic Combustion Process,"* Aeronautics and astronautics, Vol. 2, No. 8, pp. 32-37.

Freymuth, P. 1966 *"On Transition in a Separated Laminar Boundary Layer,"* J. Fluid Mech. Vol. 25, PP. 683-704.

Greenough, J., Riley, J. Soetrisno, M. and Eberhardt, D., 1989 *"The Effects of Walls on a Compressible Mixing Layer,"* AIAA Paper No. 89-0372.

Gropengiesser, H., 1970 *"Study on the Stability of Boundary Layers and Compressible Fluids,"* NASA Technical Translations, F-12, 786.

Herbert, Th., 1981 *"A Secondary Instability Mechanism in Plane Poiseuille Flow,"* Bull. am. Phys. Soc. 26:1257.

Herbert, Th., 1983a *"Secondary Instability of Plane Channel Flow to Subharmonic Three-Dimensional Disturbances,"* Phys. Fluids vol. 26, pp. 871-874.

Herbert, Th., 1983b *"Subharmonic Three-Dimensional Disturbances in Unstable Shear Flow,"* AIAA Paper No. 83-1759.

Herbert, Th., 1984 *"Analysis of the Subharmonic Route to Transitional in Boundary Layers,"* AIAA Paper No. 84-0009.

Herbert, Th., 1985 *"Three-Dimensional Phenomena in the TRansitional Flat-Plate Boundary Layer,"* AIAA Paper No. 85-0489.

Herbert, Th., 1986 *"Vortical Mechanism in Shear Flow Transition,"* In Direct and Large Eddy Simulation of Turbulence, ed. U. Schumann, R. Friedrich, pp. 19-36. Braunschweig: Vieweg-Verlag

Herbert, Th., Bertolotti, F. P., Santos, G. R. 1986 *"Floquet Analysis of Seconary Instability in Shear Flows,"* In Stability of Time-Dependent and Spatially Varying Flows, ed. Dwoyer, M. Y. Hussaini, pp. 43-57. New York: Springer-Verlag

Herbert, Th., 1988 *"Seconary Instability of Boundary Layers,"* Ann. Rev. Fluid Mech. vol. 20, pp. 487-526.

Ho, C. M., and Huang, L. S., 1982 *"Subharmonics and Vortex Merging in a Mixing Layers,"* J. Fluid Mech., Vol. 119, pp. 443-473.

Ho, C. M., and Huerre, P., 1984 *"Perturbed Free Shear Layers,"* Ann. Rev. Fluid Mech., Vol. 16, pp. 365-424.

Huerre, P. and Monkewitz, P. A., 1985 *"Absolute and Convective Instabilities in Free Shear Layers,"* J. Fluid. Mech., Vol. 159, pp. 151-168.

Ikawa, H., and Kubota, T., 1975 *"Investigation of Supersonic Turbulent Mixing Layer with Zero Presure Gradient,"* AIAA J., Vol. 13, No. 5, pp. 566-572.

Jackson, T. L., and Grosch, C. E., 1988 *"Spatial Stability of a Compressible Mixing Layer,"* NASA Contractor Report 181671, ICASE Report No. 88-33.

Jackson, T. L., and Grosch, C. E., 1989 *"Inviscid Spatial Stability of a Compressible Mixing Layer. Part 3. Effect of Thermodynamics,"* NASA Contractor Report 181855, ICASE Report No. 89-32.

Jimenez, J., 1983 *"A Spanwise Structure in the Planar Shear Layer,"* J. Fluid Mech., Vol. 132, pp. 319-336.

Keller, Herbert B., 1978 *"Numerical Methods in Boundary-Layer Theory,"* Ann. Rev. Fluid Mech., Vol. 10 pp. 417-433.

Kelly, R. E., 1967 *"On the Stability of an Inviscid Shear Layer which is Periodic in Space and Time,"* J. Fluid Mech., Vol. 27 pp. 657-689.

Klaassen, G. P., and Peltier, W. R., 1989 *"The Role of Transverse Secondary Instabilities in the Evolution of Free Shear Layers,"* J. Fluid Mech., Vol. 202, pp. 367-402.

Klemp, J., B., and Acrivos, A., 1972 *"A Note on the Laminar Mixing of Two Uniform Parallel Semi-Infinite Streams,"* J. Fluid Mech., Vol. 55, pp. 25-30.

Lees, L. and Lin, C. C., 1946 *"Investigation of the Stability of a Laminar Boundary layer in a Compressible Fluid,"* TN 1115, NACA.

Lele, Sanjiva K., 1989 *"Direct Numerical Simulation of Compressible Free Shear Flows,"* AIAA Paper No. 89-0374.

Lessen, M., Fox, J. A., and Zien, H. M., 1965 *"On the Inviscid Stability of the Laminar Mixing of Two Parallel Streams of a Compressible Fluid,"* J. Fluid Mech., Vol. 23, Part 2, pp. 355-367.

Lessen, M., Fox, J. A., and Zien, H. M., 1966 *"Stability of the Laminar Mixing of Two Parallel Streams with Respect to Supersonic Disturbances,"* J. Fluid Mech., Vol. 25, Part 4, pp. 737-742.

Mack, L. M., 1969 *"Boundary Layer Stability Theory,"* Notes Prepared for the AIAA professional Study Series High-Speed Boundary-Layer Stability and Transition, San Francisco, California.

Mack, L. M., 1984 *"Boundary Layer Linear Stability Theory,"* Special Course on Stability and Transition of Laminar Flow, edited by R. Michel, AGARD Report No. 709, pp. 3-1 to 3-81, 1984.

Mack, L. M., 1989 *"On the Inviscid Acoustic Mode Instability of Suppersonic Shear Flow,"* Fourth Symposium on Numerical and Physical Aspects of Aerodynamic Flows.

Malik, Mujeeb R., 1988 *"Numerical Methods for Boundary Layer Stability,"* HTC Report NO. 88-6.

Michalke, A., 1984 *"Survey on Jet Instability Theory,"* Prog. Aerospace Sci., Vol. 21, pp. 159-199.

Monkewitz, P., and Huerre, P., 1982 *"Influence of the Velocity Ratio on the Spatial Instability of Mixing Layer,"* Phys. Fluids 25(7), pp. 1137-1143.

Monkewitz, P., 1988 *"Subharmonic Resonance, Pairing and Shredding in the Mixing Layer,"* J. Fluid Mech., Vol. 188, pp. 223-252.

Nayfeh, A. H., 1980 *"Stability of Three Dimensional Boundary Layers,"* AIAA J., Vol. 18, No. 4, pp. 406-416.

Nayfeh, A. H., and Reed, H. L., 1982 *"Stability of Compressible Three-dimensional Boundary Layers,"* AIAA Paper No. 82-1009.

Nayfeh, A. H., 1981 *"Introduction to Perturbation Techniques,"* Wiley and Sons, New York.

Nayfeh, A. H., 1988 *"Stability of Compressible Boundary Layers,"* Proc. of the Transonic symp., NASA Langley Research Center, Hampton, Virginia.

Oretel, H., 1980 *"Mach Wave Radiation of Hot Supersonic Jets Investigated by Means of the Shock Tube and New Optical Techniques,"* Proceedings of the 12th International Symposium of Shock Tubes and Waves (The Magnes Press, The Hebrew University, Jerusalem), pp. 266.

Oretel, H., 1982 *"Coherent Structures Producing Mach Waves Inside and Outside of the Supersonic Jet,"* Structure of Complex Turbulent Shear Flow, IUTAM Symposium, Marseill.

Papamoschou, D., and Roshko, A., 1986 *"Observations of Supersonic Free Shear Layers,"* AIAA Paper 86-0162.

Papamoschou, D., 1986 *"Experimental Investigation of Heterogeneous Compressible Shear Layers,"* Ph.D. Thesis, Calif. Inst. of Tech.

Pereyra, V., 1978 *"An Adaptive Finite-Difference FORTRAN Program for First Order Nonlinear Boundary Value Problem,"* in Lecture Notes in Computer Science, 76, Springer-Verlag, Berlin, 67-88, PASVA3.

Pierrehumbert, R.T., and Widnall, S.E., 1982 *"The Two- and Three- Dimensional Instabilities of a Spatially Periodic Shear Layer,"* J. Fluid Mech., Vol. 114, pp. 59-82.

Ragab, S. A. and Wu, J. L., 1989 *"Linear Instability Waves in Supersonic Turbulent Shear Layer,"* AIAA J., Vol. 27, No. 6, pp. 677-686.

Ragab, S. A. and Wu, J. L., 1988 *"Instabilities in the Free Shear Layer Formed by Two Supersonic Streams,"* AIAA Paper No. 88-0038.

Reed, H. L., 1981 *"The Tollmien-Schilichting Instability of Laminar Viscous Flows,"* Ph.D. Dissertation, Virginia Polytechnic Institute and State University, Blacksburg, VA 24061.

Samimy, M., and Elliott, G. S., 1989 *"Effects of Compressibility on the Mean Flow and Turbulence Characteristics of Free Shear Layers,"* To appear in AIAA J..

Sandham N. D., and Reynolds W. C., 1989 *"The Compressible Mixing Layer: Linear Theory and Direct Simulation,"* AIAA Paper No. 89-0371.

Santos, G. R., and Herbert, Th., 1986 *"Combination Resonance in Boundary Layers,"* Bull. Am. Phys. Soc., Vol. 31, p. 1718.

Santos, G. R., 1987 *"Studies on Secondary Instabilities,"* Ph.D. Dissertation, Virginia Polytechnic Institute and State University, Blacksburg, VA 24061.

Saric, W. S., and Nayfeh, A. H., 1982 *"Influence of the Velocity Ratio on the Spatial Instability of Mixing Layers,"* Phys. of Fluids, Vol. 25, No. 7, pp. 1137-1143.

Sato, H., 1959 *"Further Investigation on the Transition of Two-Dimensional Separated Layers at Subsonic Speed,"* J. Phys. Soc. Jpn. Vol. 14, pp. 1797-1810.

Schilichting, 1979 *"Boundary Layer Theory,"* 7th ed. McGraw-Hill, New York.

Scott, M. R., and Watts, H. A., 1977 *"Computational Solutions of Two-Point Boundary Value Problems via Orthonormalization,"* SIAM Journal of Numerical Analysis, Vol. 14, 40.

Stuart, J. T., 1967 *"On Finite Amplitude Oscillations in Laminar Mixing Layers,"* J. Fluid Mech. Vol. 29, pp. 417-440.

Tam, C. K. and Hu, F. Q., 1988 *"Instabilities of Supersonic Mixing Layers Inside a Rectangular Channel,"* AIAA Paper No. 88-3675-cp.

Tang, W., Komerath N., and Sankar L., 1989 *"Numerical Simulation of the Growth of Instabilities in Supersonic Free Shear Layers,"* AIAA Paper No. 88-0376.

Ting, L., 1959 *"On the Mixing of Two Parallel Streams,"* J. Math. and Physics, 38, 153-165.

Waltrup, P. J., 1986 *"Liquid Fueled Supersonic Combustion Ramjets: A Research Perspective of the Past, Present and Future,"* No. AIAA-86-0158.

Winant, C. D. and Browand, F. K., 1974 *"Vortex Pairing: The Mechanism of Turbulent Mixing Layer Growth at Moderate Reynolds Number,"* J. Fluid Mech., Vol. 41, No. 6, pp. 388-396.

Wornum, Stephen F., 1977a *"A Critical Study of Higher-Order Numerical Methods for Solving the Boundary-Layer Equations,"* AIAA 77-637.

Wornum, Stephen F., 1977b *"A Fourth-Order Box Method for Solving the Boundary-Layer Equations,"* NASA TM X-7400.

Wray, A. A., 1987 *"Very Low Storage Time-Advancement Schemes,"* Sumitted to J. Comput. Phys.

Zhuang, Mei, Kubota, T., and Dimotakis, P. E., 1988 *"On the Instability of Inviscid Compressible Free Shear Layers,"* Conference Proc. 1st National Fluid Dyn. Cong., Cincinnati, Oh, pp. 768-773.

Appendix A.

Continuity Equation :

$$\frac{\partial \rho}{\partial t} + \frac{\partial \rho u}{\partial x} + \frac{\partial \rho v}{\partial y} + \frac{\partial \rho w}{\partial z} = 0$$

X-Momentum Equation :

$$\rho \frac{Du}{Dt} = -\frac{\partial p}{\partial x} + \frac{1}{R}\{\frac{\partial}{\partial x}[\mu(r\frac{\partial u}{\partial x} + m\frac{\partial v}{\partial y} + m\frac{\partial w}{\partial z})] + \frac{\partial}{\partial y}[\mu(\frac{\partial u}{\partial y} + \frac{\partial v}{\partial x})] + \frac{\partial}{\partial z}[\mu(\frac{\partial w}{\partial x} + \frac{\partial u}{\partial z})]\}$$

Y-Momentum Equation :

$$\rho \frac{Dv}{Dt} = -\frac{\partial p}{\partial y} + \frac{1}{R}\{\frac{\partial}{\partial y}[\mu(r\frac{\partial v}{\partial y} + m\frac{\partial u}{\partial x} + m\frac{\partial w}{\partial z})] + \frac{\partial}{\partial z}[\mu(\frac{\partial v}{\partial z} + \frac{\partial w}{\partial y})] + \frac{\partial}{\partial x}[\mu(\frac{\partial u}{\partial y} + \frac{\partial v}{\partial x})]\}$$

Z-Momentum Equation :

$$\rho \frac{Dw}{Dt} = -\frac{\partial p}{\partial z} + \frac{1}{R}\{\frac{\partial}{\partial z}[\mu(r\frac{\partial w}{\partial z} + m\frac{\partial u}{\partial x} + m\frac{\partial v}{\partial y})] + \frac{\partial}{\partial x}[\mu(\frac{\partial u}{\partial z} + \frac{\partial w}{\partial x})] + \frac{\partial}{\partial y}[\mu(\frac{\partial v}{\partial z} + \frac{\partial w}{\partial y})]\}$$

Energy Equation :

$$\rho \frac{DT}{Dt} = (\gamma_g - 1)M_\infty^2 \left(\frac{Dp}{Dt} + \frac{\phi}{R} \right) + \frac{1}{PrR} \nabla \bullet (\mu \nabla T)$$

Equation of State :

$$p = \rho R_g T$$

where

$$\phi = \mu \{ 2 [(\frac{\partial u}{\partial x})^2 + (\frac{\partial v}{\partial y})^2 + (\frac{\partial w}{\partial z})^2] + (\frac{\partial u}{\partial y} + \frac{\partial v}{\partial x})^2 + (\frac{\partial u}{\partial z} + \frac{\partial w}{\partial x})^2 + (\frac{\partial v}{\partial z} + \frac{\partial w}{\partial y})^2 \} + \lambda (\frac{\partial u}{\partial x} + \frac{\partial v}{\partial y} + \frac{\partial w}{\partial z})^2$$

$$m = \frac{\lambda}{\mu} \quad , \quad r = 2 + m$$

Appendix B.

$$F_{12} = F_{56} = F_{78} = 1$$

$$F_{21} = \alpha^2 + \beta^2 - i\hat{\omega}R/\mu_o T_o$$

$$F_{22} = -D\mu_o/\mu_o$$

$$F_{23} = -i\alpha(1+m)DT_o/T_o - i\alpha D\mu_o/\mu_o + RDU_o/\mu_o T_o$$

$$F_{24} = i\alpha R/\mu_o + (1+m)\gamma_g M^2 \alpha\hat{\omega}$$

$$F_{25} = -\alpha(1+m)\hat{\omega}/T_o - D(\mu_T DU_o)/\mu_o$$

$$F_{26} = -\mu_T DU_o/\mu_o$$

$$F_{31} = -i\alpha$$

$$F_{33} = DT_o/T_o$$

$$F_{34} = i\gamma_g M^2\hat{\omega}$$

$$F_{35} = -i\hat{\omega}/T_o$$

$$F_{37} = -i\beta$$

$$F_{41} = -i\chi\alpha(rDT_o/T_o + 2D\mu_o/\mu_o)$$

$$F_{42} = -i\chi\alpha$$

$$F_{43} = \chi(-\alpha^2 - \beta^2 + i\hat{\omega}R/\mu_o T_o + rD^2T_o/T_o + rD\mu_o DT_o/\mu_o T_o)$$

$$F_{44} = -i\chi r\gamma_g M^2(\alpha DU_o - \hat{\omega}DT_o/T_o - \hat{\omega}D\mu_o/\mu_o)$$

$$F_{45} = i\chi[r\alpha DU_o/T_o + \mu_T\alpha DU_o/\mu_o - r\hat{\omega}D\mu_o/\mu_o T_o]$$

$$F_{46} = -i\chi r\hat{\omega}/T_o$$

$$F_{47} = -i\chi\beta(rDT_o/T_o + 2D\mu_o/\mu_o)$$

$$F_{48} = -i\chi\beta$$

$$F_{62} = -2(\gamma_g - 1)M^2PrDU_o$$

$$F_{63} = -2i(\gamma_g - 1)M^2Pr\alpha DU_o + RPrDT_o/\mu_o T_o$$

$$F_{64} = i(\gamma_g - 1)M^2PrR\hat{\omega}/\mu_o$$

$$F_{65} = \alpha^2 + \beta^2 - iRPr\hat{\omega}/\mu_o T_o - (\gamma_g - 1)M^2Pr\mu_T(DU_o)^2/\mu_o - D^2\mu_o/\mu_o$$

$$F_{66} = -2D\mu_o/\mu_o$$

$$F_{83} = -i(1 + m)\beta DT_o/T_o - i\beta D\mu_o/\mu_o$$

$$F_{84} = (1 + m)\gamma_g M^2\beta\hat{\omega} + i\beta R/\mu_o$$

$$F_{85} = -(1 + m)\beta\hat{\omega}/T_o$$

$$F_{87} = \alpha^2 + \beta^2 - i\hat{\omega}R/\mu_o T_o$$

$$F_{88} = -D\mu_o/\mu_o$$

where

$$m = \frac{\lambda}{\mu}\,,\quad r = 2 + m\,,$$

$$\mu_T = d\mu_o/dT_o\,,\quad DF = \partial F/\partial y\,,$$

$$\hat{\omega} = \omega - \alpha U_o\,,\quad \chi = (R/\mu_o - ir\gamma_g M^2\hat{\omega})^{-1}$$

Appendix C.

$$C_{12} = C_{56} = C_{78} = 1$$

$$C_{21} = \alpha^2 + \beta^2 - i\hat{\omega}R/\mu_o T_o$$

$$C_{24} = i\alpha R/\mu_o + (1+m)\gamma_g M^2 \alpha\hat{\omega}$$

$$C_{25} = -\alpha(1+m)\hat{\omega}/T_o$$

$$C_{31} = -i\alpha$$

$$C_{34} = i\gamma_g M^2\hat{\omega}$$

$$C_{35} = -i\hat{\omega}/T_o$$

$$C_{37} = -i\beta$$

$$C_{42} = -i\chi\alpha$$

$$C_{43} = \chi(-\alpha^2 - \beta^2 + i\hat{\omega}R/\mu_o T_o)$$

$$C_{46} = -i\chi r\hat{\omega}/T_o$$

$$C_{48} = -i\chi\beta$$

$$C_{64} = i(\gamma_g - 1)M^2 PrR\hat{\omega}/\mu_o$$

$$C_{65} = \alpha^2 + \beta^2 - iRPr\hat{\omega}/\mu_o T_o$$

$$C_{84} = (1+m)\gamma_g M^2 \beta\hat{\omega} + i\beta R/\mu_o$$

$$C_{85} = -(1+m)\beta\hat{\omega}/T_o$$

$$C_{87} = \alpha^2 + \beta^2 - i\hat{\omega}R/\mu_o T_o$$

where

$$m = \frac{\lambda}{\mu}, \quad r = 2+m,$$

$$\hat{\omega} = \omega - \alpha U_o, \quad \chi = (R/\mu_o - ir\gamma_g M^2\hat{\omega})^{-1}$$

Appendix D.

D.1 Eigenvalues λ displayed

$$\lambda_{1,5} = \pm\sqrt{C_{21}}$$

$$\lambda_{2,6} = \pm\sqrt{C_{21}}$$

$$\lambda_{3,7} = \pm\{\frac{1}{2}(B_{22}+C_{65}) + [\frac{(B_{22}-C_{65})^2}{4} + B_{23}C_{64}]^{1/2}\}^{1/2}$$

$$\lambda_{4,8} = \pm\{\frac{1}{2}(B_{22}+C_{65}) - [\frac{(B_{22}-C_{65})^2}{4} + B_{23}C_{64}]^{1/2}\}^{1/2}$$

where

$$B_{22} = C_{42}C_{24} + C_{43}C_{34} + C_{46}C_{64} + C_{48}C_{84}$$
$$B_{23} = C_{42}C_{25} + C_{43}C_{35} + C_{46}C_{65} + C_{48}C_{85}$$

D.2 Eigenvector matrix

[Q] of the original system

$$[Q] = \begin{bmatrix} 1 & 0 & 1 & 1 & 1 & 0 & 1 & 1 \\ \lambda_1 & 0 & \lambda_3 & \lambda_4 & \lambda_5 & 0 & \lambda_7 & \lambda_8 \\ \frac{C_{31}}{\lambda_1} & \frac{C_{37}}{\lambda_1} & K_3 & K_3 & \frac{C_{31}}{\lambda_5} & \frac{C_{37}}{\lambda_6} & K_3 & K_3 \\ 0 & 0 & K_4 & K_4 & 0 & 0 & K_4 & K_4 \\ 0 & 0 & K_5 & K_5 & 0 & 0 & K_5 & K_5 \\ 0 & 0 & K_6 & K_6 & 0 & 0 & K_6 & K_6 \\ 0 & 1 & K_7 & K_7 & 0 & 1 & K_7 & K_7 \\ 0 & \lambda_1 & \lambda_3 K_7 & \lambda_4 K_7 & 0 & \lambda_6 & \lambda_7 K_7 & \lambda_8 K_7 \end{bmatrix}$$

where

$$K_3 = \frac{(C_{31} + C_{34}K_4 + C_5K_{35} + C_{37}K_7)}{\lambda} \ ,$$

$$K_4 = \frac{(\lambda^2 - C_{21})(\lambda^2 - C_{65})}{C_{24}(\lambda^2 - C_{65}) + C_{25}C_{64}} \ ,$$

$$K_5 = \frac{C_{64}}{\lambda^2 - C_{65}} K_4 \ ,$$

$$K_6 = \lambda K_5$$

$$K_7 = \frac{C_{84}(\lambda^2 - C_{65}) + C_{85}}{(\lambda^2 - C_{87})(\lambda^2 - C_{65})} K_4 \quad , \text{ for } \lambda = 3, 4, 7, 8$$

D.3 Eigenvector matrix

$[Q^*]$ of the adjoint system

$$[Q^*]_{1,4} = \begin{bmatrix} 1 & 0 & 0 & 0 \\ \dfrac{-1-C_{42}g_1}{\lambda_1} & \dfrac{-C_{42}L_1}{\lambda_1} & \dfrac{C_{42}C_{64}}{\lambda_3} & \dfrac{C_{42}C_{64}}{\lambda_4} \\ \dfrac{-C_{43}g_1}{\lambda_1} & \dfrac{-C_{43}L_1}{\lambda_1} & \dfrac{C_{43}C_{64}}{\lambda_3} & \dfrac{C_{43}C_{64}}{\lambda_4} \\ g_1 & L_1 & -C_{64} & -C_{64} \\ g_2 & L_2 & B_{22}-\lambda_3^2 & B_{22}-\lambda_4^2 \\ \dfrac{-g_2-C_{46}g_1}{\lambda_1} & \dfrac{-L_2-C_{46}L_1}{\lambda_1} & \dfrac{-B_{22}+\lambda_3^2+C_{46}C_{64}}{\lambda_3} & \dfrac{-B_{22}+\lambda_4^2+C_{46}C_{64}}{\lambda_4} \\ 0 & 1 & 0 & 0 \\ \dfrac{-C_{48}g_1}{\lambda_1} & \dfrac{-1-C_{48}L_1}{\lambda_1} & \dfrac{C_{48}C_{64}}{\lambda_3} & \dfrac{C_{48}C_{64}}{\lambda_4} \end{bmatrix}$$

$$[\dot{Q}]_{5,6} = \begin{bmatrix} 1 & 0 & 0 & 0 \\ \dfrac{1+C_{42}g_1}{\lambda_1} & \dfrac{C_{42}L_1}{\lambda_1} & -\dfrac{C_{42}C_{64}}{\lambda_3} & -\dfrac{C_{42}C_{64}}{\lambda_4} \\ \dfrac{C_{43}g_1}{\lambda_1} & \dfrac{C_{43}L_1}{\lambda_1} & -\dfrac{C_{43}C_{64}}{\lambda_3} & -\dfrac{C_{43}C_{64}}{\lambda_4} \\ g_1 & L_1 & -C_{64} & -C_{64} \\ g_2 & L_2 & B_{22}-\lambda_3^2 & B_{22}-\lambda_4^2 \\ \dfrac{g_2+C_{46}g_1}{\lambda_1} & \dfrac{L_2+C_{46}L_1}{\lambda_1} & \dfrac{B_{22}-\lambda_3^2-C_{46}C_{64}}{\lambda_3} & \dfrac{B_{22}-\lambda_4^2-C_{46}C_{64}}{\lambda_4} \\ 0 & 1 & 0 & 0 \\ \dfrac{C_{48}g_1}{\lambda_1} & \dfrac{1+C_{48}L_1}{\lambda_1} & \dfrac{-C_{48}C_{64}}{\lambda_3} & \dfrac{-C_{48}C_{64}}{\lambda_4} \end{bmatrix}$$

where

$$g_1 = [C_{24}(\lambda_1^2 - C_{65}) + C_{25}C_{64}]/C_o \ ,$$

$$g_2 = [C_{24}B_{23} - C_{25}(B_{22} - \lambda_1^2)]/C_o \ ,$$

$$L_1 = [C_{84}(\lambda_1^2 - C_{65}) + C_{85}C_{64}]/C_o \ ,$$

$$L_2 = [C_{84}B_{23} - C_{85}(B_{22} - \lambda_1^2)]/C_o \ ,$$

$$C_o = (B_{22} - \lambda_1^2)(C_{65} - \lambda_1^2) - C_{64}B_{23}$$

Appendix E.

$$E_n = -i\sum_{m=1}^{6}\frac{\partial F_{nm}}{\partial \alpha}\zeta_m\ , \qquad n = 1, \ldots, 6$$

$$G_1 = 0$$

$$G_2 = \frac{R}{\mu_o T_o}\left[U_o\frac{\partial \zeta_1}{\partial x_1} + \zeta_1\frac{\partial U_o}{\partial x_1} + V_o\frac{\partial \zeta_1}{\partial y} + T_o\frac{\partial \zeta_4}{\partial x_1}\right.$$
$$\left. + (\gamma_g M^2\zeta_4 - \frac{\zeta_5}{T_o})\left(U_o\frac{\partial U_o}{\partial x_1} + V_o\frac{\partial U_o}{\partial y}\right)\right] + O(1)$$

$$G_3 = \frac{\zeta_1}{T_o}\frac{\partial T_o}{\partial x_1} - \frac{\partial \zeta_1}{\partial x_1} - (\gamma_g M^2\zeta_4 - \frac{\zeta_5}{T_o})(\frac{\partial U_o}{\partial x_1} + \frac{\partial V_o}{\partial y})$$
$$- \frac{U_o}{T_o}(\frac{2\zeta_5}{T_o}\frac{\partial T_o}{\partial x_1} - \frac{\partial \zeta_5}{\partial x_1}) - U_o\gamma_g M^2(\frac{\partial \zeta_4}{\partial x_1} - \frac{\zeta_4}{T_o}\frac{\partial T_o}{\partial x_1})$$
$$- \frac{V_o}{T_o}(\frac{2\zeta_5}{T_o}\frac{\partial T_o}{\partial y} - \frac{\partial \zeta_5}{\partial y}) - V_o\gamma_g M^2(\frac{\partial \zeta_4}{\partial y} - \frac{\zeta_4}{T_o}\frac{\partial T_o}{\partial y}) + O(\varepsilon)$$

$$G_4 = \frac{-1}{T_o}(U_o\frac{\partial \zeta_3}{\partial x_1} + V_o\frac{\partial \zeta_3}{\partial y} + \zeta_3\frac{\partial V_o}{\partial y}) + O(\varepsilon)$$

$$G_5 = 0$$

$$G_6 = \frac{RPr}{\mu_o T_o}[\zeta_1\frac{\partial T_o}{\partial x_1} + U_o\frac{\partial \zeta_5}{\partial x_1} + V_o\frac{\partial \zeta_5}{\partial y} + (\gamma_g M^2\zeta_4 - \frac{\zeta_5}{T_o})(U_o\frac{\partial T_o}{\partial x_1} + V_o\frac{\partial T_o}{\partial y})$$
$$- T_o(\gamma_g - 1)M^2(U_o\frac{\partial \zeta_4}{\partial x_1} + V_o\frac{\partial \zeta_4}{\partial y})] + O(1)$$

Appendix F.

$$F_{12} = F_{56} = F_{78} = 1$$

$$F_{21} = \frac{\rho_o R}{\mu_o}[(\sigma - \frac{i\omega}{2}) + u_o(\gamma + \frac{i\alpha}{2})] - [(\gamma + \frac{i\alpha}{2})^2 - \beta^2]$$

$$F_{22} = -\frac{1}{\mu_o}\frac{d\mu_o}{dy}$$

$$F_{23} = \frac{\rho_o R}{\mu_o}\frac{du_o}{dy} - (\gamma + \frac{i\alpha}{2})\frac{d\mu_o}{dy}/\mu_o - (1 + m)(\gamma + \frac{i\alpha}{2})B_3$$

$$F_{24} = \frac{R}{\mu_o}(\gamma + \frac{i\alpha}{2}) - (1 + m)(\gamma + \frac{i\alpha}{2})B_4$$

$$F_{25} = -\frac{\mu_{TT}}{\mu_o}\frac{dT_o}{dy}\frac{du_o}{dy} - \frac{\mu_T}{\mu_o}\frac{d^2u_o}{dy^2} - (1 + m)(\gamma + \frac{i\alpha}{2})B_5$$

$$F_{26} = -\frac{\mu_T}{\mu_o}\frac{du_o}{dy}$$

$$E_{21} = \frac{R}{\mu_o}\{\rho_o(\gamma + \frac{i\alpha}{2})u_1 + [(\sigma + \frac{i\omega}{2}) + u_o(\gamma - \frac{i\alpha}{2})]\rho_1\}$$

$$E_{22} = \frac{\rho_o R}{\mu_o}v_1$$

$$E_{23} = \frac{R}{\mu_o}(\rho_o\frac{du_1}{dy} + \rho_1\frac{du_o}{dy})$$

$$E_{24} = -\frac{R}{\mu_o}\frac{\gamma_g M^2}{T_o}\left[i(\omega - \alpha u_o)u_1 - \frac{du_o}{dy}v_1\right]$$

$$E_{25} = \frac{R}{\mu_o}\frac{1}{T_o^2}\left[i(\omega - \alpha u_o)u_1 - \frac{du_o}{dy}v_1\right]$$

$$F_{31} = -\left(\gamma + \frac{i\alpha}{2}\right)$$

$$F_{33} = \frac{1}{T_o}\frac{dT_o}{dy}$$

$$F_{34} = -\gamma_g M^2\left[\left(\sigma - \frac{i\omega}{2}\right) + u_o\left(\gamma + \frac{i\alpha}{2}\right)\right]$$

$$F_{35} = \left[\left(\sigma - \frac{i\omega}{2}\right) + u_o\left(\gamma + \frac{i\alpha}{2}\right)\right]/T_o$$

$$F_{37} = -\beta$$

$$E_{31} = -\rho_1\left[\left(\gamma + \frac{i\alpha}{2}\right) + \tilde{B}_1\right]/\rho_o$$

$$E_{33} = -\left(\frac{d\rho_1}{dy} + \rho_1\bar{B}_3\right)/\rho_o + \frac{\gamma_g M^2}{T_o}\left[\left(\sigma + \frac{i\omega}{2}\right) + u_o\left(\gamma - \frac{i\alpha}{2}\right)\right]v_1$$

$$E_{34} = -\frac{\rho_1}{\rho_o}\tilde{B}_4 + \frac{\gamma_g M^2}{T_o}\frac{dT_o}{dy}v_1 + \frac{\gamma_g M^2}{T_o}\left[\left(\sigma - \frac{i\omega}{2}\right) + u_o\left(\gamma + \frac{i\alpha}{2}\right)\right]T_1$$
$$- \gamma_g M^2\left[\left(\gamma + \frac{i\alpha}{2}\right)u_1 + \frac{dv_1}{dy}\right]$$

$$E_{35} = -\frac{\rho_1}{\rho_o}\tilde{B}_5 - \frac{2\frac{dT_o}{dy}}{T_o^2}v_1 + (\rho_1 - \frac{T_1}{T_o^2})[(\sigma - \frac{i\omega}{2}) + u_o(\gamma + \frac{i\alpha}{2})]$$
$$+ [(\gamma + \frac{i\alpha}{2})u_1 + \frac{dv_1}{dy}]/T_o$$

$$E_{36} = \frac{v_1}{T_o}$$

$$F_{41} = \frac{\Upsilon}{R}[m(\gamma + \frac{i\alpha}{2})\frac{d\mu_o}{dy} + (2+m)(\frac{d\mu_o}{dy}B_1 + \mu_o G_1)]$$

$$F_{42} = \frac{\Upsilon}{R}[(1+m)(\gamma + \frac{i\alpha}{2})\mu_o + (2+m)\mu_o G_2]$$

$$F_{43} = \Upsilon\{-\rho_o[(\sigma - \frac{i\omega}{2}) + u_o(\gamma + \frac{i\alpha}{2})] + \frac{\mu_o}{R}[(\gamma + \frac{i\alpha}{2})^2 - \beta^2]$$
$$+ \frac{(2+m)}{R}(\frac{d\mu_o}{dy}B_3 + \mu_o G_3)\}$$

$$F_{44} = \Upsilon\frac{(2+m)}{R}(\frac{d\mu_o}{dy}B_4 + \mu_o G_4)$$

$$F_{45} = \frac{\Upsilon}{R}[(\gamma + \frac{i\alpha}{2})\frac{du_o}{dy}\mu_T + (2+m)(\frac{d\mu_o}{dy}B_5 + \mu_o G_5)]$$

$$F_{46} = \Upsilon\frac{(2+m)\mu_o}{R}G_6$$

$$F_{47} = \frac{\Upsilon}{R}[m\beta\frac{d\mu_o}{dy} + (2+m)(\frac{d\mu_o}{dy}B_7 + \mu_o G_7)]$$

$$F_{48} = \frac{\Upsilon}{R}[(1+m)\beta\mu_o + (2+m)\mu_o G_8]$$

$$E_{41} = -\Upsilon\rho_o(i\alpha + \tilde{B}_1)v_1$$

$$E_{43} = -\Upsilon\{\rho_o(\gamma - \frac{i\alpha}{2})u_1 + \rho_o\frac{dv_1}{dy} + [(\sigma + \frac{i\omega}{2}) + u_o(\gamma - \frac{i\alpha}{2})]\rho_1 + \rho_o\bar{B}_3v_1\}$$

$$E_{44} = \Upsilon[i(\omega - \alpha u_o)\frac{\gamma_g M^2}{T_o} - \rho_o\tilde{B}_4]v_1$$

$$E_{45} = -\Upsilon[i\frac{(\omega - \alpha u_o)}{T_o^2} + \rho_o\tilde{B}_5]v_1$$

$$E_{47} = -\Upsilon\rho_o\bar{B}_7v_1$$

$$F_{62} = -2(\gamma_g - 1)M^2Pr\frac{du_o}{dy}$$

$$F_{63} = \frac{\rho_oRPr}{\mu_o}\frac{dT_o}{dy} - 2(\gamma_g - 1)M^2Pr(\gamma + \frac{i\alpha}{2})\frac{du_o}{dy}$$

$$F_{64} = -\frac{R}{\mu_o}(\gamma_g - 1)M^2Pr[(\sigma - \frac{i\omega}{2}) + u_o(\gamma + \frac{i\alpha}{2})]$$

$$F_{65} = \frac{\rho_oR}{\mu_o}Pr[(\sigma - \frac{i\omega}{2}) + u_o(\gamma + \frac{i\alpha}{2})] - (\gamma_g - 1)M^2Pr\frac{\mu_T}{\mu_o}(\frac{du_o}{dy})^2$$
$$- [(\gamma + \frac{i\alpha}{2})^2 - \beta^2] - (\mu_T\frac{d^2T_o}{dy^2} + \mu_{TT}(\frac{dT_o}{dy})^2)/\mu_o$$

$$F_{66} = -(\mu_T\frac{dT_o}{dy} + \frac{d\mu_o}{dy})/\mu_o$$

$$E_{61} = \frac{RPr}{\mu_o}i\alpha[\rho_oT_1 - (\gamma_g - 1)M^2p_1]$$

$$E_{63} = \frac{RPr}{\mu_o}\{[\rho_o\frac{dT_1}{dy} + \rho_1\frac{dT_o}{dy} - (\gamma_g - 1)M^2\frac{dp_1}{dy}]$$
$$+ \rho_o(\gamma_g - 1)M^2[(\sigma + \frac{i\omega}{2}) + u_o(\gamma - \frac{i\alpha}{2})]v_1\}$$

$$E_{64} = -\frac{R}{\mu_o}(\gamma_g - 1)M^2Pr(\gamma - \frac{i\alpha}{2})u_1 + \frac{RPr}{\mu_o}\frac{\gamma_g M^2}{T_o}[-i(\omega - \alpha u_o)T_1 + \frac{dT_o}{dy}v_1]$$

$$E_{65} = \frac{RPr}{\mu_o}\{\rho_o(\gamma - \frac{i\alpha}{2})u_1 + \rho_1[(\sigma + \frac{i\omega}{2}) + u_o(\gamma - \frac{i\alpha}{2})]$$
$$-\frac{1}{T_o^2}[-i(\omega - \alpha u_o)T_1 + \frac{dT_o}{dy}v_1]\}$$

$$E_{66} = \frac{\rho_o RPr}{\mu_o}v_1$$

$$F_{83} = \beta\frac{d\mu_o}{dy}/\mu_o + \beta(1 + m)B_3$$

$$F_{84} = -\frac{\beta R}{\mu_o} + \beta(1 + m)B_4$$

$$F_{85} = \beta(1 + m)B_5$$

$$F_{87} = \frac{\rho_o R}{\mu_o}[(\sigma - \frac{i\omega}{2}) + u_o(\gamma + \frac{i\alpha}{2})] - [(\gamma + \frac{i\alpha}{2})^2 - \beta^2]$$

$$F_{88} = \frac{-1}{\mu_o}\frac{d\mu_o}{dy}$$

$$E_{87} = \frac{R}{\mu_o}\{\rho_o(\gamma - \frac{i\alpha}{2})u_1 + \rho_1[(\sigma + \frac{i\omega}{2}) + u_o(\gamma - \frac{i\alpha}{2})]\}$$

$$E_{88} = \frac{\rho_o R}{\mu_o}v_1$$

where

$$m = \frac{\lambda}{\mu} \ , \ r = 2 + m$$

$$B_1 = -(\gamma + \frac{i\alpha}{2}) \ , \ B_3 = \frac{1}{T_o}\frac{dT_o}{dy} \quad \tilde{B}_1 = -(\gamma - \frac{i\alpha}{2})$$

$$B_4 = -\gamma_g M^2 [(\sigma - \frac{i\omega}{2}) + u_o(\gamma + \frac{i\alpha}{2})]$$

$$B_5 = [(\sigma - \frac{i\omega}{2}) + u_o(\gamma + \frac{i\alpha}{2})] / T_o \ , \ B_7 = -\beta$$

$$\tilde{B}_4 = -\gamma_g M^2 [(\sigma + \frac{i\omega}{2}) + u_o(\gamma - \frac{i\alpha}{2})]$$

$$\tilde{B}_5 = [(\sigma + \frac{i\omega}{2}) + u_o(\gamma - \frac{i\alpha}{2})] / T_o$$

$$G_1 = B_3 \times B_1 \ , \ G_2 = -(\gamma + \frac{i\alpha}{2})$$

$$G_3 = -\frac{d}{dy}(\frac{1}{\rho_o}\frac{d\rho_o}{dy}) + B_3 \times B_3$$

$$G_4 = B_3 \times B_4 - (\gamma + \frac{i\alpha}{2})\gamma_g M^2 \frac{du_o}{dy}$$

$$G_5 = B_3 \times B_5 + \frac{(\gamma + \frac{i\alpha}{2})}{T_o}\frac{du_o}{dy} - [(\sigma - \frac{i\omega}{2}) + u_o(\gamma + \frac{i\alpha}{2})] \frac{\frac{dT_o}{dy}}{T_o^2}$$

$$G_6 = [(\sigma - \frac{i\omega}{2}) + u_o(\gamma + \frac{i\alpha}{2})] / T_o$$

$$G_7 = B_3 \times B_7 \ , \ G_8 = -\beta$$

$$\Upsilon = \{ 1 + \frac{(2+m)\,\mu_o}{R} \gamma_g M^2 [(\sigma - \frac{i\omega}{2}) + u_o (\gamma + \frac{i\alpha}{2})] \}^{-1}$$

$$\mu_T = \frac{d\mu}{dT} \ , \ \mu_{TT} = \frac{d^2\mu}{dT^2}$$

$\overline{F}$ = conjugate of complex value F

Appendix G.

$$C_{21} = \frac{\rho_o R}{\mu_o}[(\sigma - \frac{i\omega}{2}) + u_o(\gamma + \frac{i\alpha}{2})] - [(\gamma + \frac{i\alpha}{2})^2 - \beta^2]$$

$$C_{24} = \frac{R}{\mu_o}(\gamma + \frac{i\alpha}{2}) - (1 + m)(\gamma + \frac{i\alpha}{2})B_4$$

$$C_{25} = -(1 + m)(\gamma + \frac{i\alpha}{2})B_5$$

$$C_{31} = -(\gamma + \frac{i\alpha}{2})$$

$$C_{34} = -\gamma_g M^2[(\sigma - \frac{i\omega}{2}) + u_o(\gamma + \frac{i\alpha}{2})]$$

$$C_{35} = [(\sigma - \frac{i\omega}{2}) + u_o(\gamma + \frac{i\alpha}{2})]/T_o$$

$$C_{37} = -\beta$$

$$C_{42} = \frac{\Upsilon}{R}[(1 + m)(\gamma + \frac{i\alpha}{2})\mu_o + (2 + m)\mu_o G_2]$$

$$C_{43} = \Upsilon\{-\rho_o[(\sigma - \frac{i\omega}{2}) + u_o(\gamma + \frac{i\alpha}{2})] + \frac{\mu_o}{R}[(\gamma + \frac{i\alpha}{2})^2 - \beta^2]\}$$

$$C_{46} = \Upsilon\frac{(2 + m)\mu_o}{R}G_6$$

$$C_{48} = \frac{\Upsilon}{R}[(1+m)\beta\mu_o + (2+m)\mu_o G_8]$$

$$C_{64} = -\frac{R}{\mu_o}(\gamma_g - 1)M^2 Pr[(\sigma - \frac{i\omega}{2}) + u_o(\gamma + \frac{i\alpha}{2})]$$

$$C_{65} = \frac{\rho_o R}{\mu_o} Pr[(\sigma - \frac{i\omega}{2}) + u_o(\gamma + \frac{i\alpha}{2})] - [(\gamma + \frac{i\alpha}{2})^2 - \beta^2]$$

$$C_{81} = \beta(1+m)[(\gamma + \frac{i\alpha}{2}) + B_1]$$

$$C_{84} = -\frac{\beta R}{\mu_o} + \beta(1+m)B_4$$

$$C_{85} = \beta(1+m)B_5$$

$$C_{87} = \frac{\rho_o R}{\mu_o}[(\sigma - \frac{i\omega}{2}) + u_o(\gamma + \frac{i\alpha}{2})] - [(\gamma + \frac{i\alpha}{2})^2 - \beta^2]$$

where

$$m = \frac{\lambda}{\mu}, \quad r = 2 + m$$

$$B_1 = -(\gamma + \frac{i\alpha}{2})$$

$$B_4 = -\gamma_g M^2 [(\sigma - \frac{i\omega}{2}) + u_o(\gamma + \frac{i\alpha}{2})]$$

$$B_5 = [(\sigma - \frac{i\omega}{2}) + u_o(\gamma + \frac{i\alpha}{2})] / T_o$$

$$B_7 = -\beta$$

$$G_2 = -(\gamma + \frac{i\alpha}{2})$$

$$G_6 = [(\sigma - \frac{i\omega}{2}) + u_o(\gamma + \frac{i\alpha}{2})]/T_o$$

$$G_8 = -\beta$$

$$\Upsilon = \{1 + \frac{(2+m)\,\mu_o}{R}\,\gamma_g M^2 [(\sigma - \frac{i\omega}{2}) + u_o(\gamma + \frac{i\alpha}{2})]\}^{-1}$$

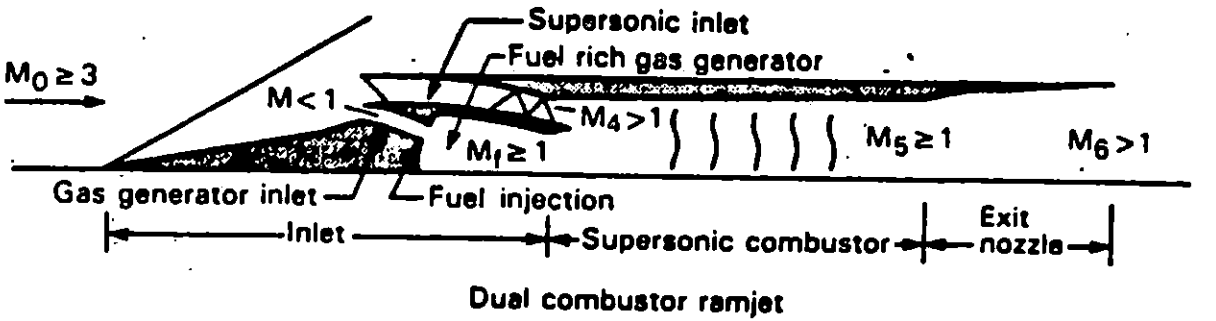

Figure 1.1 Schematic of generic supersonic combustion engine (Waltrup, 1986).

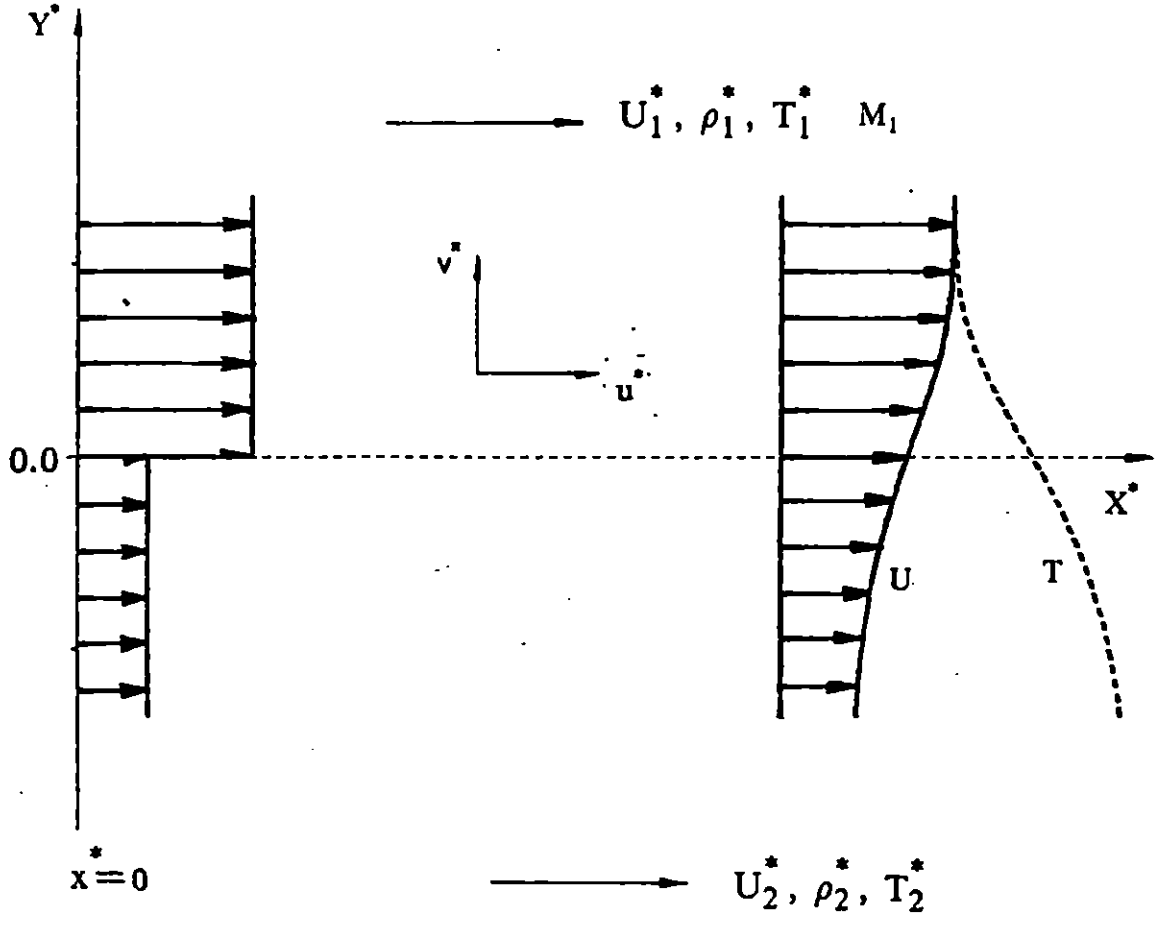

Figure 2.1 Definition of flow parameter in a mixing layer.

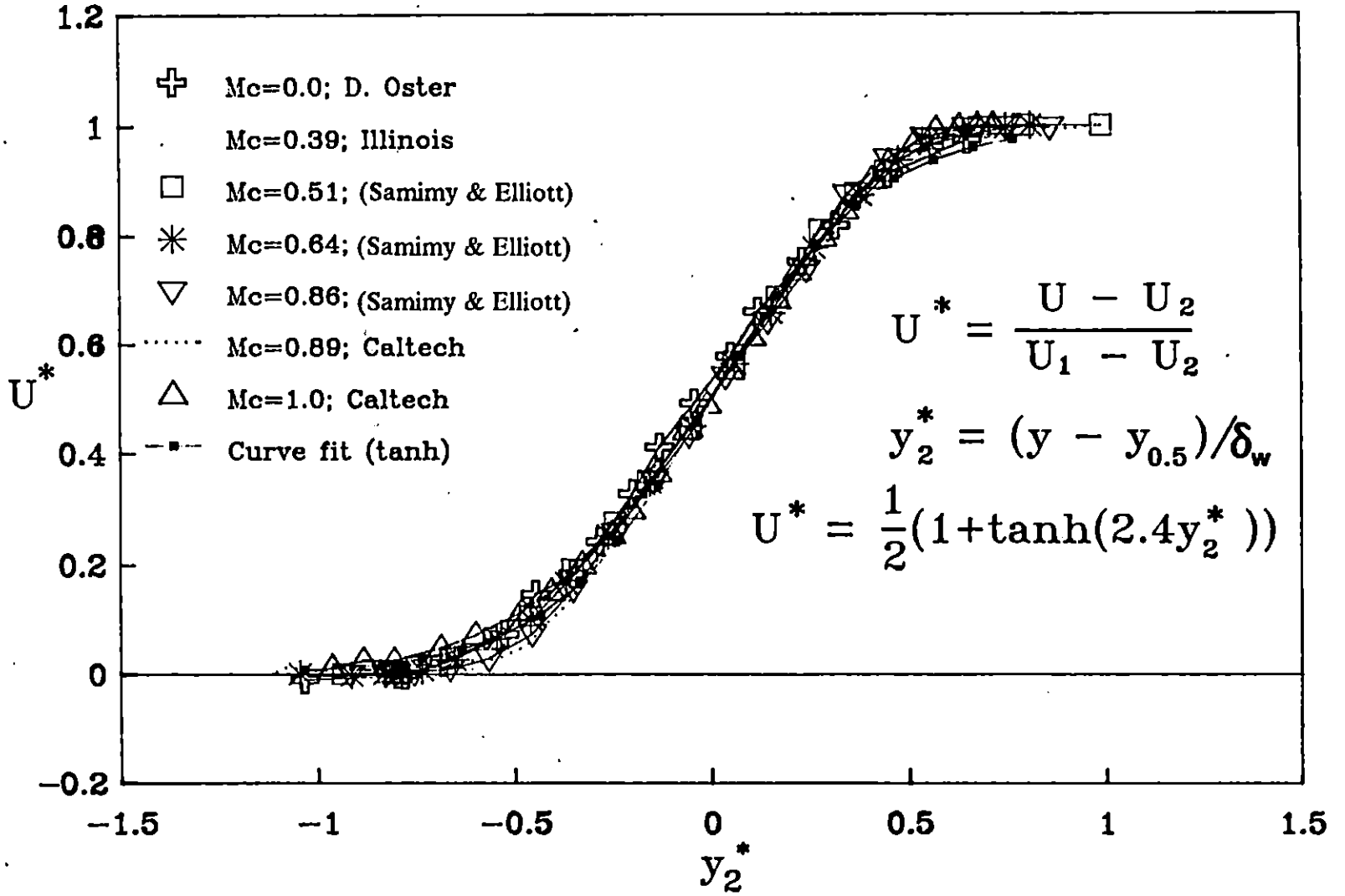

Figure 2.2 Turbulent mean velocity profiles from various experiments and hyperbolic tangent approximation (Samimy and Elliott, 1989).

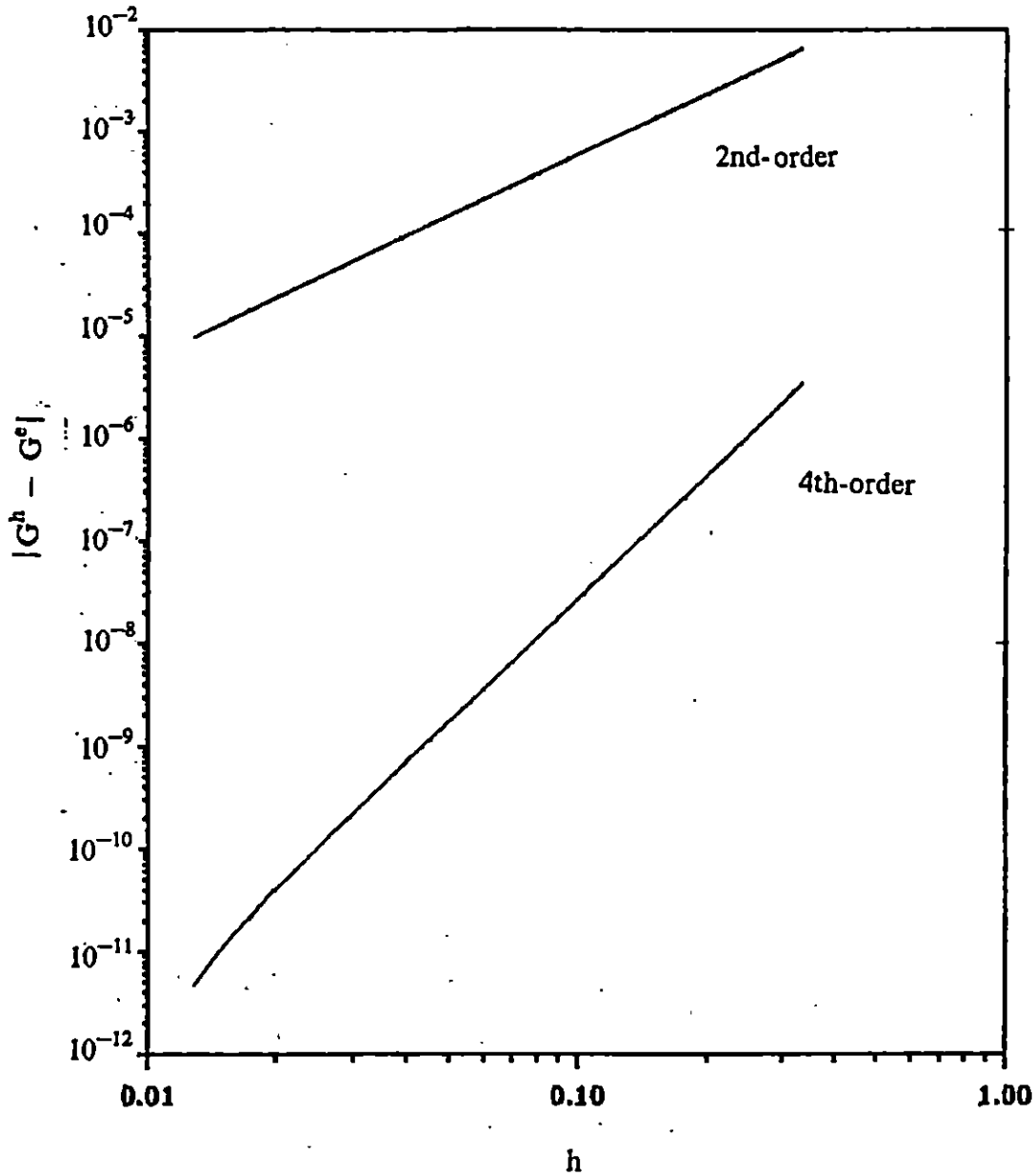

Figure 2.3 $|G^h - G^e|$ vs. h; Blasius profile at $M_1 = 4.5$, $G = \partial F/\partial \eta$ at $\eta = 0$, $G^e = 0.56199026569$.

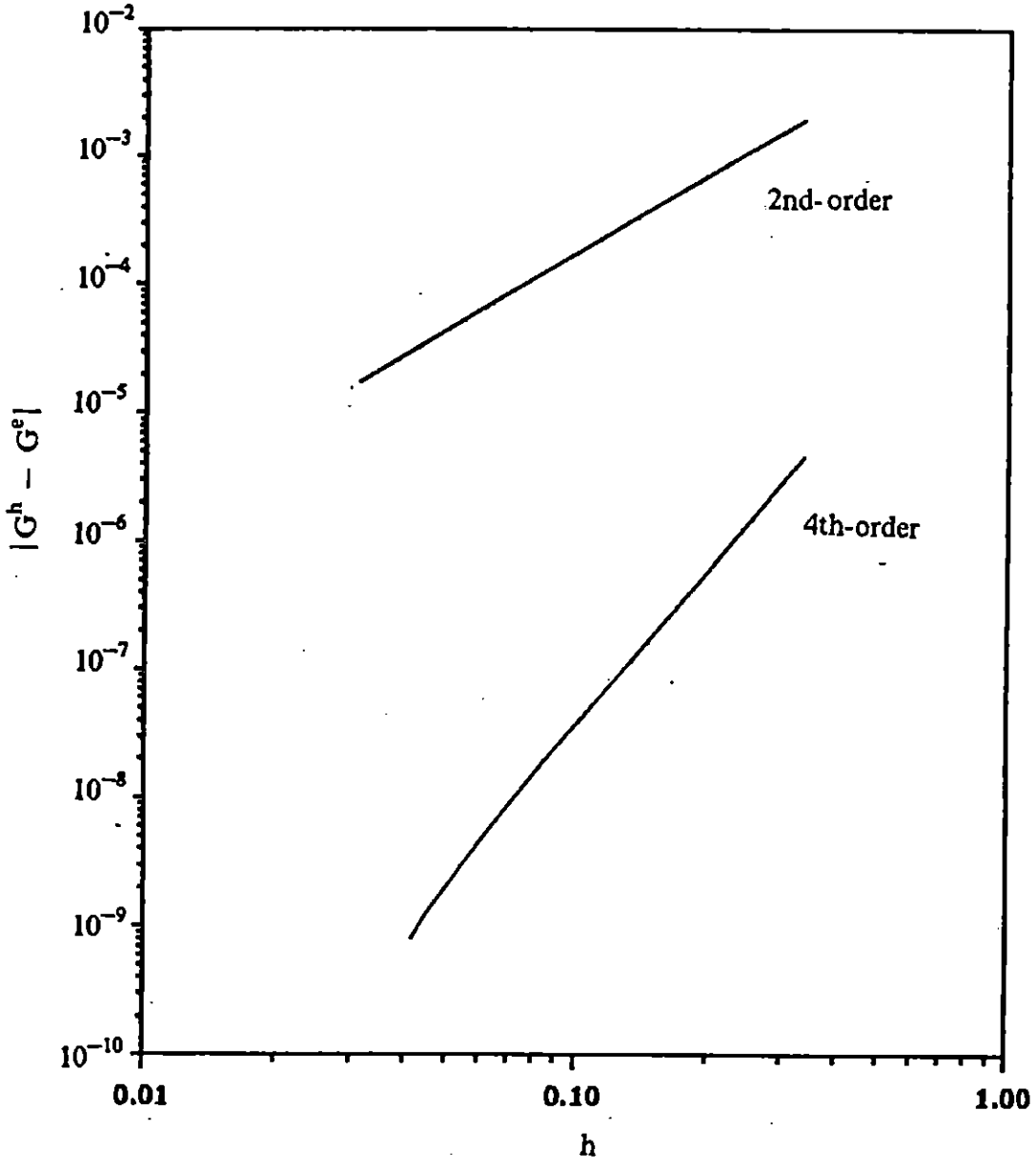

Figure 2.4 $|G^h - G^e|$ vs. h; Mixing flow at $M_1 = 5.0$, $T_2 = 2.0$ and $U_2 = 0.0$, $G = \partial F/\partial\eta$ at $\eta = 0$, $G^e = 0.32713077060$.

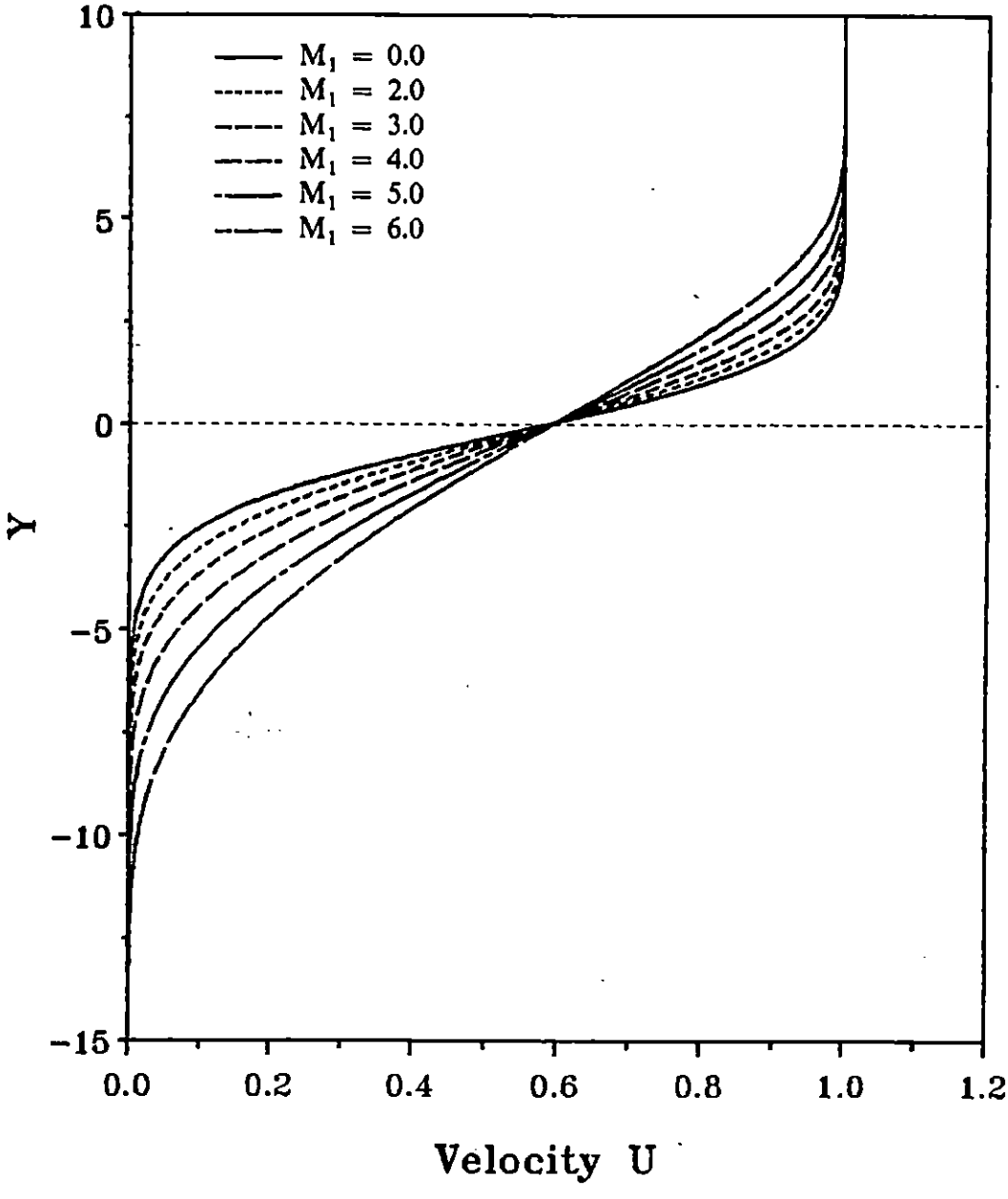

Figure 2.5 Velocity profiles at $T_2 = 0.5$ and $U_2 = 0.0$ for various Mach numbers.

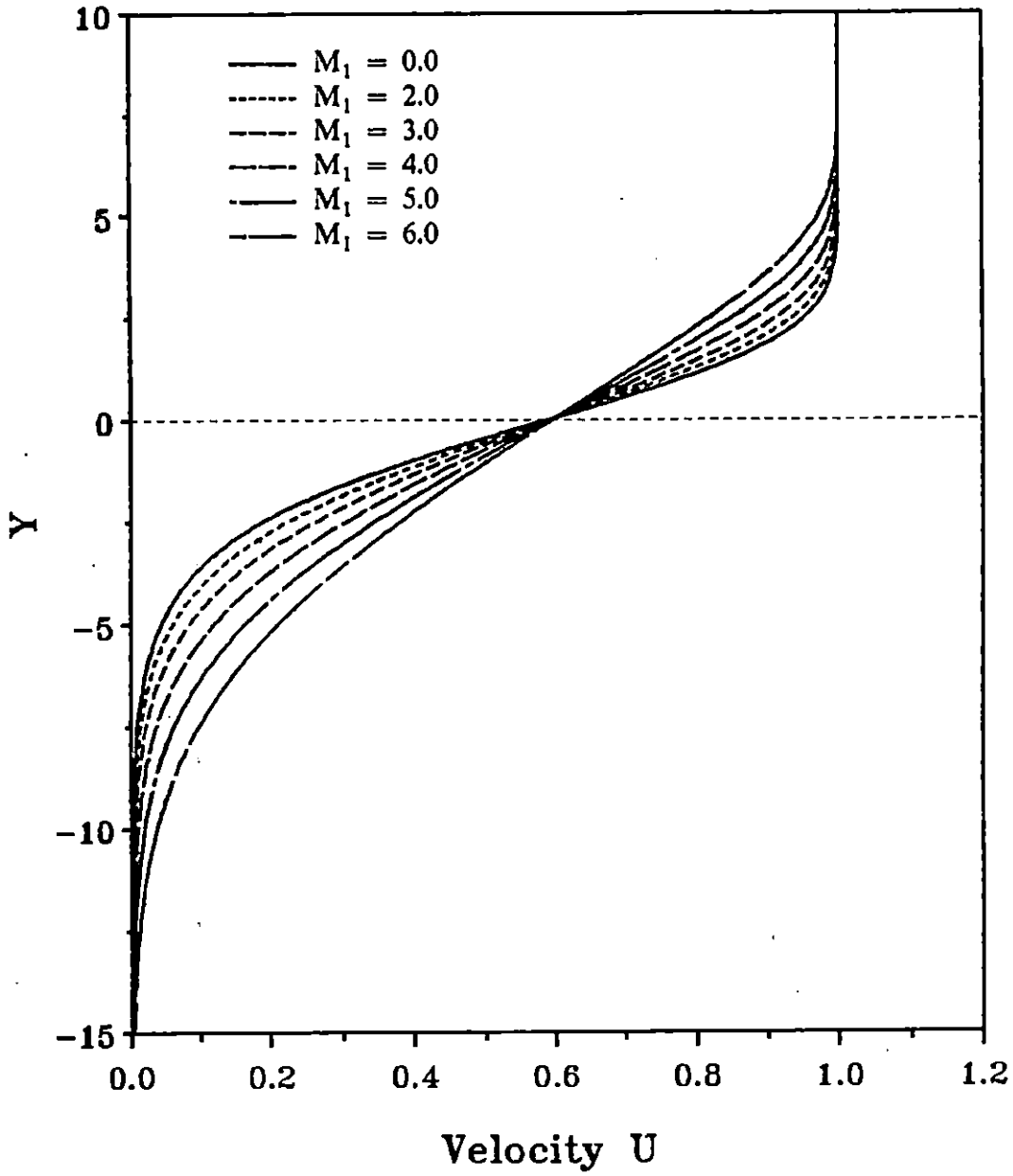

Figure 2.6 Velocity profiles at $T_2 = 1.0$ and $U_2 = 0.0$ for various Mach numbers.

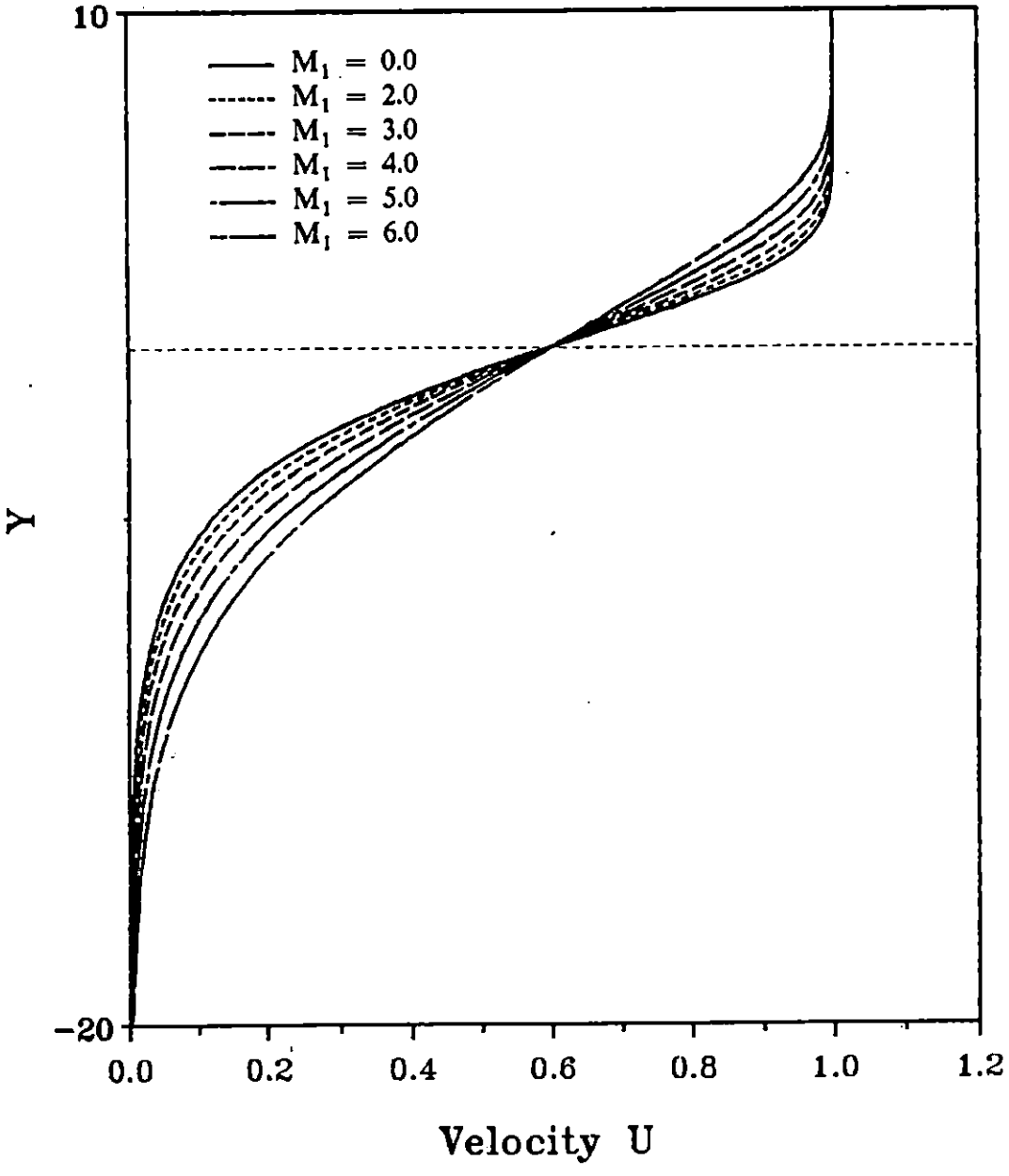

Figure 2.7 Velocity profiles at $T_2 = 2.0$ and $U_2 = 0.0$ for various Mach numbers.

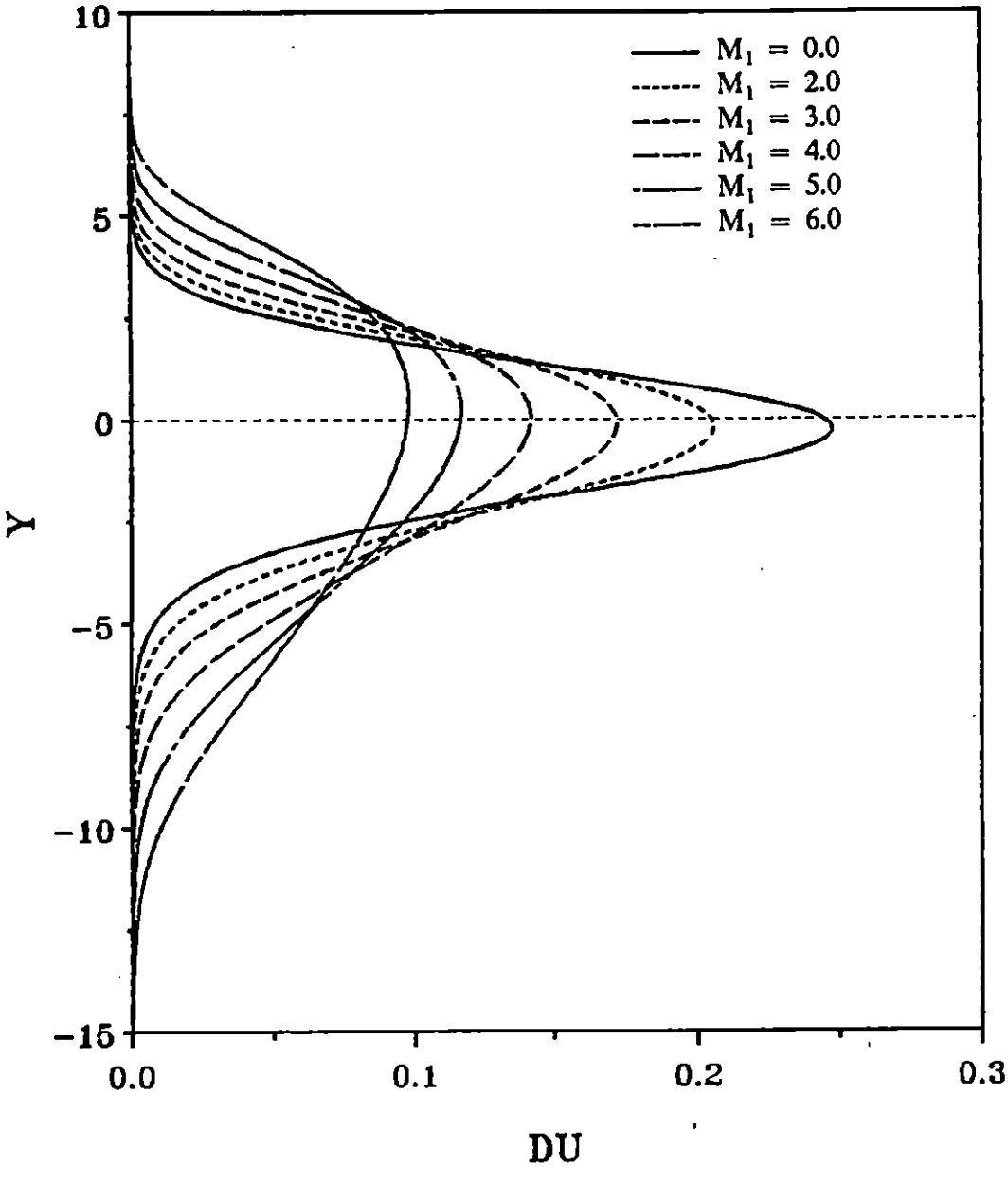

Figure 2.8 Vorticity profiles at $T_2 = 0.5$ and $U_2 = 0.0$ for various Mach numbers.

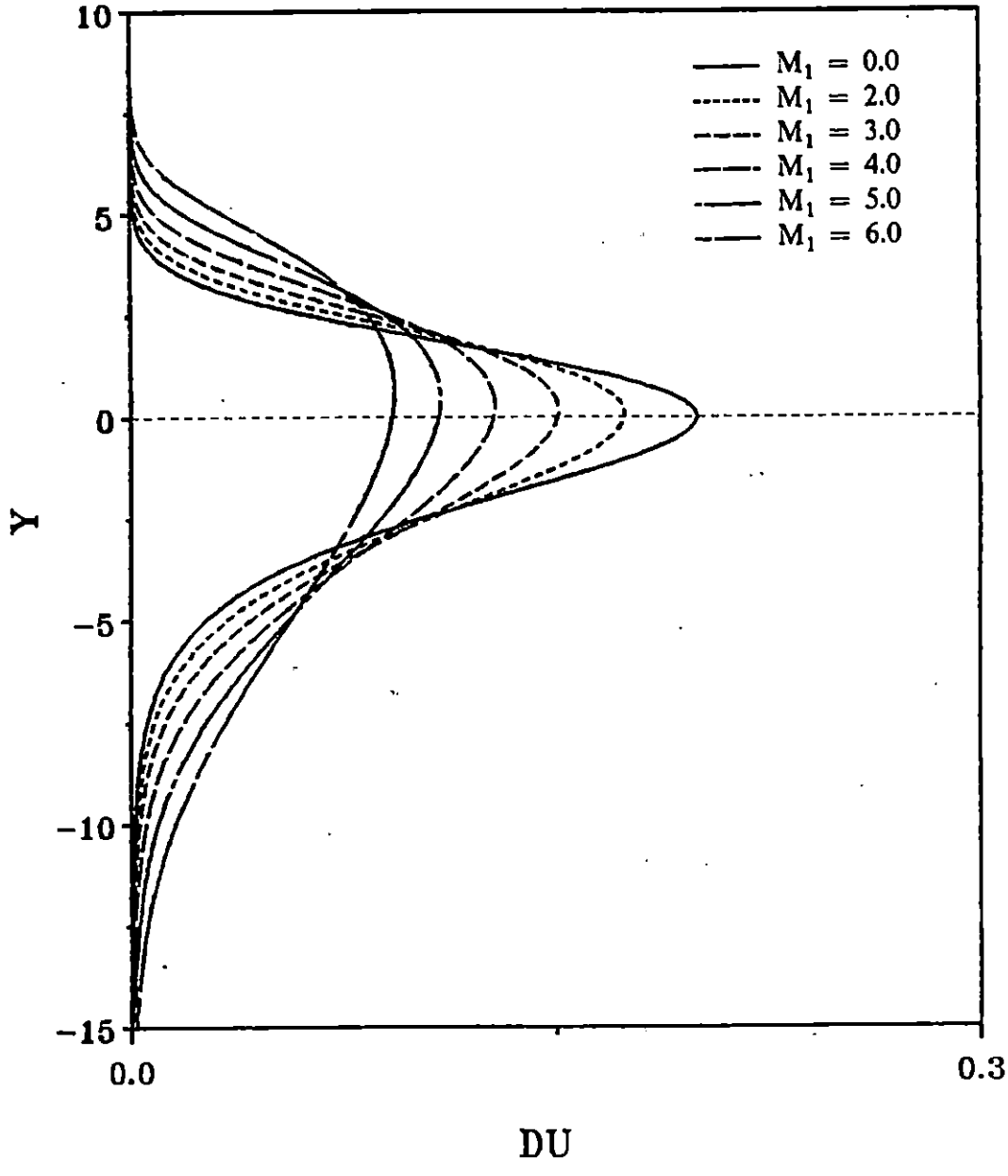

Figure 2.9 Vorticity profiles at $T_2 = 1.0$ and $U_2 = 0.0$ for various Mach numbers.

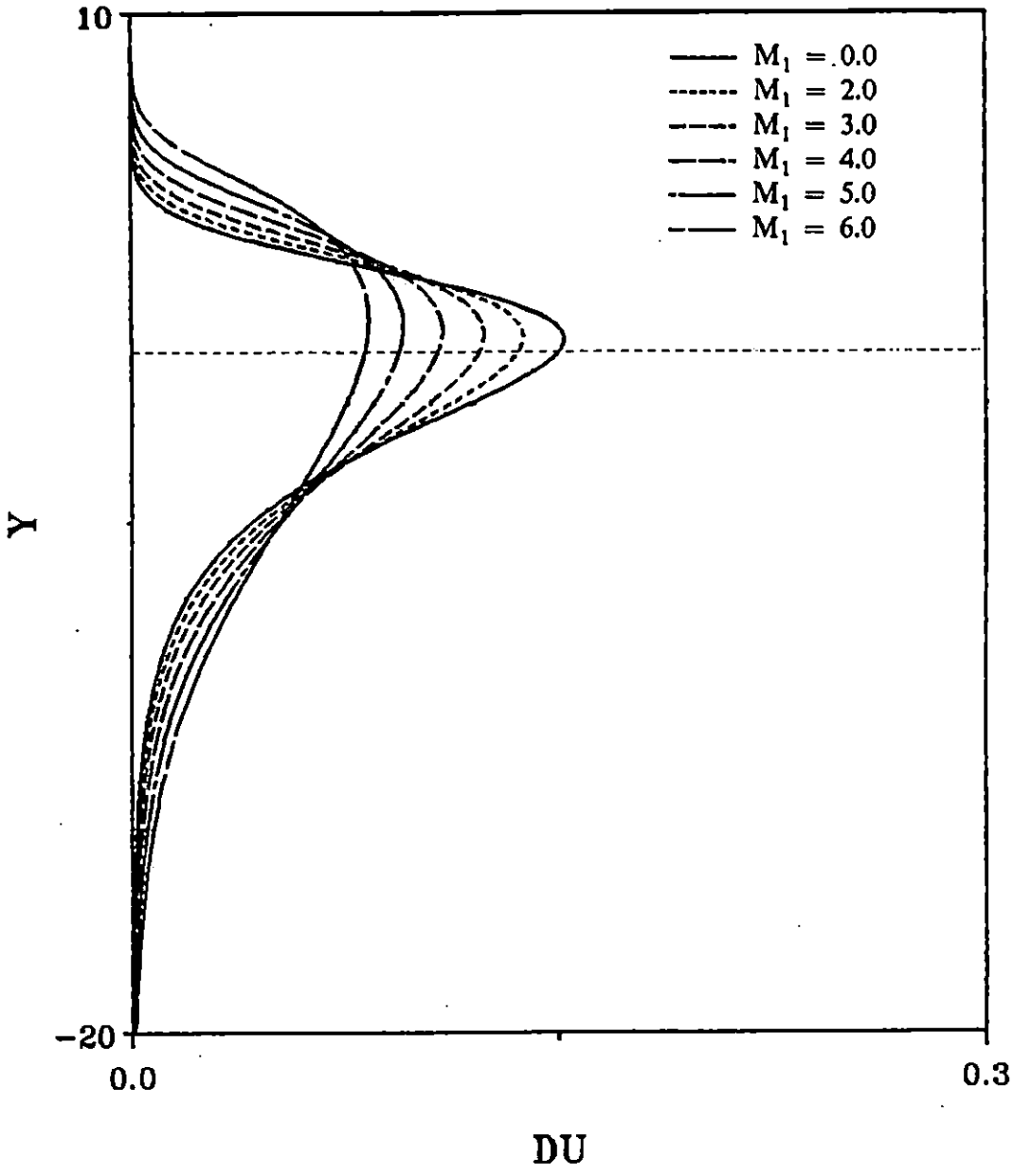

Figure 2.10 Vorticity profiles at $T_2 = 2.0$ and $U_2 = 0.0$ for various Mach numbers.

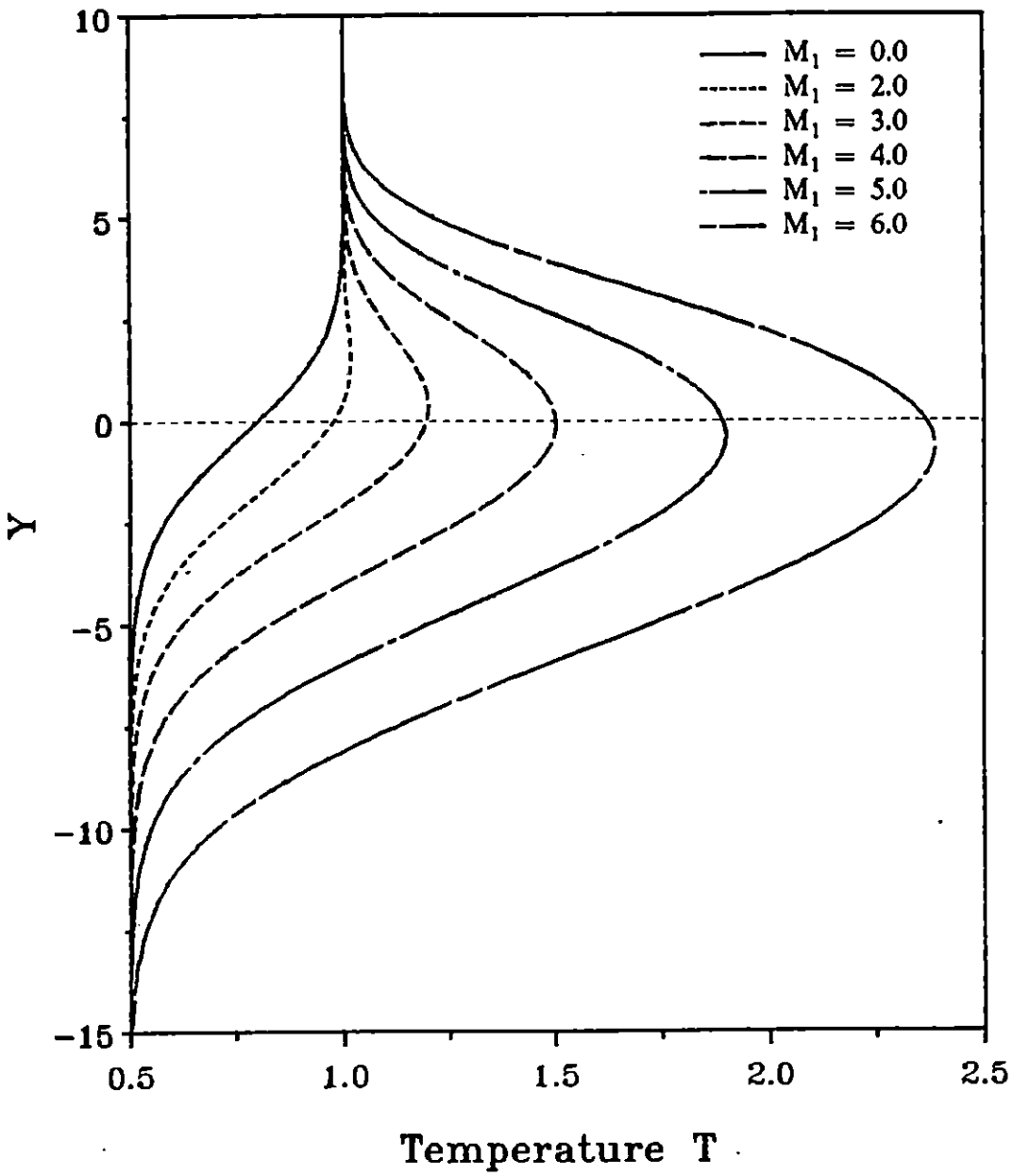

Figure 2.11 Temperature profiles at $T_2 = 0.5$ and $U_2 = 0.0$ for various Mach numbers.

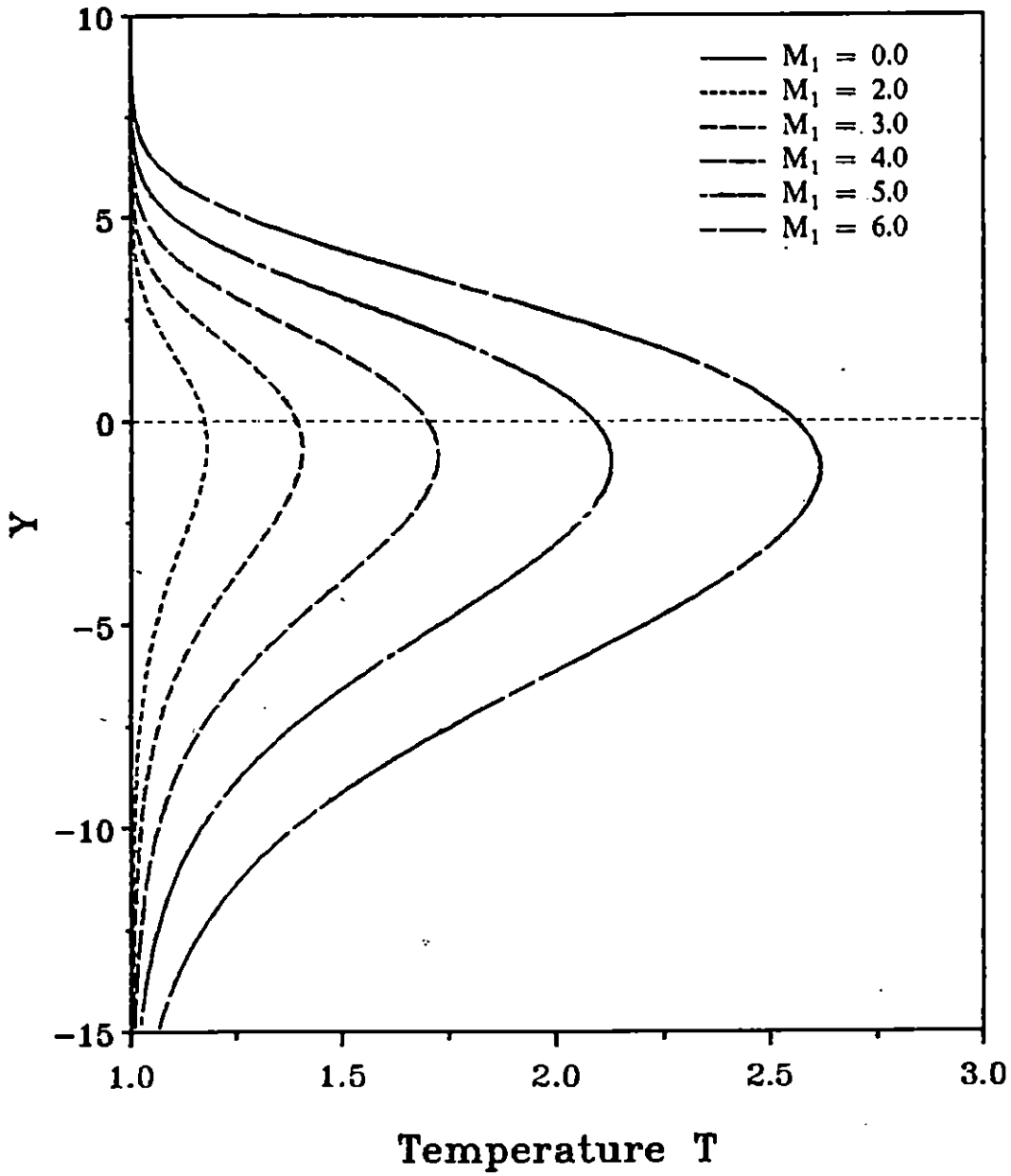

Figure 2.12 Temperature profiles at $T_2 = 1.0$ and $U_2 = 0.0$ for various Mach numbers.

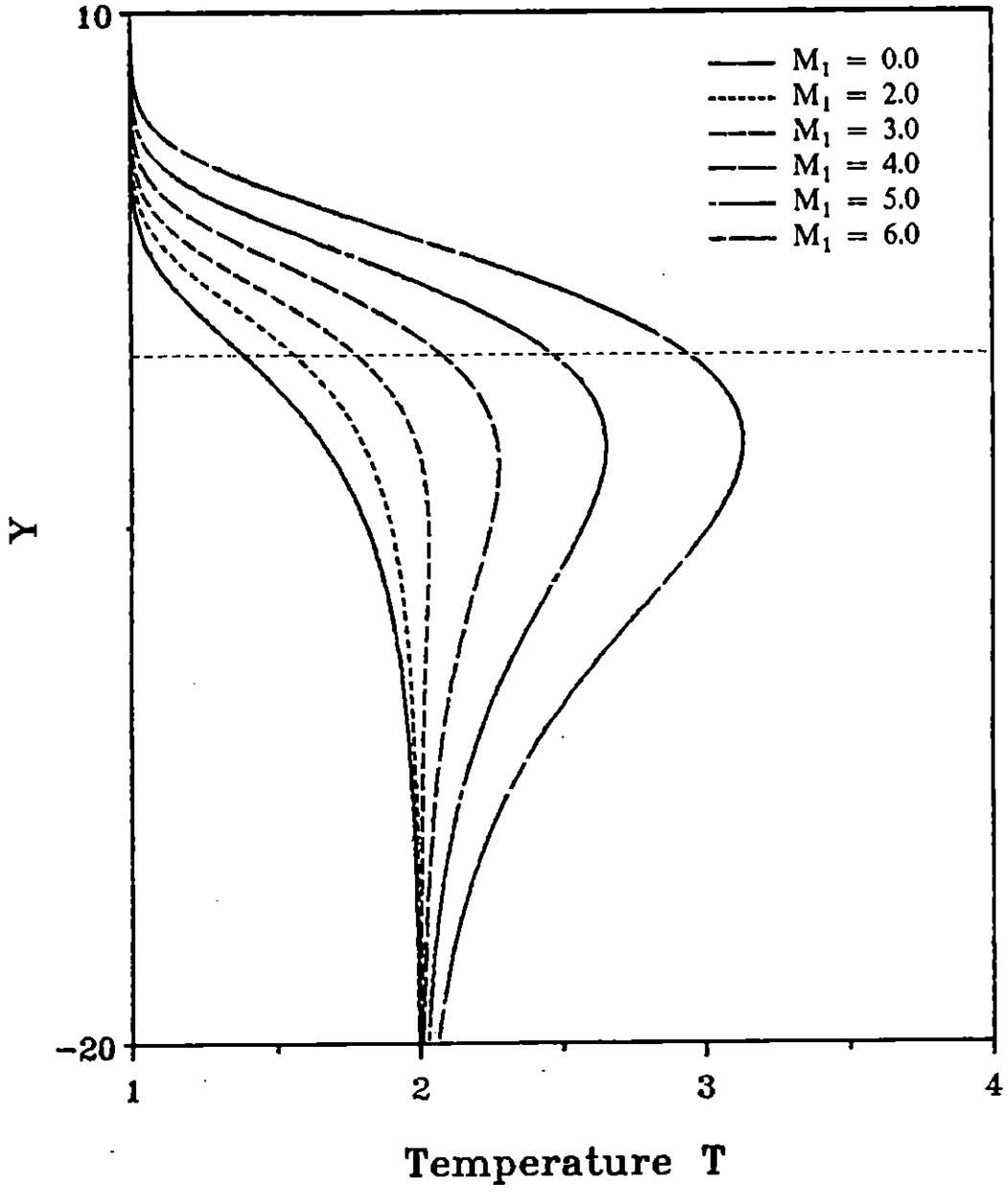

Figure 2.13 Temperature profiles at $T_2 = 2.0$ and $U_2 = 0.0$ for various Mach numbers.

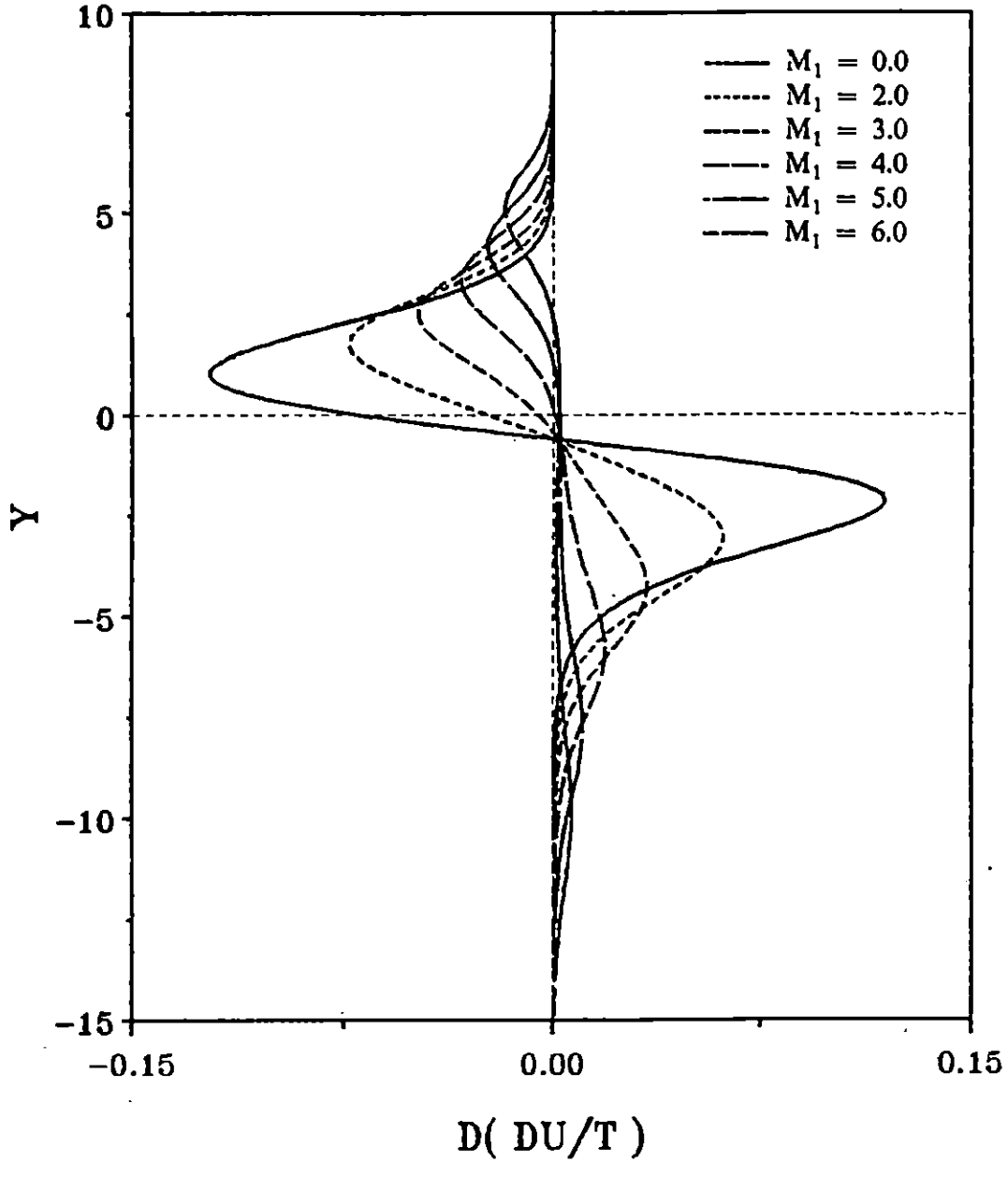

Figure 2.14 D(DU/T) Distribution at $T_2 = 0.5$ and $U_2 = 0.0$ for various Mach numbers.

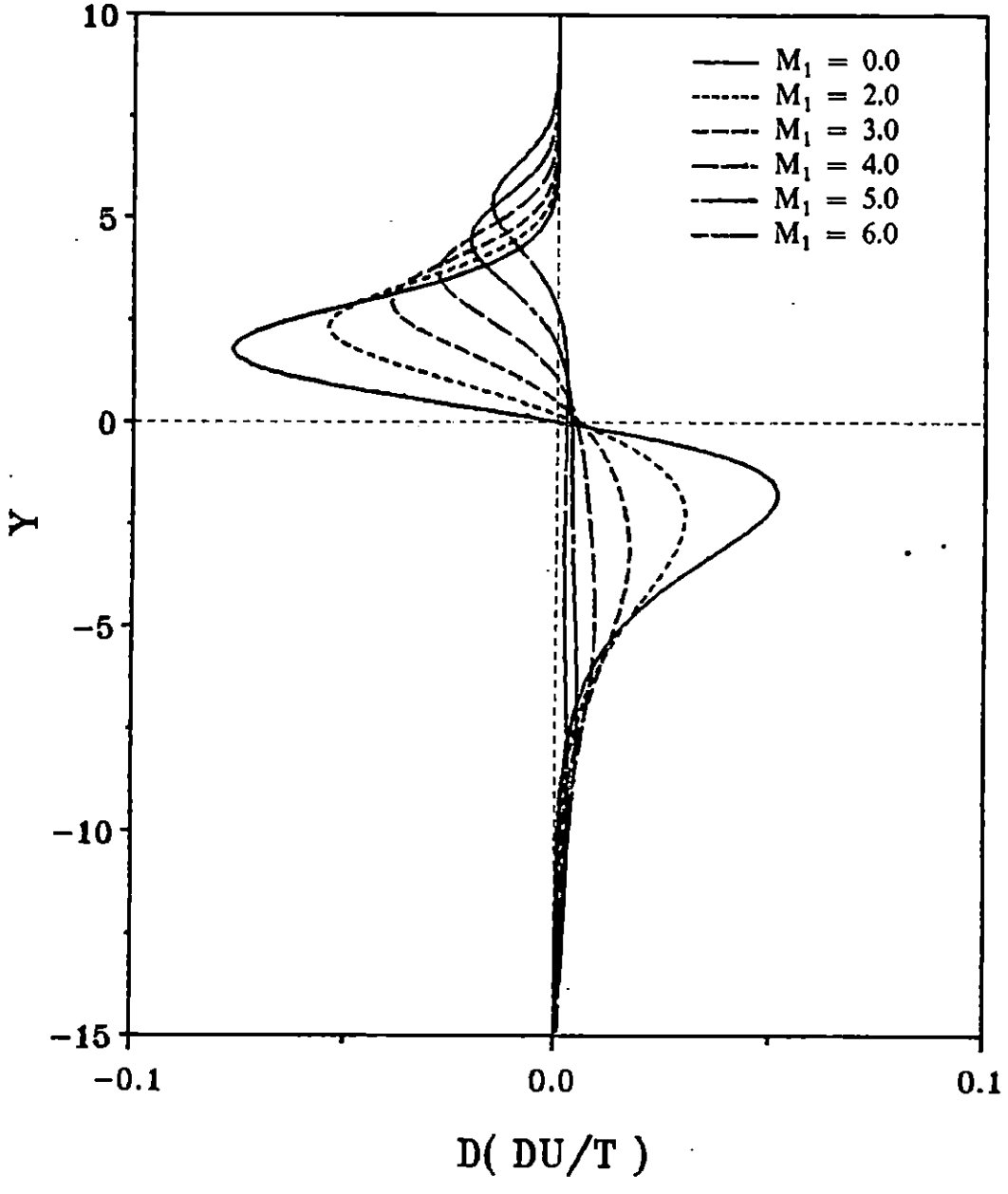

Figure 2.15 D(DU/T) Distribution at $T_2 = 1.0$ and $U_2 = 0.0$ for various Mach numbers.

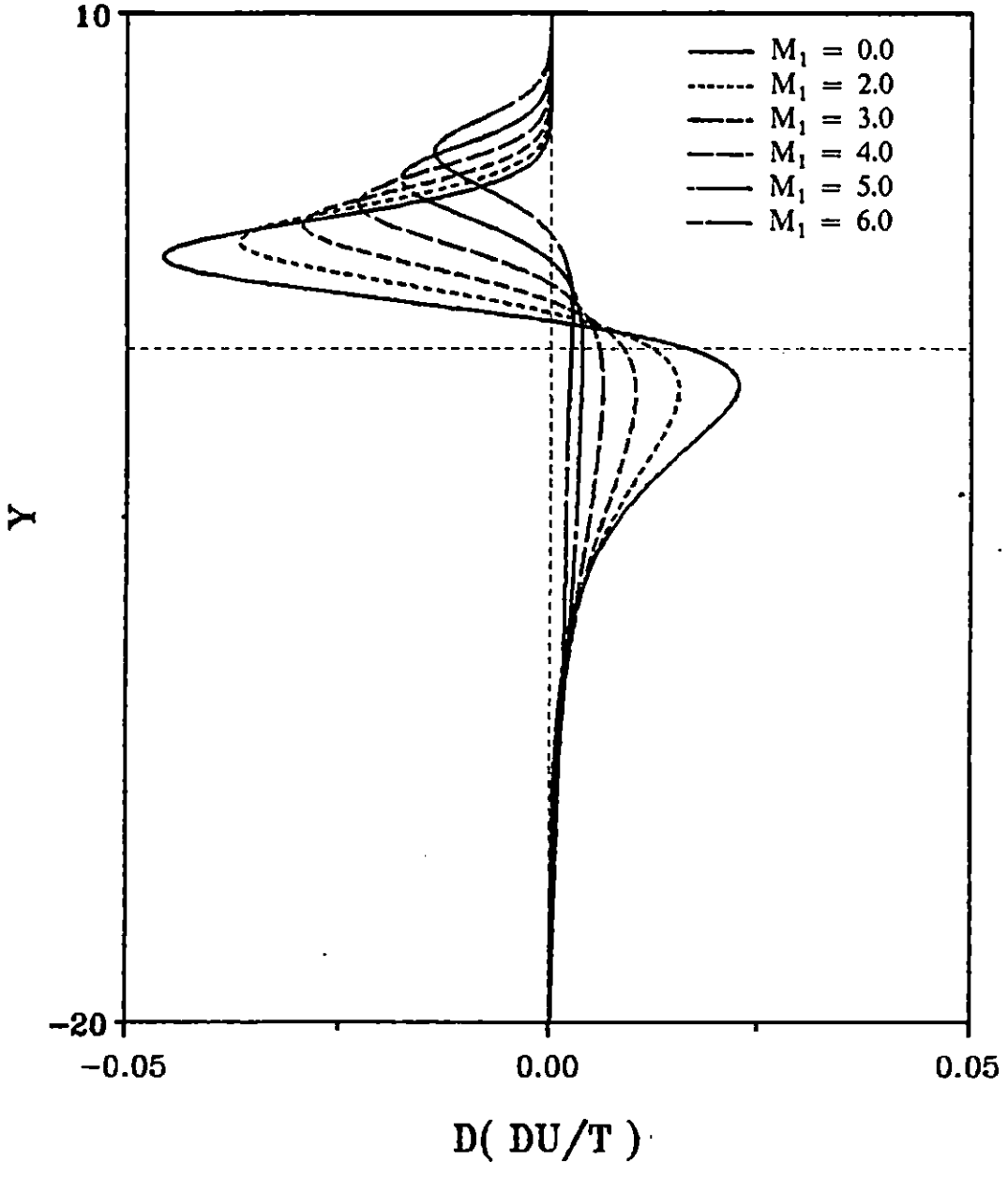

Figure 2.16 D(DU/T) Distribution at $T_2 = 2.0$ and $U_2 = 0.0$ for various Mach numbers.

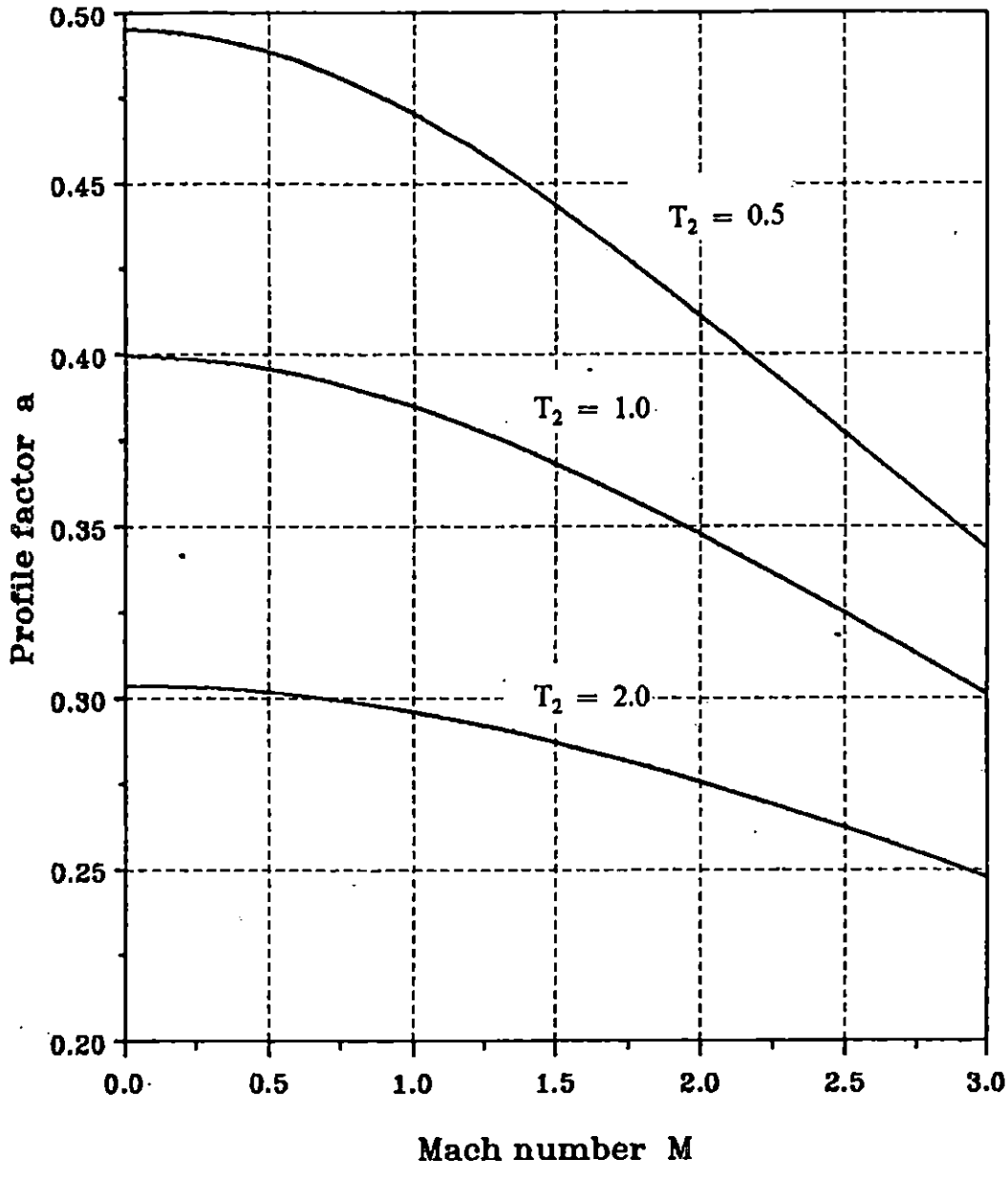

Figure 2.17 Variation of parameter "a" vs. Mach number at $T_2 = 1.0$ and $U_2 = 0.0$.

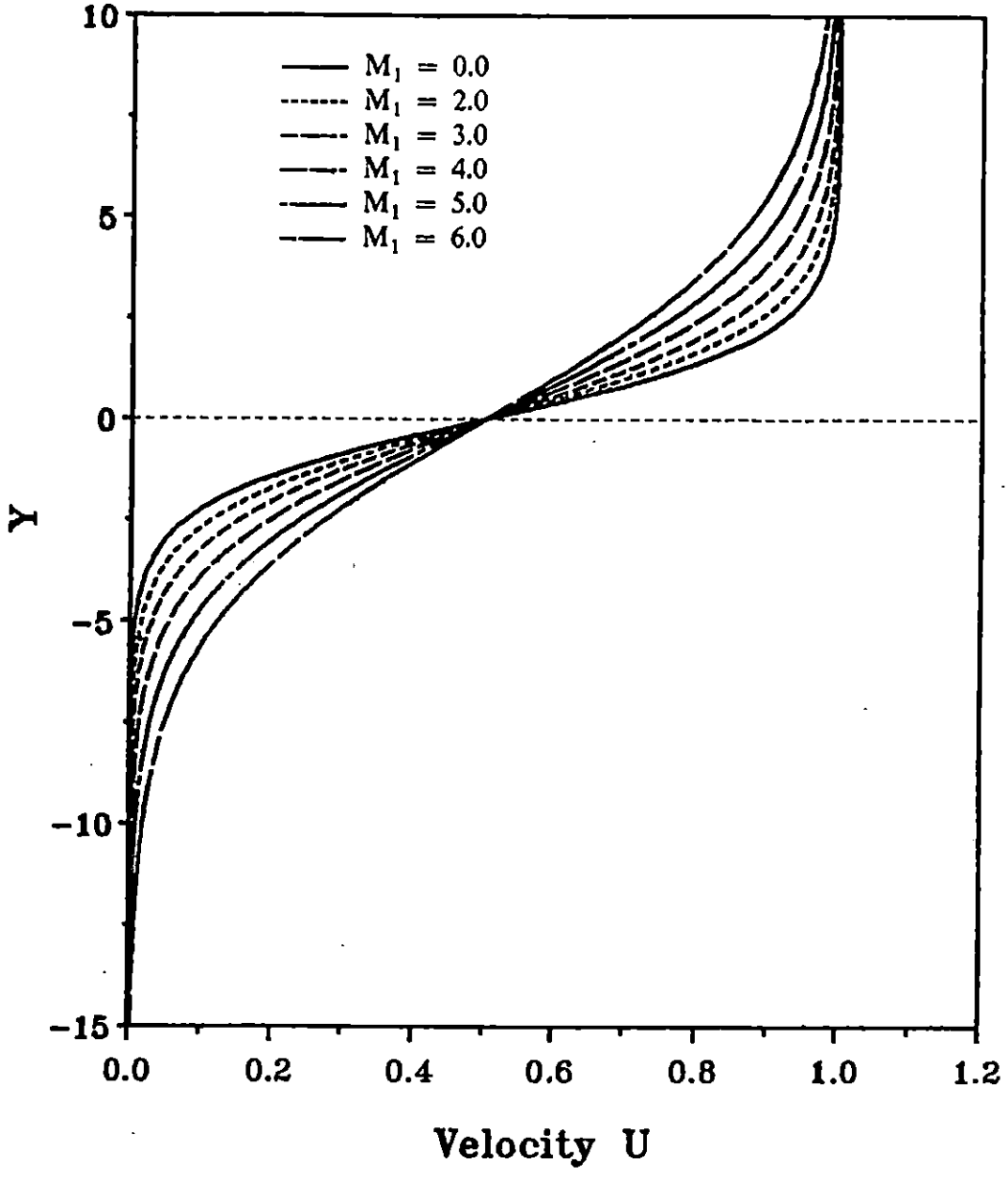

Figure 2.18 Velocity profiles at $T_2 = 0.5$ and $U_2 = 0.0$ for various Mach numbers, $U(y) = 0.5(1 + \tanh ay)$.

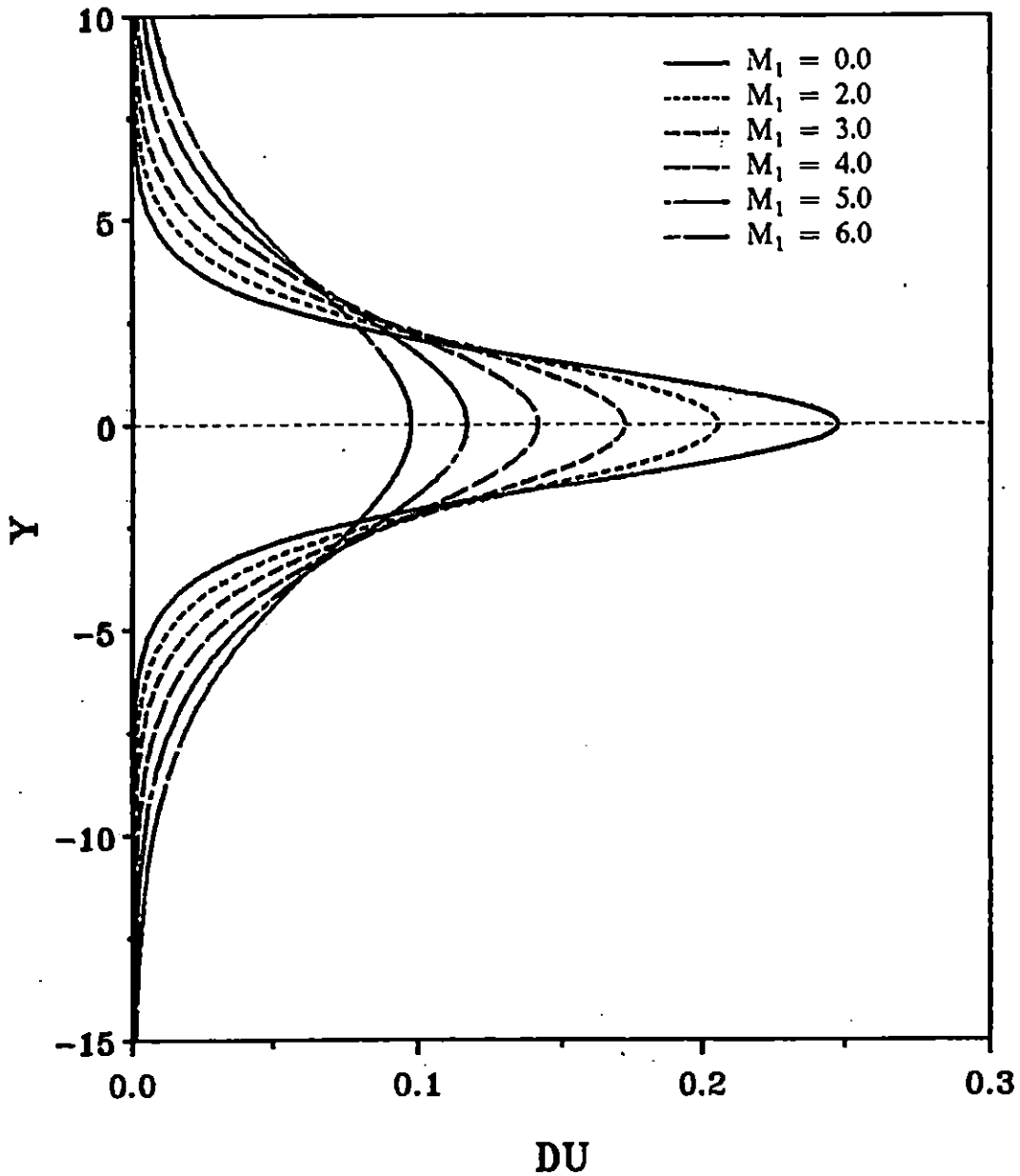

Figure 2.19 Vorticity profiles at $T_2 = 0.5$ and $U_2 = 0.0$ for various Mach numbers, $U(y) = 0.5\,(1 + \tanh ay)$.

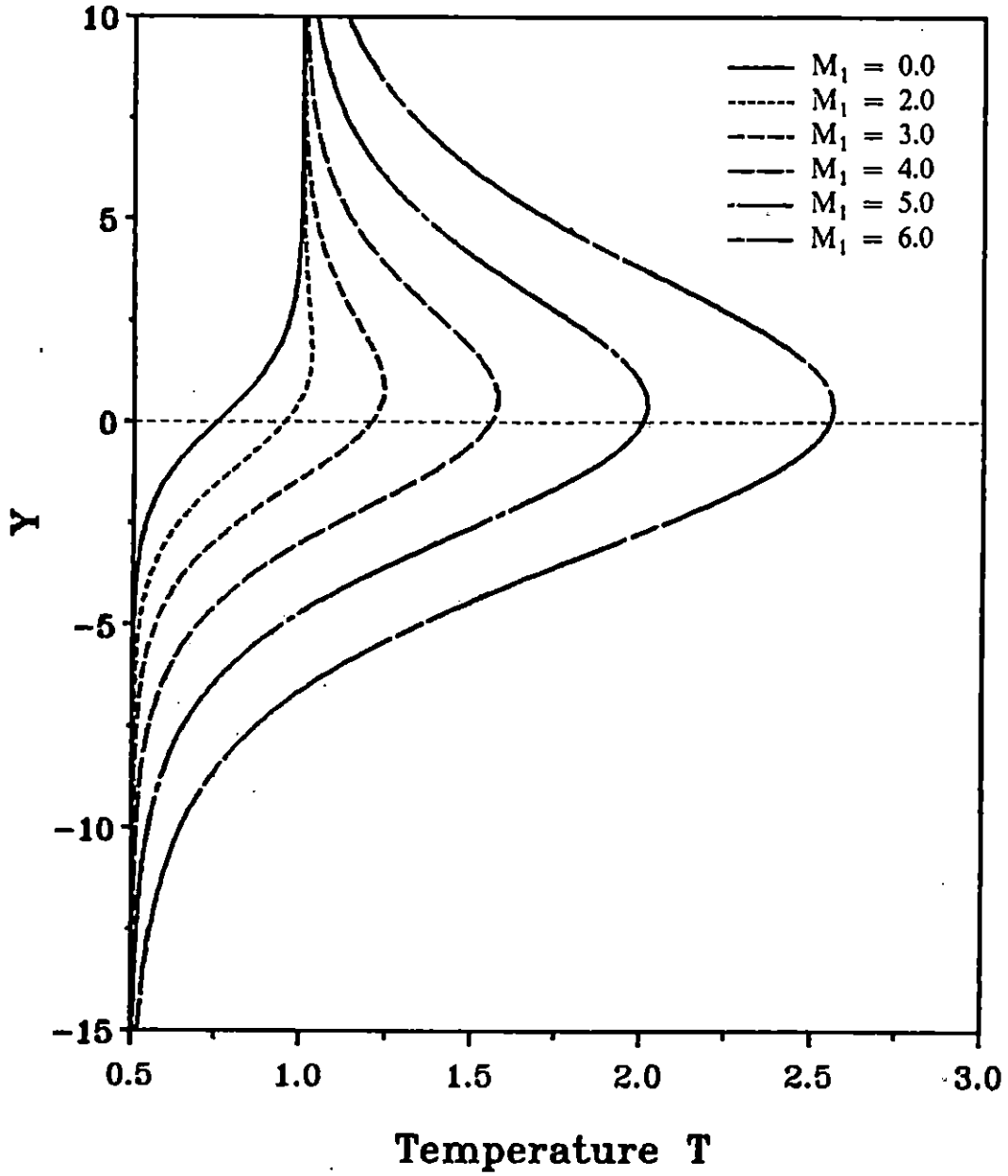

Figure 2.20 Temperature profiles at $T_2 = 0.5$ and $U_2 = 0.0$ for various Mach numbers, $U(y) = 0.5\,(1 + \tanh ay)$.

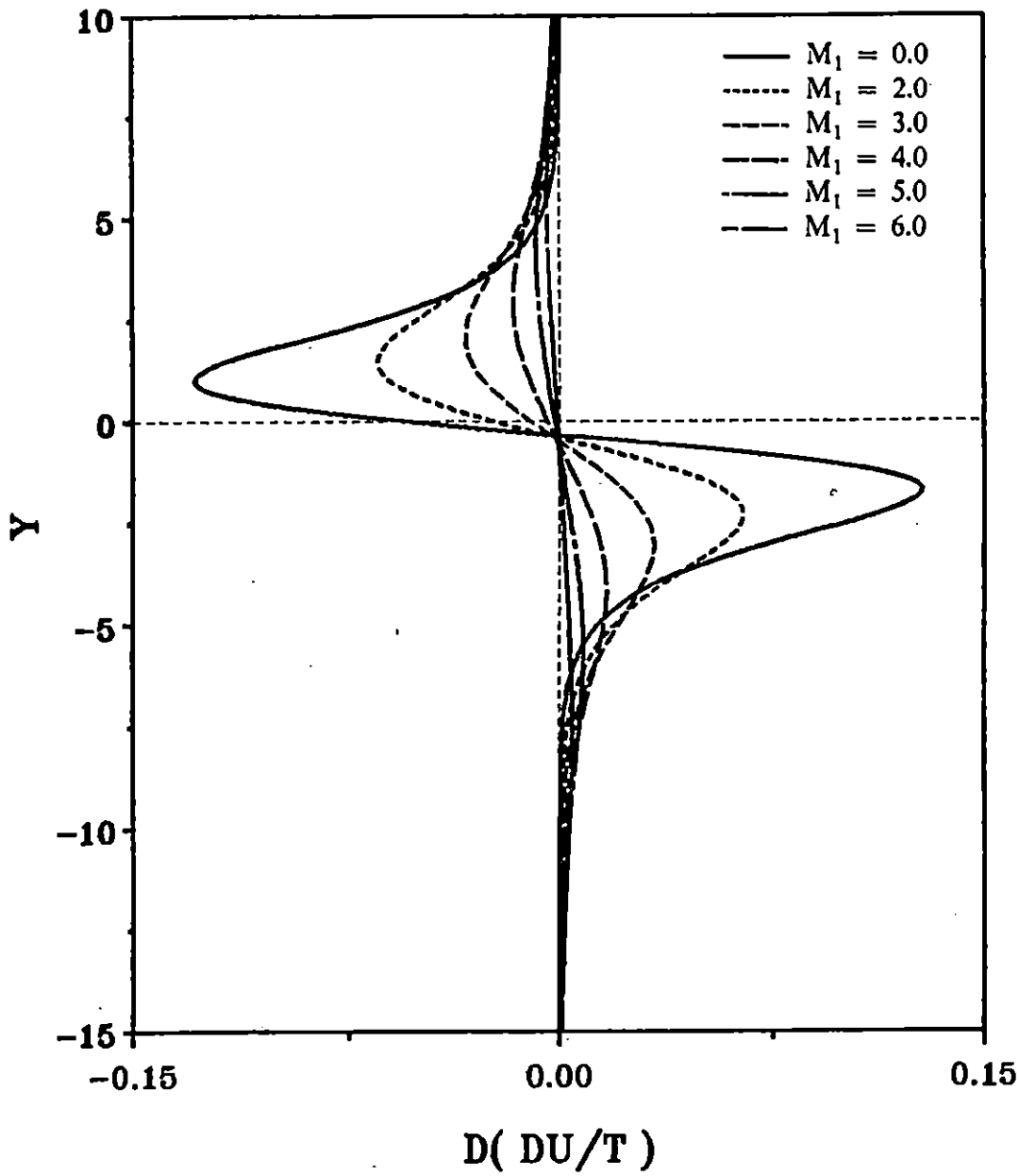

Figure 2.21 D(DU/T) Distribution at $T_2 = 0.5$ and $U_2 = 0.0$ for various Mach numbers, $U(y) = 0.5 (1 + \tanh ay)$.

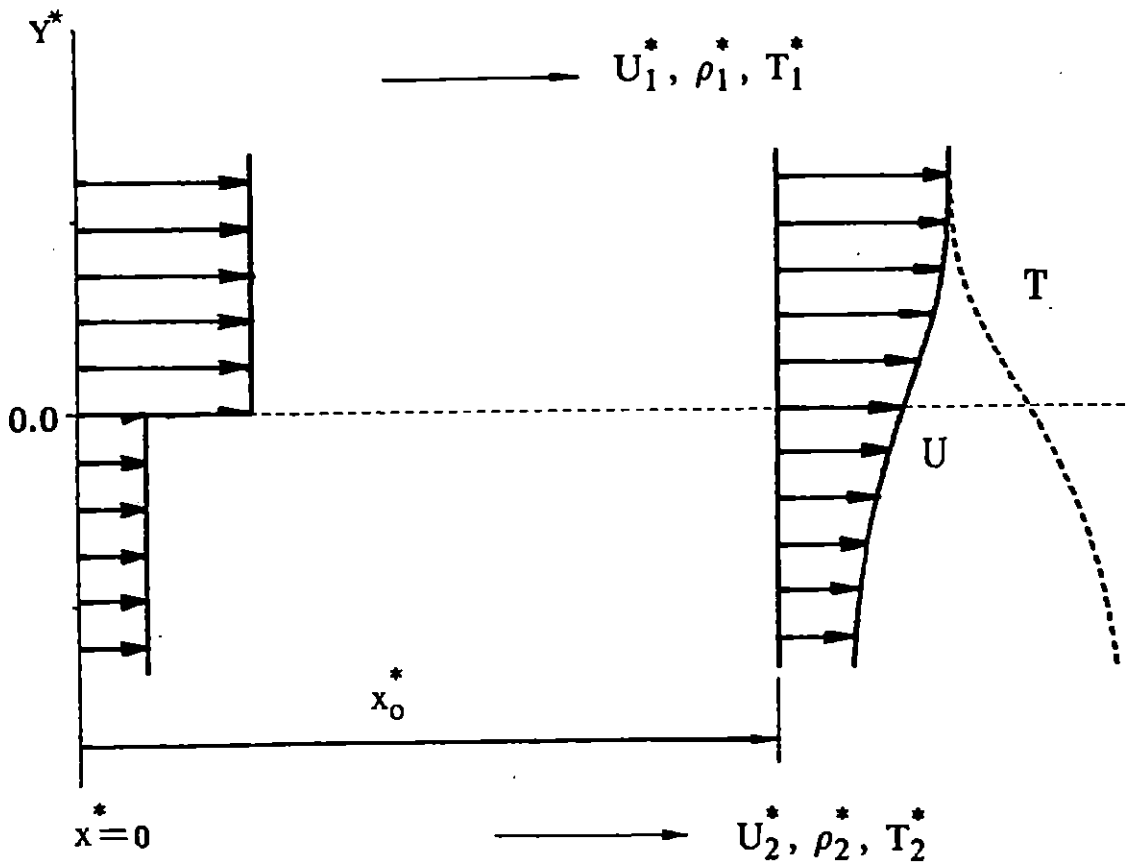

Figure 3.1 Definition of flow parameter in a mixing layer.

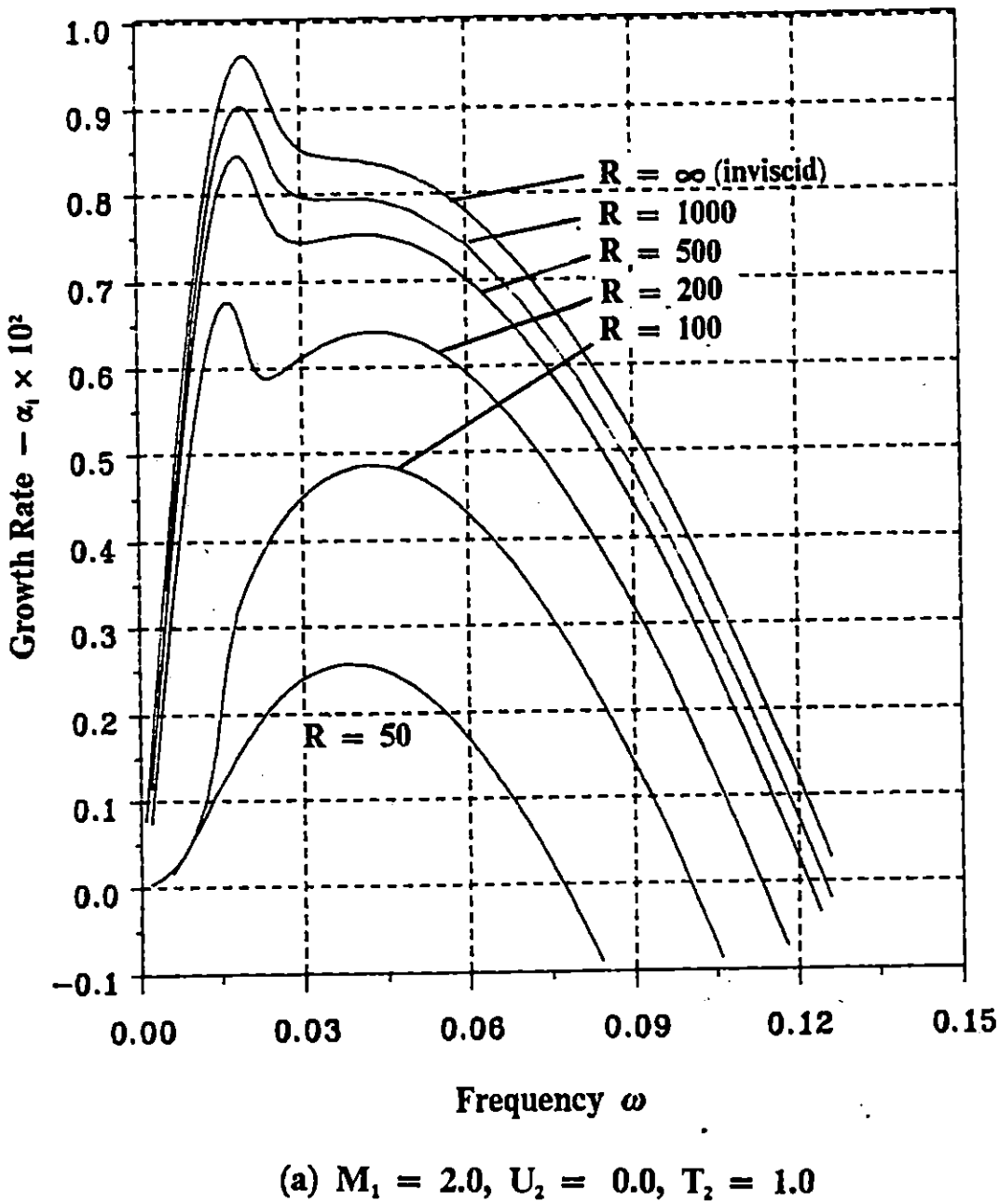

Figure 5.1a The growth rates of 2D viscous disturbances. Viscosity-temperature relation is given by the Sutherland formula with $M_1 = 2.0$, $U_2 = 0.0$, $T_2 = 1.0$, $T_1^* = 273°K$.

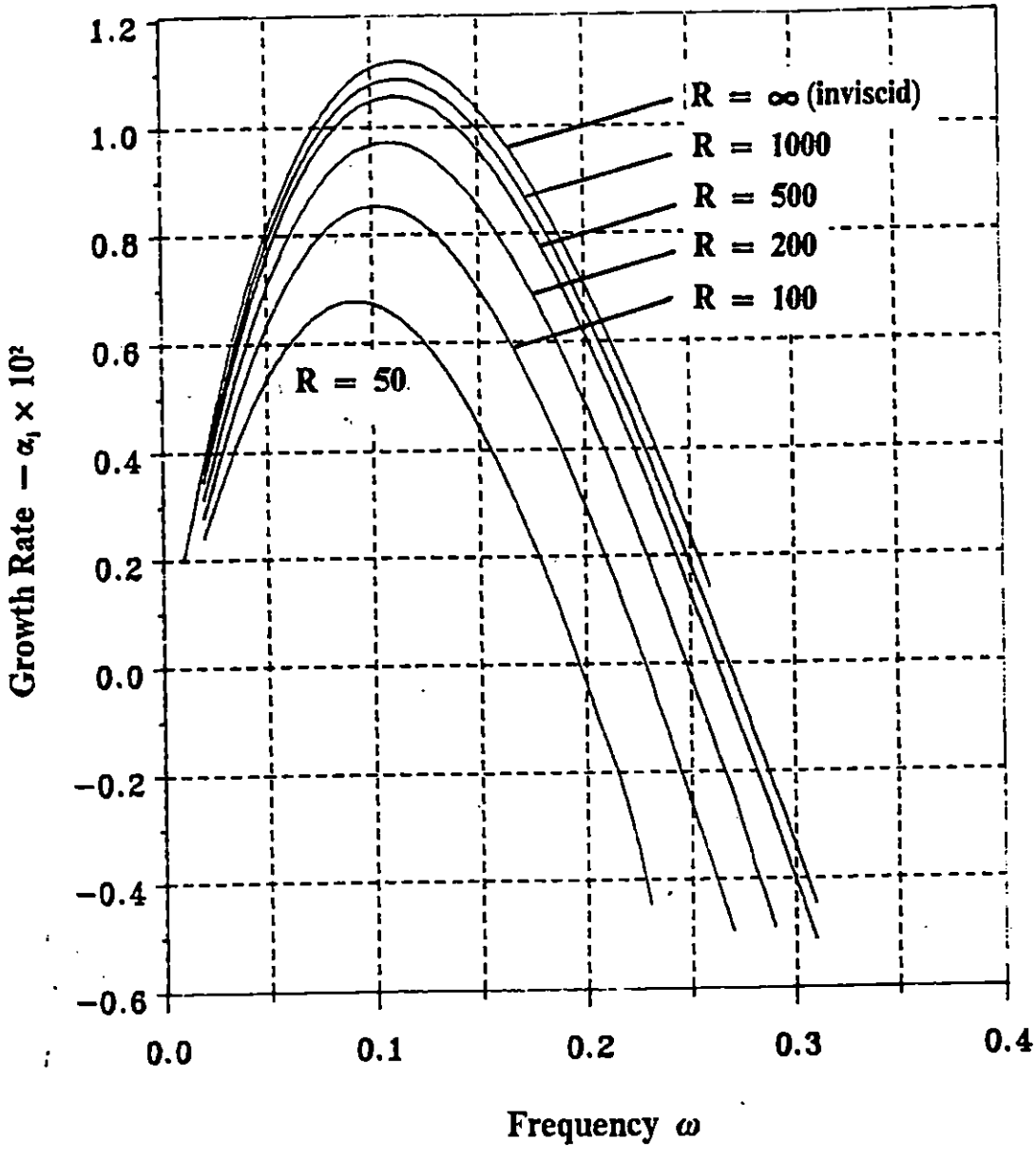

(b) $M_1 = 3.0$, $U_2 = 0.6$, $T_2 = 2.0$

Figure 5.1b The growth rates of 2D viscous disturbances. Viscosity-temperature relation is given by the Sutherland formula with $M_1 = 3.0$, $U_2 = 0.6$, $T_2 = 2.0$, $T_1^* = 273°K$.

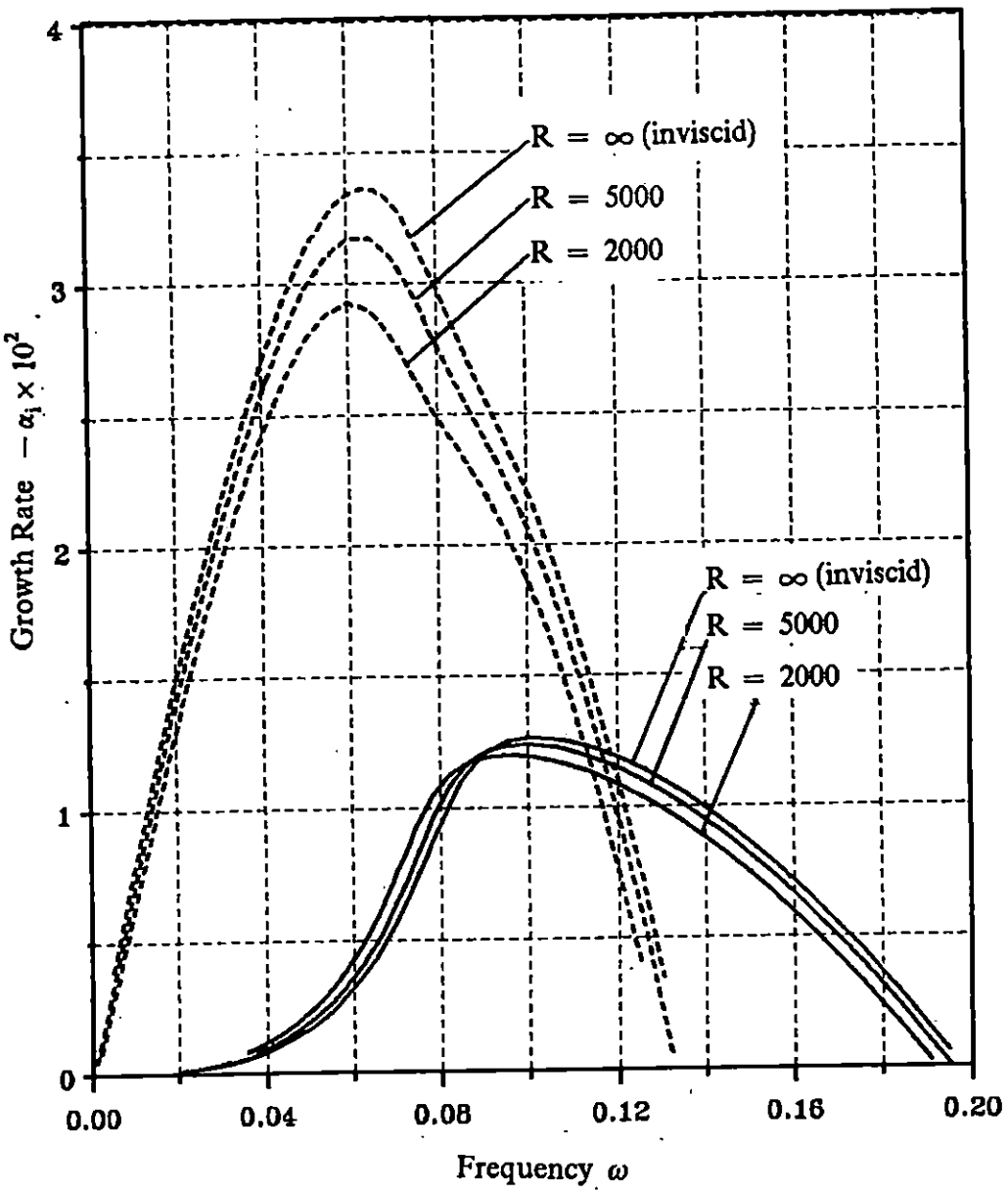

Figure 5.2a The growth rates of 2D viscous disturbances; $u_o = 0.5(1 + \tanh y)$, $M_1 = 2.0$, $T_2 = 1.0$.

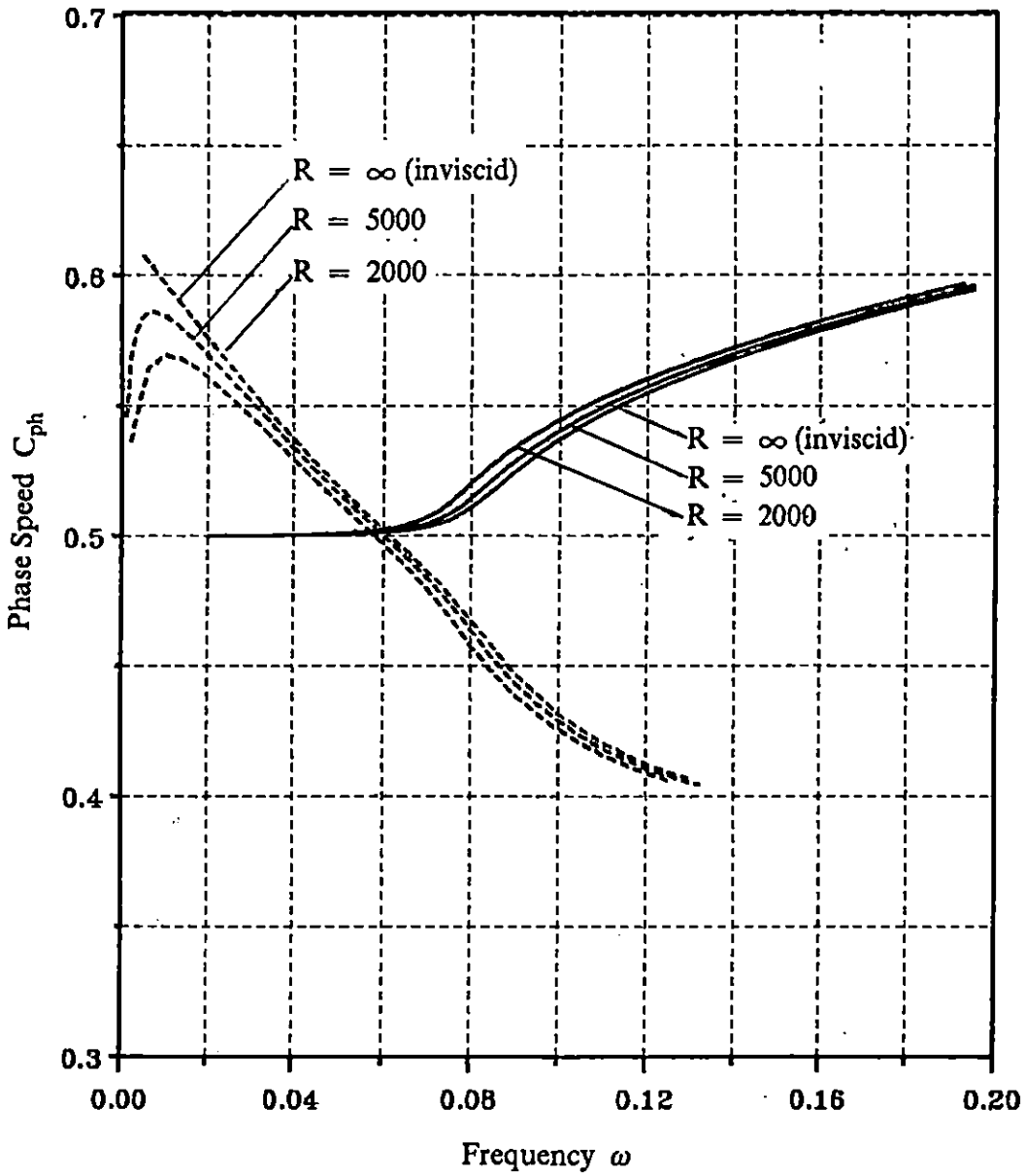

Figure 5.2b The phase speeds of 2D viscous disturbances; $u_0 = 0.5(1 + \tanh y)$, $M_1 = 2.0$, $T_2 = 1.0$.

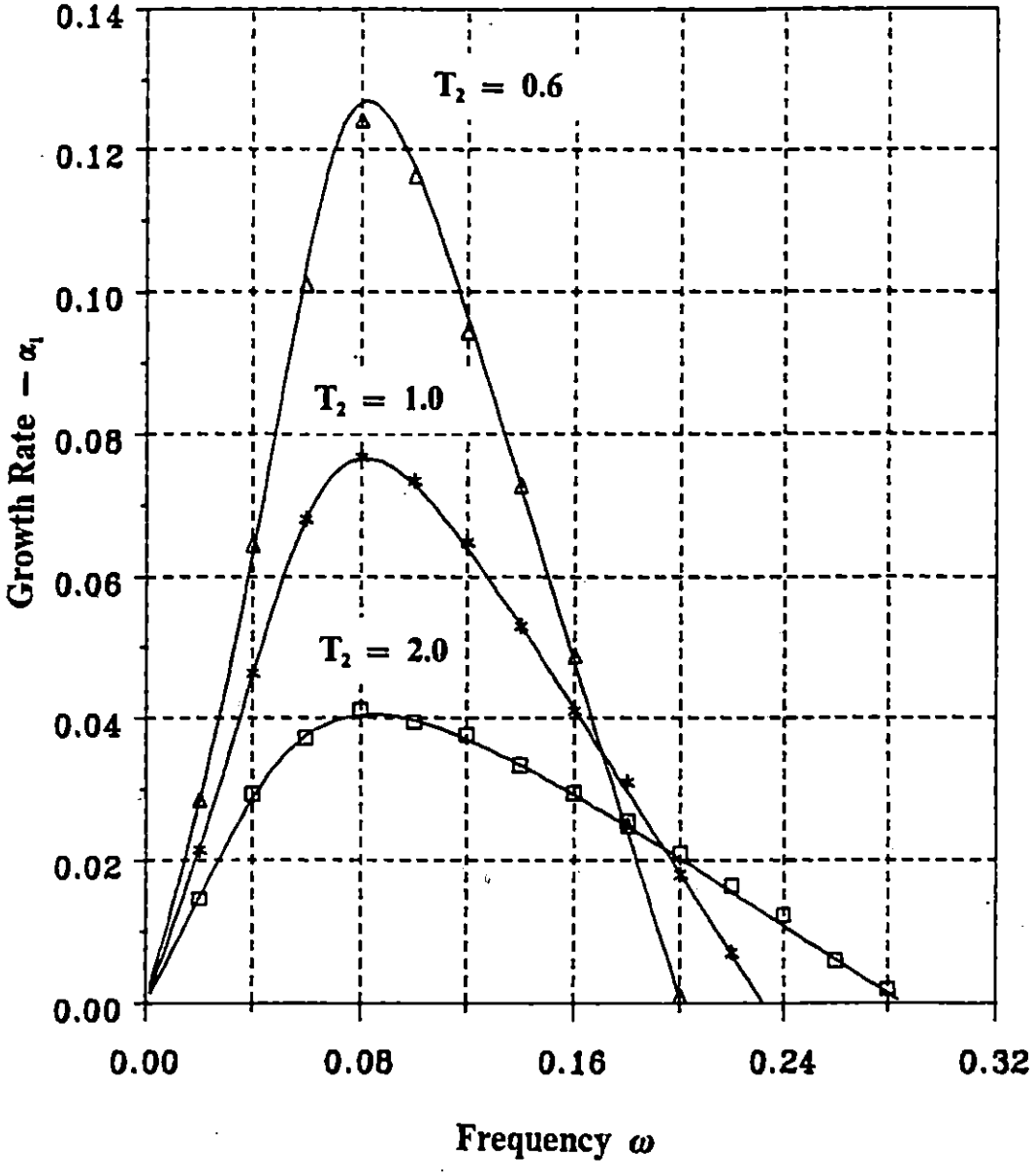

Figure 5.3 A comparison with Gropengiesser's results for various T_2, $M_1 = 0.0$, $U_2 = 0.0$.

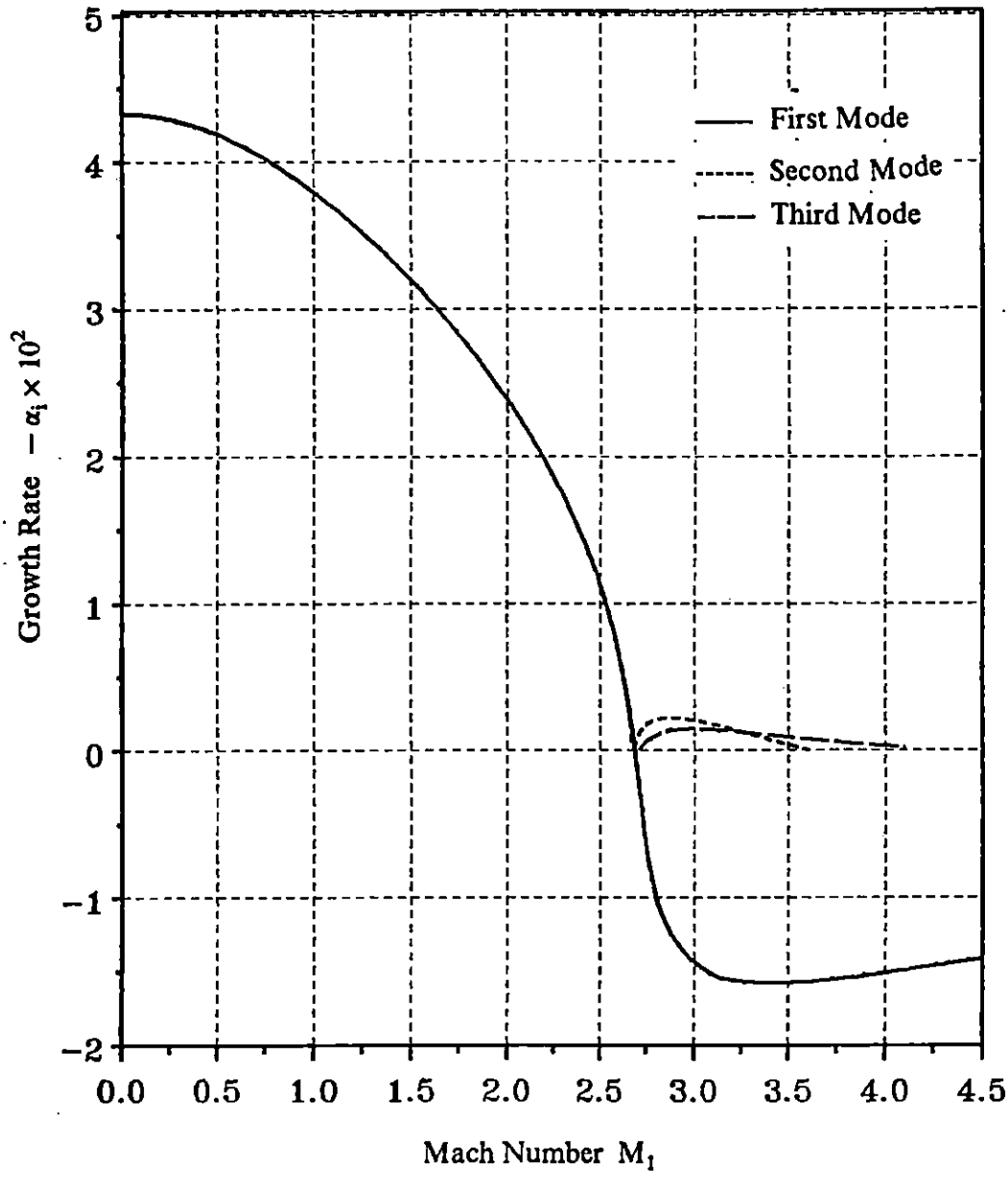

Figure 5.4 The growth rates of 2D viscous disrurbances vs. Mach number at $\omega = 0.1$, $U_2 = 0.4$, $T_2 = 0.6$ and $R = 1000$.

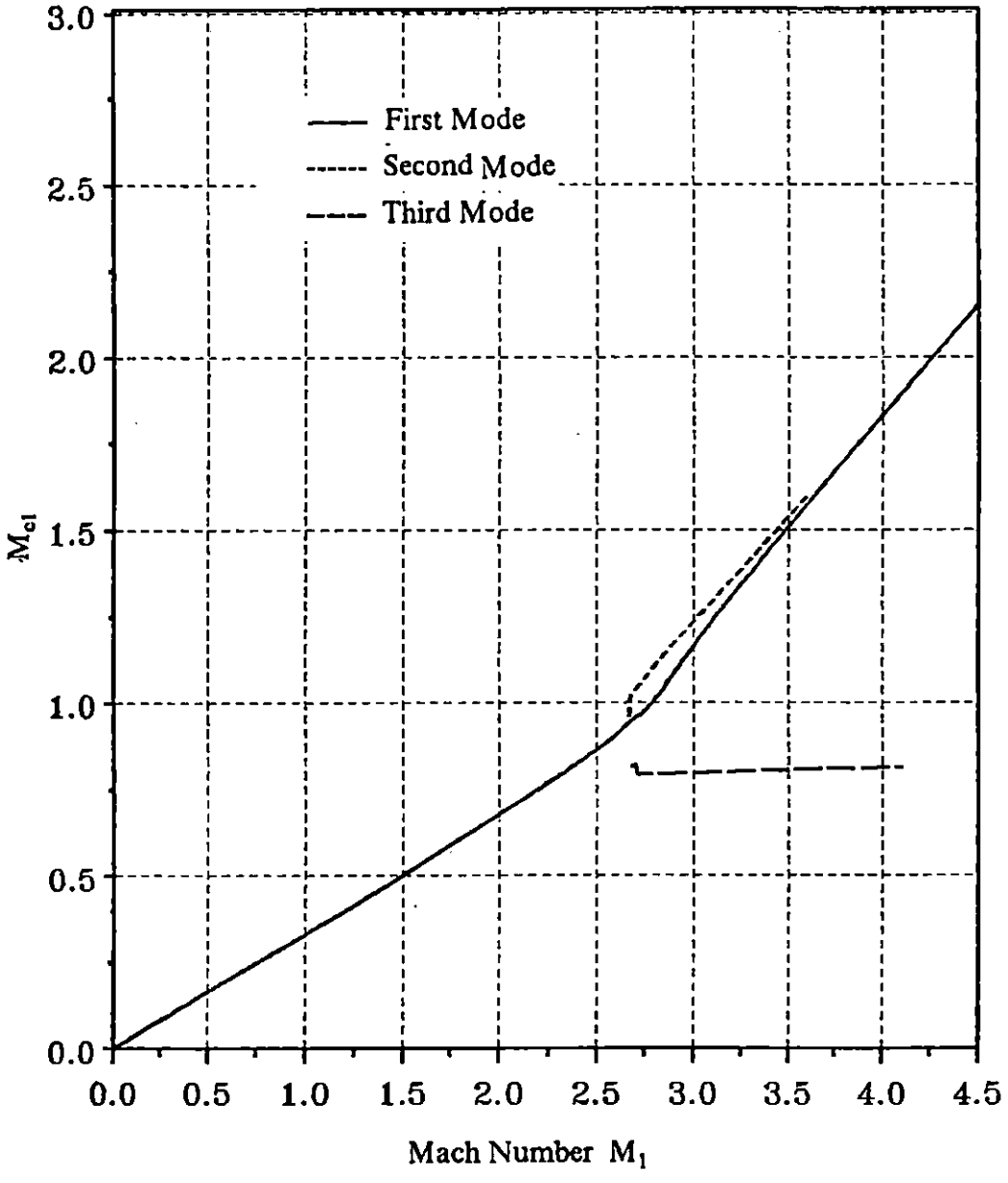

Figure 5.5a The convective Mach number M_{c1} vs. Mach number at $\omega = 0.1$, $U_2 = 0.4$, $T_2 = 0.6$ and $R = 1000$.

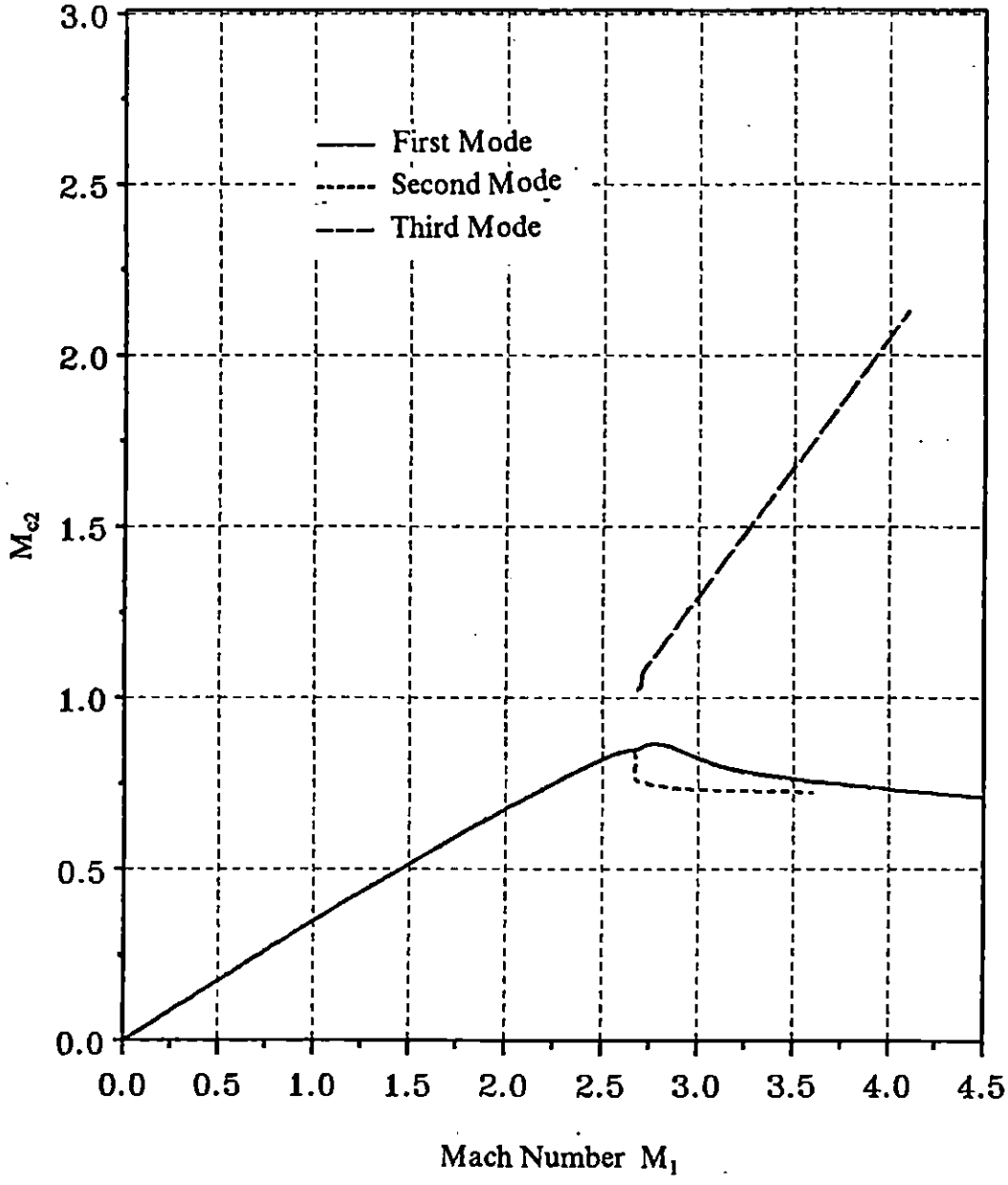

Figure 5.5b The convective Mach number M_{c2} vs. Mach number at $\omega = 0.1$, $U_2 = 0.4$, $T_2 = 0.6$ and $R = 1000$.

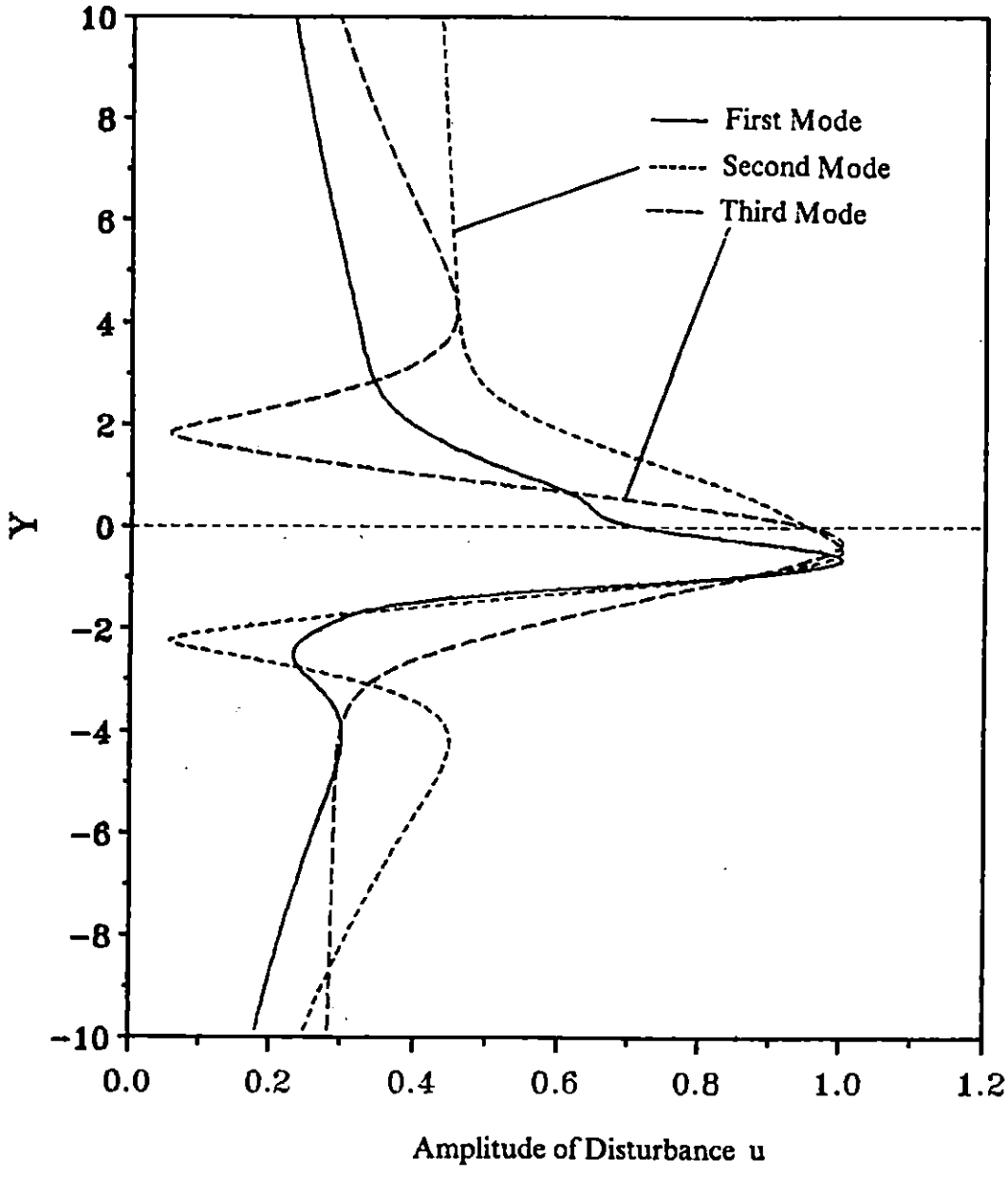

Figure 5.6 The distributions of amplitude of velocity disturbance u-component at $M_1 = 2.9$, $\omega = 0.1$, $U_2 = 0.4$, $T_2 = 0.6$ and $R = 1000$.

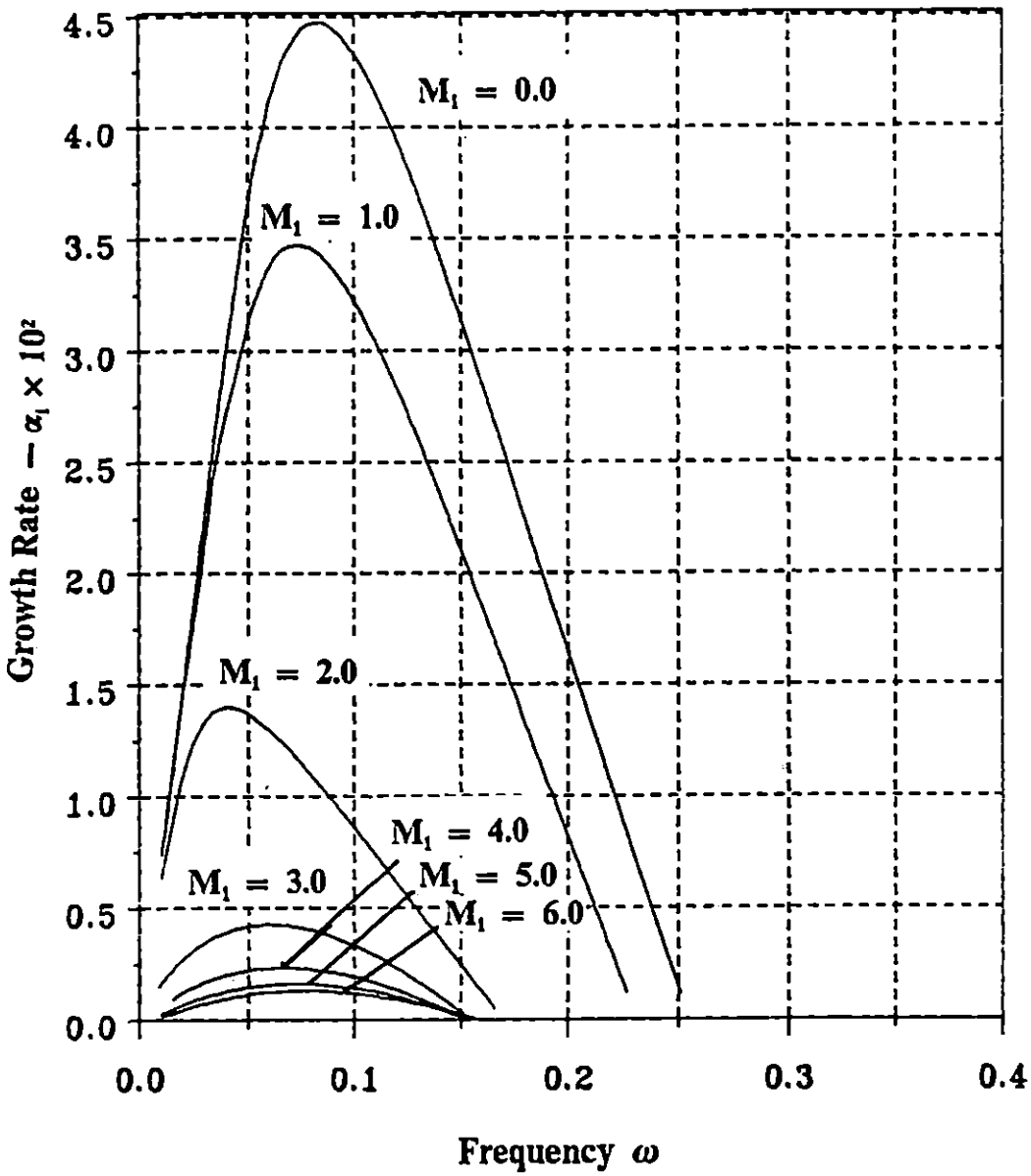

Figure 5.7a The growth rates of 2D inviscid disturbances for various M_1, $U_2 = 0.0$, $T_2 = 2.0$.

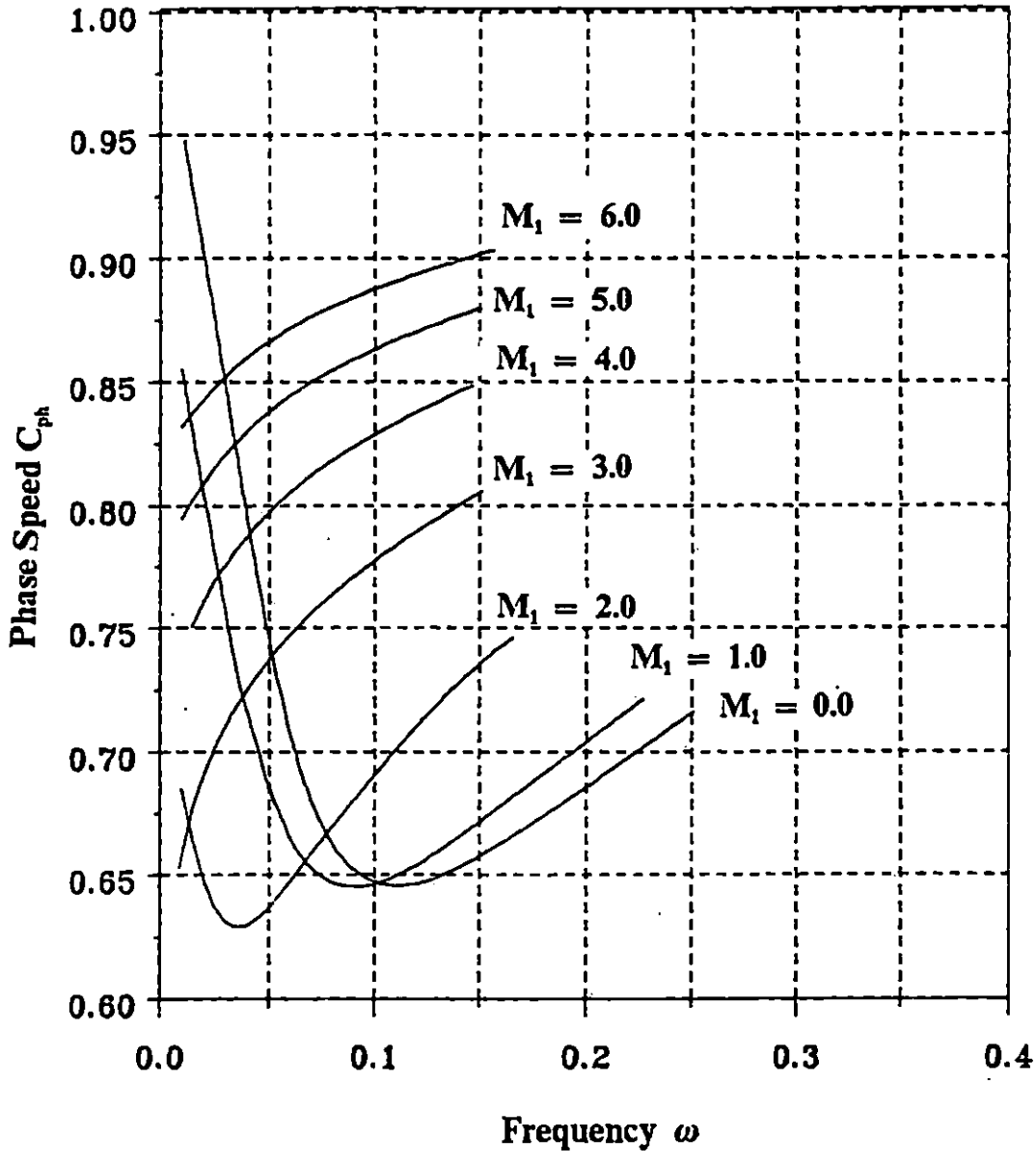

Figure 5.7b The phase speeds of 2D inviscid disturbances for various M_1, $U_2 = 0.0$, $T_2 = 2.0$.

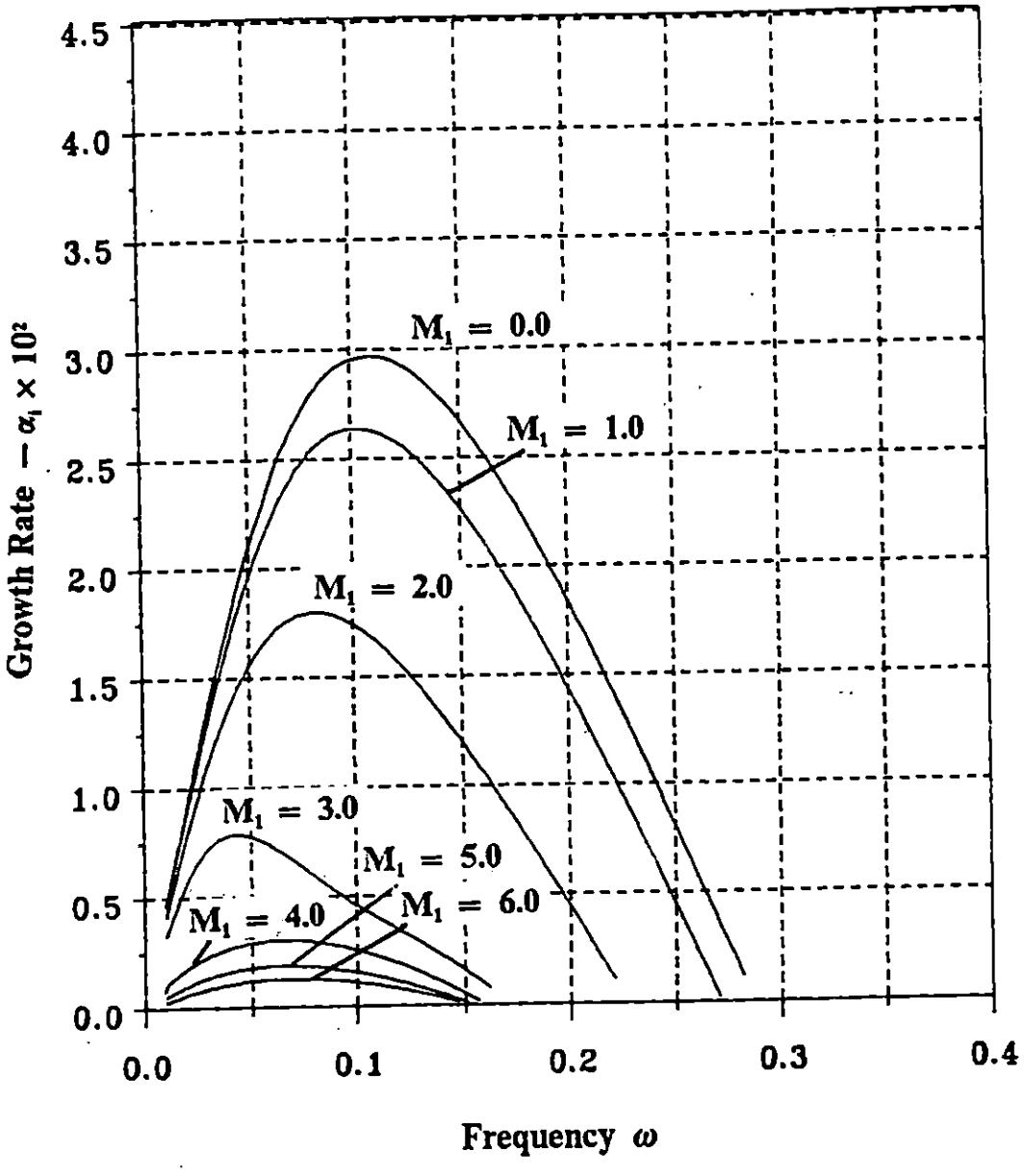

Figure 5.8a The growth rates of 2D inviscid disturbances for various M_1, $U_2 = 0.3$, $T_2 = 2.0$.

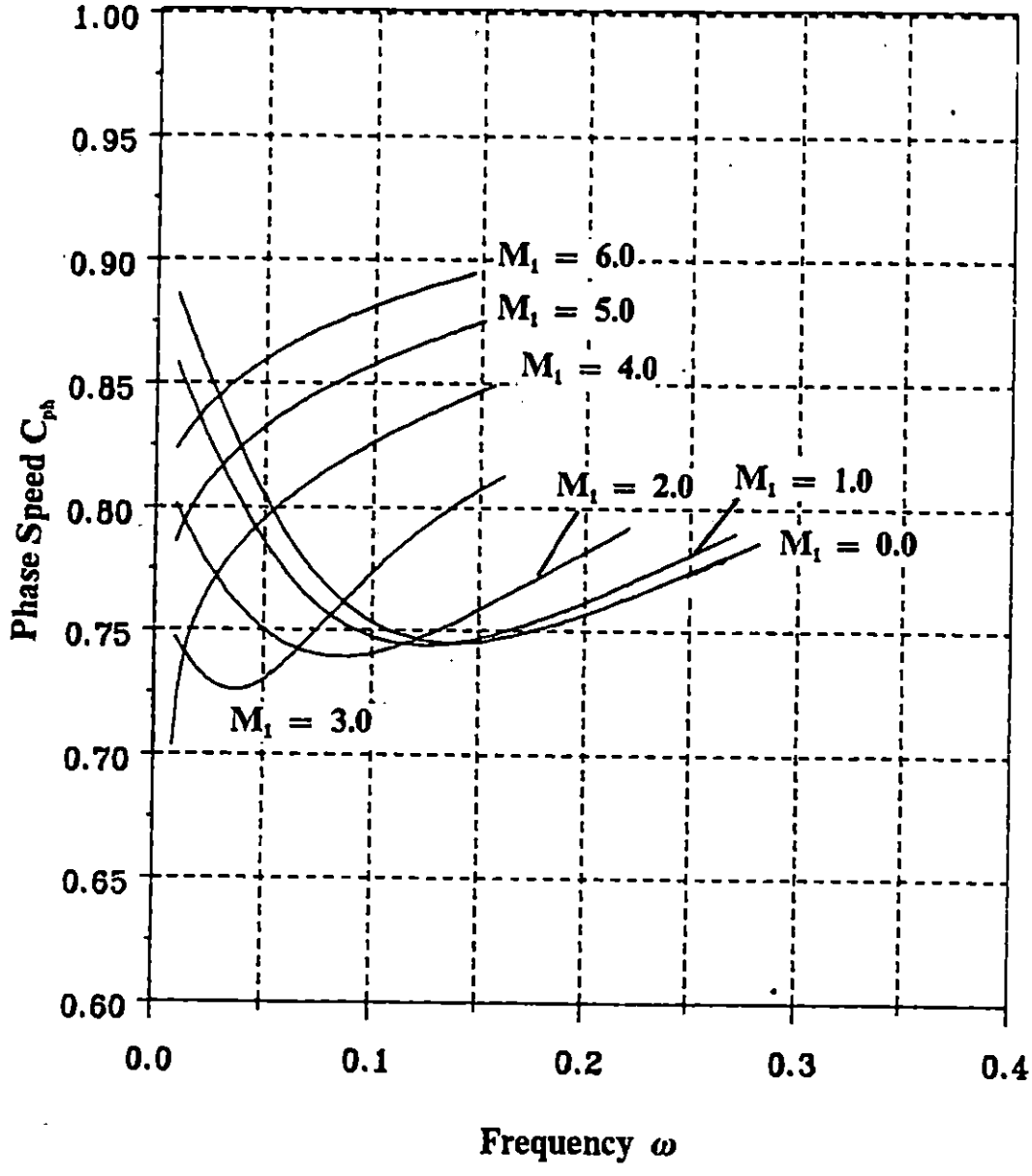

Figure 5.8b The phase speeds of 2D inviscid disturbances for various M_1, $U_2 = 0.3$, $T_2 = 2.0$.

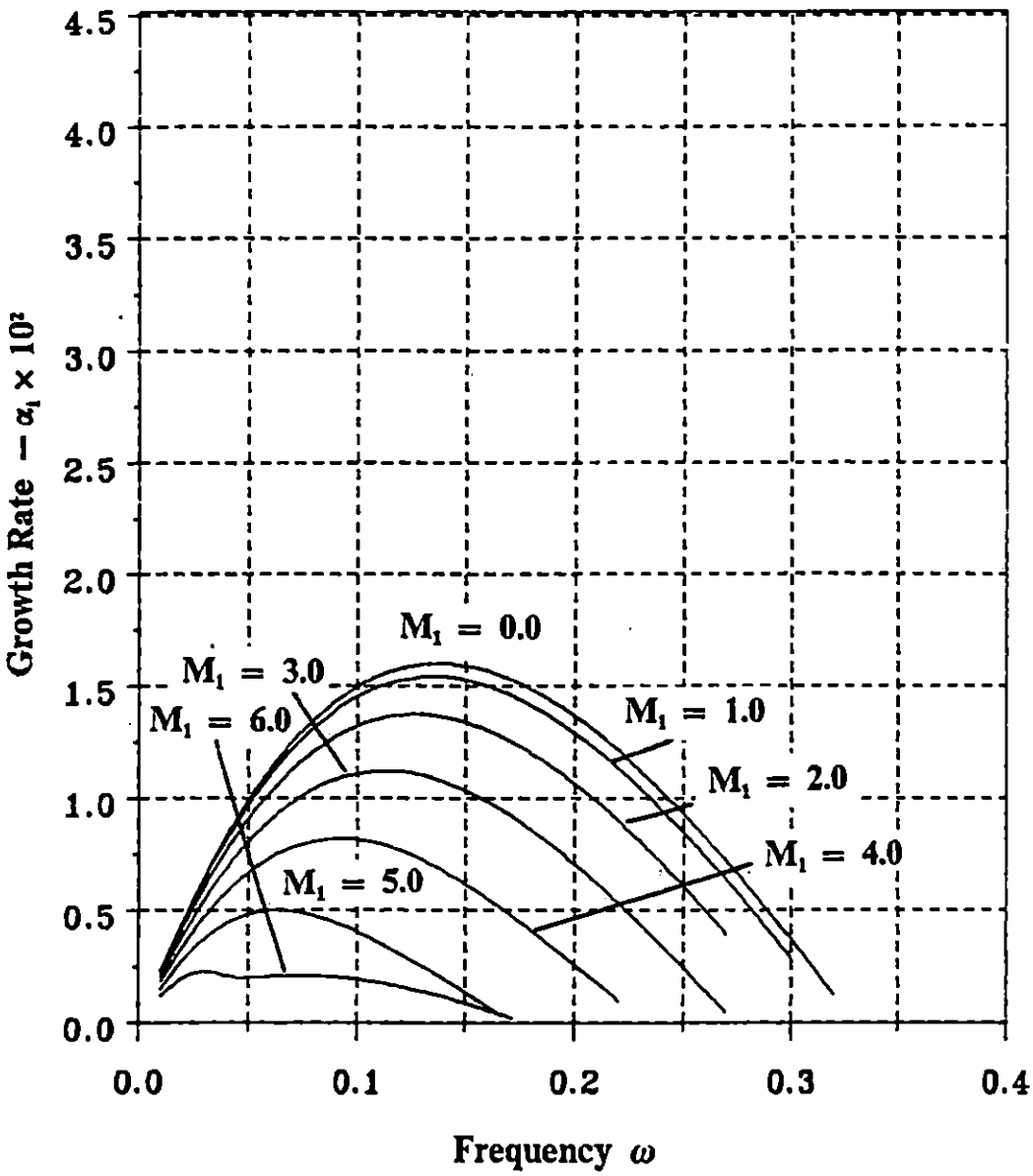

Figure 5.9a The growth rates of 2D inviscid disturbances for various M_1, $U_2 = 0.6$, $T_2 = 2.0$.

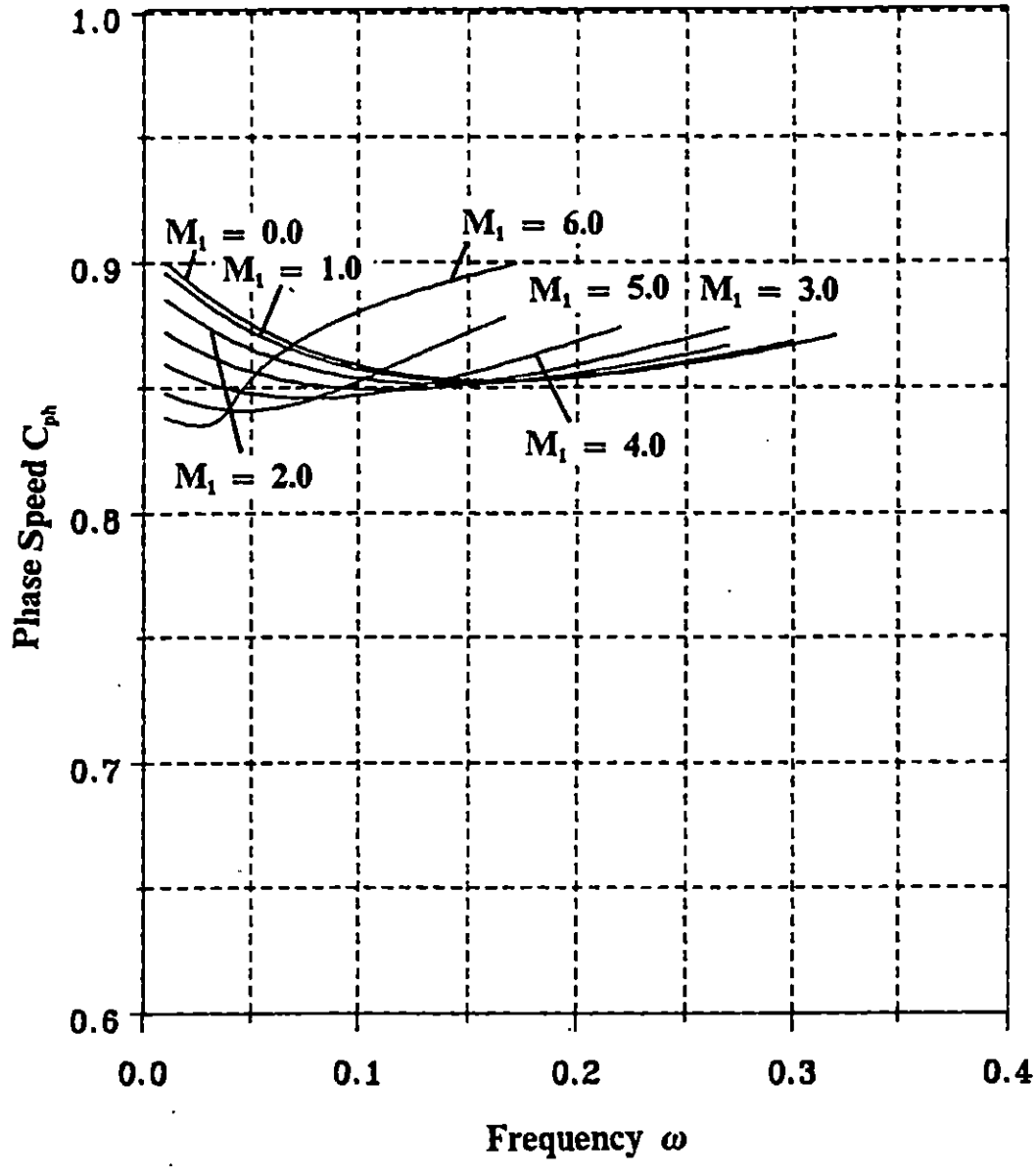

Figure 5.9b The phase speeds of 2D inviscid disturbances for various M_1, $U_2 = 0.6$, $T_2 = 2.0$.

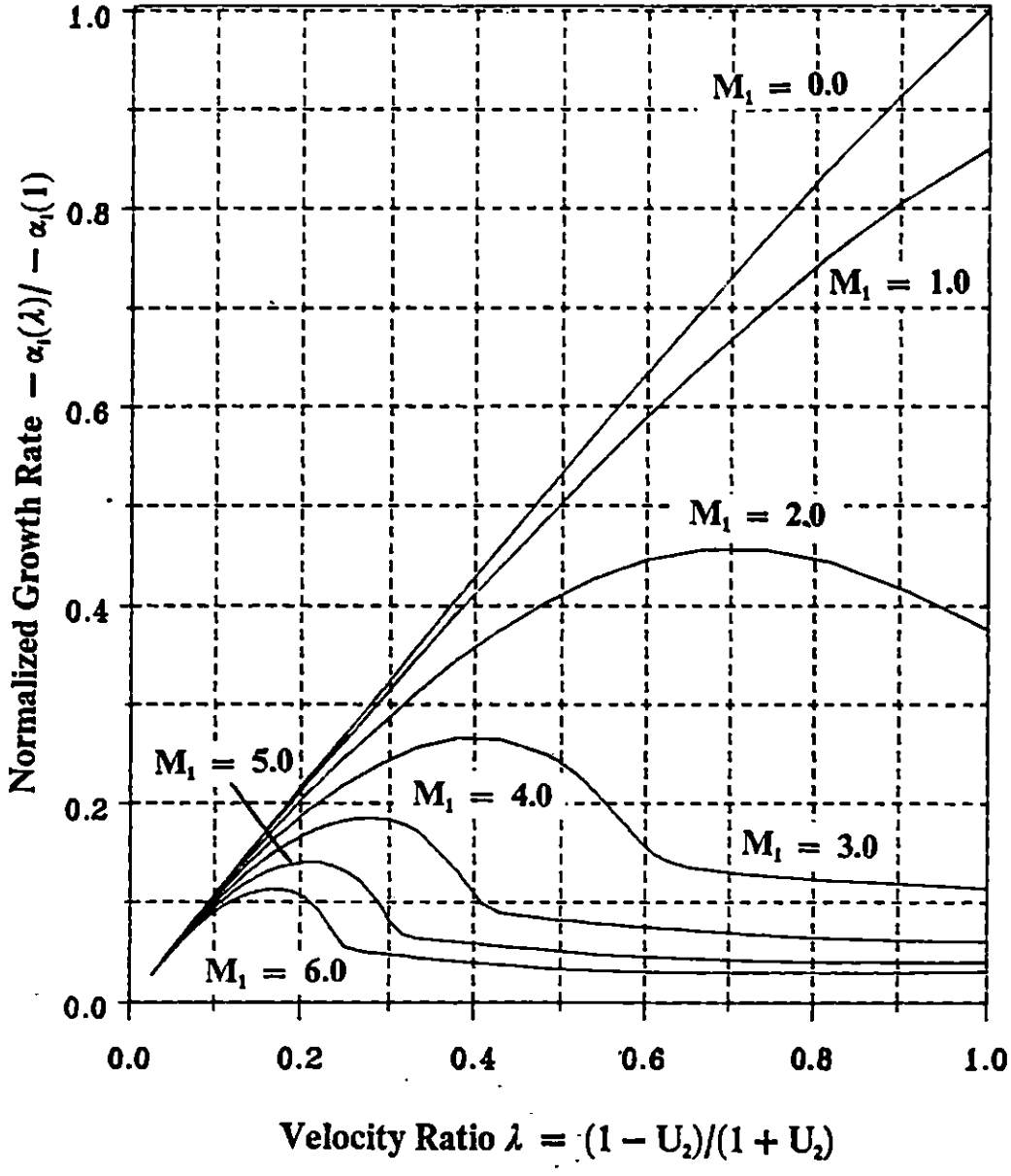

Figure 5.10a The normalized growth rates of 2D inviscid disturbances for various M_1, $T_2 = 2.0, \omega = 0.05$.

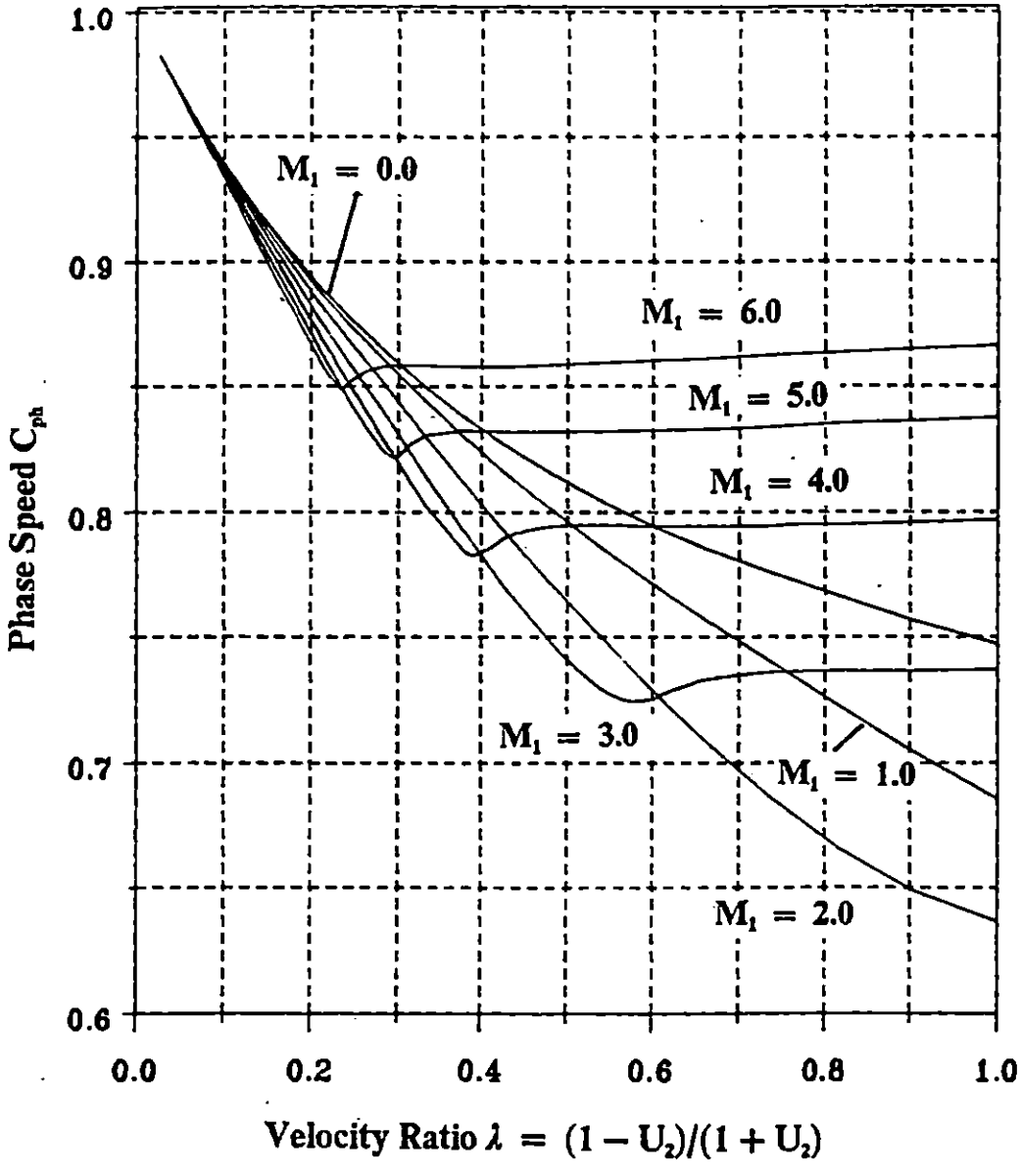

Figure 5.10b The phase speeds of 2D inviscid disturbances for various M_1, $T_2 = 2.0, \omega = 0.05$.

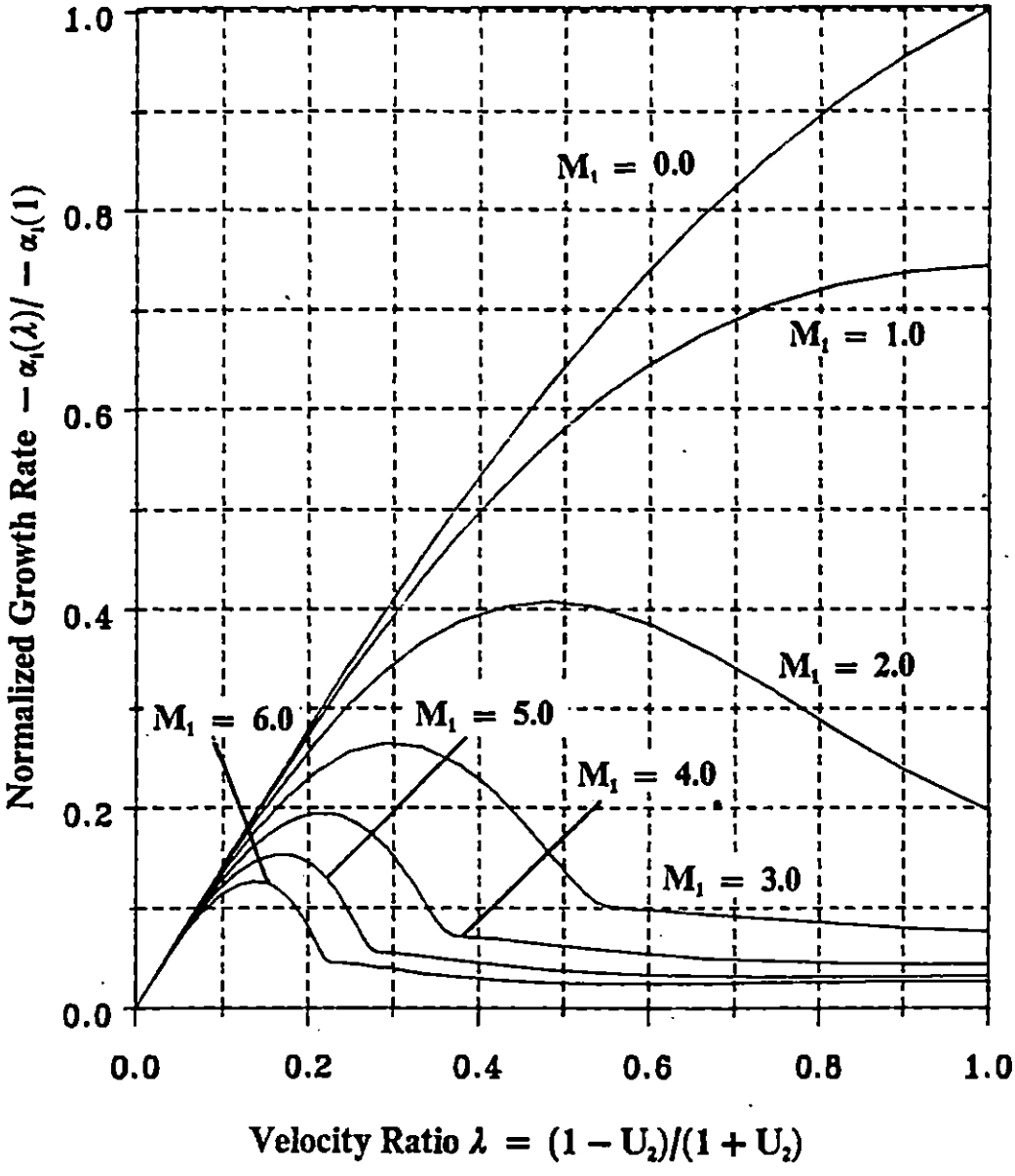

Figure 5.11a The normalized growth rates of 2D inviscid disturbances for various M_1 $T_2 = 2.0, \omega = 0.10$.

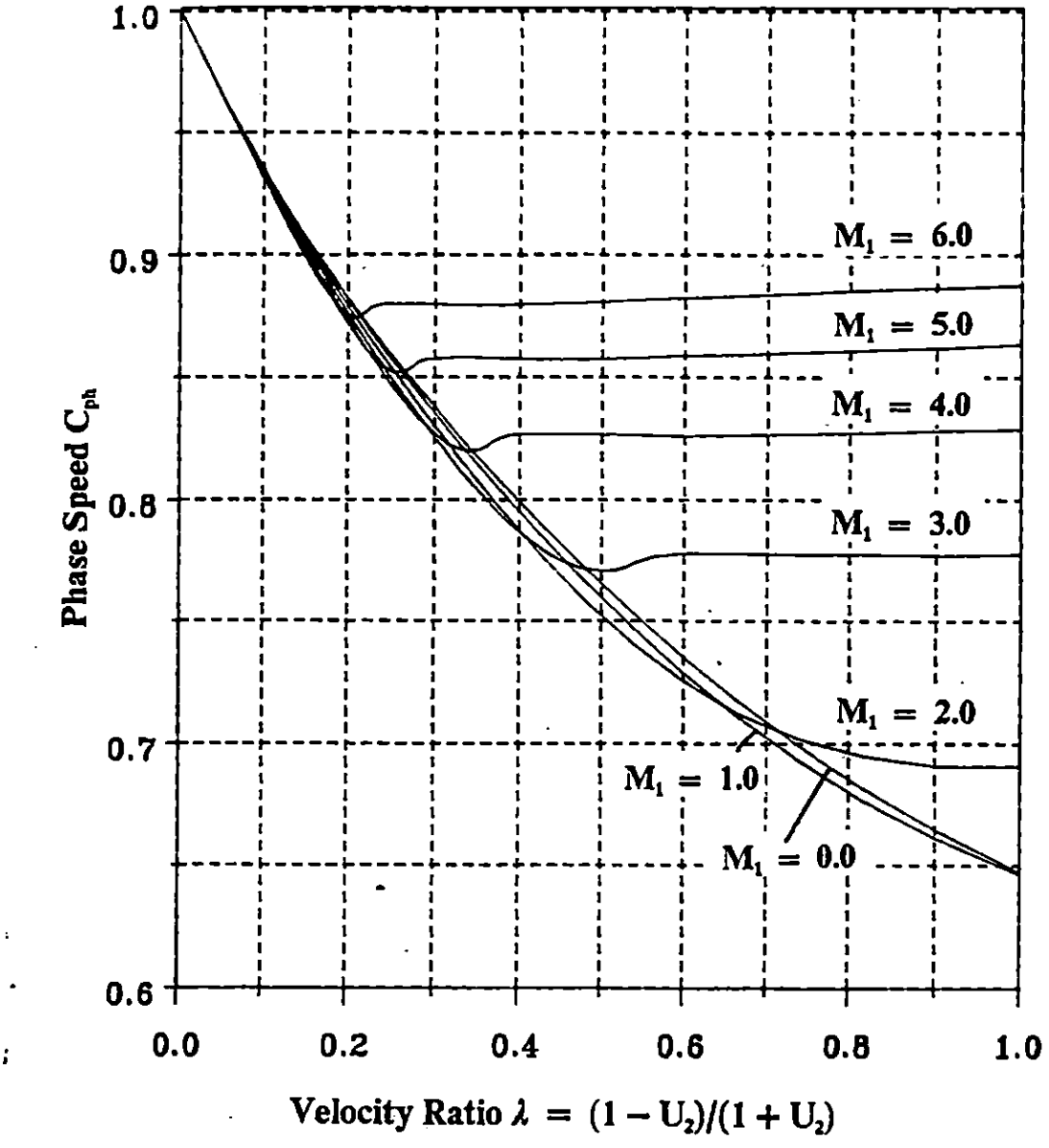

Figure 5.11b The phase speeds of 2D inviscid disturbances for various M_1, $T_2 = 2.0, \omega = 0.10$.

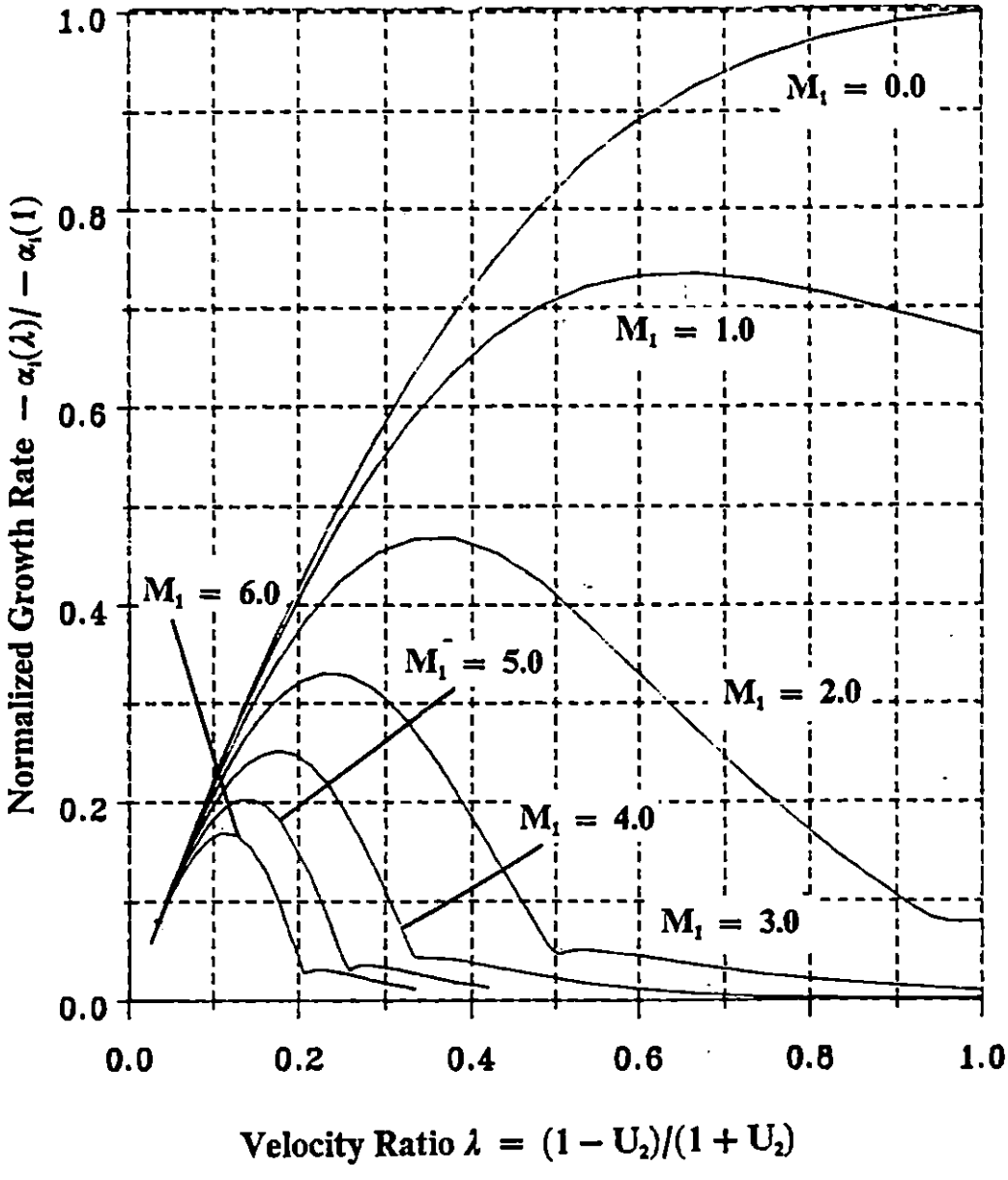

Figure 5.12a The normalized growth rates of 2D inviscid disturbances for various M_1, $T_2 = 2.0, \omega = 0.15$.

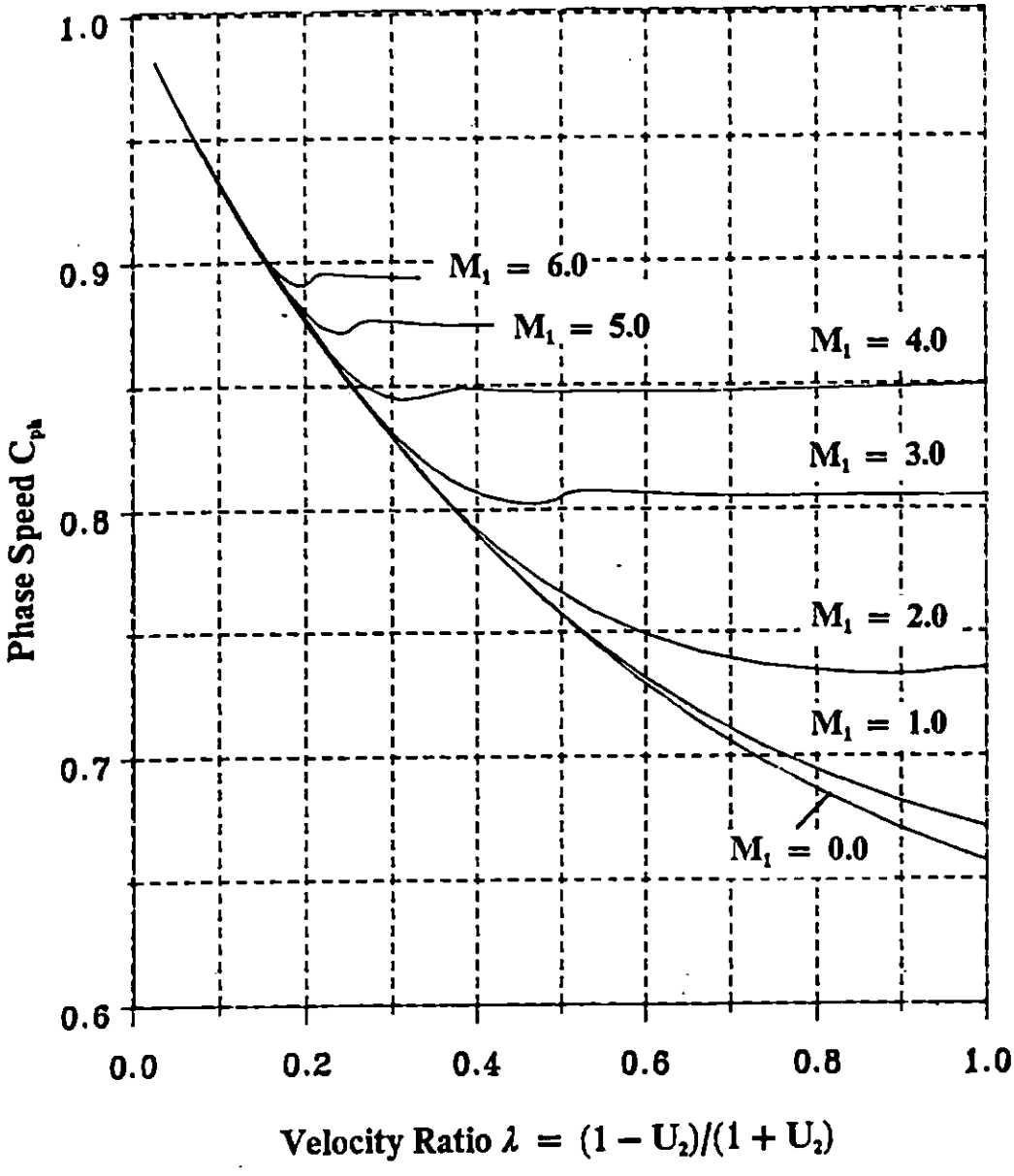

Figure 5.12b The phase speeds of 2D inviscid disturbances for various M_1, $T_2 = 2.0, \omega = 0.15$.

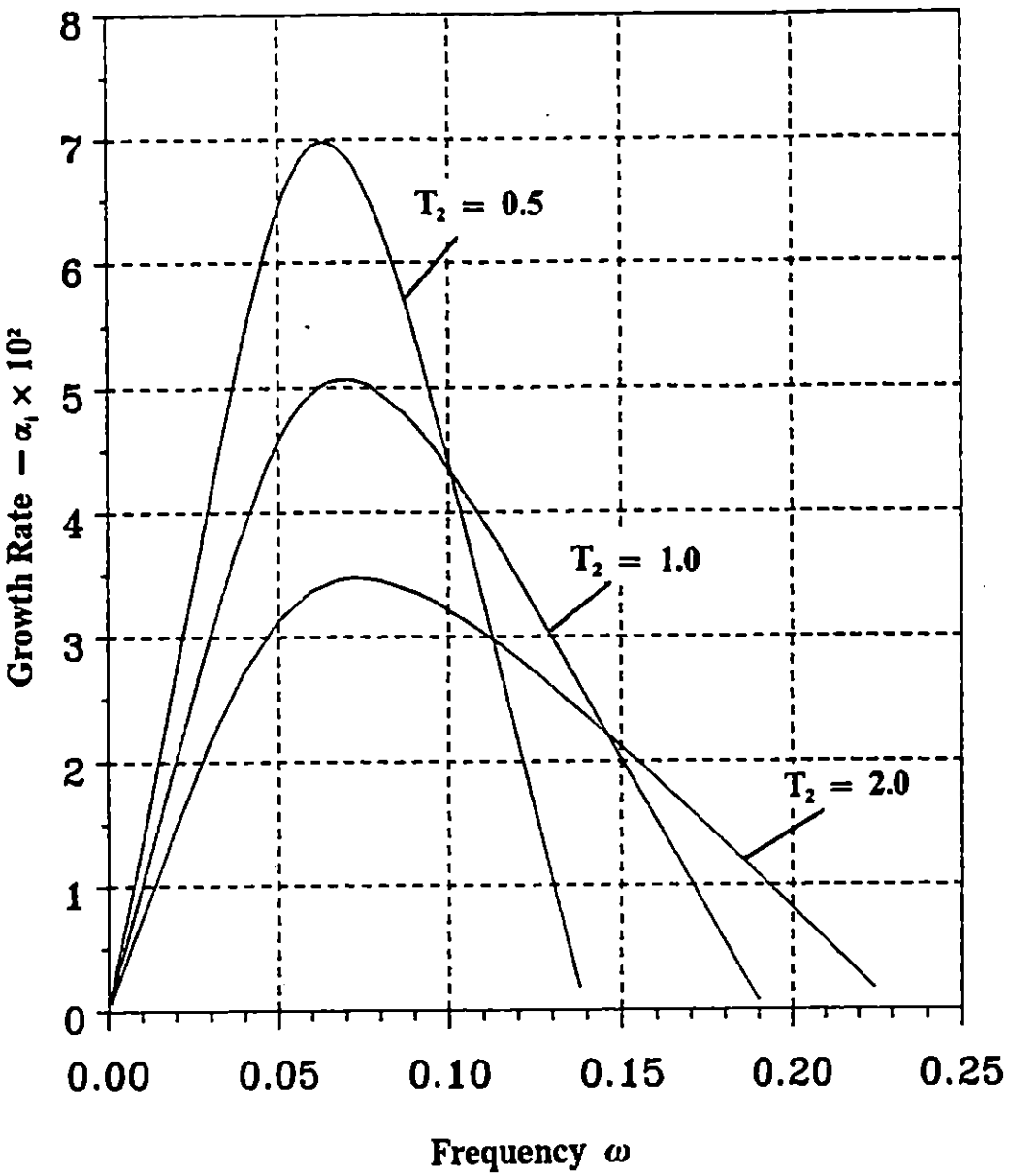

Figure 5.13a The growth rates of 2D inviscid disturbances for various T_2, $M_1 = 1.0$, $U_2 = 0.0$.

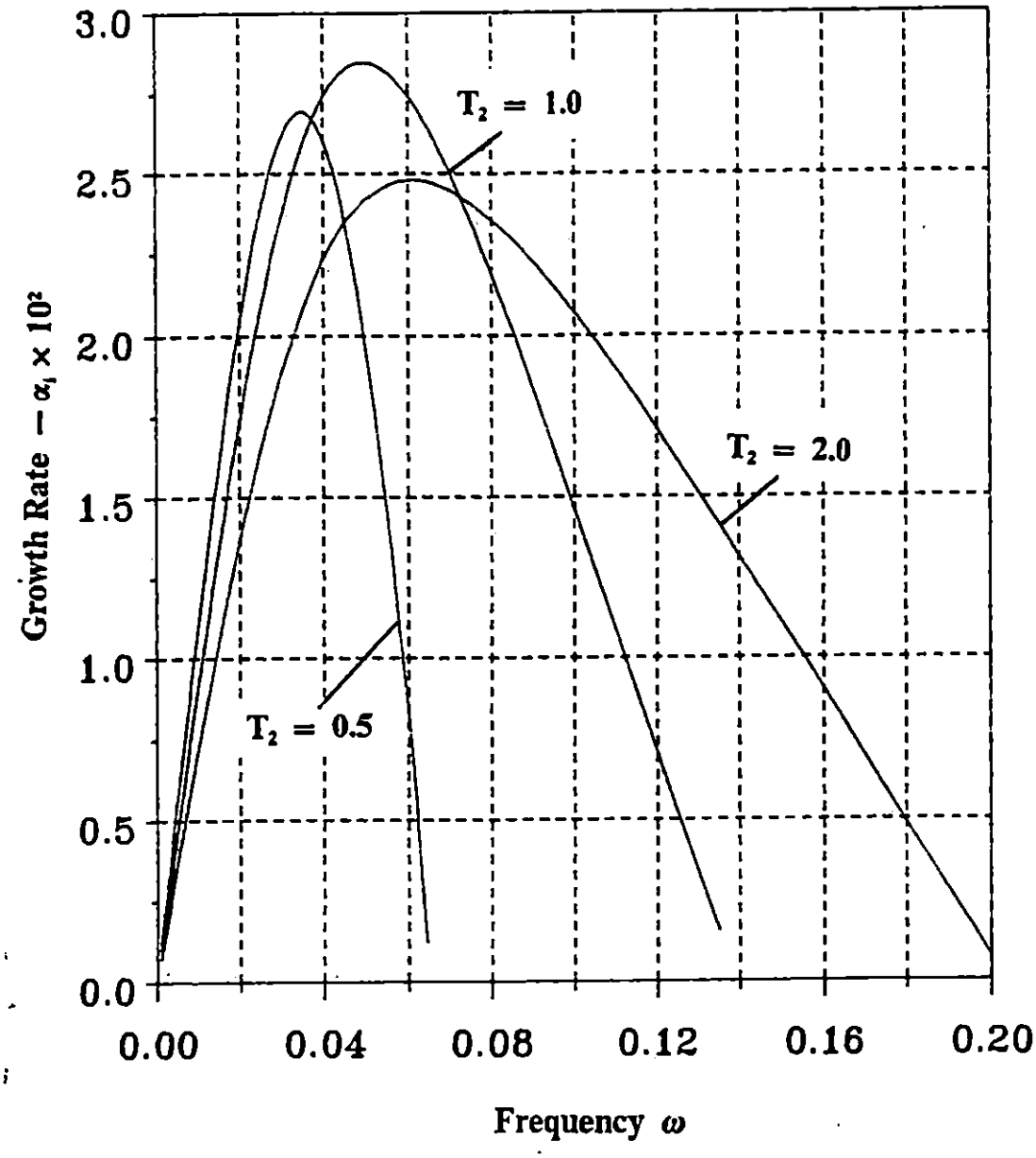

Figure 5.13b The growth rates of 2D inviscid disturbances for various T_2, $M_1 = 1.5, U_2 = 0.0$.

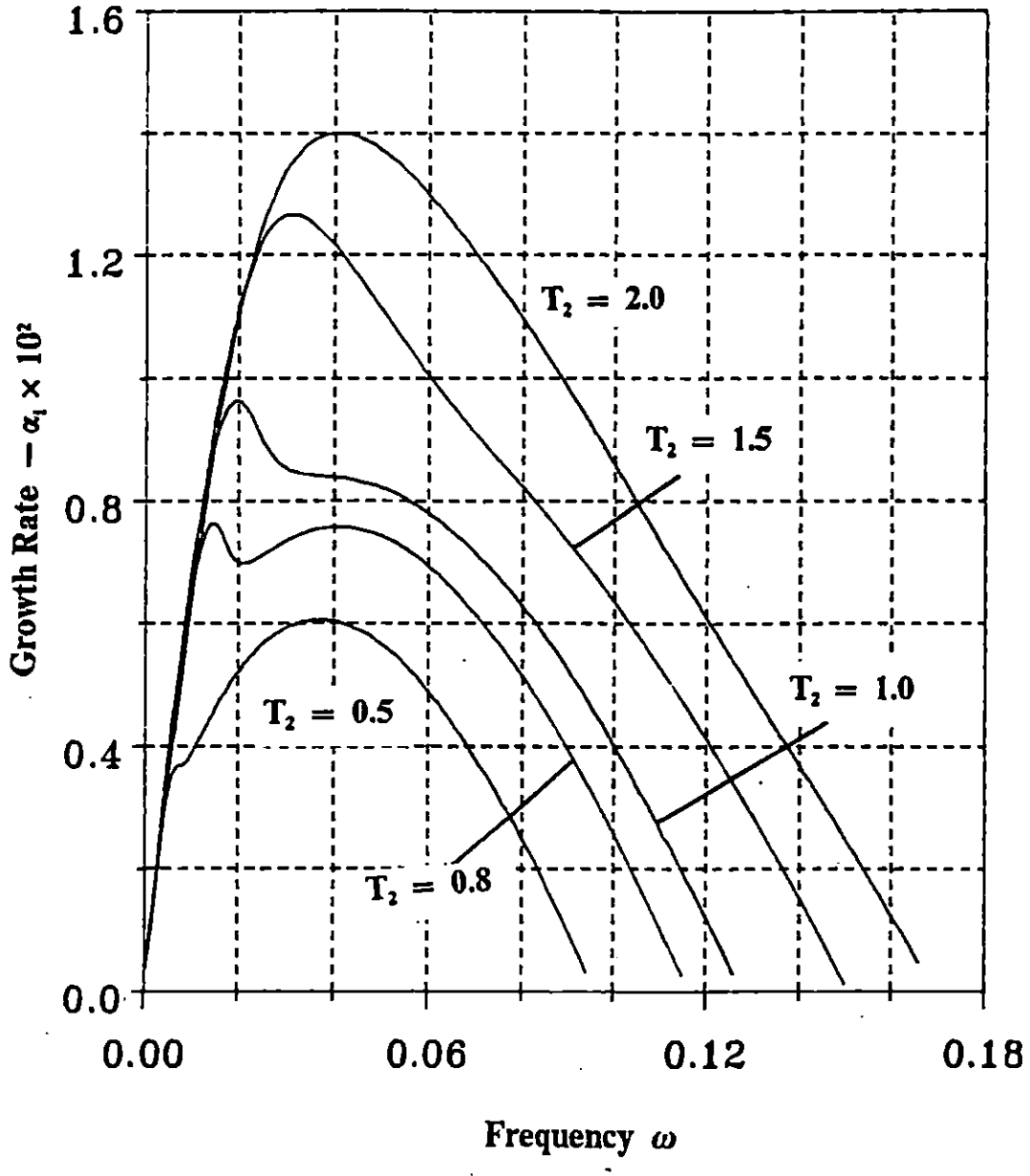

Figure 5.13c The growth rates of 2D inviscid disturbances for various T_2, $M_1 = 2.0$, $U_2 = 0.0$. $T_2 = 0.5$, 0.8 and 1.0 are fast modes.

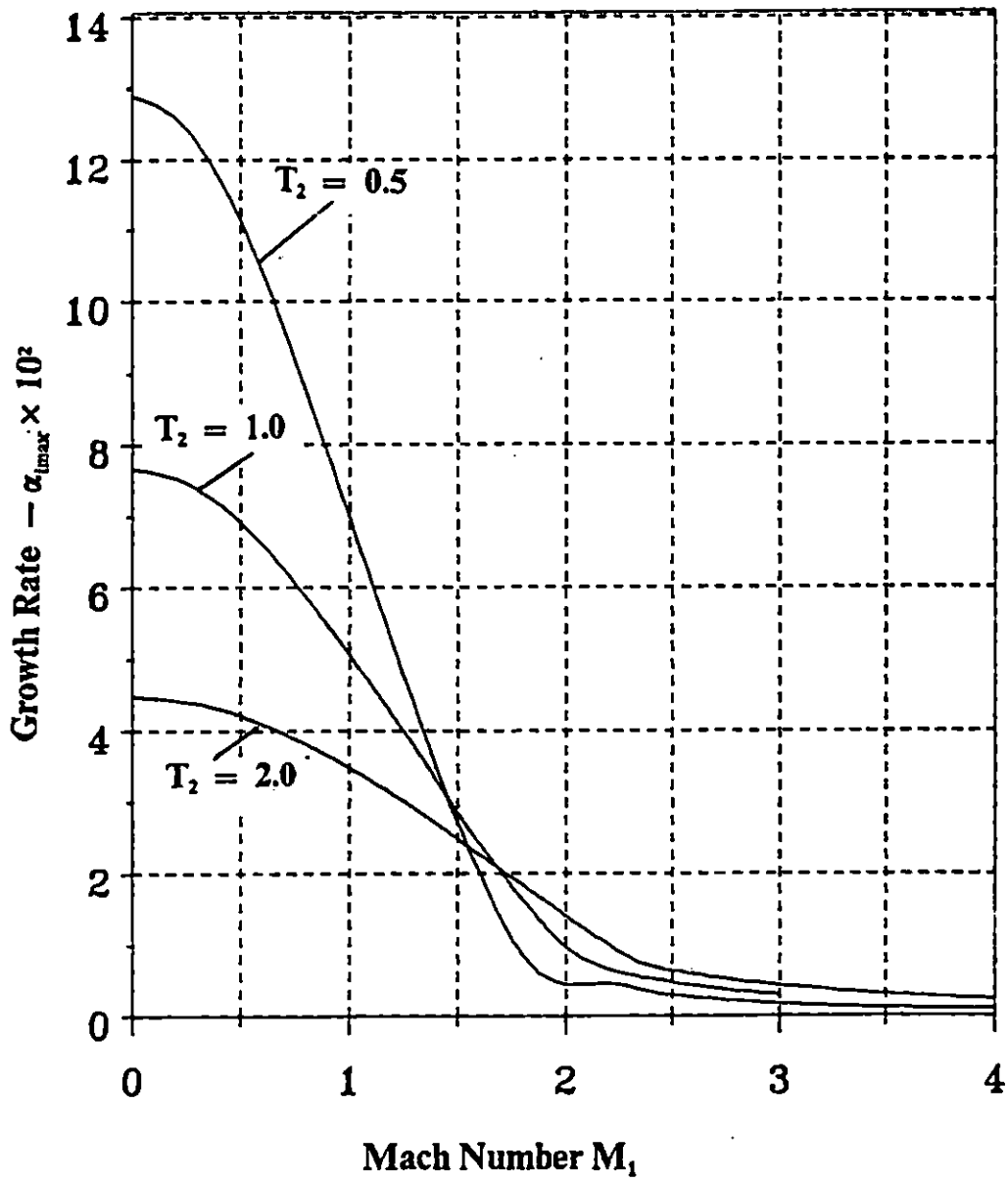

Figure 5.14 The maximum growth rates against Mach number M_1 for different T_2, (The first mode).

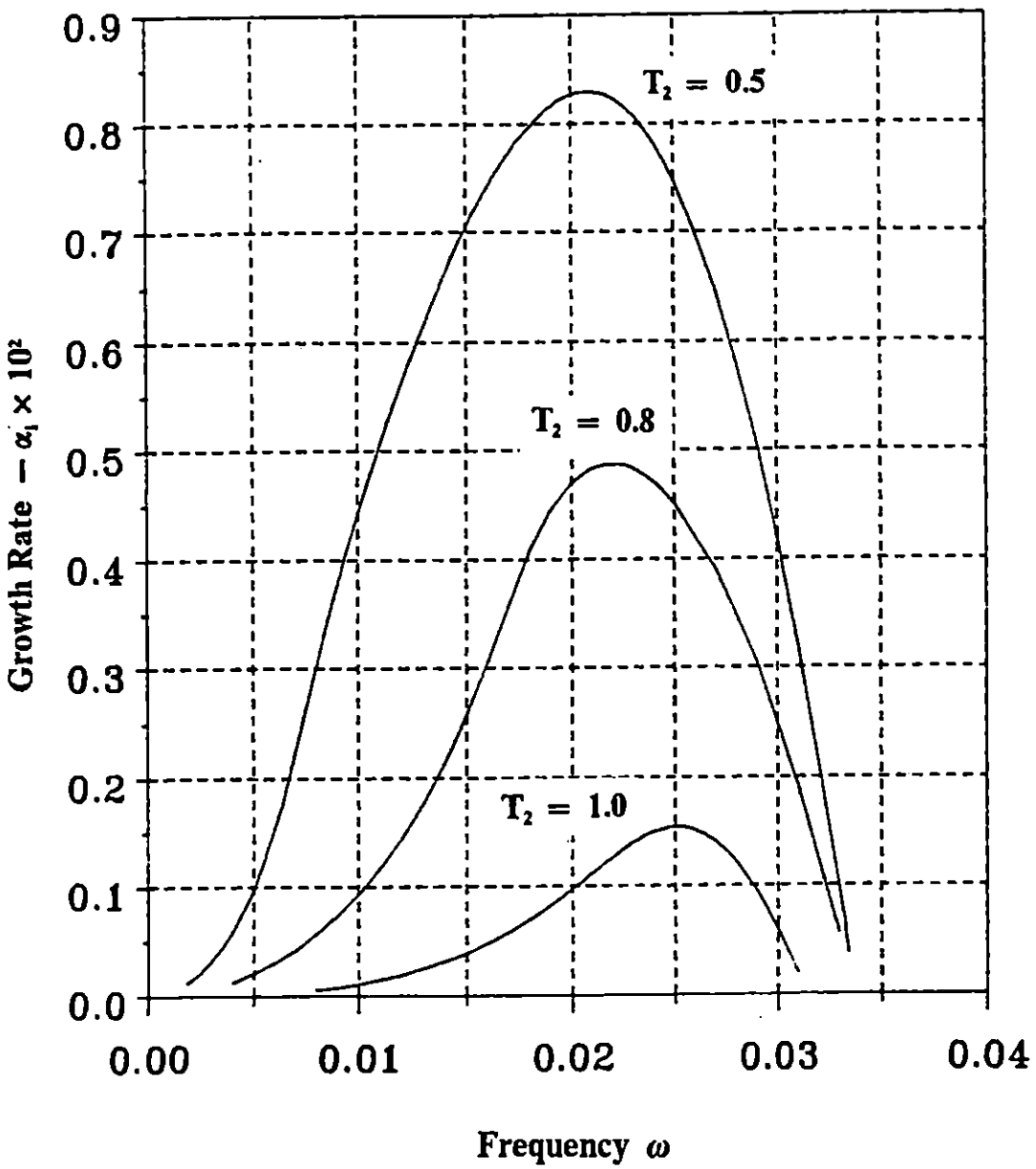

Figure 5.15 The growth rates of 2D inviscid disturbances for various T_2, $M_1 = 2.0, U_2 = 0.0$. (slow mode).

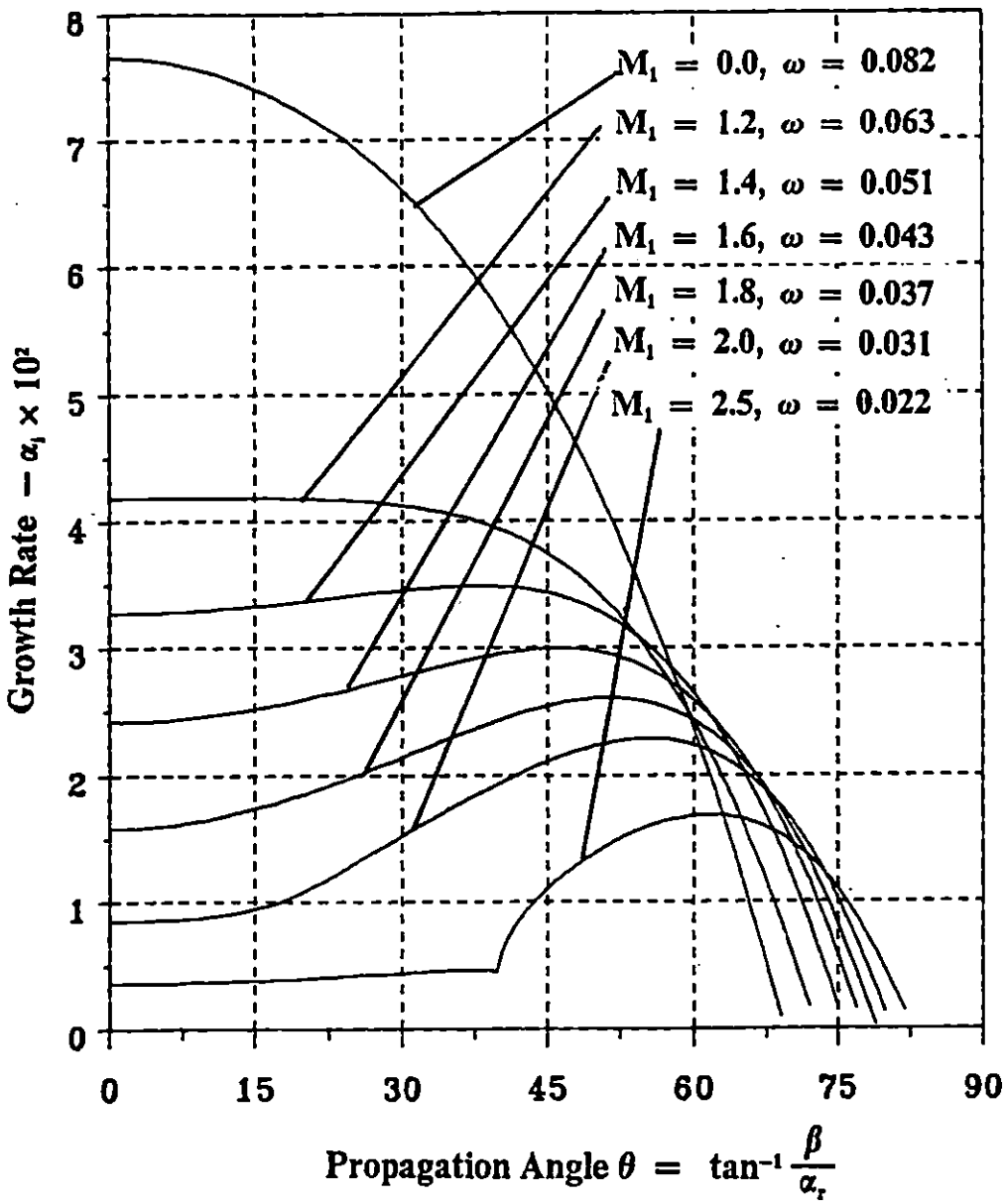

Figure 5.16 The growth rates of oblique waves for various M_1, $U_2 = 0.0$, $T_2 = 1.0$.

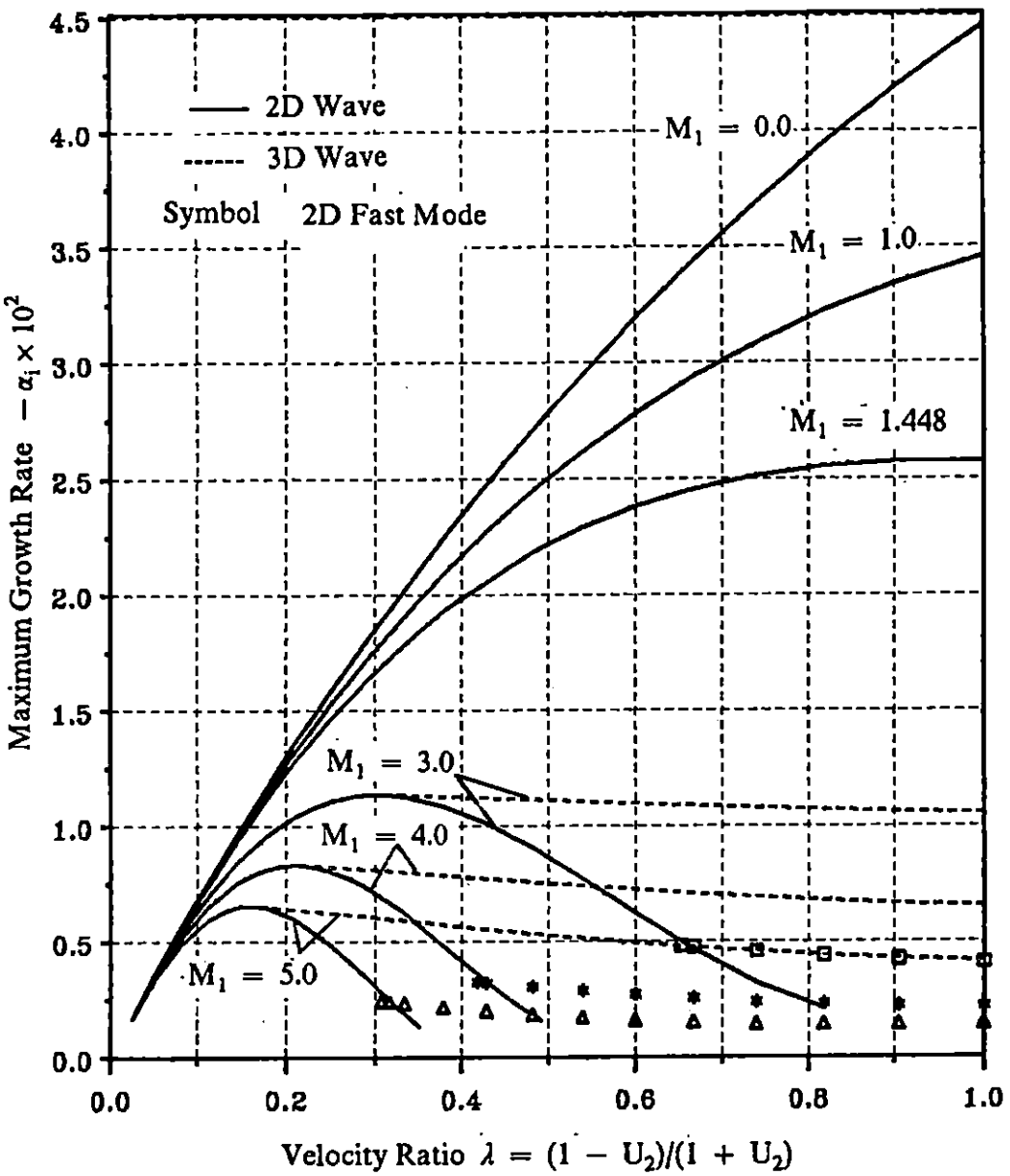

Figure 5.17 The maximum growth rates of 2D waves and oblique waves for various M_1, R = 2000.0, T_2 = 2.0.

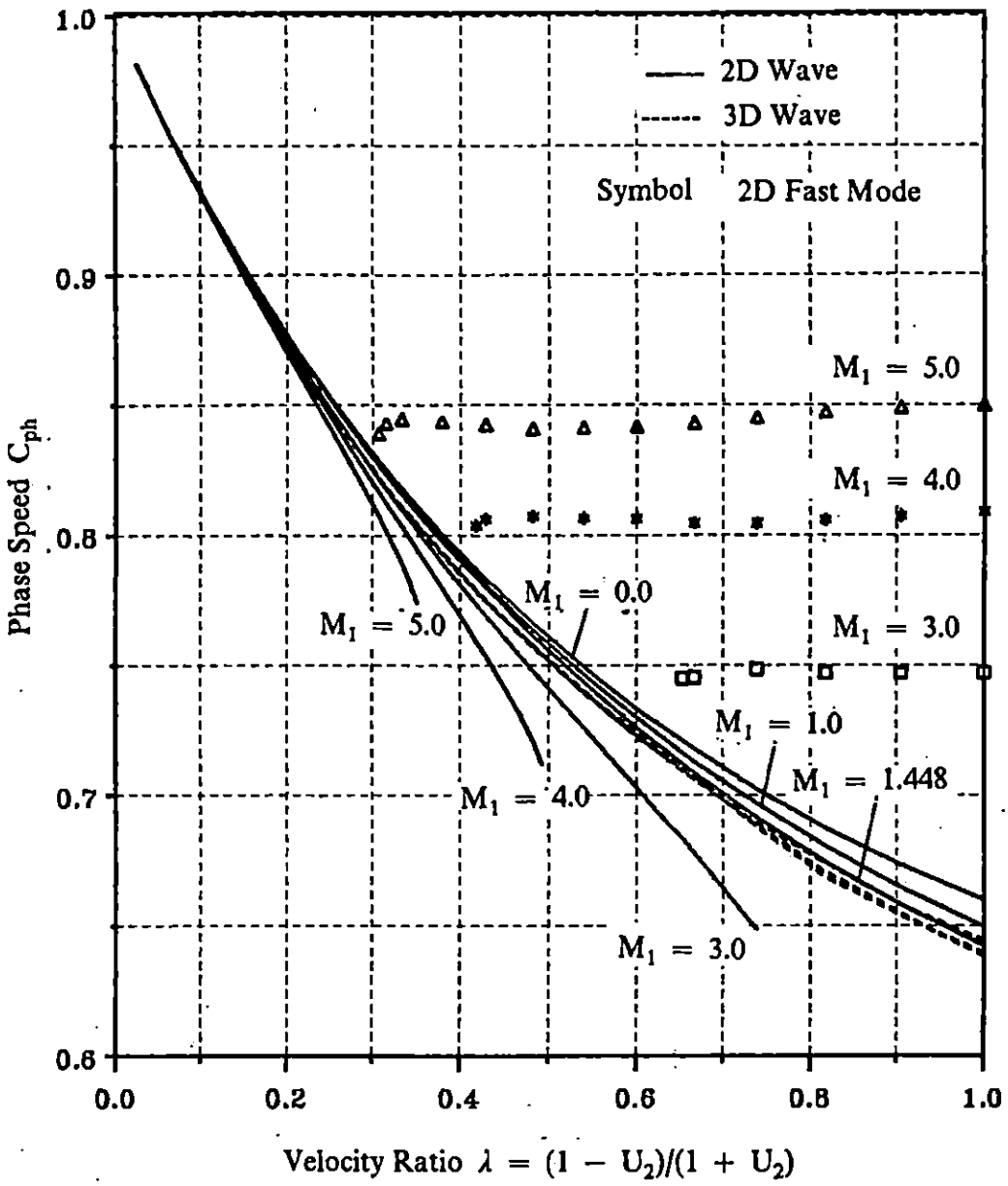

Figure 5.18 The phase speeds of 2D waves and oblique waves for various M_1, R = 2000.0, T_2 = 2.0.

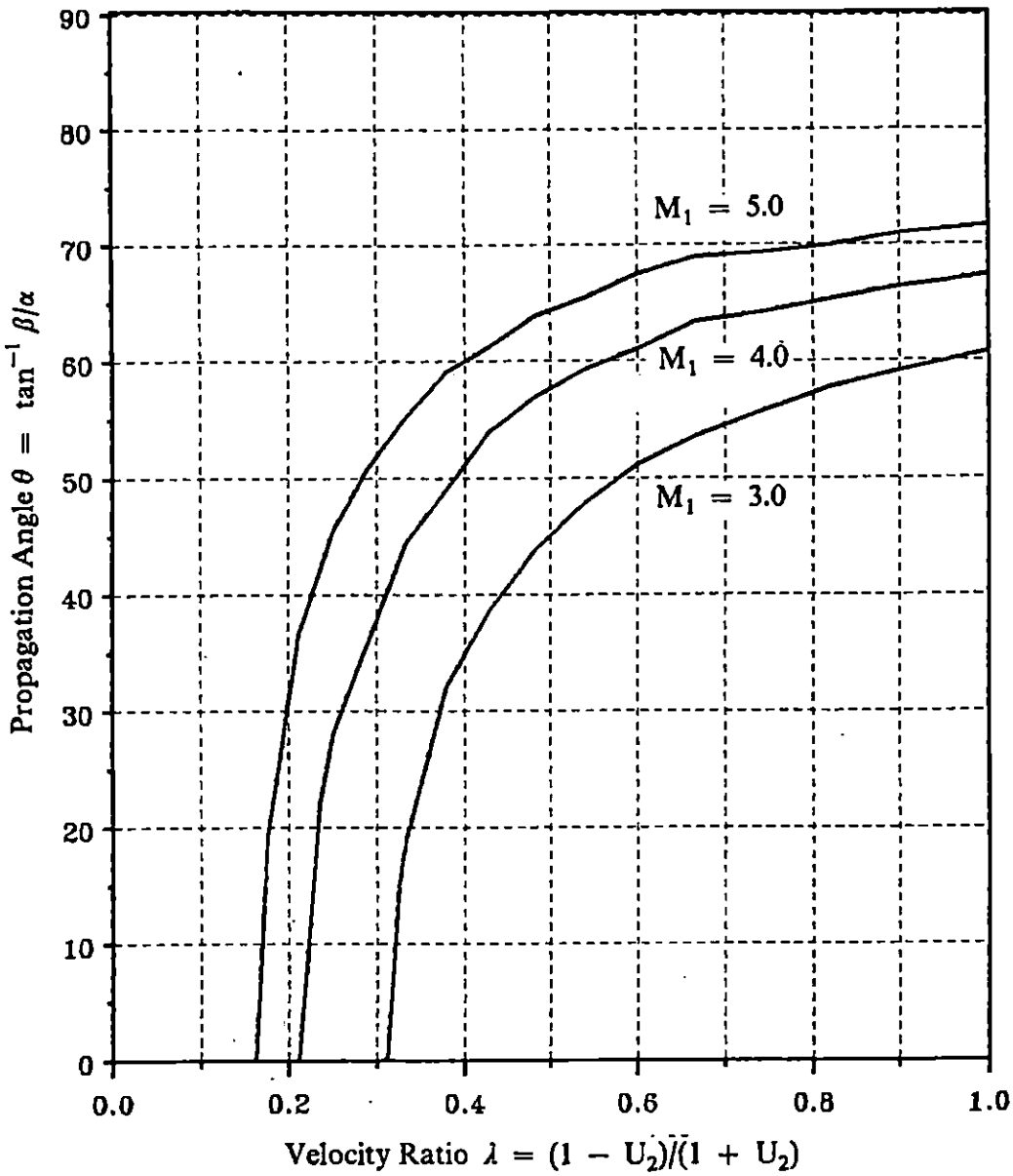

Figure 5.19 The Propagation angles of the most amplified oblique waves for various M_1, R = 2000.0, T_2 = 2.0.

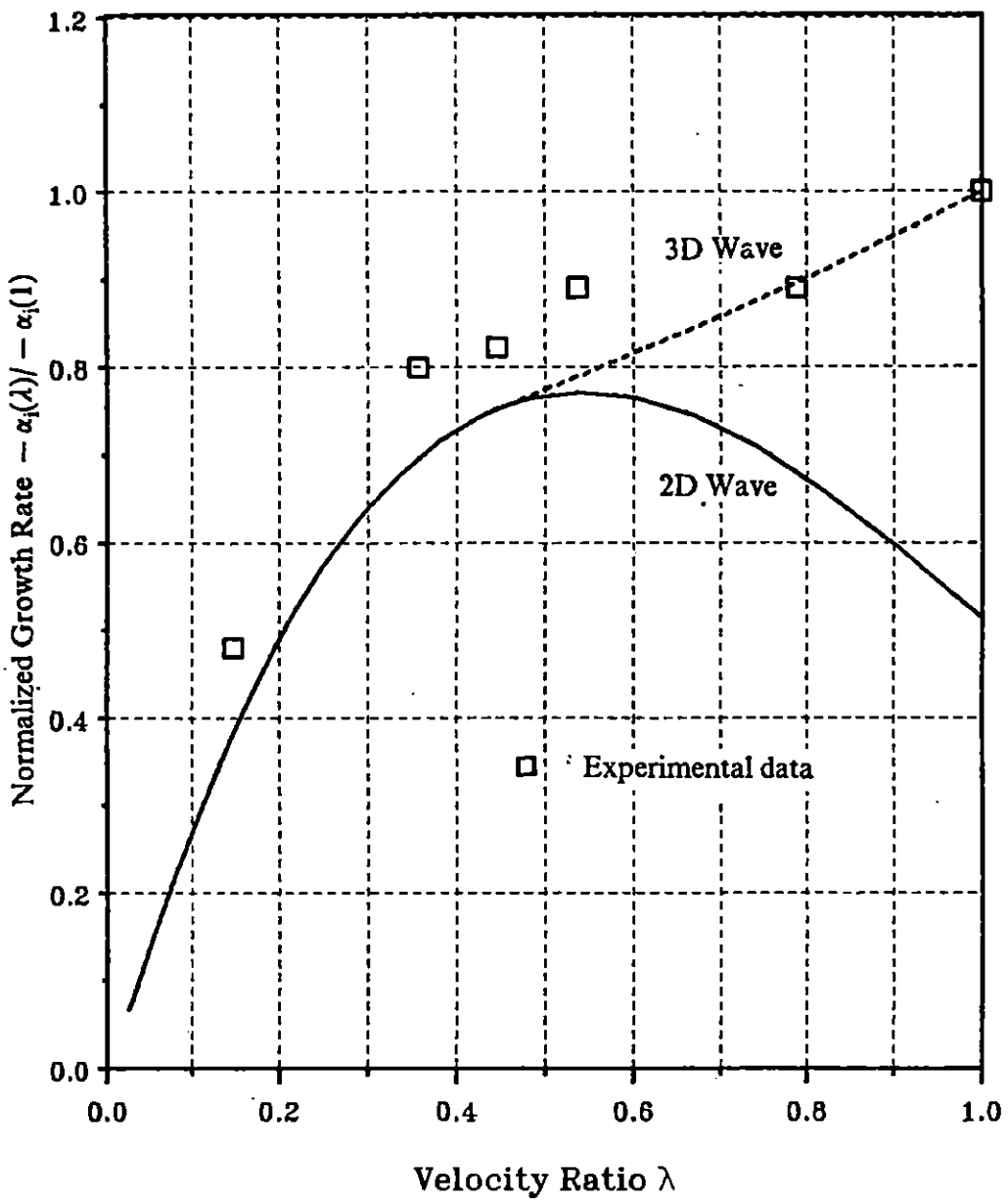

Figure 5.20 A comparison with Chinzei et. al. experiments; ω = most amplified frequency, $M_j = 2.3$, $U_o = 0.5(1 + \tanh y)$, $T_{o1} = T_{o2}$.

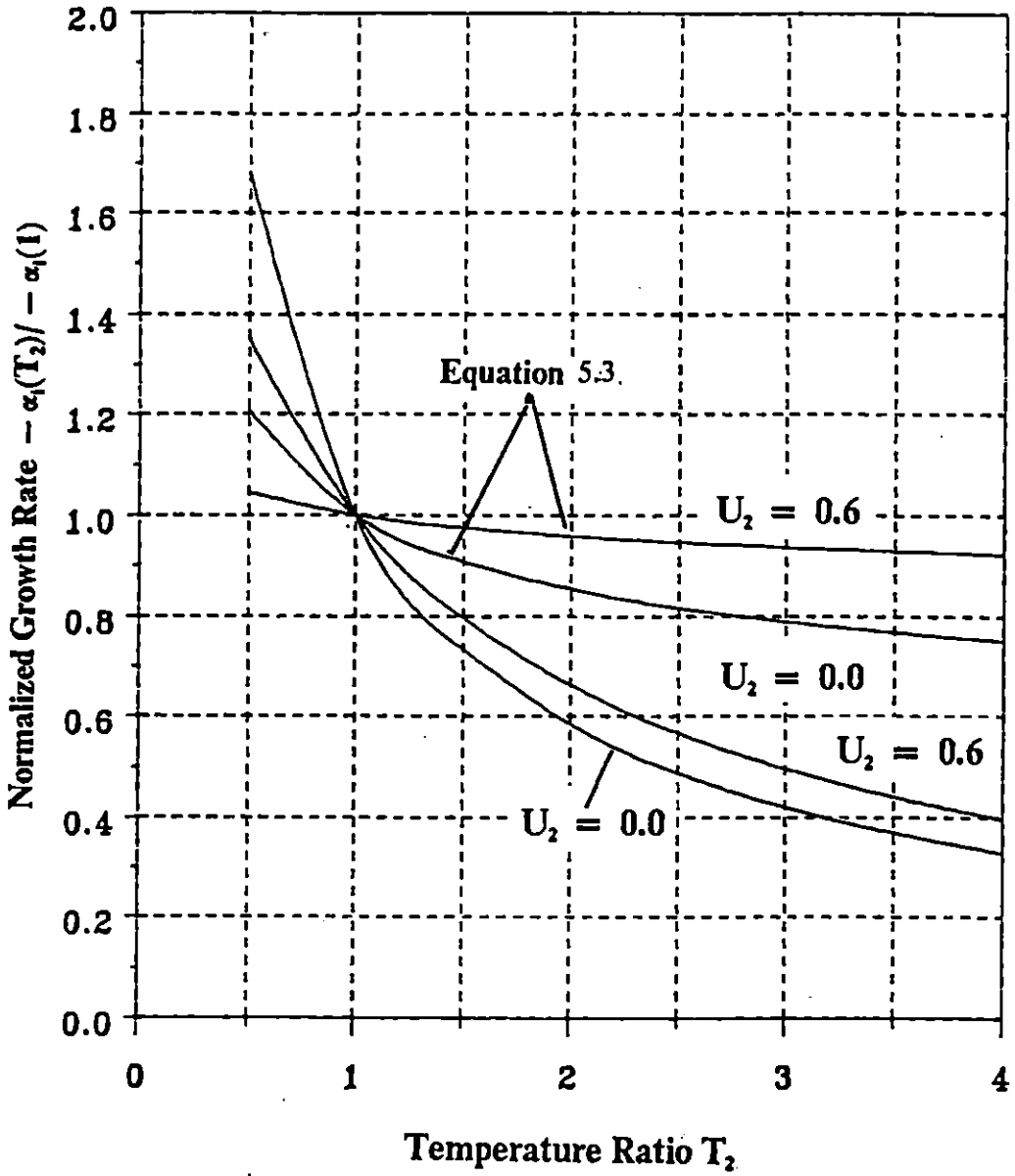

Figure 5.21 A comparison with Papamoschou and Roshko's model for incompressible layer (Eq. 5.3); ω = the most amplified frequency.

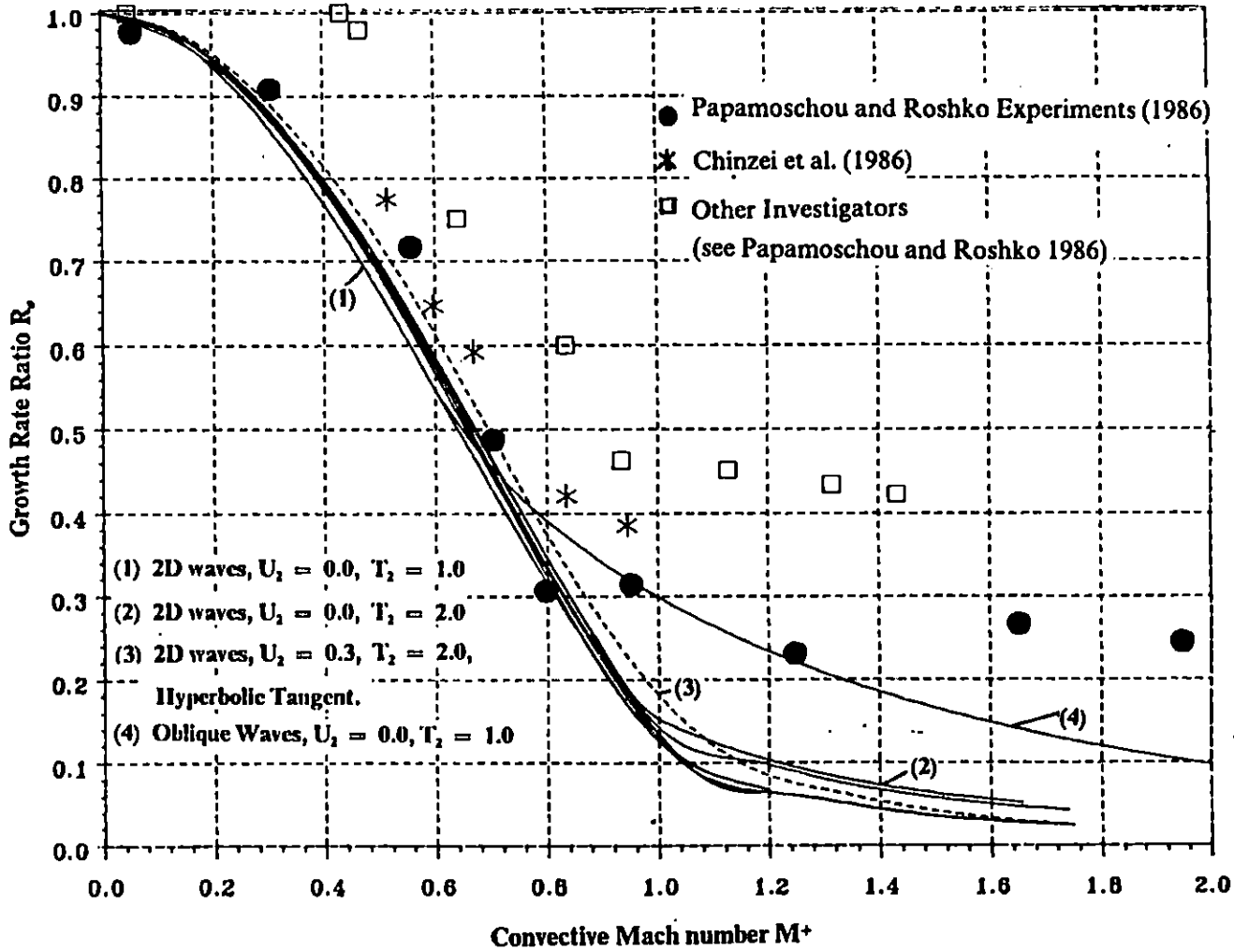

Figure 5.22 The correlation with the convective Mach number; ω = most amplified frequency.

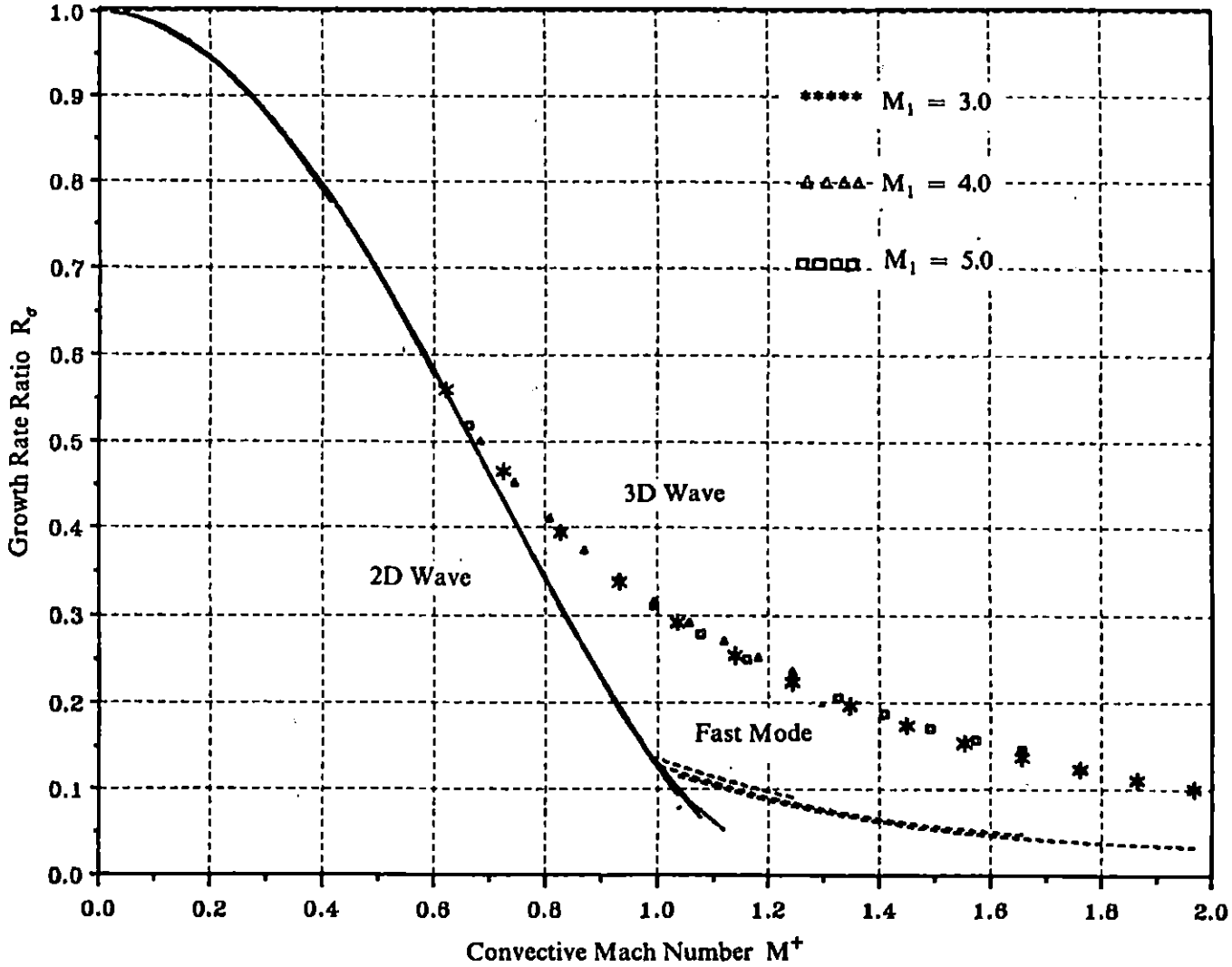

Figure 5.23 The correlation with the convective Mach number; ω = most amplified frequency, $u_o = 0.5(1 + \tanh y)$, R = 2000.

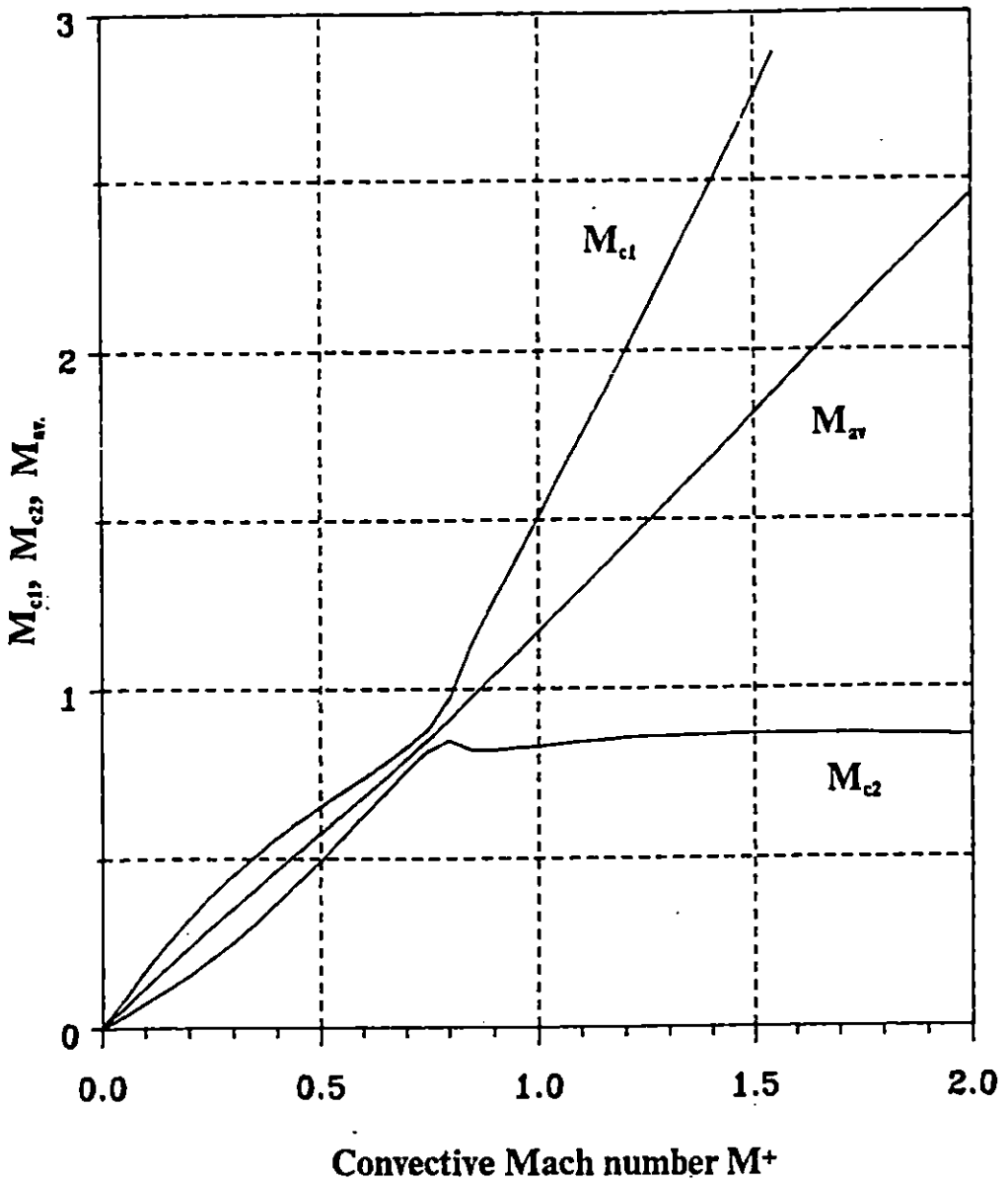

Figure 5.24a Mach numbers M_{c1}, M_{c2}, and $M_{av} = (M_{c1} + M_{c2})/2$ against M^+; $U_2 = 0.0, T_2 = 0.6$.

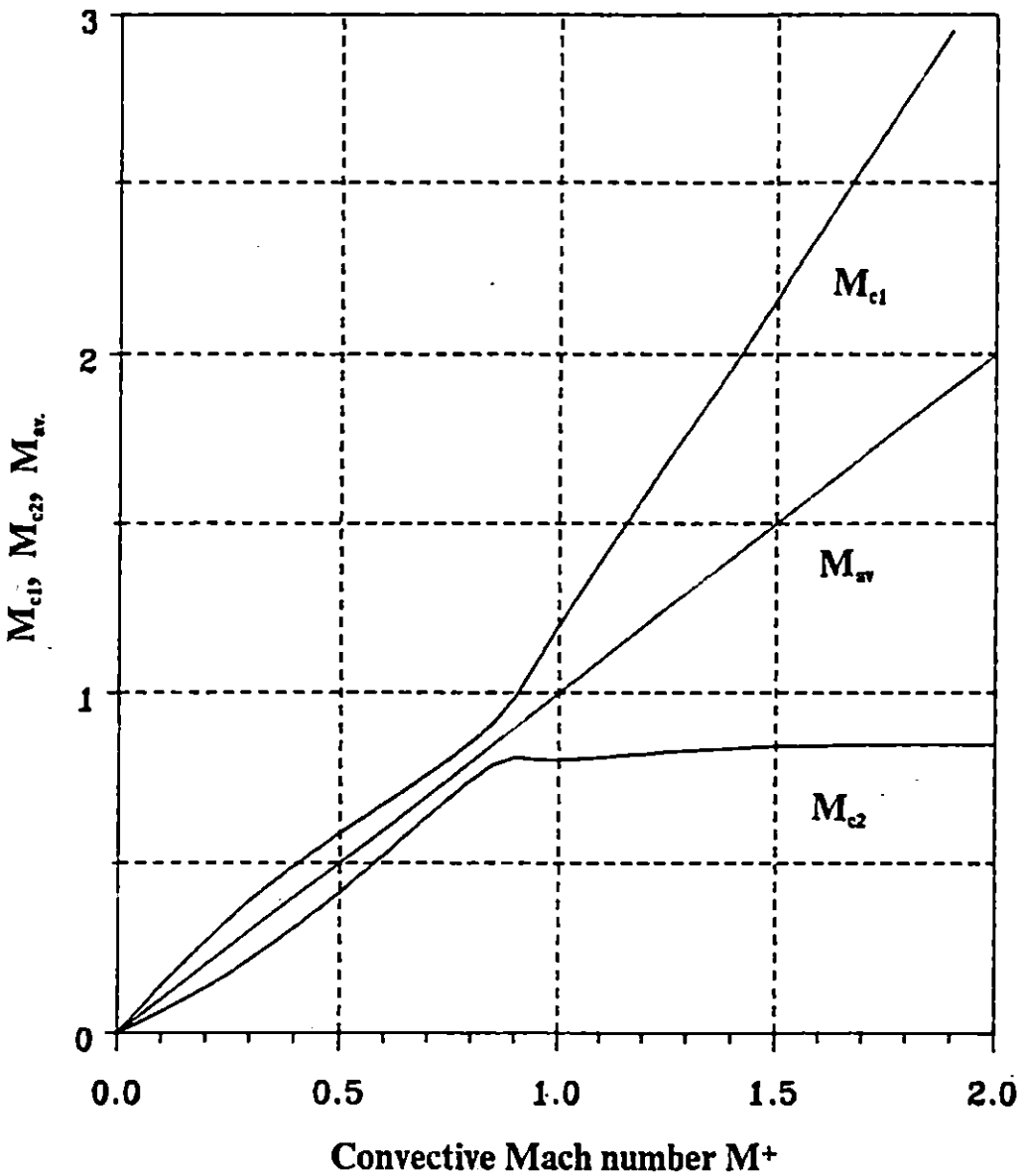

Figure 5.24b Mach numbers M_{c1}, M_{c2}, and $M_{av} = (M_{c1} + M_{c2})/2$ against M^+; $U_2 = 0.0, T_2 = 1.0$.

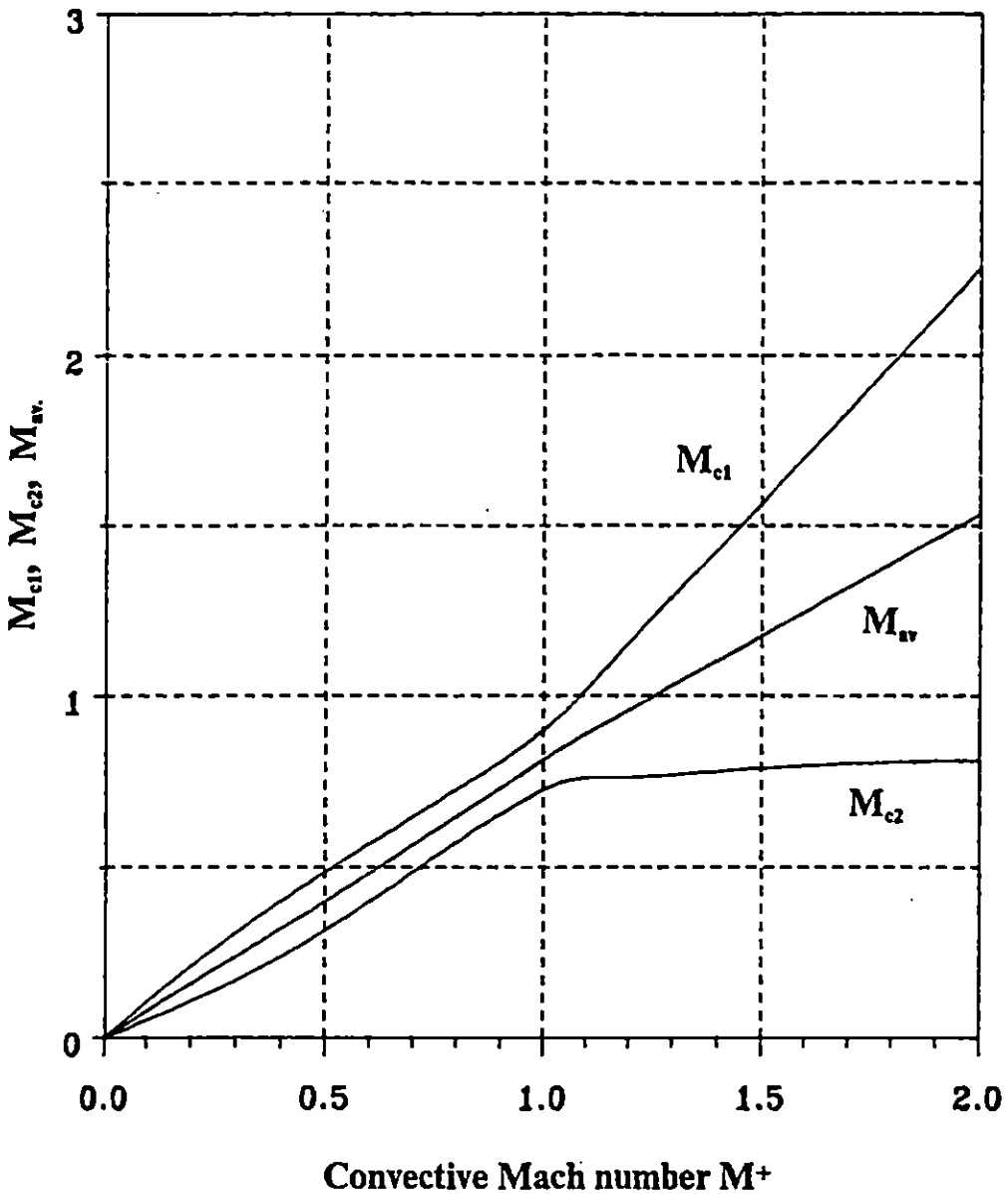

Figure 5.24c Mach numbers M_{c1}, M_{c2}, and $M_{av} = (M_{c1} + M_{c2})/2$ against M^+; $U_2 = 0.0$, $T_2 = 2.0$.

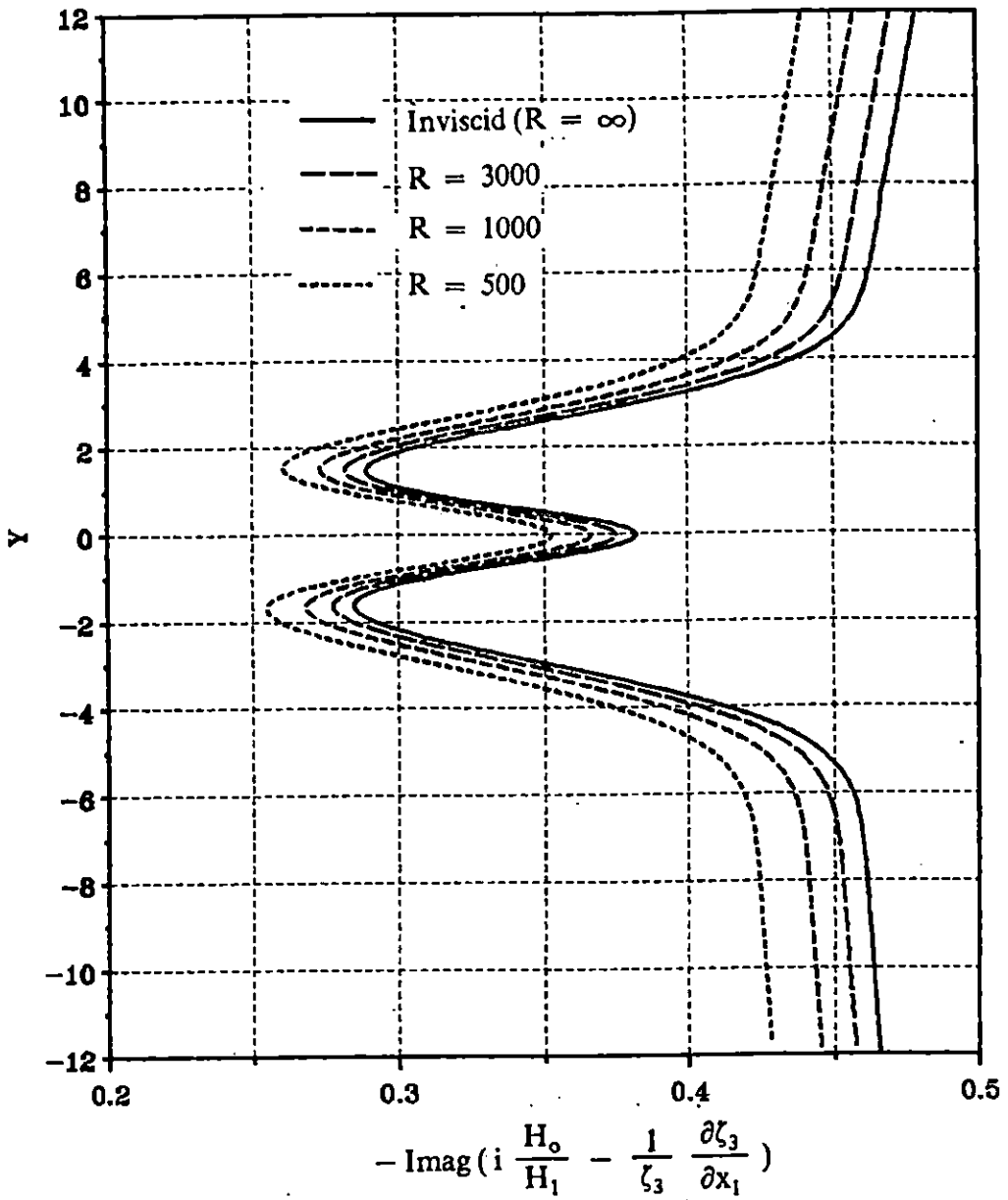

Figure 5.25 The variations of nonparallel corrections for v of 2D inviscid and viscous disturbances with y. $U_2 = 0.6$, $T_2 = 1.0$, ω = most amplified frequency.

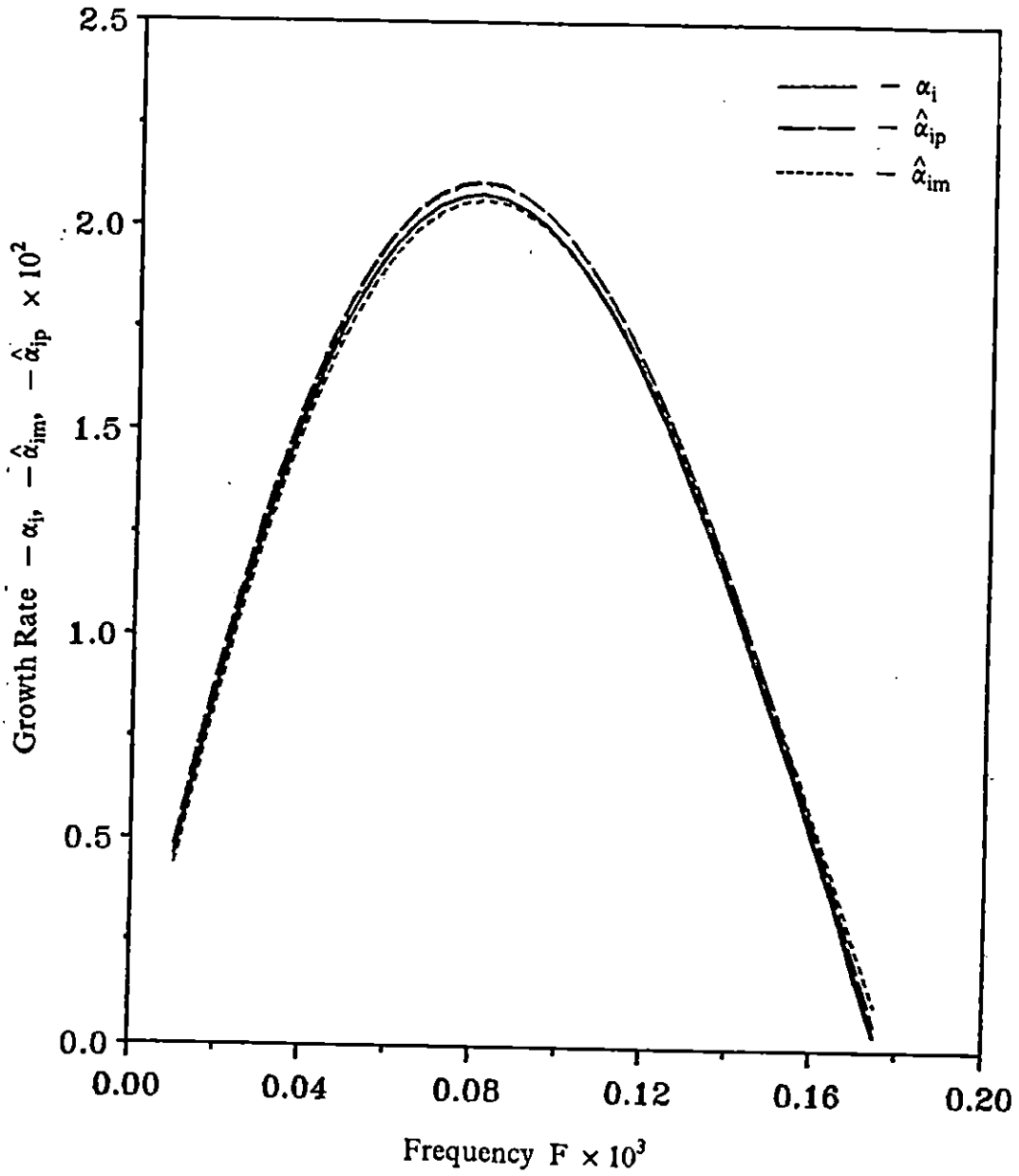

Figure 5.26 The growth rates of the parallel flow, nonparallel correction with respect to ρu and p; $M_1 = 2.0$, $U_2 = 0.3$, $T_2 = 1.0$, and $R = 1000$.

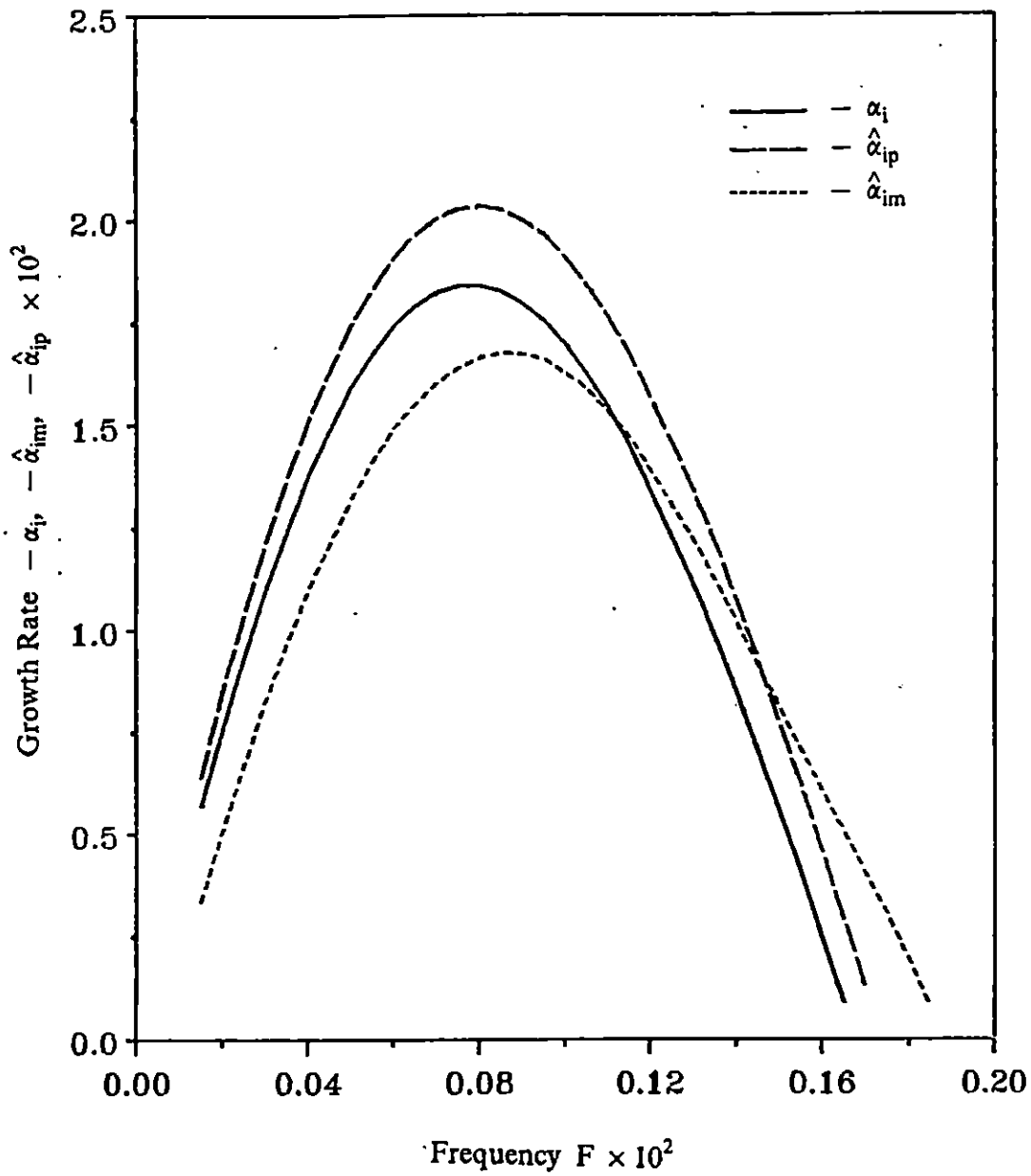

Figure 5.27 The growth rates of the parallel flow, nonparallel correction with respect to ρu and p; $M_1 = 2.0$, $U_2 = 0.3$, $T_2 = 1.0$, and $R = 100$.

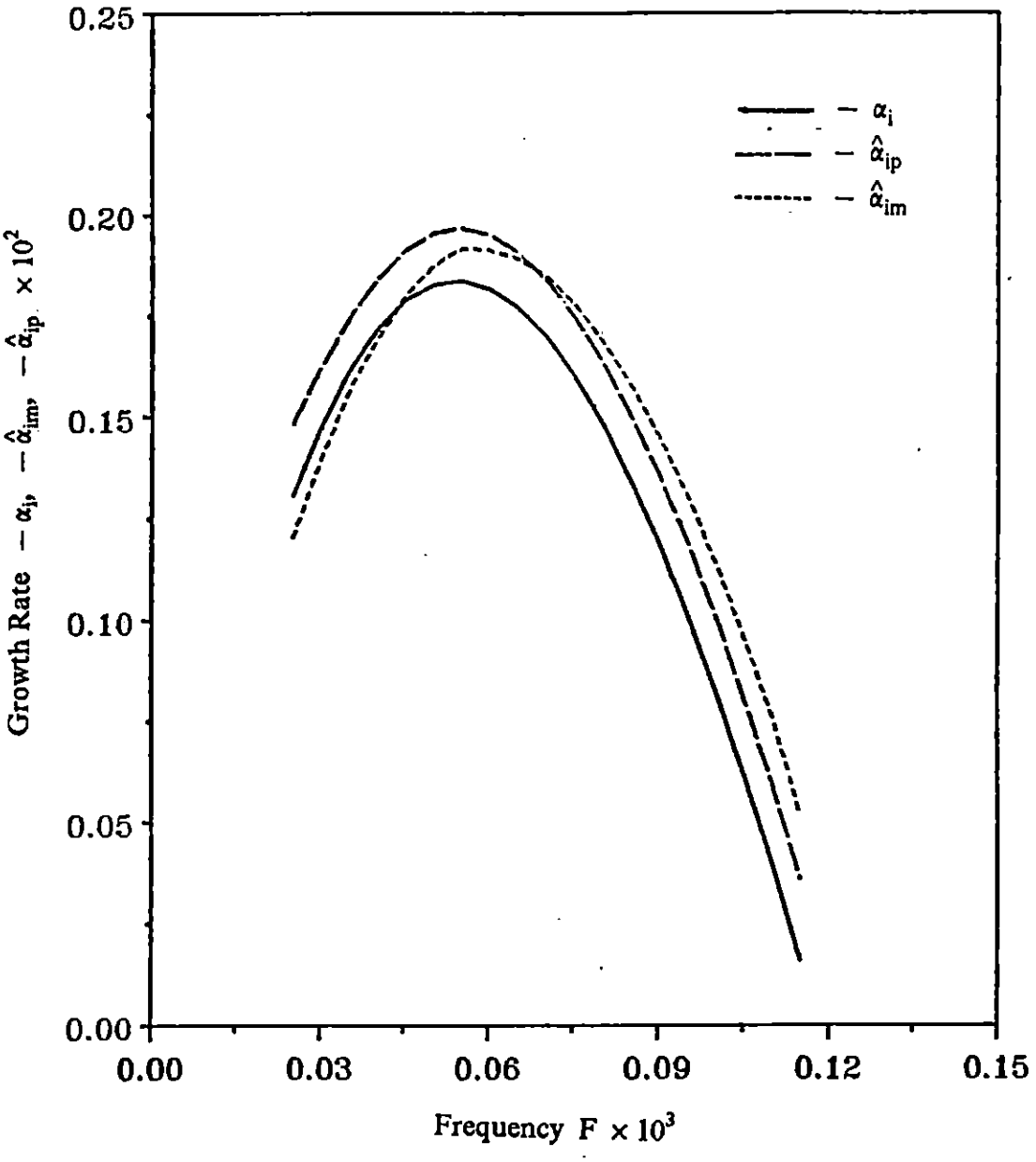

Figure 5.28 The growth rates of the parallel flow, nonparallel correction with respect to ρu and p; $M_1 = 4.0$, $U_2 = 0.3$, $T_2 = 1.0$, and $R = 1000$.

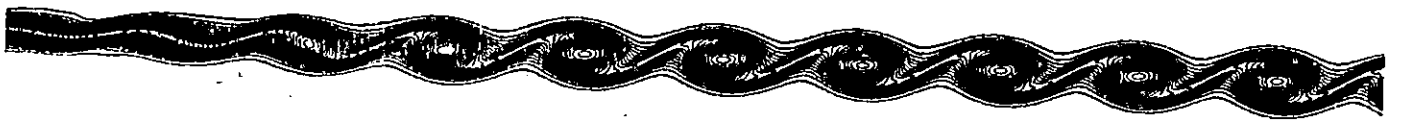

Figure 6.1a Vorticity coutours of direct simulation $M_1 = 2.0$, $R = 100$, $T_2 = 1.0$, $U_2 = 0.6$. Inflow = hyperbolic tangent + most amplified waves.

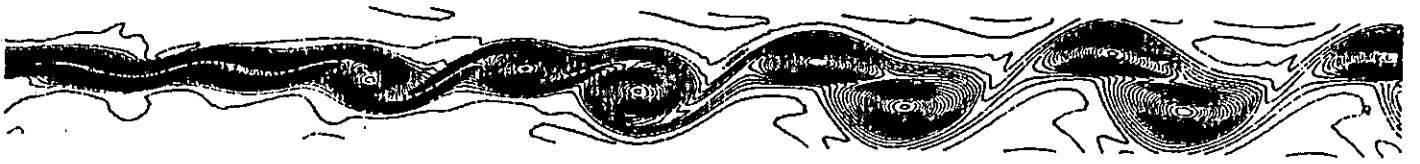

Figure 6.1b Vorticity coutours of direct simulation $M_1 = 2.0$, $R = 100$, $T_2 = 1.0$, $U_2 = 0.6$. Inflow = hyperbolic tangent + most amplified waves + first subharmonic wave.

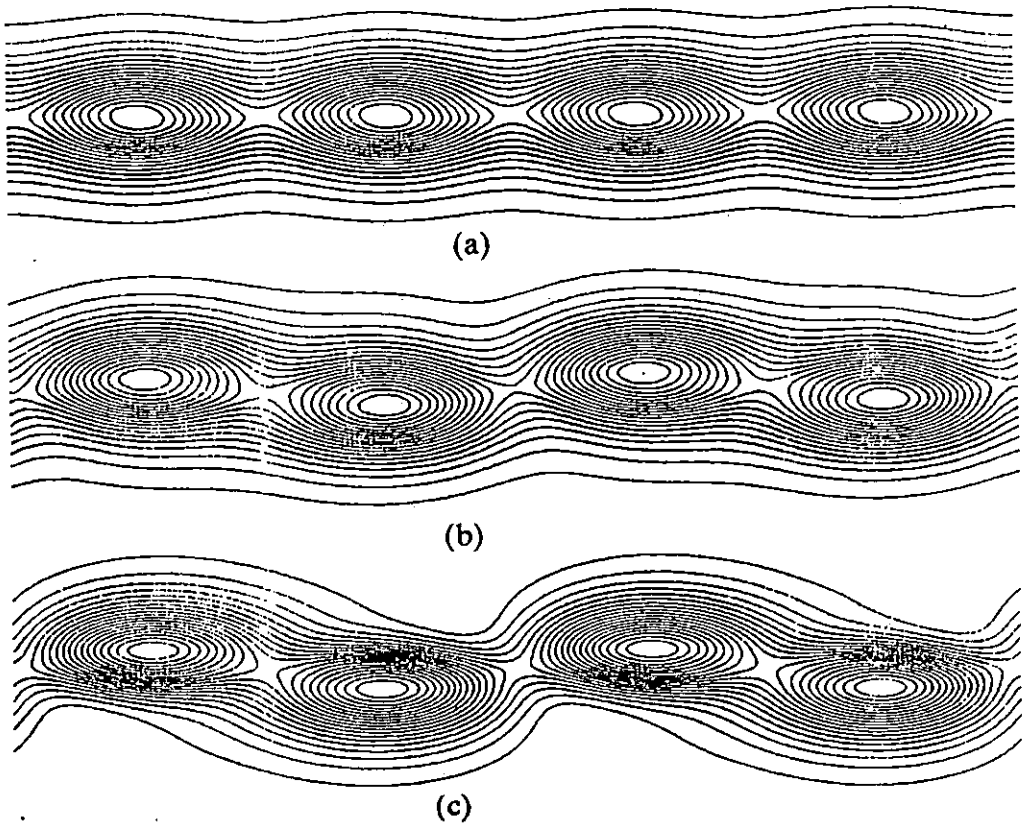

Figure 6.2 Vorticity coutours for $U = 0.5 \times (1 + \tanh ay)$ at $M_1 = 1.4$, $R = 500$, $T_2 = 1.0$, $U_2 = 0.6$.
(a) $A_{rms} = 0.04$, $B_{rms} = 0.0$, (b) $A_{rms} = 0.04$, $B_{rms} = 0.1$, and (c) $A_{rms} = 0.04$, $B_{rms} = 0.2$.

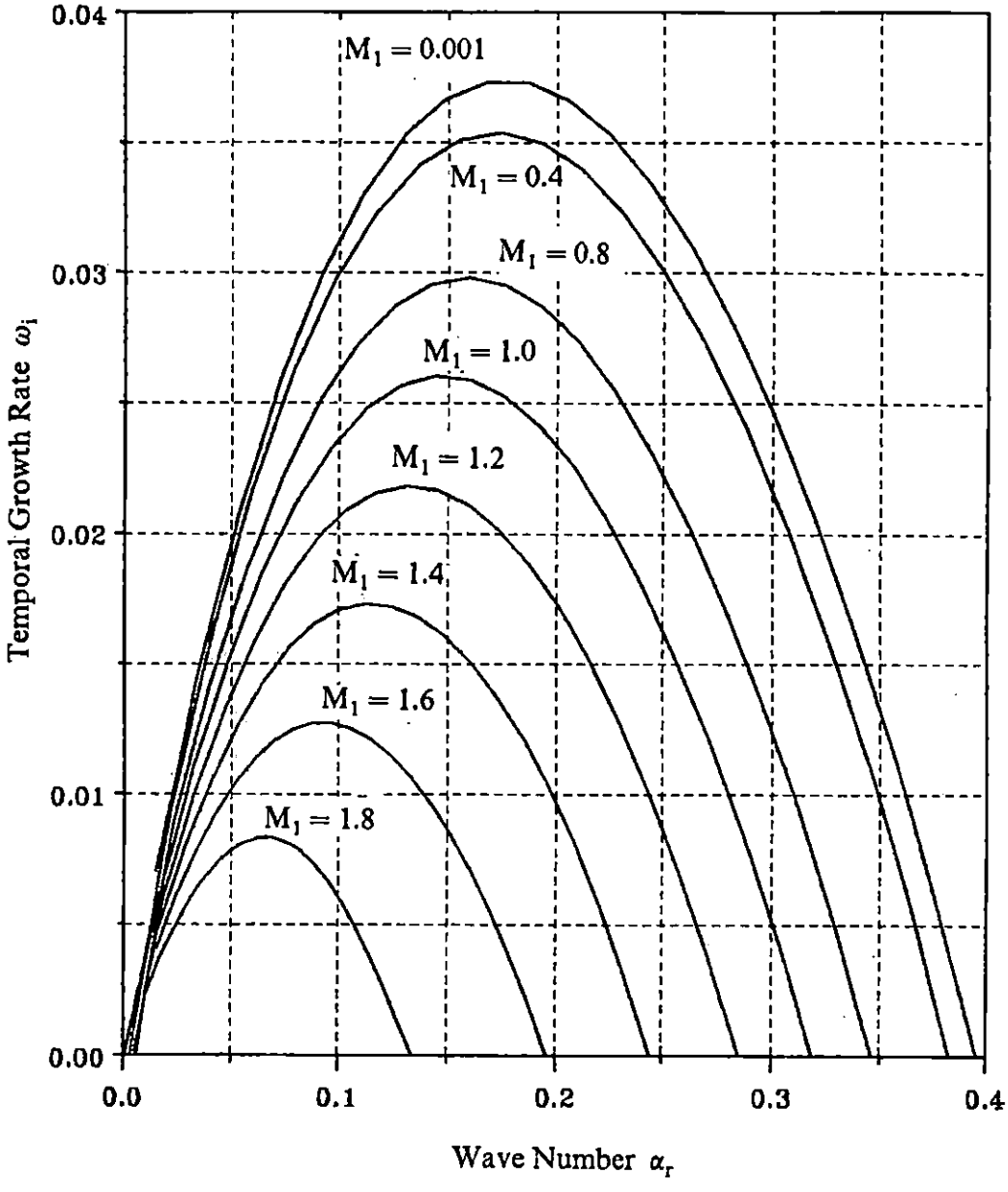

Figure 7.1 The temporal growth rates ω_i of 2D viscous disturbances. TANH Profile, $R = 500.0$, $U_2 = 0.0$ and $T_2 = 1.0$.

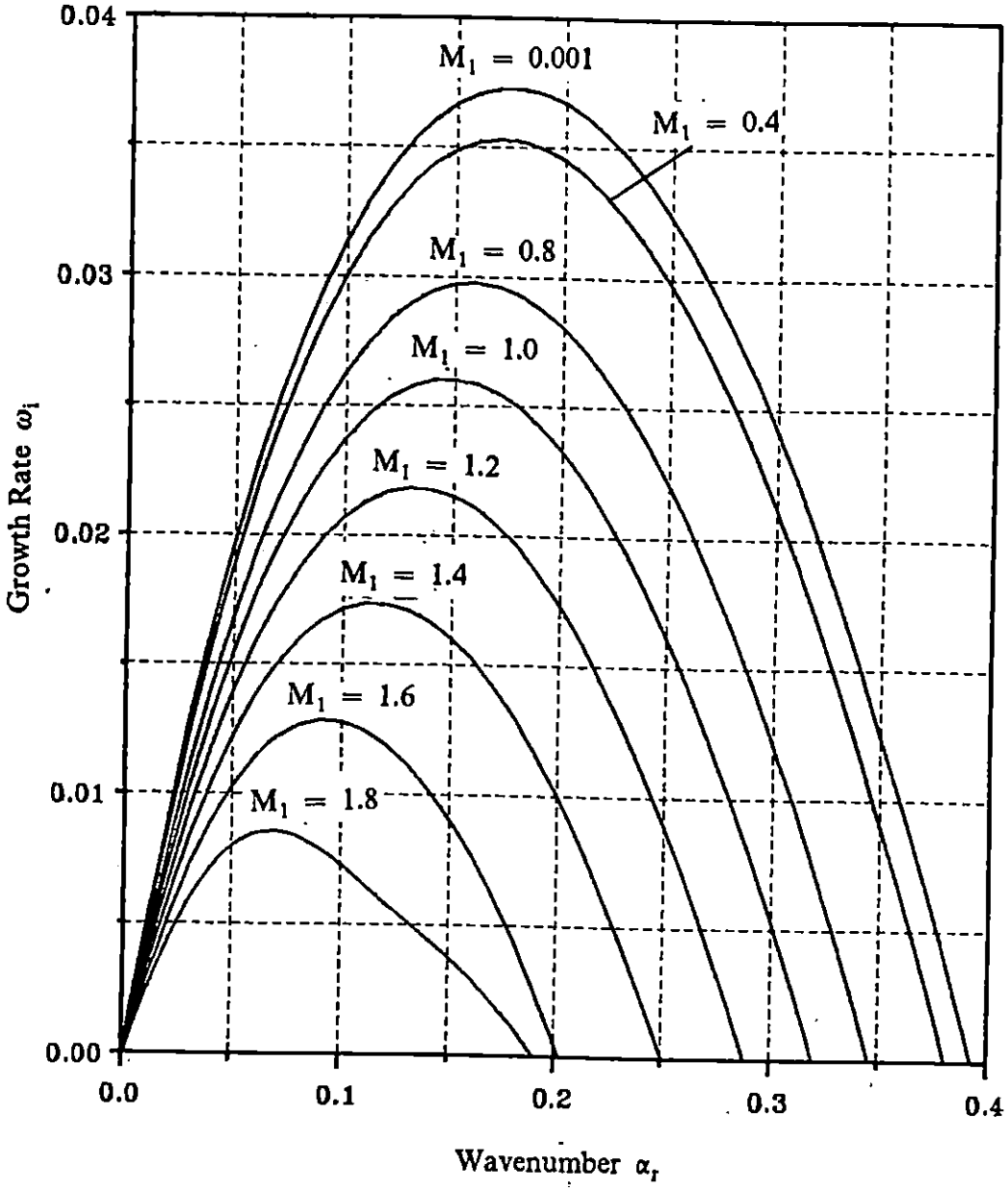

Figure 7.2 The temporal growth rates ω_i of 2D viscous disturbances. SHEAR Profile, R = 500.0, $U_2 = 0.0$ and $T_2 = 1.0$.

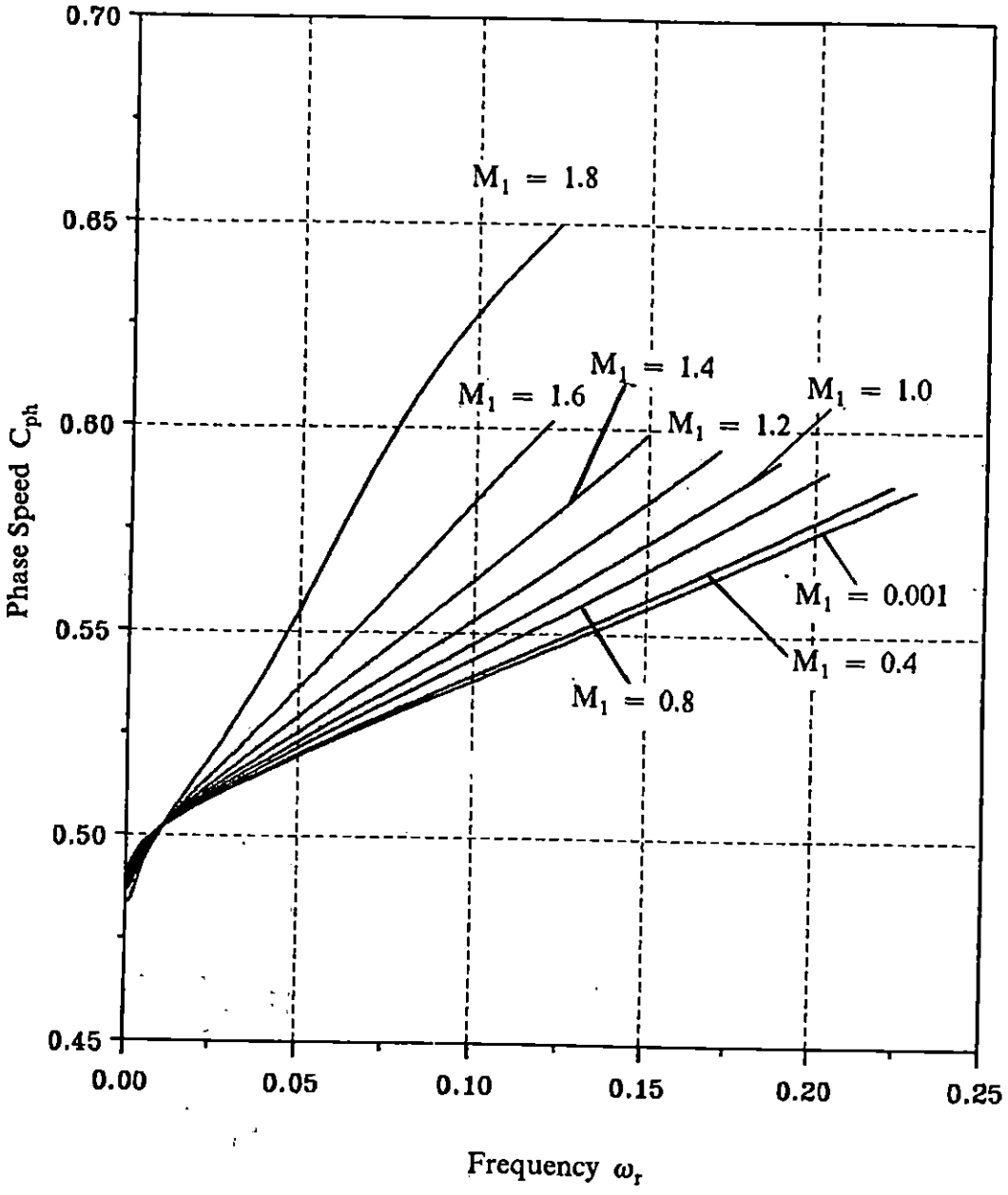

Figure 7.3 The phase speed C_{ph} of 2D viscous disturbances. SHEAR Profile, R = 500.0, $U_2 = 0.0$ and $T_2 = 1.0$ (Temporal).

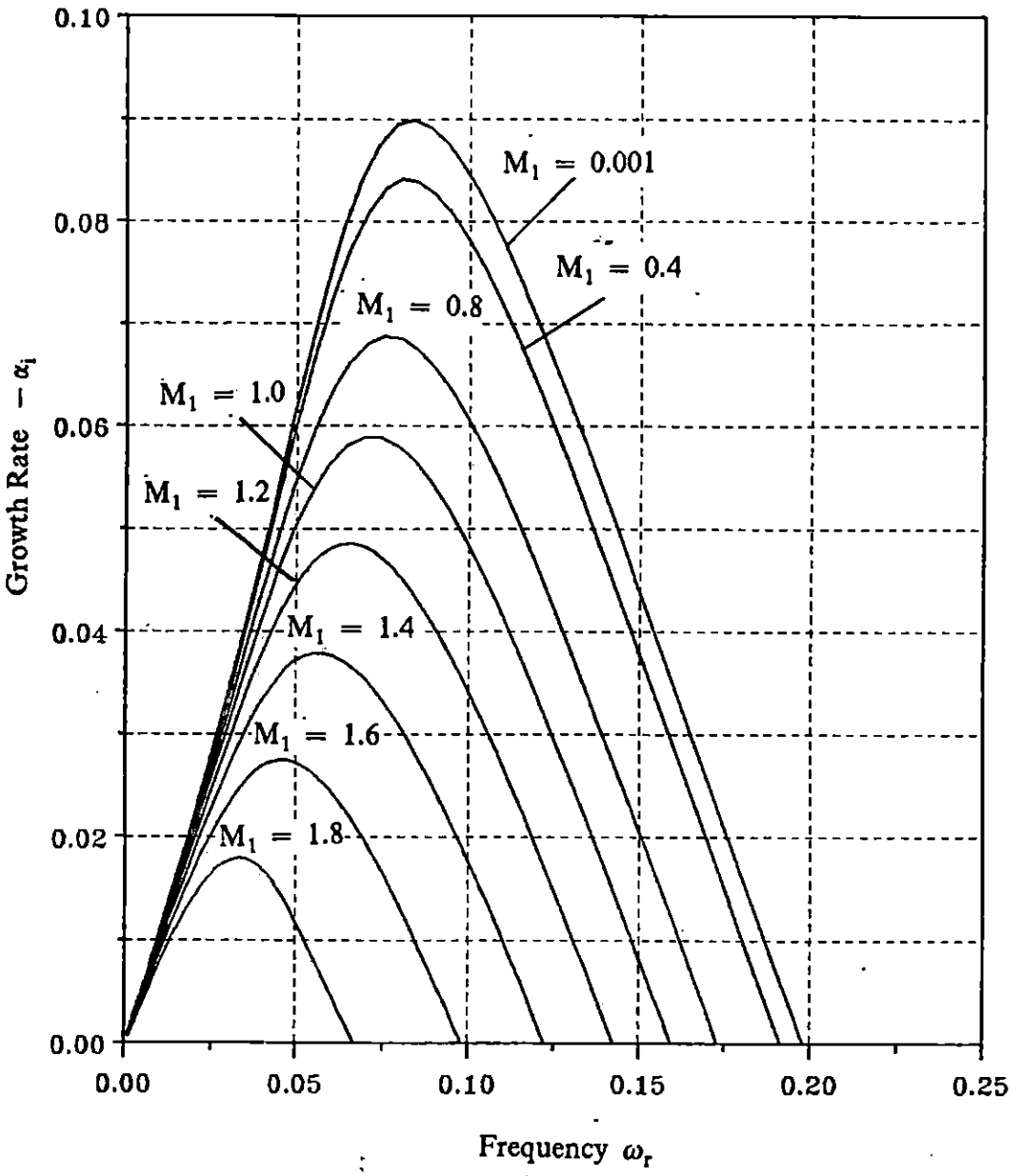

Figure 7.4 The spatial growth rates $-\alpha_i$ of 2D viscous disturbances. TANH Profile, $R = 500.0$, $U_2 = 0.0$ and $T_2 = 1.0$.

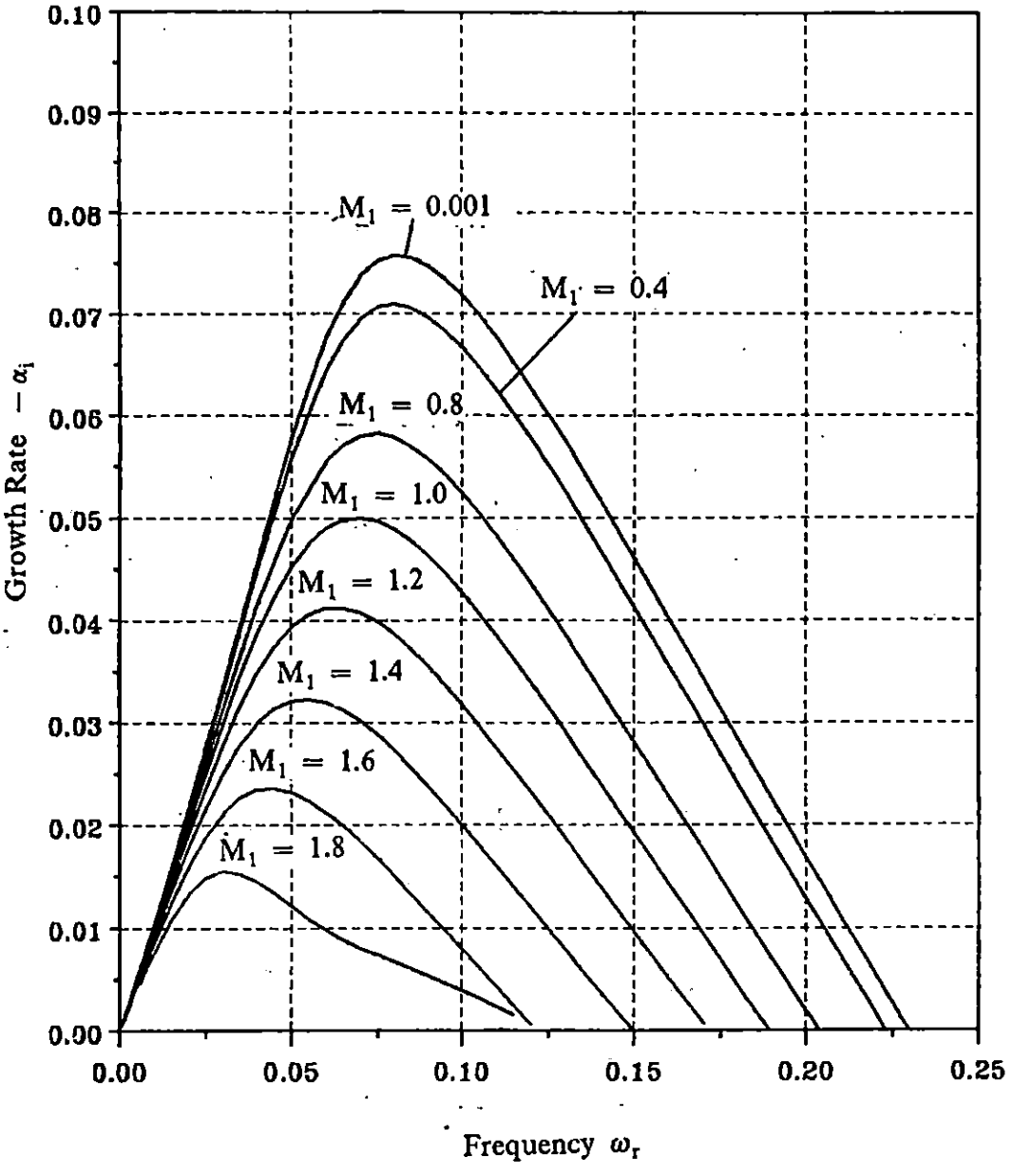

Figure 7.5 The spatial growth rates $-\alpha_i$ of 2D viscous disturbances. SHEAR Profile, $R = 500.0$, $U_2 = 0.0$ and $T_2 = 1.0$.

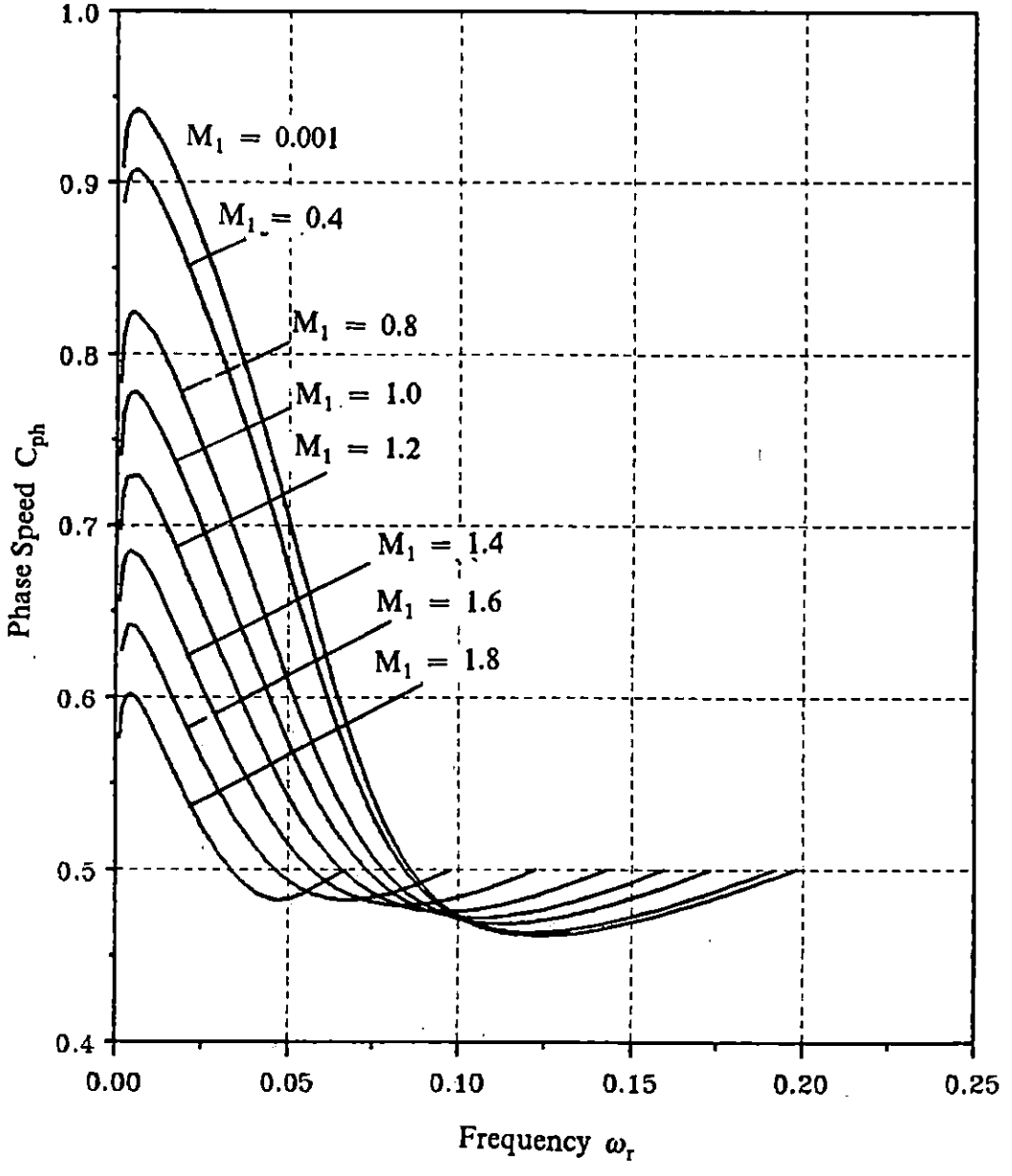

Figure 7.6 The phase speed C_{ph} of 2D viscous disturbances. TANH Profile, R = 500.0, U_2 = 0.0 and T_2 = 1.0 (Spatial).

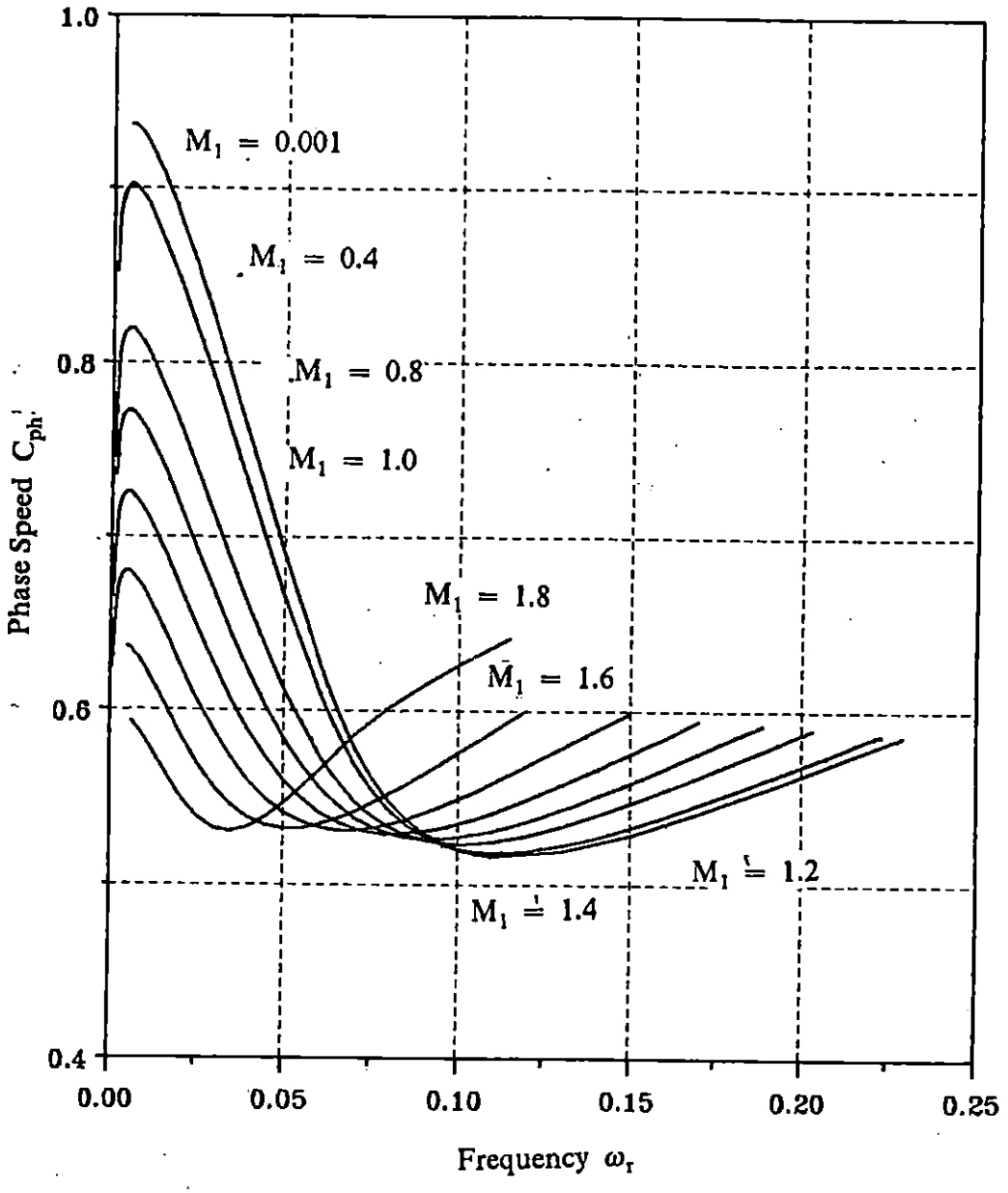

Figure 7.7 The phase speed C_{ph} of 2D viscous disturbances. SHEAR Profile, R = 500.0, $U_2 = 0.0$ and $T_2 = 1.0$ (Spatial).

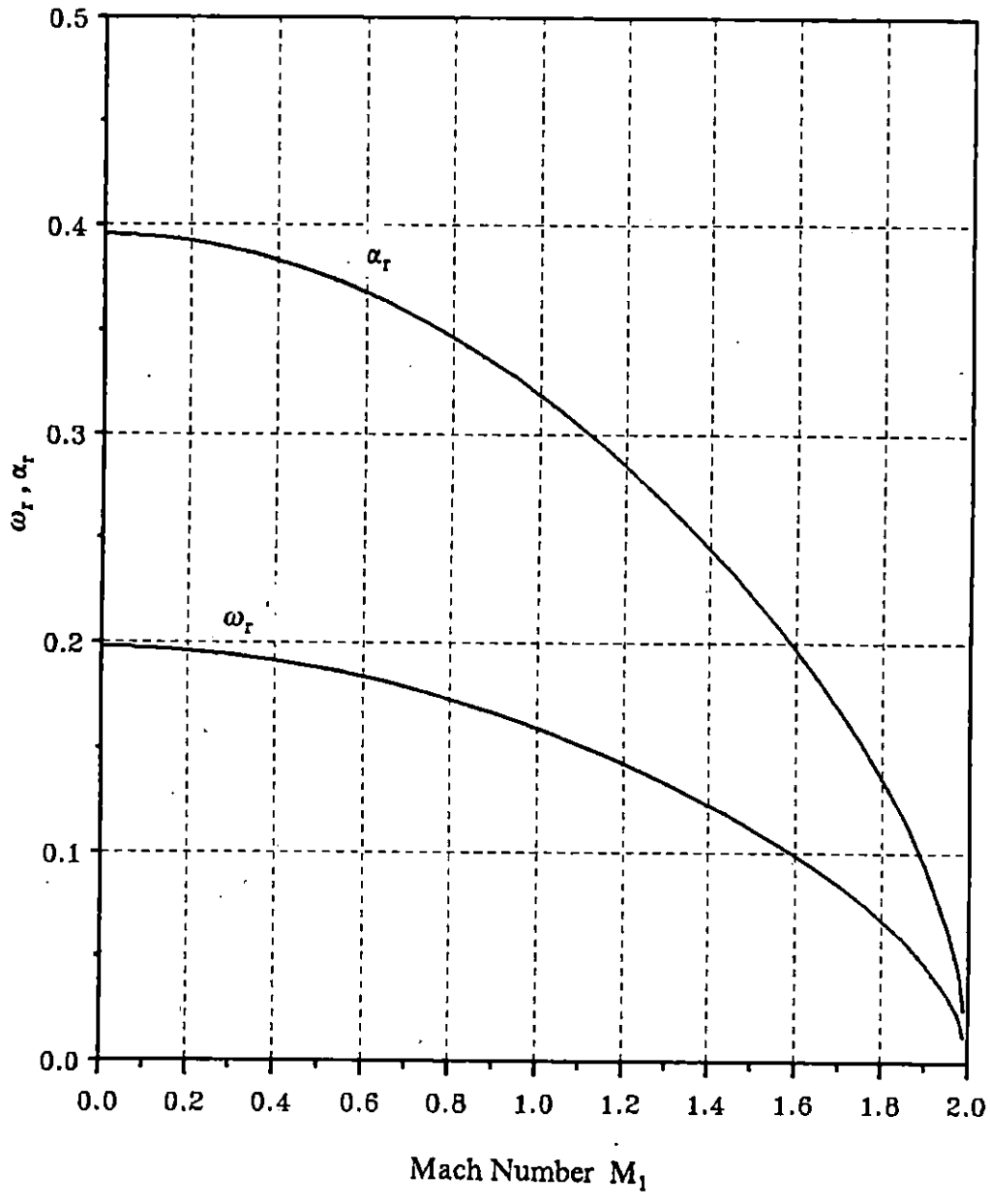

Figure 7.8 The wavenumber α_r and frequency ω_r of neutral 2D primary waves vs. Mach number M_2. TANH Profile, R = 500.0, U_2 = 0.0, T_2 = 1.0.

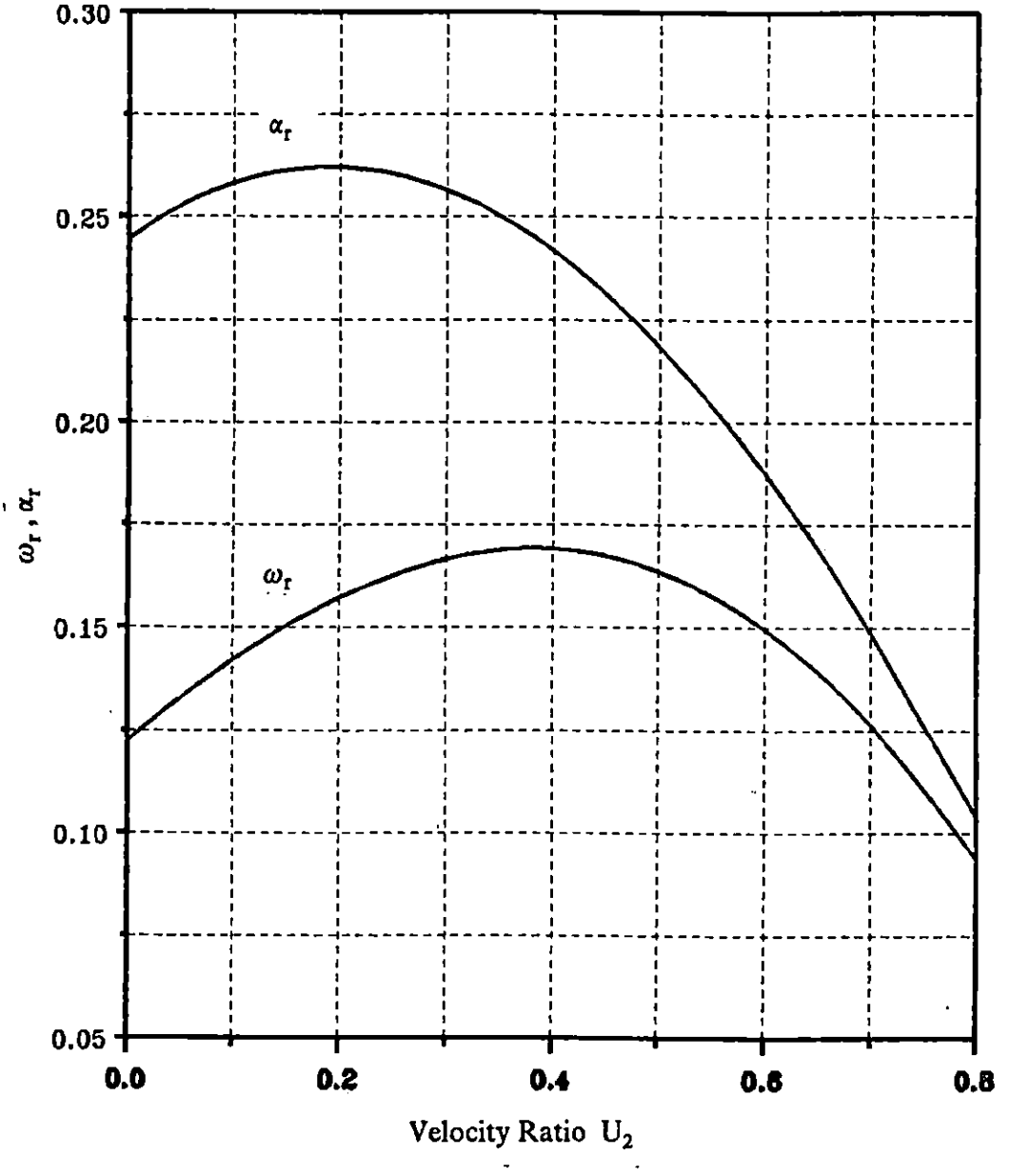

Figure 7.9 The wavenumber α_r and frequency ω_r of neutral 2D primary waves vs. velocity ratio U_2. TANH Profile, R = 500.0, T_2 = 1.0.

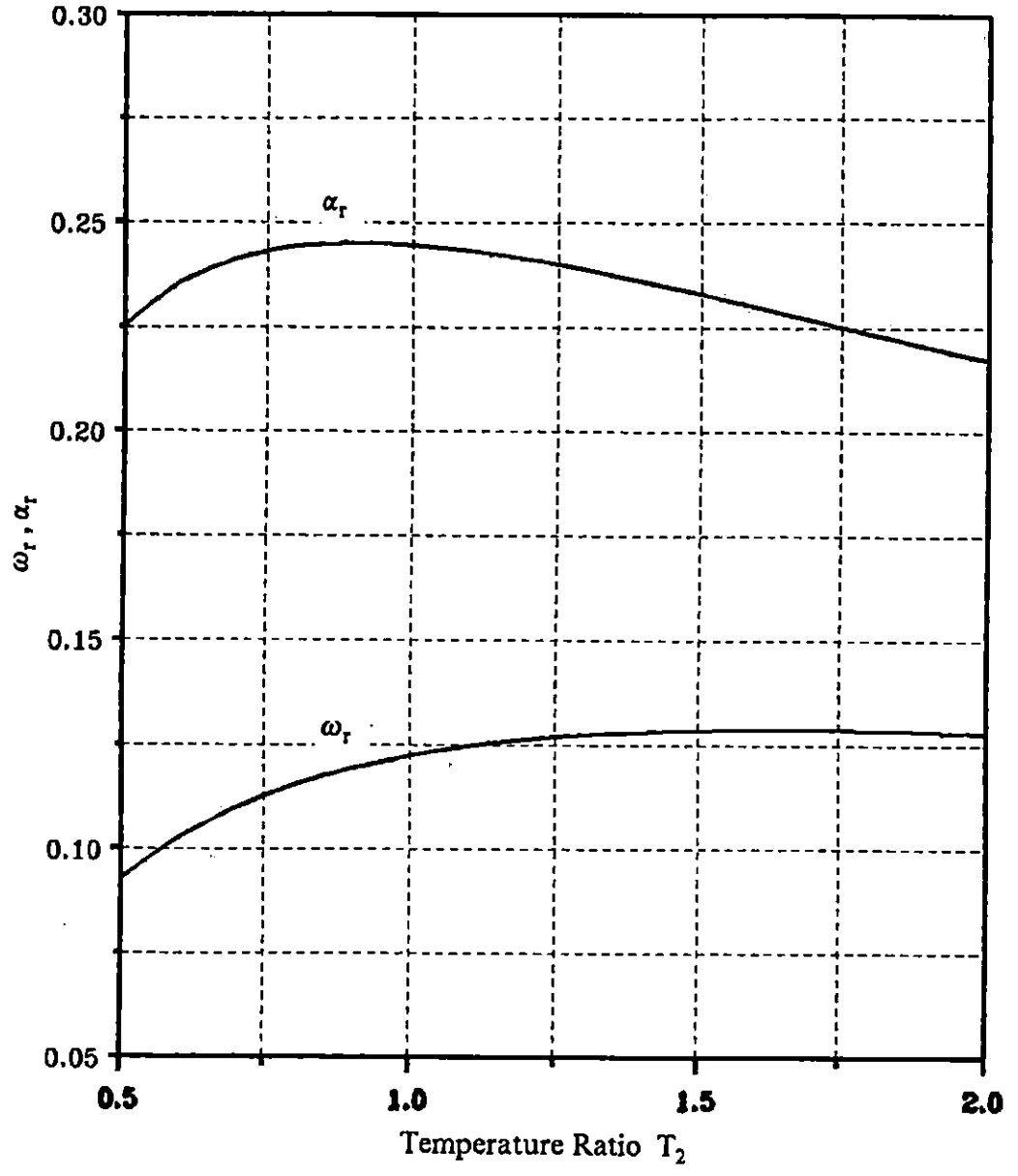

Figure 7.10 The wavenumber α_r and frequency ω_r of neutral 2D primary waves vs. temperature ratio T_2. TANH Profile, R = 500.0, U_2 = 0.0.

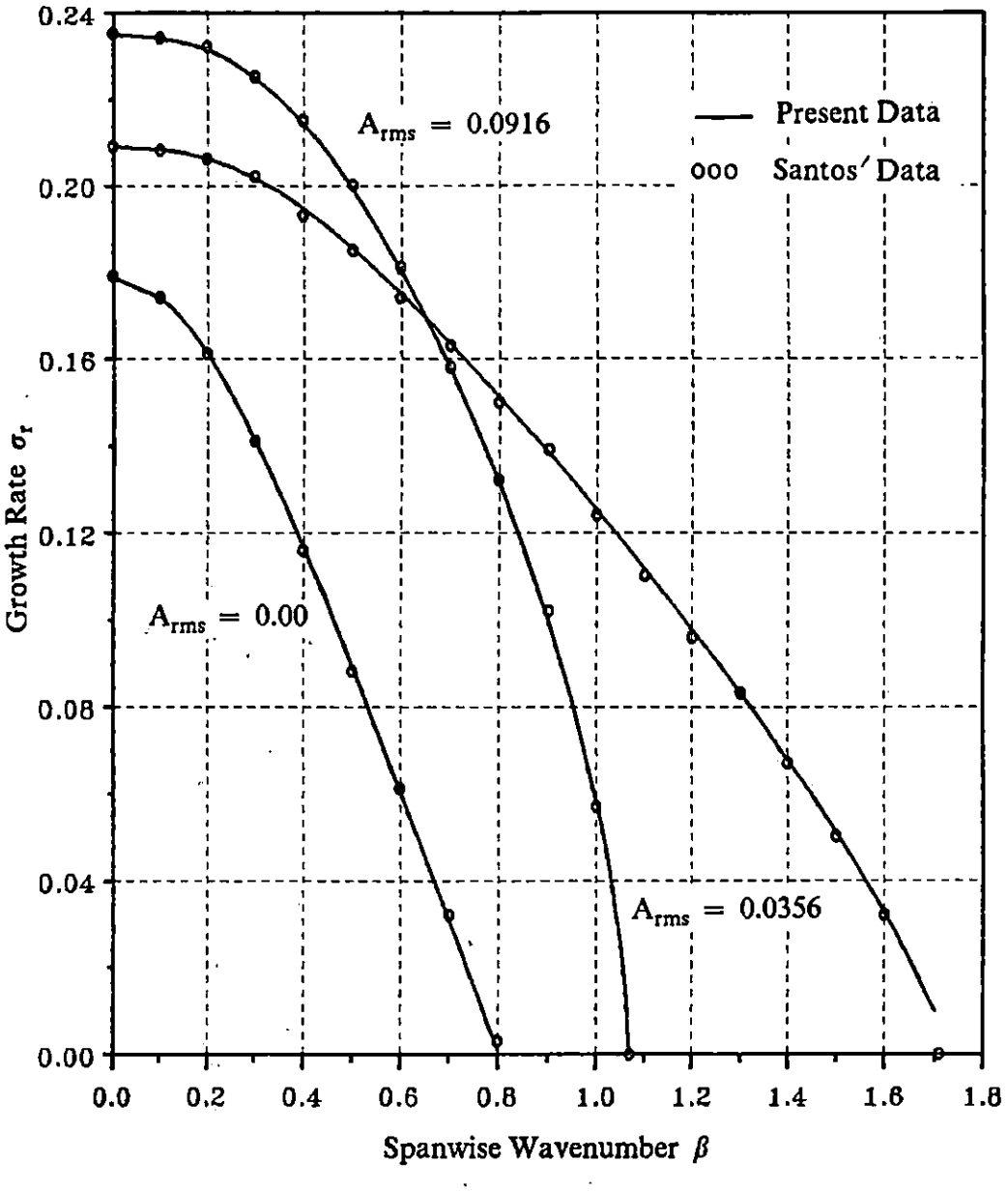

Figure 7.11 The temporal growth rates σ_r of 2D subharmonic mode vs. spanwise wavenumber β. Comparison with Santo's results; u_o = tanh y, R = 200.0, M_1 = 0.0 .

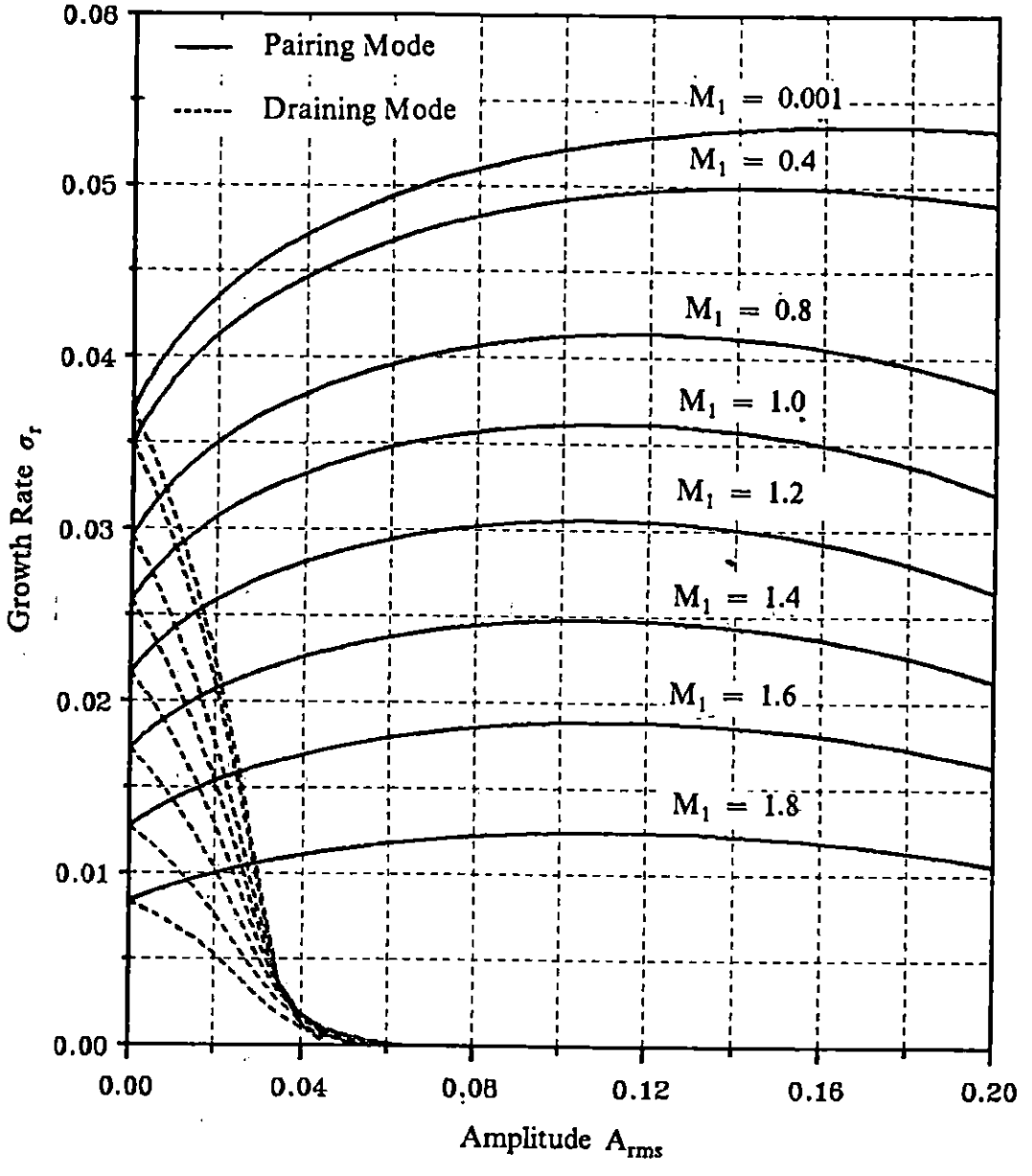

Figure 7.12 The temporal growth rates σ_r of 2D subharmonic mode vs. r.m.s. amplitude A_{rms} for various Mach number M_1. TANH Profile, R = 500.0, U_2 = 0.0, T_2 = 1.0.

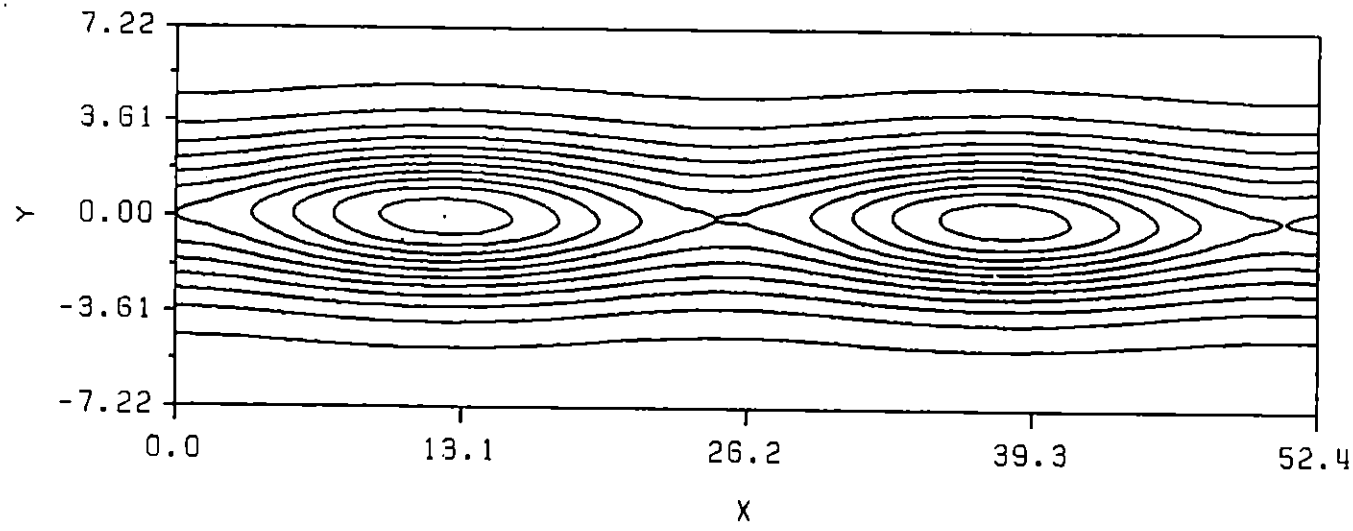

Figure 7.13 The vorticity contours of the mean flow and neutral primary wave. TANH Profile, R = 500.0, M_1 = 1.4, U_2 = 0.0, T_2 = 1.0.

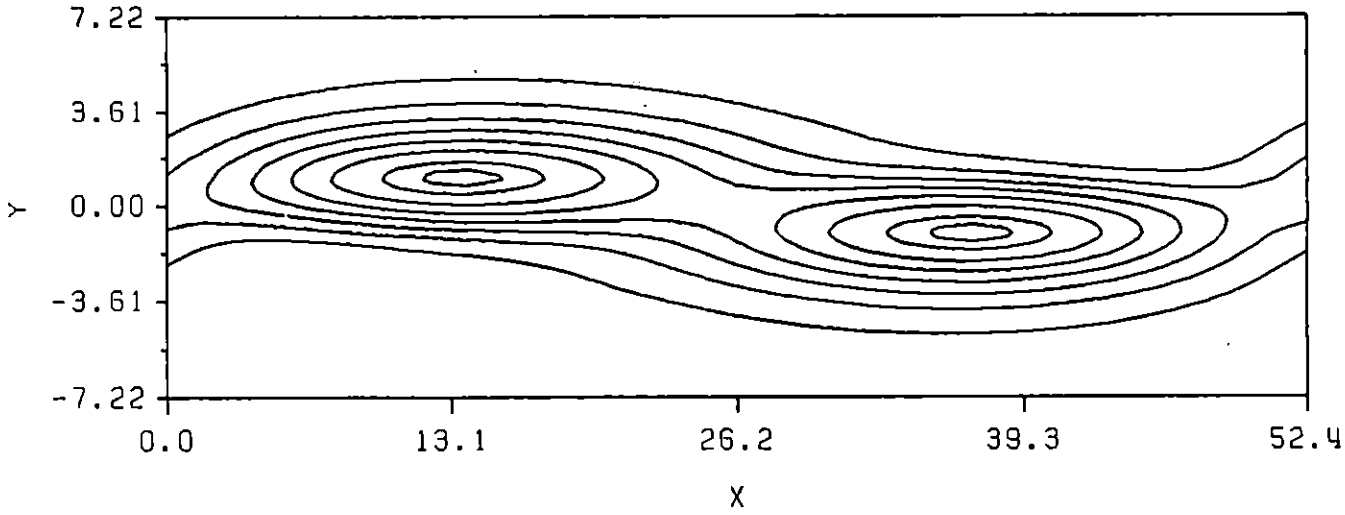

Figure 7.14 The vorticity contours of the mean flow, neutral primary wave and subharmonic pairing mode. TANH Profile, R = 500.0, $M_1 = 1.4, U_2 = 0.0, T_2 = 1.0$.

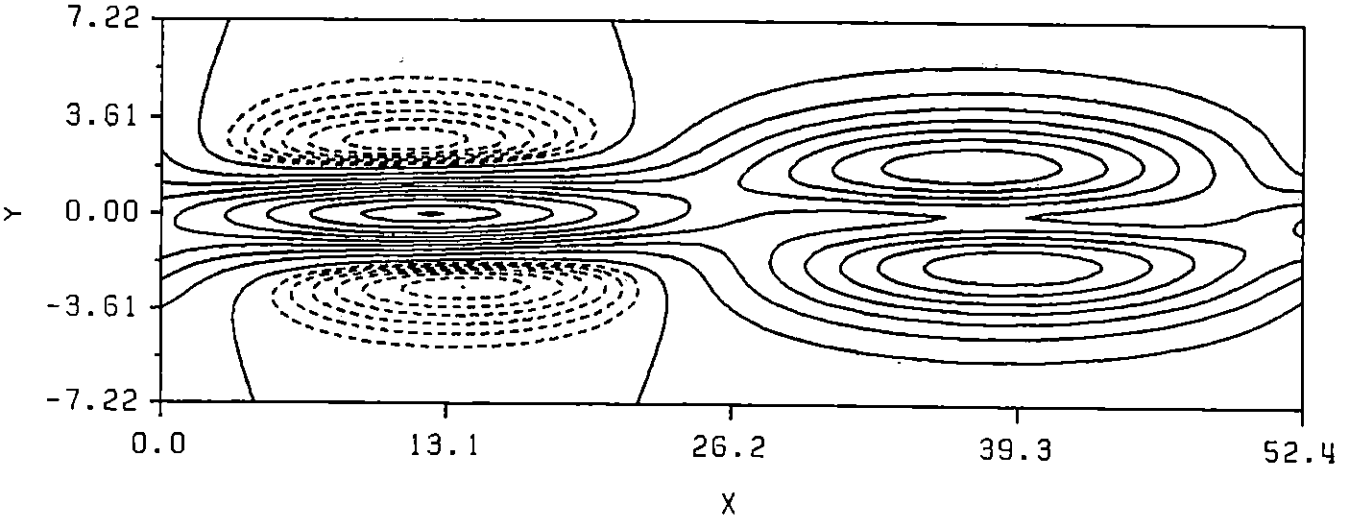

Figure 7.15 The vorticity contours of the mean flow, neutral primary wave and subharmonic draining mode. TANH Profile, R = 500.0, $M_1 = 1.4, U_2 = 0.0, T_2 = 1.0$.

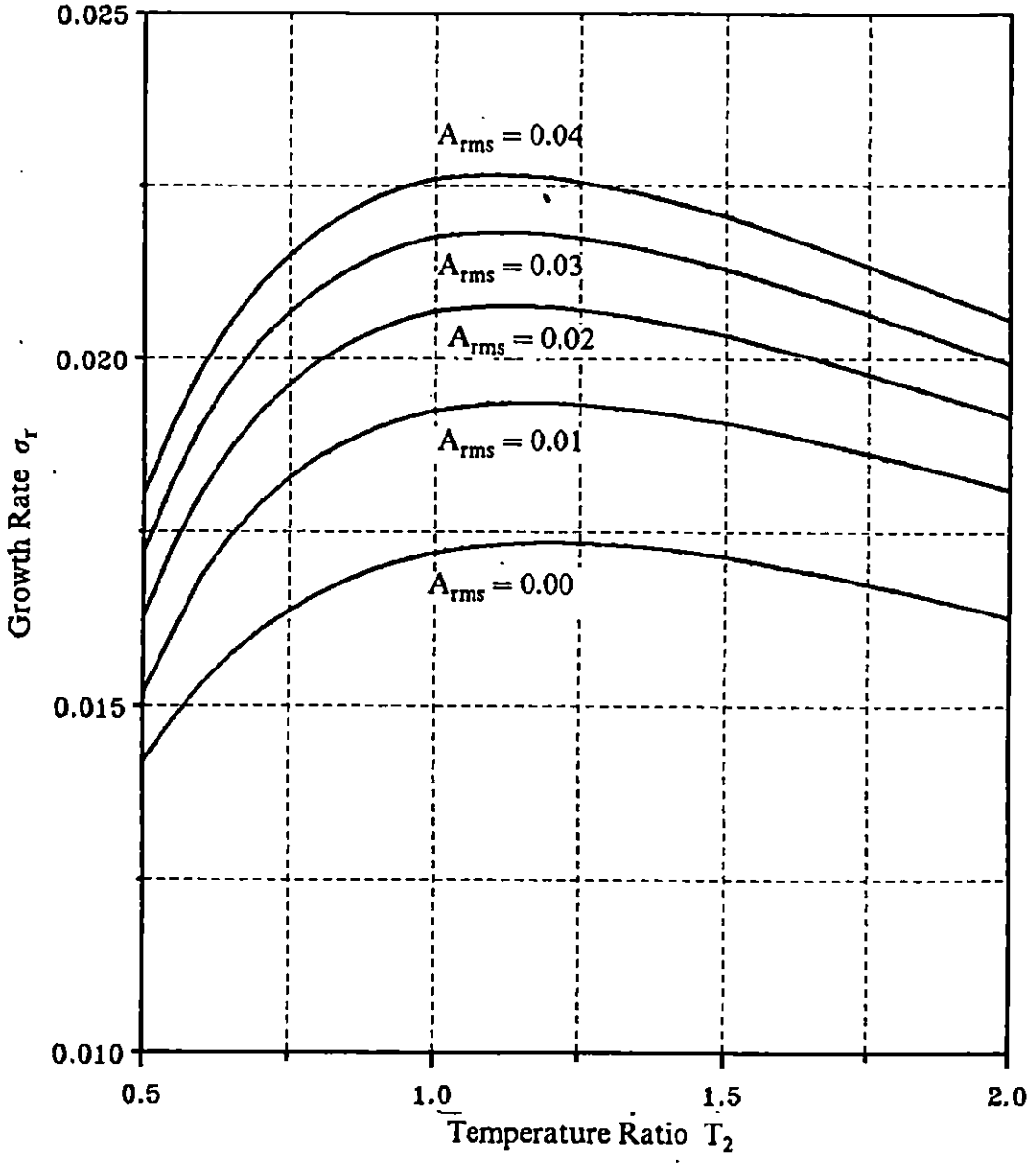

Figure 7.16 The temporal growth rates σ_r of 2D subharmonic mode vs. temperature ratio T_2 for various A_{rms}. TANH Profile, R = 500.0, $M_1 = 1.4, U_2 = 0.0, T_2 = 1.0$.

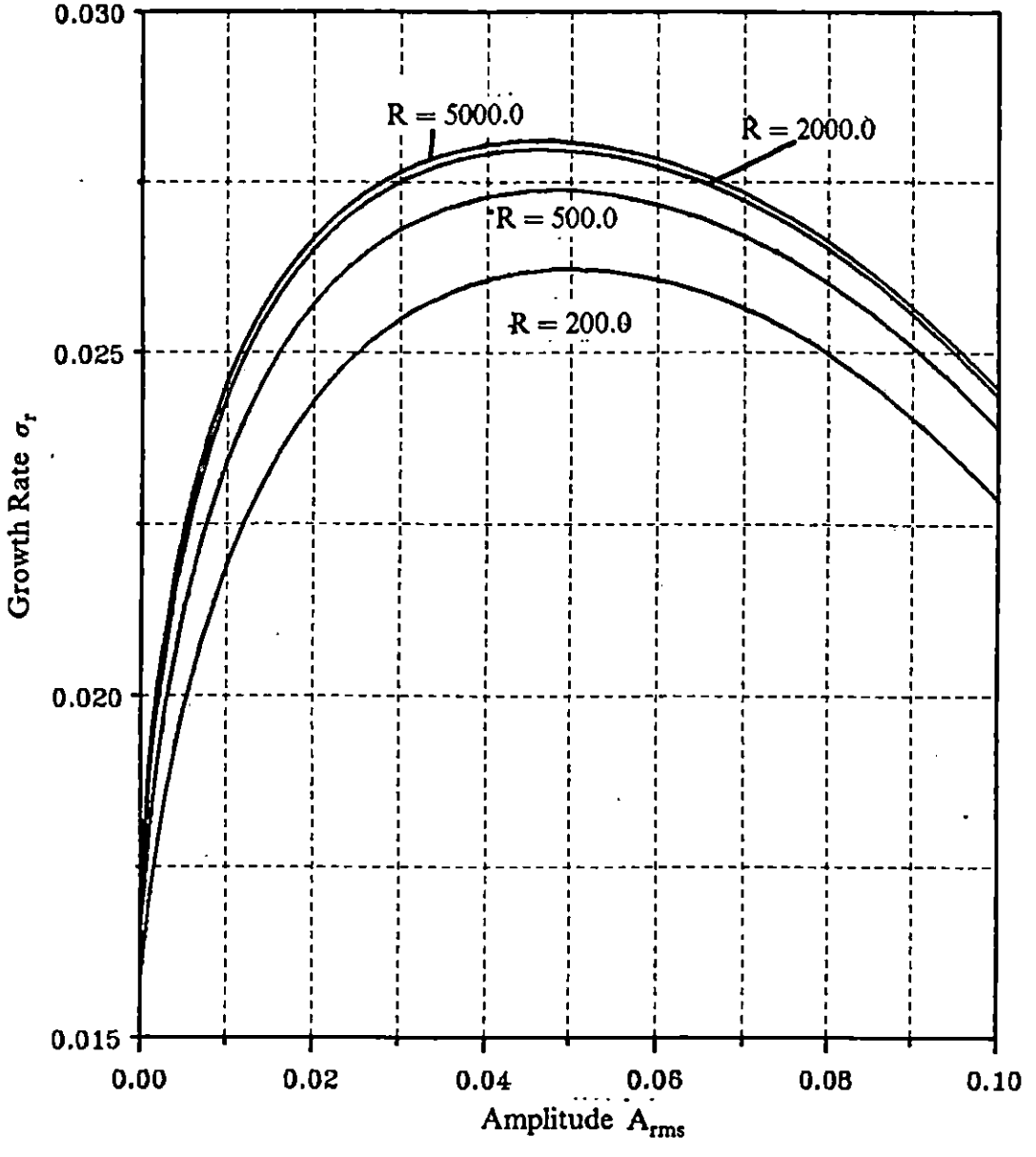

Figure 7.17 The temporal growth rates σ_r of 3D subharmonic mode vs. r.m.s. amplitude A_{rms} for various R. TANH Profile, $M_1 = 1.4$, $U_2 = 0.0, T_2 = 1.0, \beta = 0.12$.

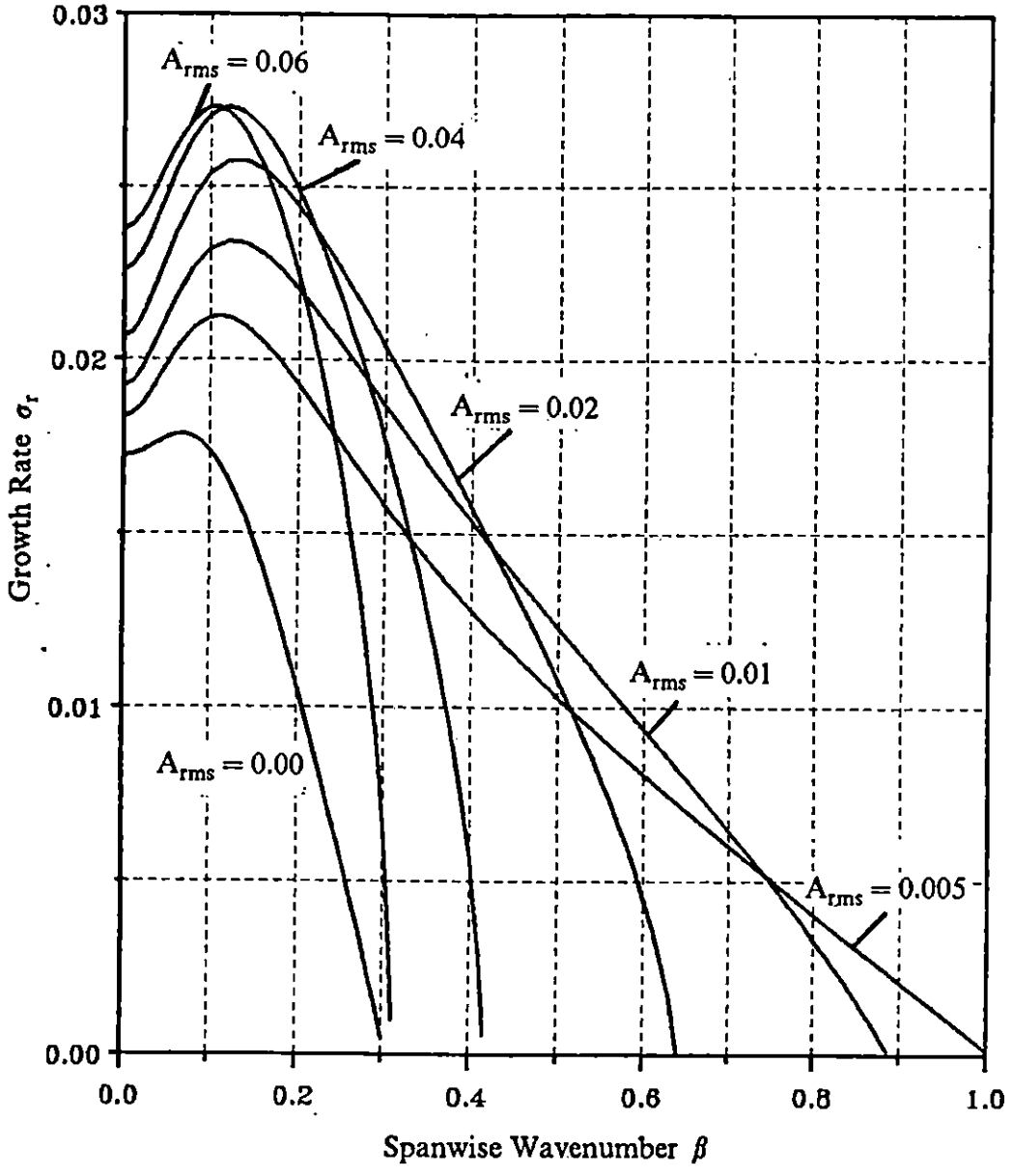

Figure 7.18 The temporal growth rates σ_r of 2D subharmonic mode vs. spanwise wavenumber β for various A_{rms}. TANH Profile, R = 500.0, $M_1 = 1.4$, $U_2 = 0.0$, $T_2 = 1.0$.

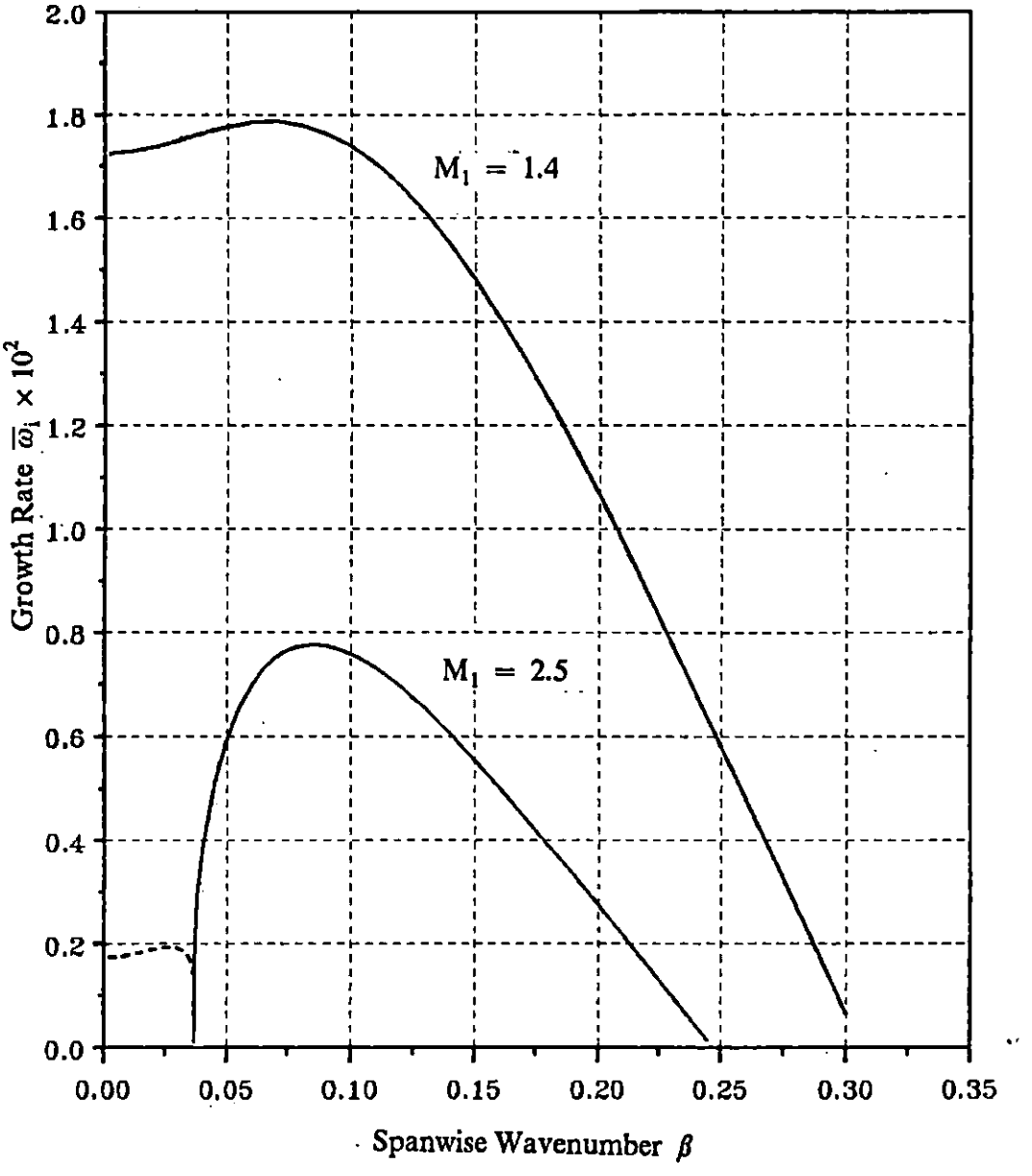

Figure 7.19 The temporal growth rates $\overline{\omega}_i$ of 3D primary wave vs. spanwise wavenumber β for $M_1 = 1.4$ and 2.5. TANH Profile, R = 500.0, $U_2 = 0.0, T_2 = 1.0$.

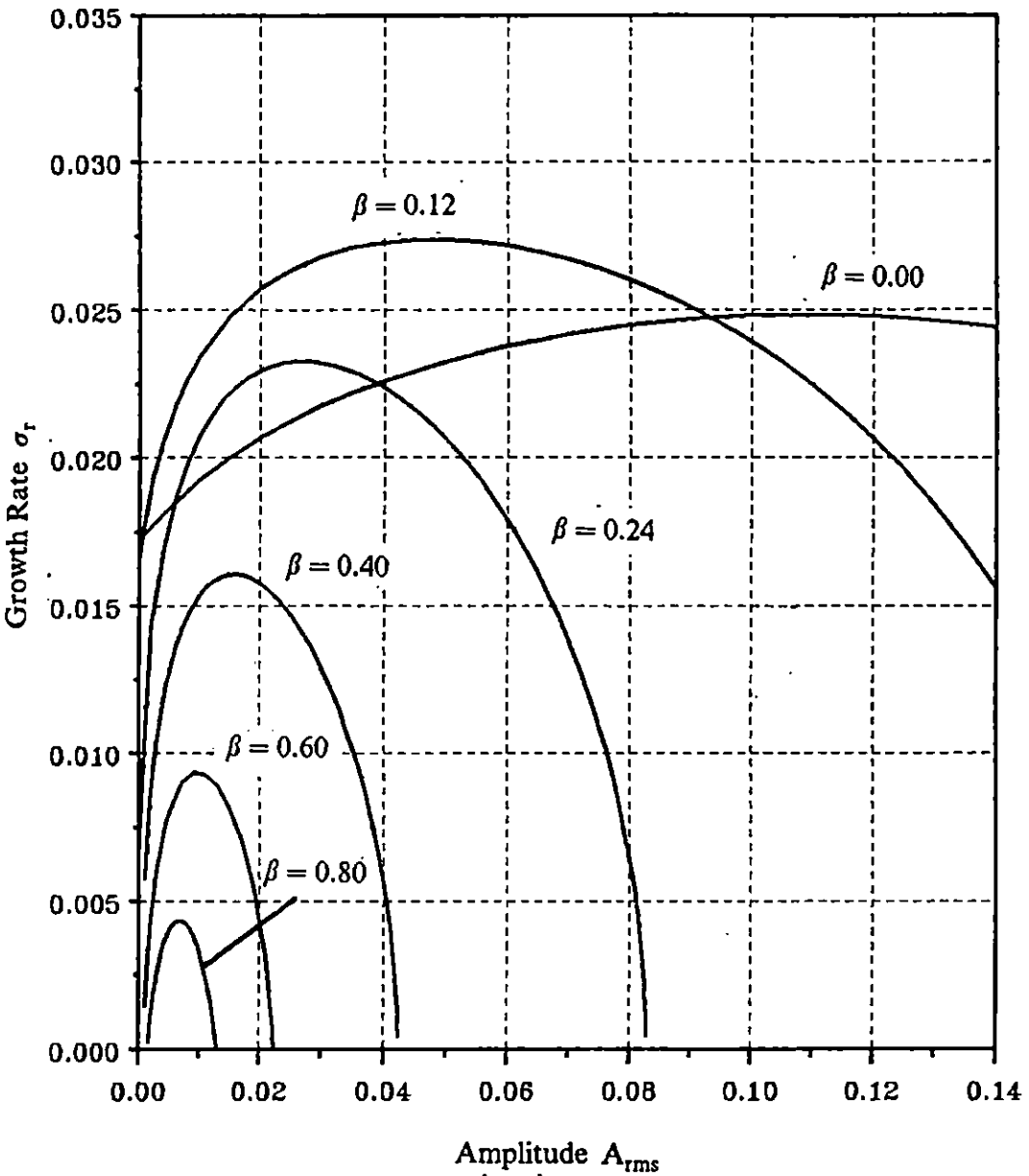

Figure 7.20 The temporal growth rates σ_r of 3D subharmonic mode vs. r.m.s. amplitude A_{rms} for various β. TANH Profile, R = 500.0, $M_1 = 1.4, U_2 = 0.0, T_2 = 1.0$.

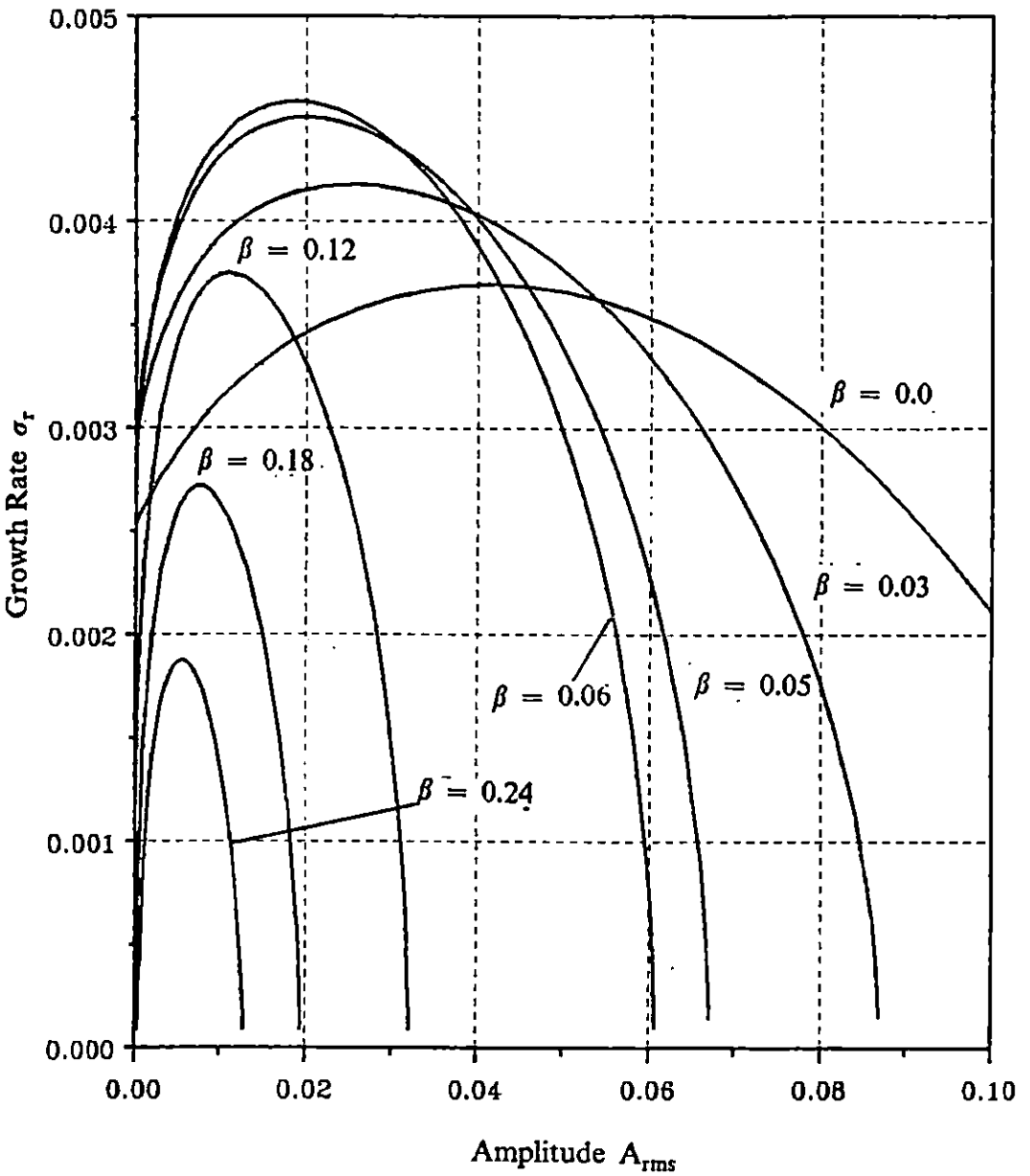

Figure 7.21 The temporal growth rates σ_r of 3D subharmonic mode vs. r.m.s. amplitude A_{rms} for various β. TANH Profile, R = 500.0, $M_1 = 4.0$, $U_2 = 0.6$, $T_2 = 1.0$.

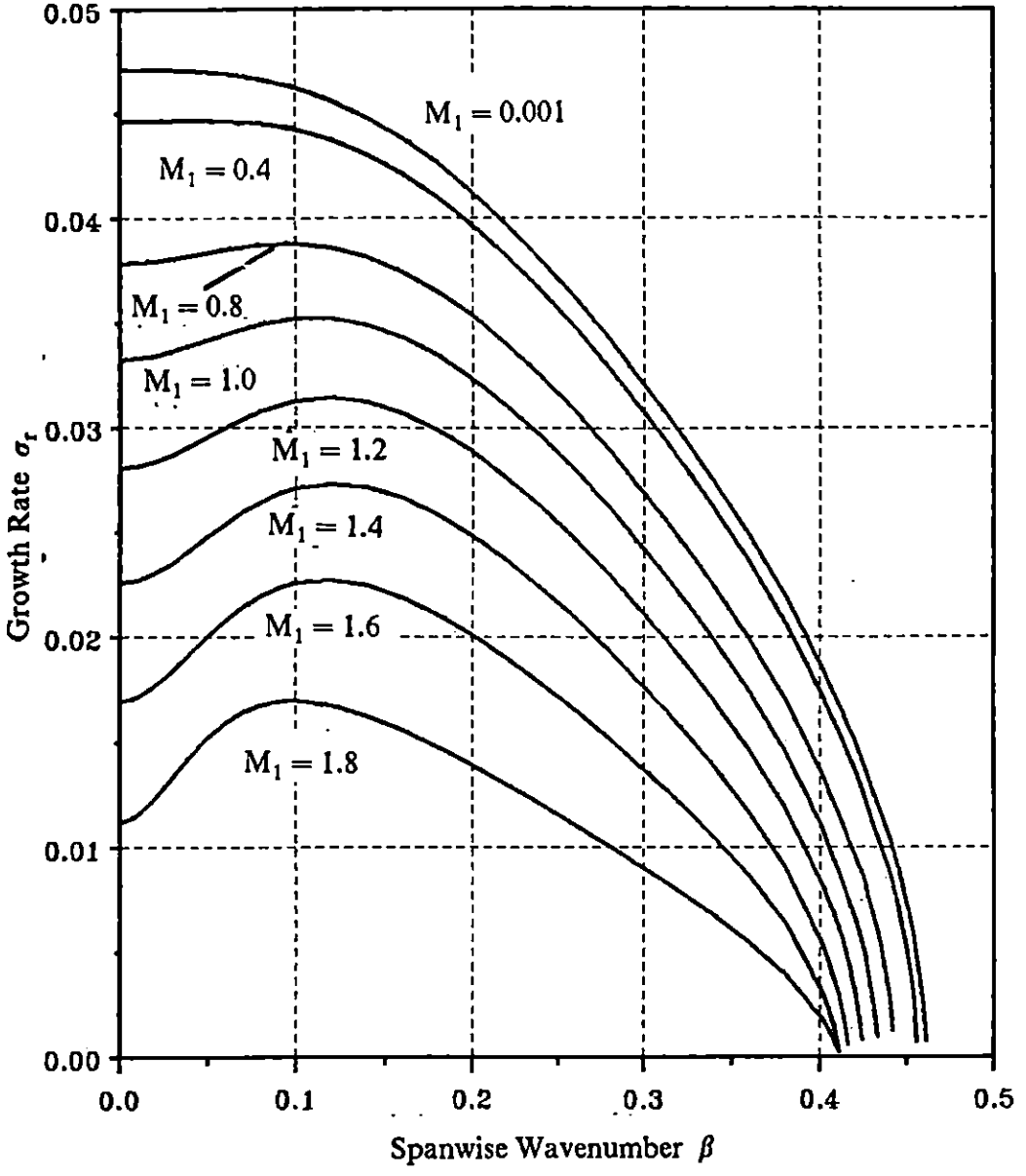

Figure 7.22 The temporal growth rates σ_r of 3D subharmonic mode vs. spanwise wavenumber β for various M_1 with $A_{rms} = 0.04$. TANH Profile, $R = 500.0$, $U_2 = 0.0$, $T_2 = 1.0$.

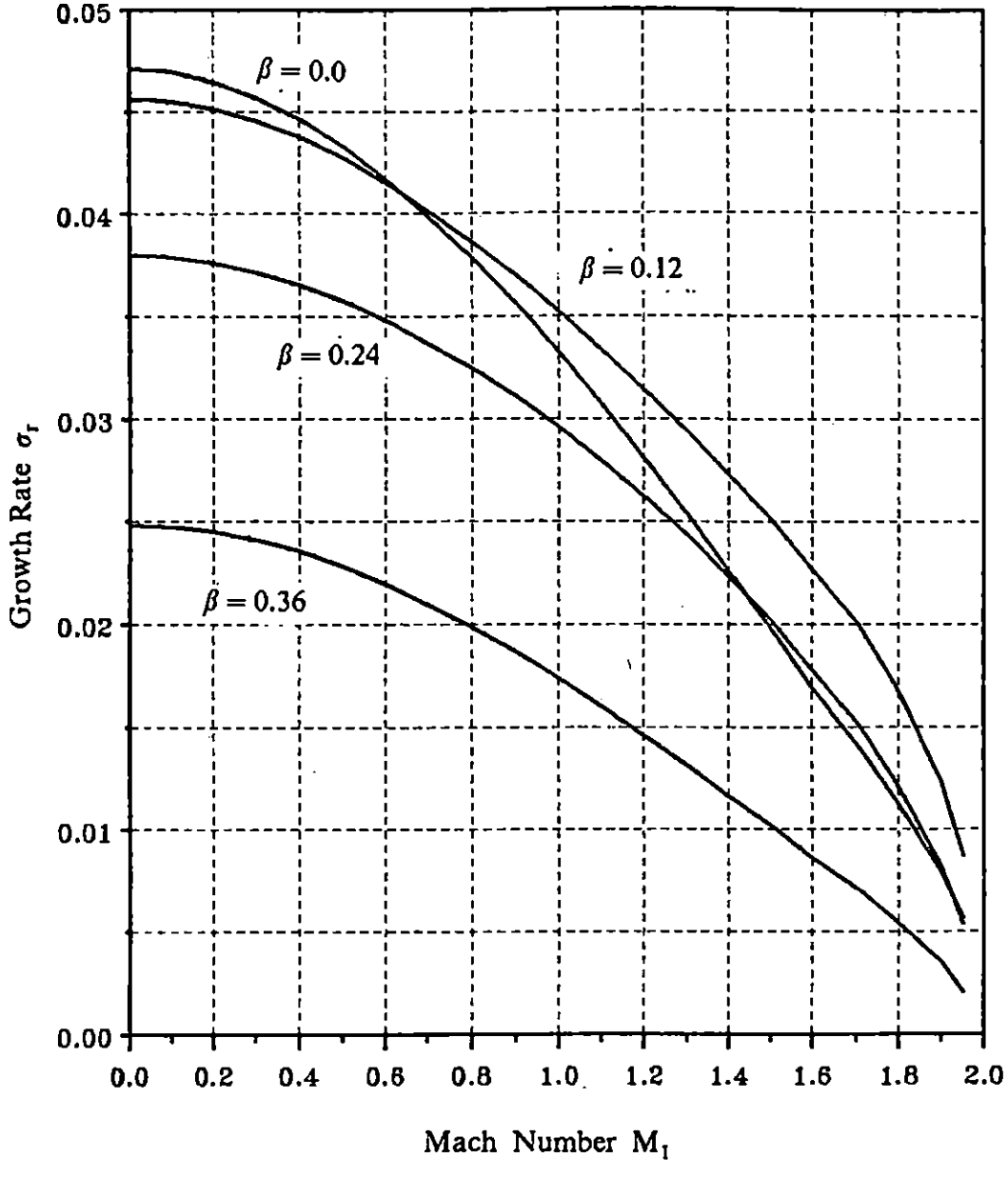

Figure 7.23 The temporal growth rates σ_r of 3D subharmonic mode vs. Mach number M_1 for various β with $A_{rms} = 0.04$. $u_0 = 0.5(1 + \tanh ay)$, $R = 500.0$, $U_2 = 0.0$, $T_2 = 1.0$.

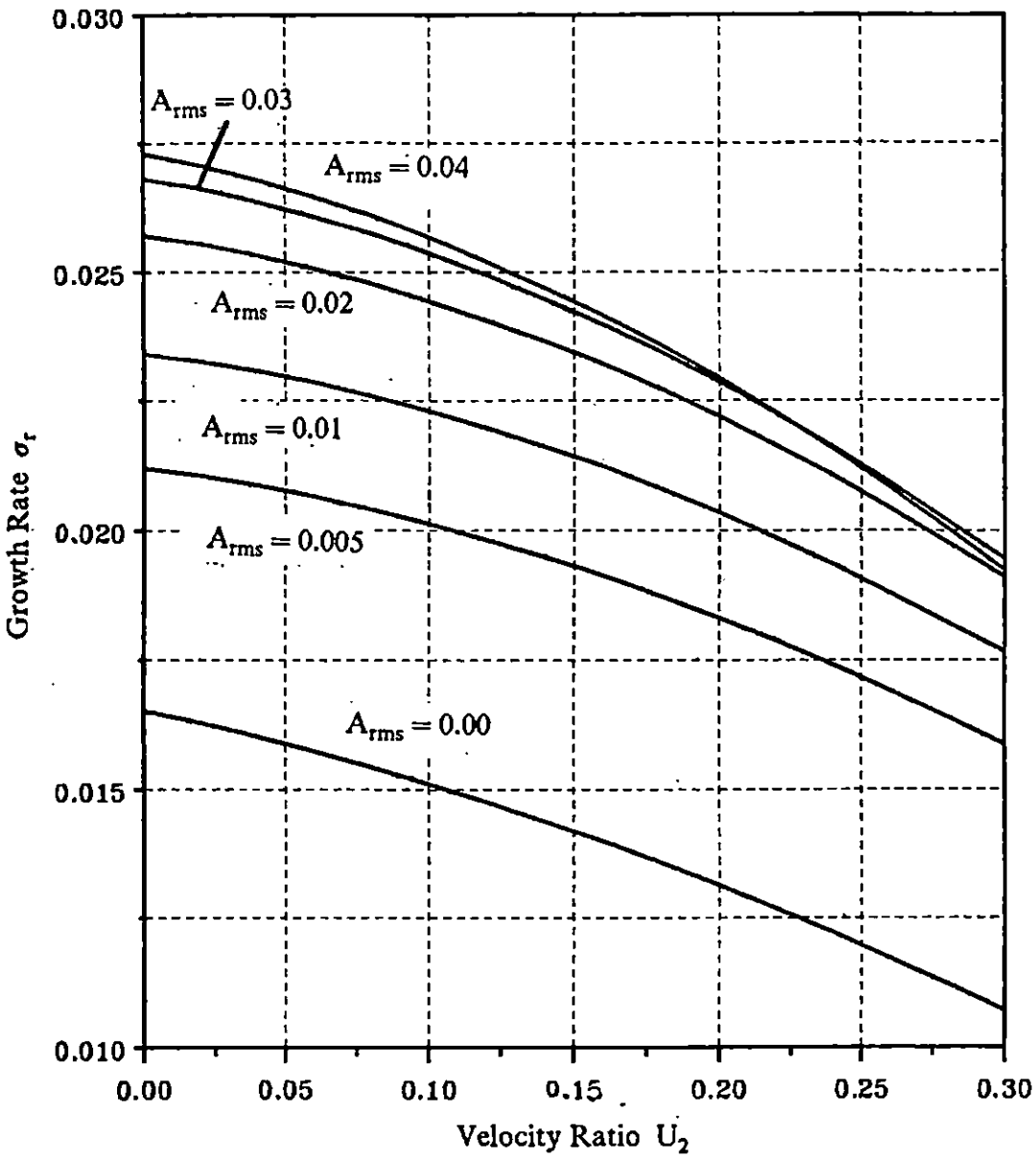

Figure 7.24 The temporal growth rates σ_r of 3D subharmonic mode vs. velocity ratio U_2 for various A_{rms}. TANH Profile, R = 500.0, M_1 = 1.4, U_2 = 0.0, T_2 = 1.0, β = 0.12.

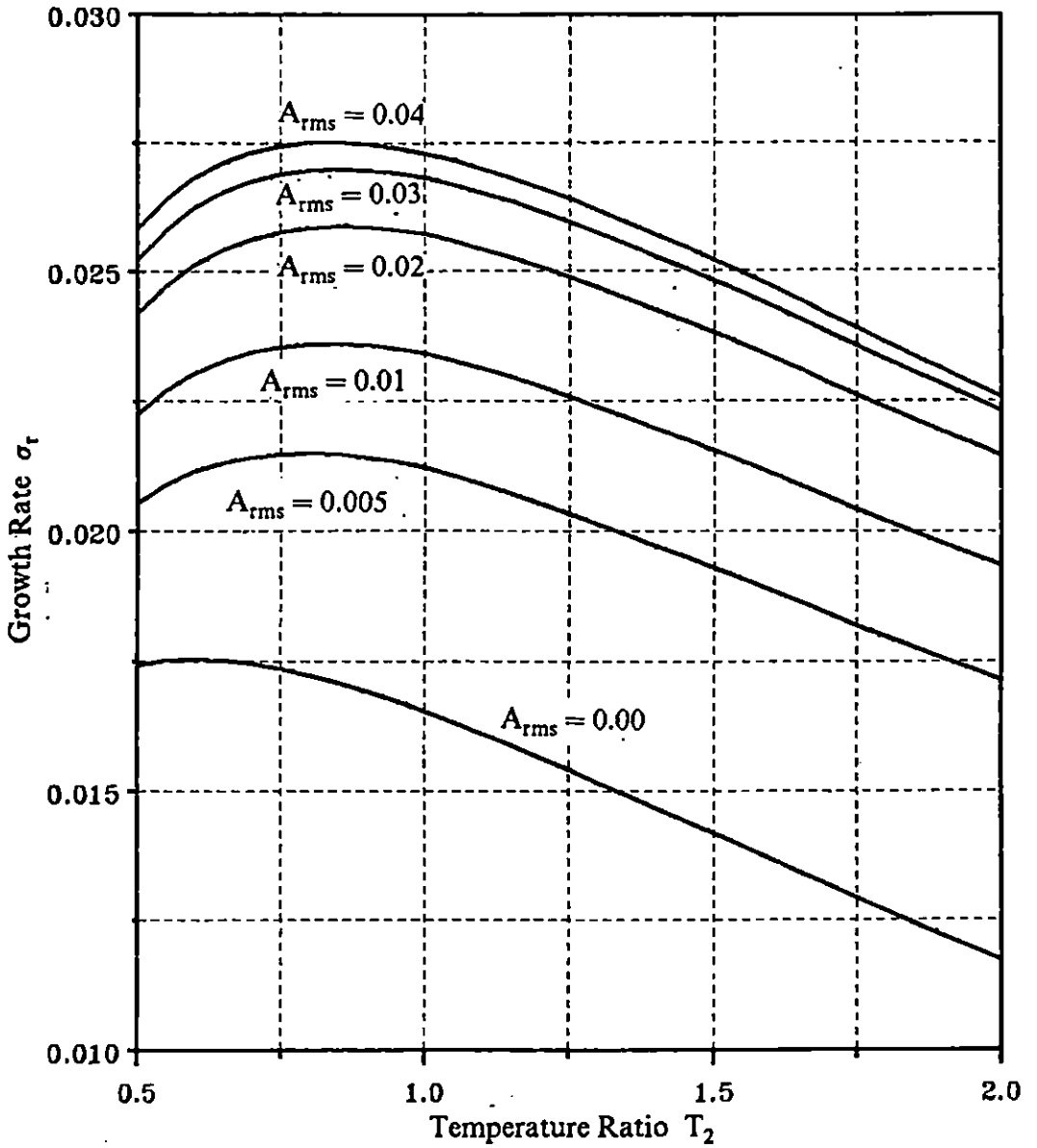

Figure 7.25 The temporal growth rates σ_r of 3D subharmonic mode vs. temperature ratio T_2 for various A_{rms}. TANH Profile, R = 500.0, $M_1 = 1.4, U_2 = 0.0, T_2 = 1.0, \beta = 0.12$.

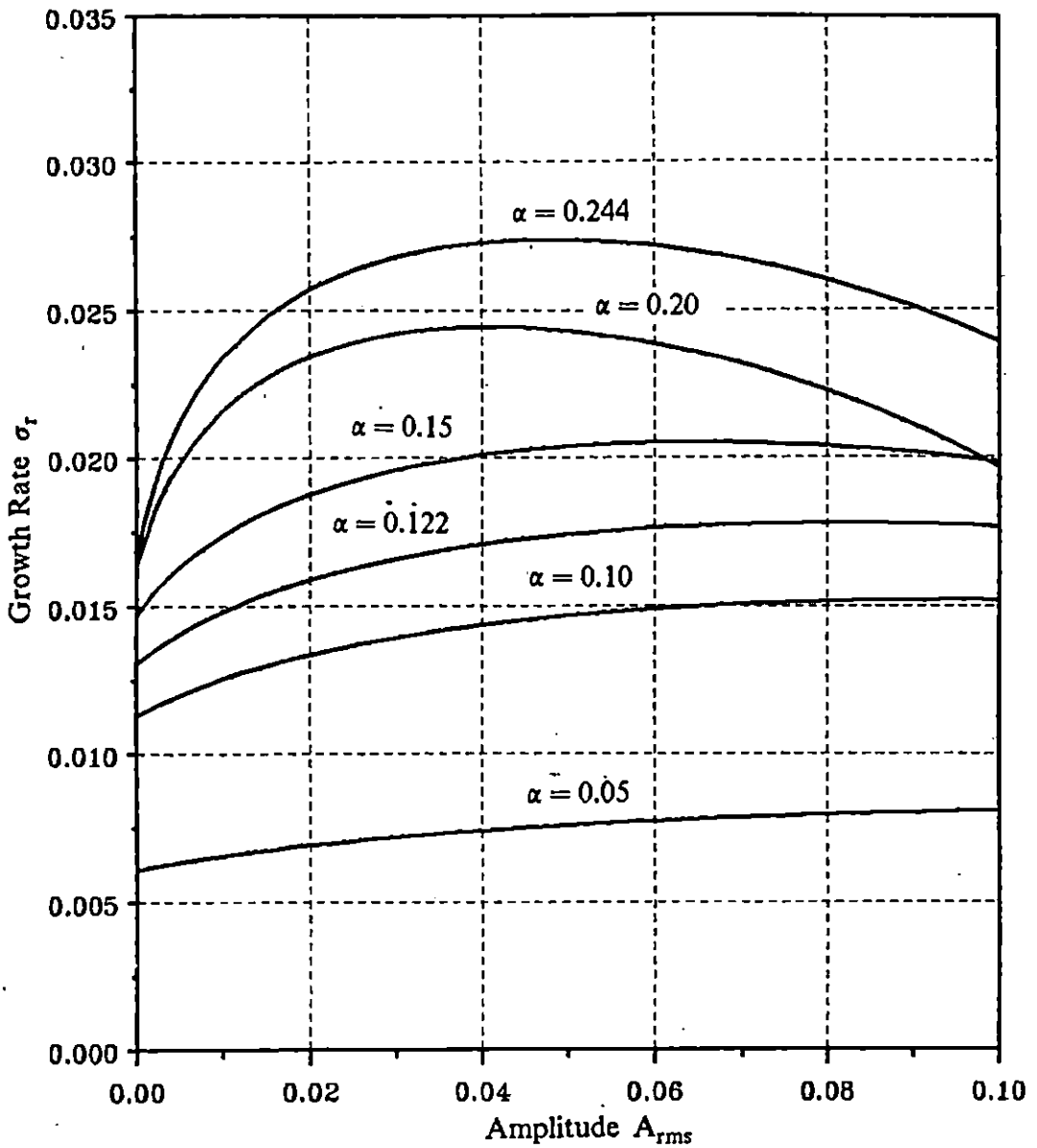

Figure 7.26 The temporal growth rates σ_r of 2D subharmonic mode vs. A_{rms} for different periodic waves. TANH Profile, R = 500.0, $M_1 = 1.4$, $U_2 = 0.0$, $T_2 = 1.0$.

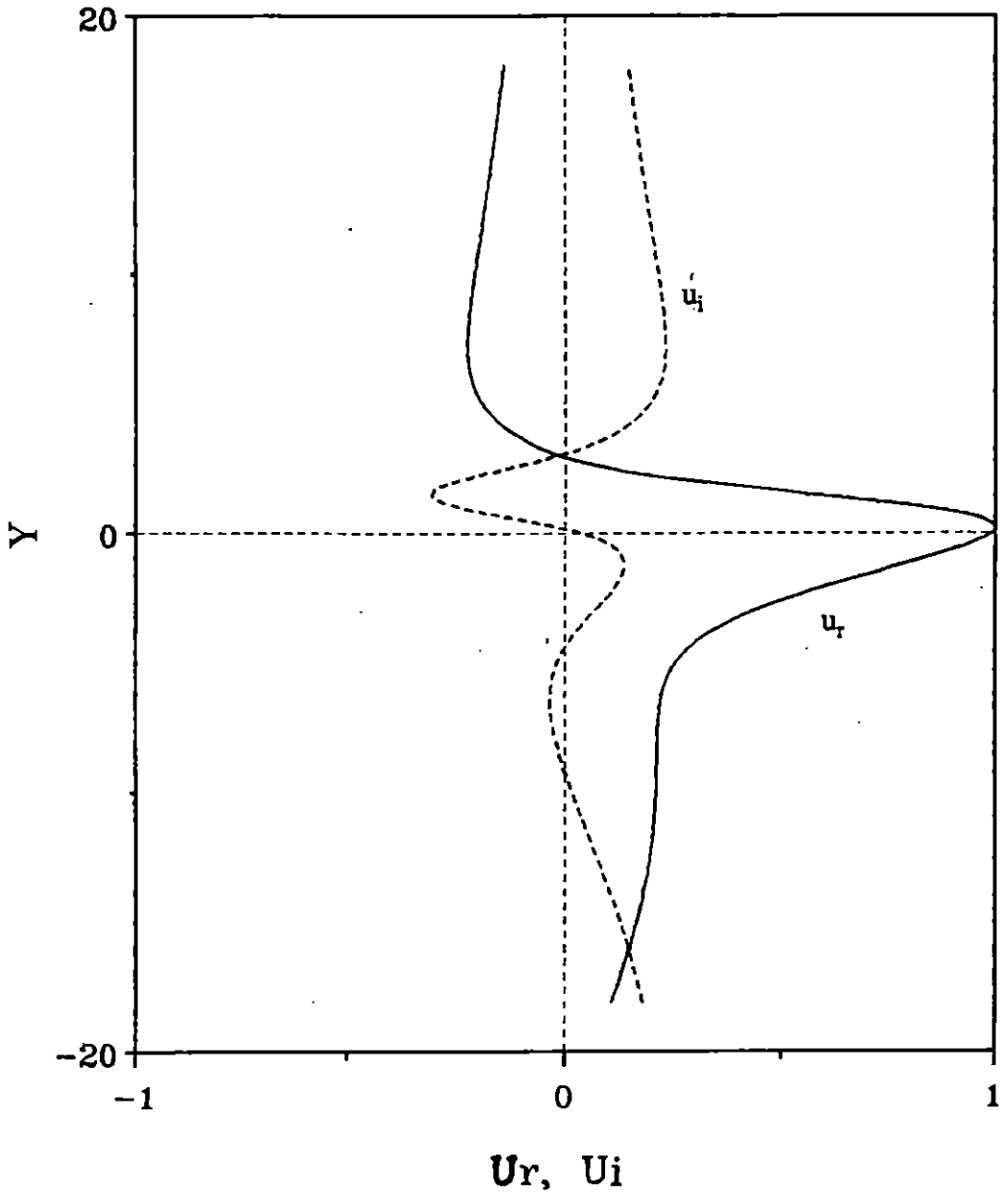

Figure 7.27 The real and imaginary parts of u-component of 2D neutral primary wave eigenfunction. TANH Profile, R = 500, M_1 = 2.5, U_2 = 0.0, T_2 = 1.0 . The wavenumber and frequency of the wave are α_r = 0.09, ω_r = 0.06.

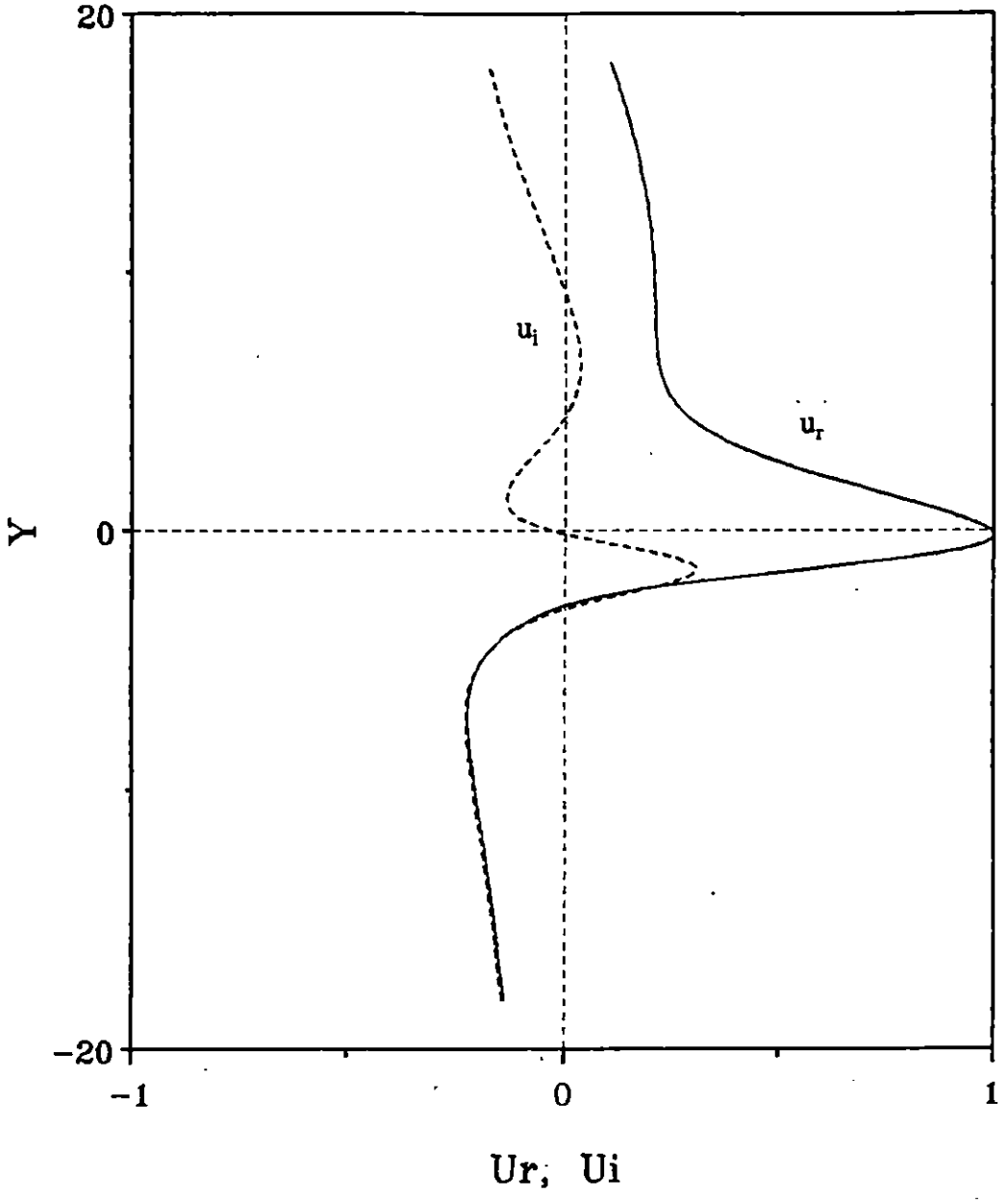

Figure 7.28 The real and imaginary parts of u-component of 2D neutral primary wave eigenfunction. TANH Profile, R = 500, M_1 = 2.5, U_2 = 0.0, T_2 = 1.0 . The wavenumber and frequency of the wave are α_r = 0.09, ω_r = 0.03.

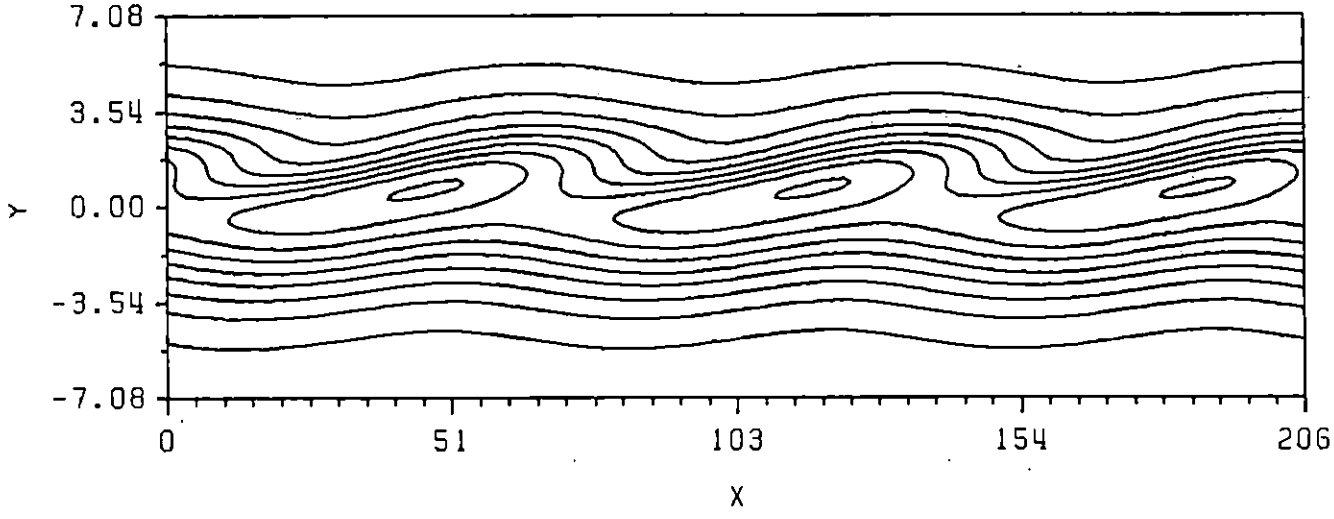

Figure 7.29 The vorticity contours of the mean flow and a periodic wave with a wavenumber $\alpha_r = 0.09$ and a frequency $\omega_r = 0.06$. TANH Profile, R = 500, $M_1 = 2.5$, $U_2 = 0.0$, $T_2 = 1.0$.

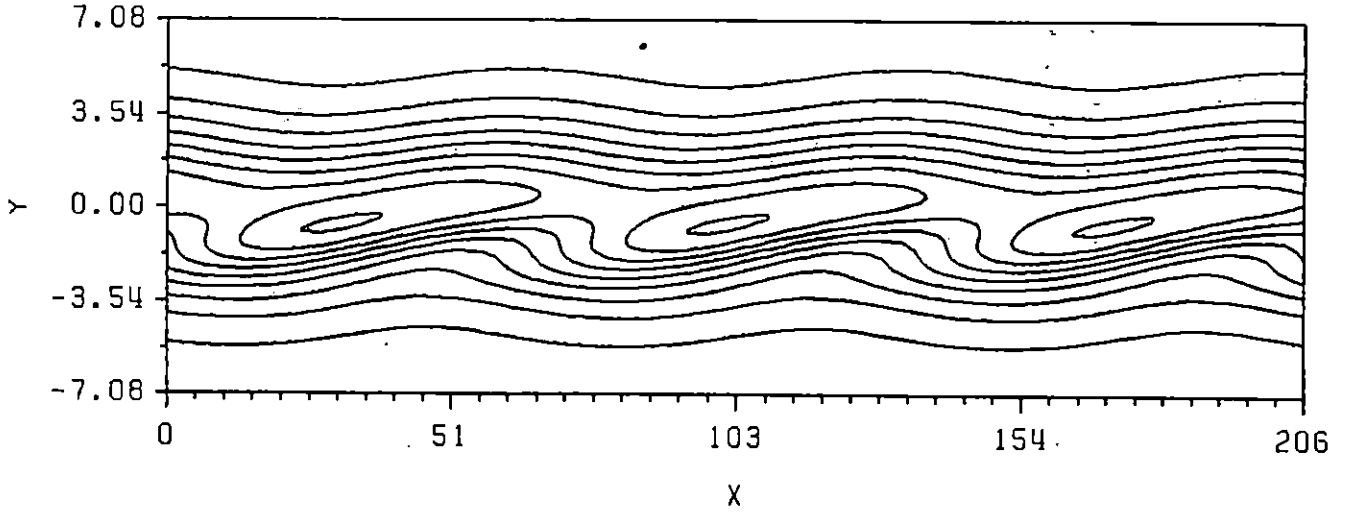

Figure 7.30 The vorticity contours of the mean flow and a periodic wave with wavenumber $\alpha_r = 0.09$ and frequency $\omega_r = 0.03$. TANH Profile, R = 500, $M_1 = 2.5$, $U_2 = 0.0$, $T_2 = 1.0$.

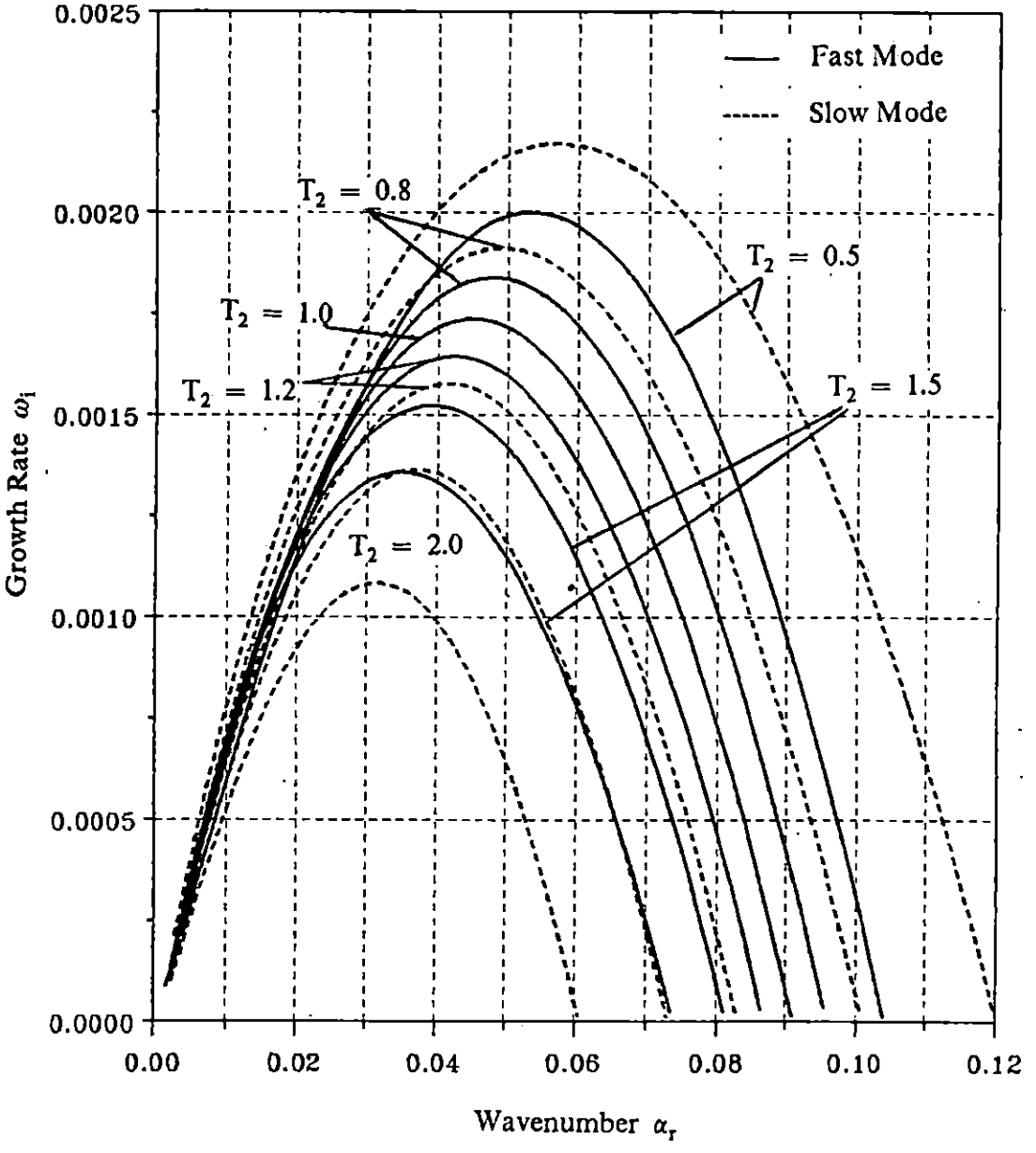

Figure 7.31 The temporal growth rates of ω_i of 2D primary wave vs. wavenumber α_r for various T_2. TANH Profile, R = 500, M_1 = 2.5 , U_2 = 0.0, T_2 = 1.0

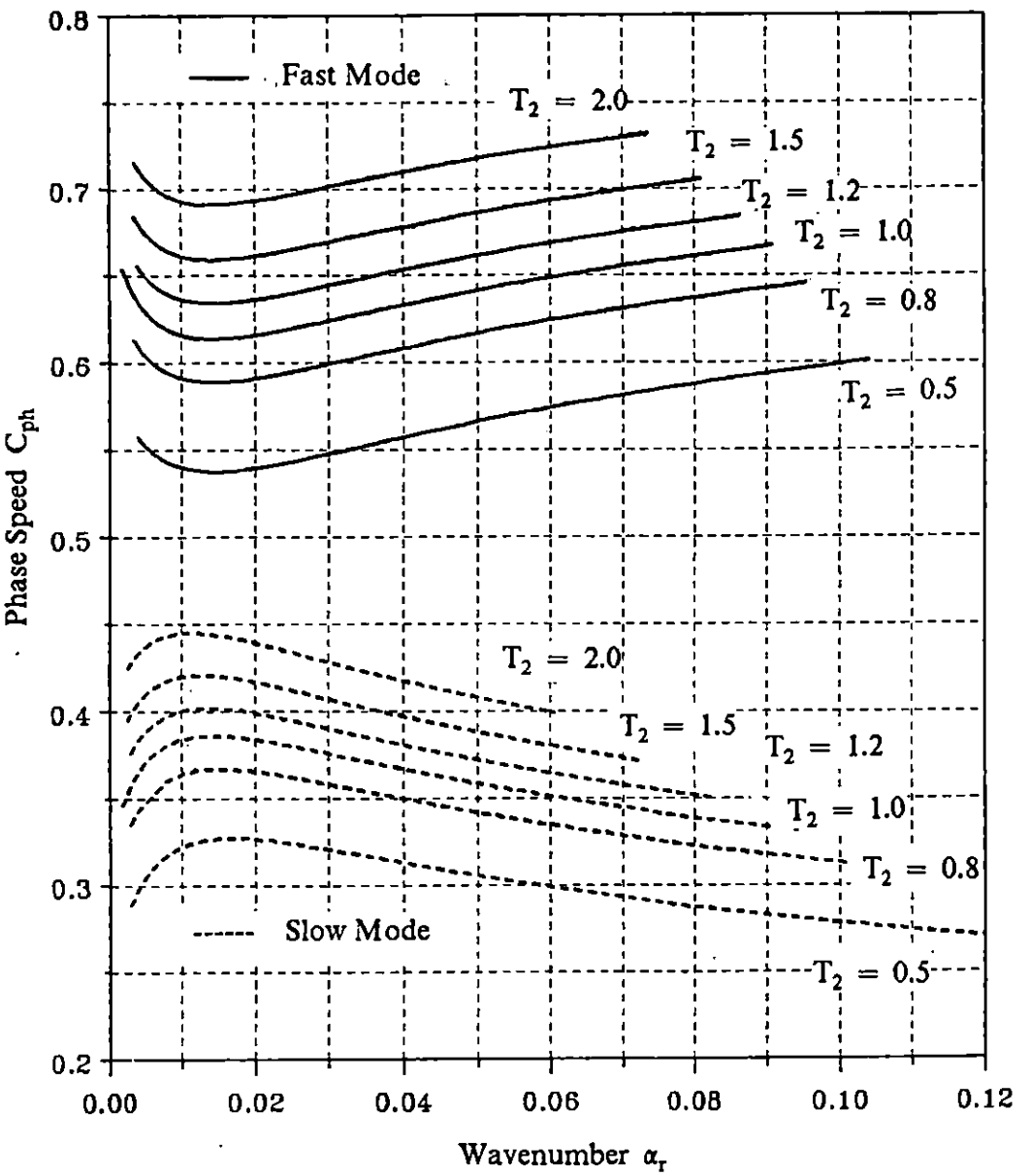

Figure 7.32 The Phase speeds of ω_1 of 2D primary wave vs. wavenumber α_r for various T_2. TANH Profile, R = 500, M_1 = 2.5, U_2 = 0.0, T_2 = 1.0

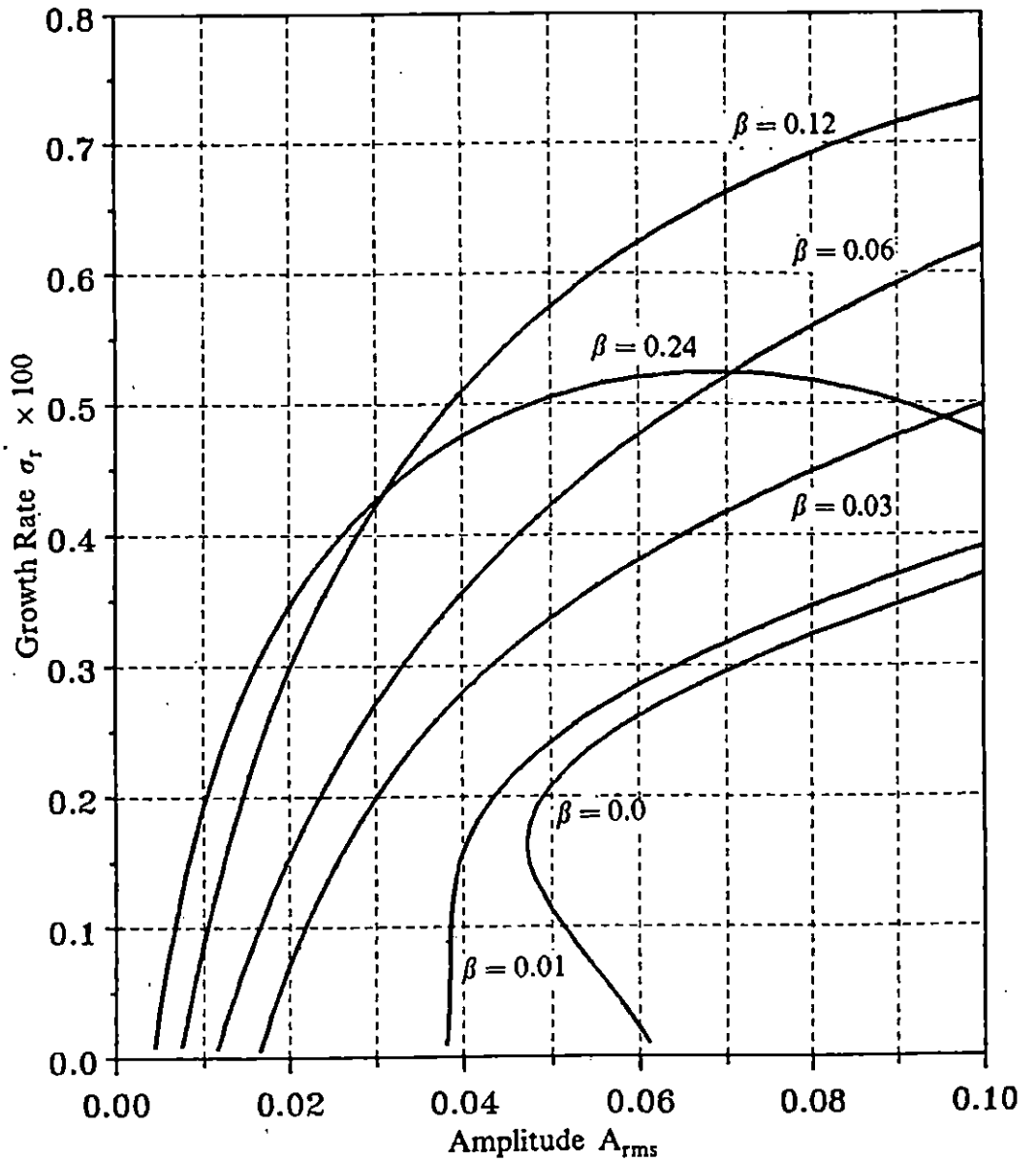

Figure 7.33 The growth rates σ_r of 3D subharmonic synchronized mode vs. r.m.s. amplitude A_{rms} for various β . TANH Profile, R = 500, $M_1 = 2.5, U_2 = 0.0, T_2 = 1.0$.

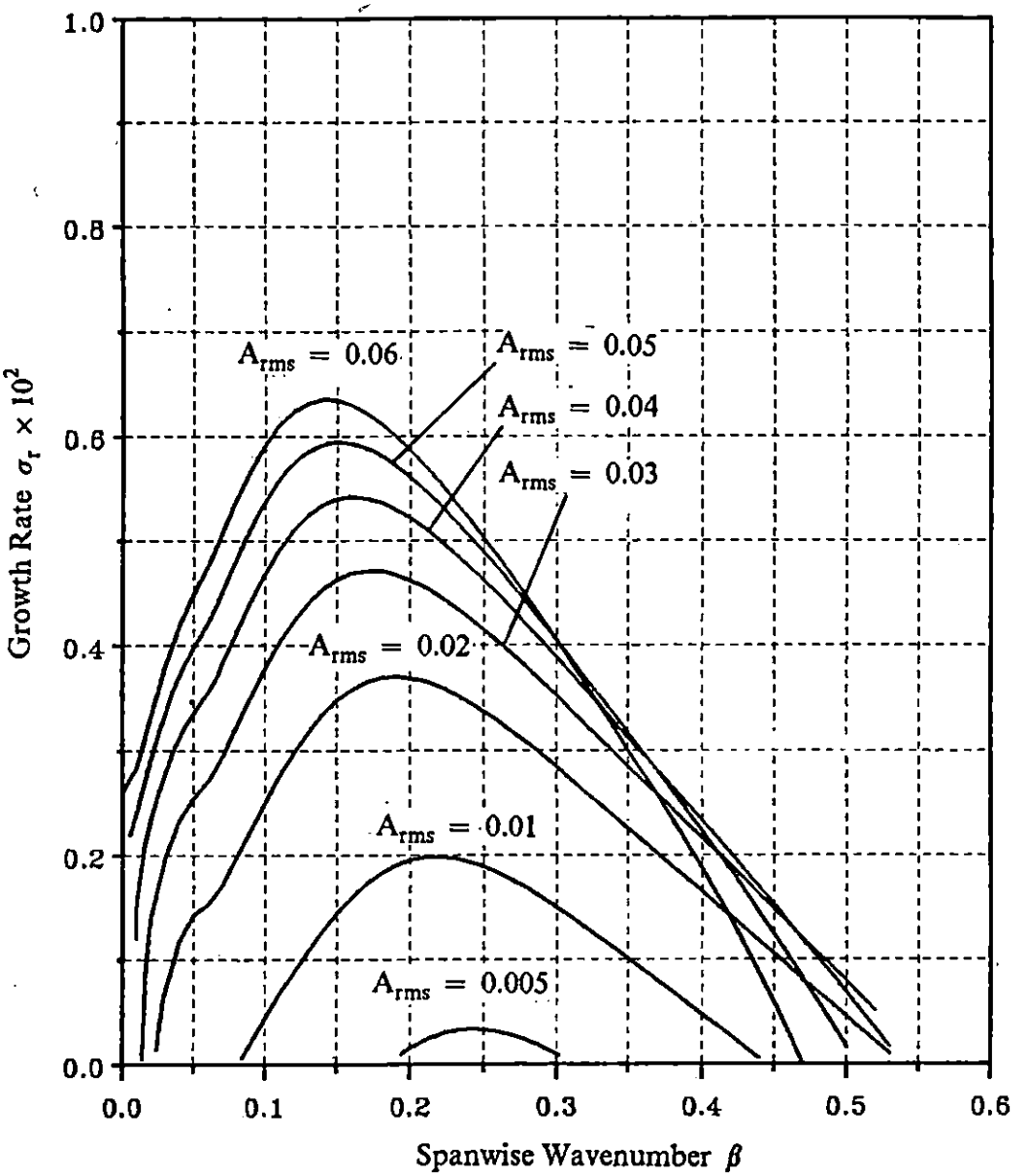

Figure 7.34 The growth rates σ_r of 3D subharmonic synchronized mode vs. spanwise wavenumber β for various A_{rms}. TANH Profile, R = 500, $M_1 = 2.5, U_2 = 0.0, T_2 = 1.0$.

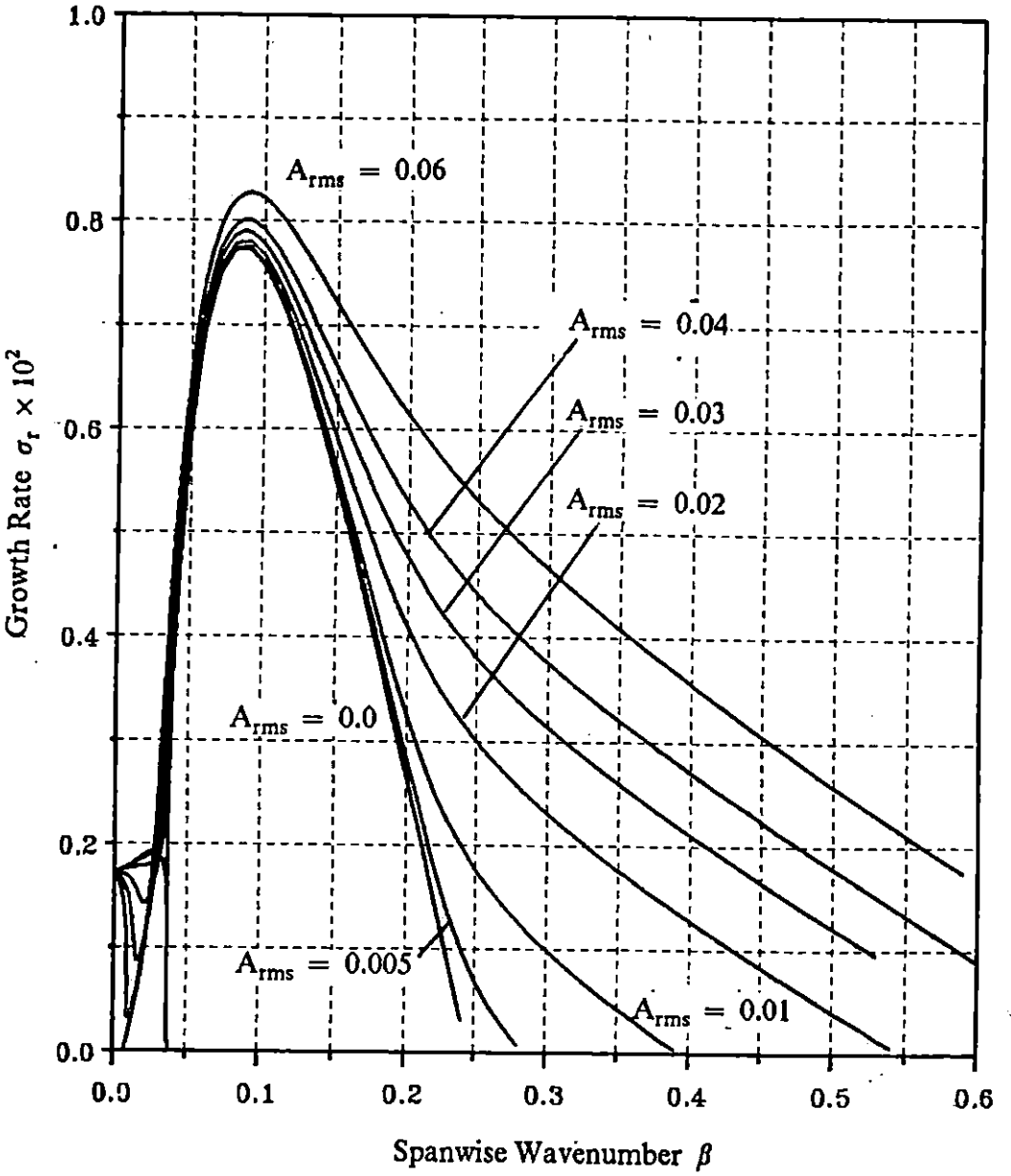

Figure 7.35 The growth rates σ_r of 3D subharmonic detuned mode vs. spanwise wavenumber β for various A_{rms} . TANH Profile, R = 500, $M_1 = 2.5$, $U_2 = 0.0$, $T_2 = 1.0$.

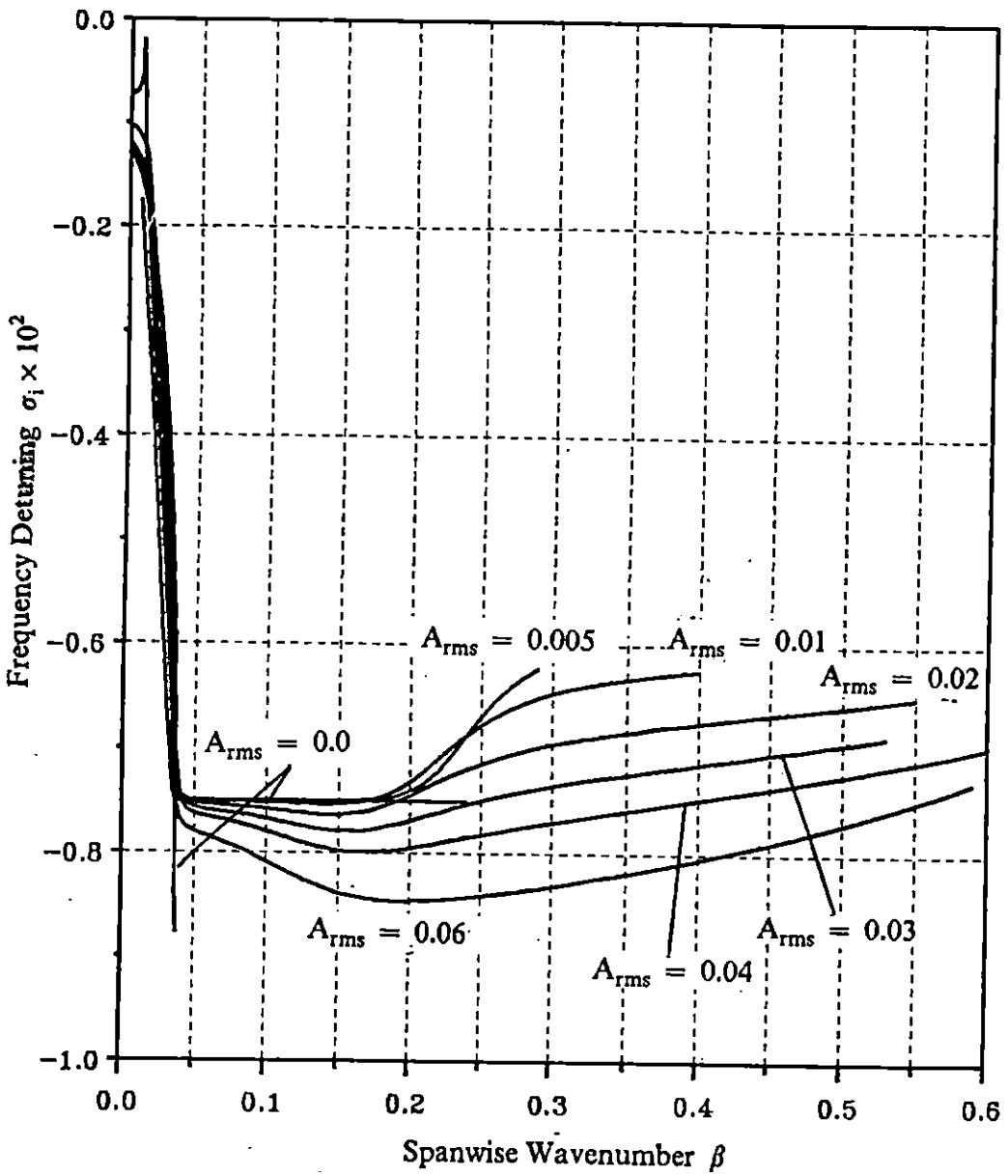

Figure 7.36 The detuned frequency σ_i of 3D subharmonic detuned mode vs. spanwise wavenumber β for various A_{rms} . TANH Profile, R = 500, $M_1 = 2.5, U_2 = 0.0, T_2 = 1.0$.

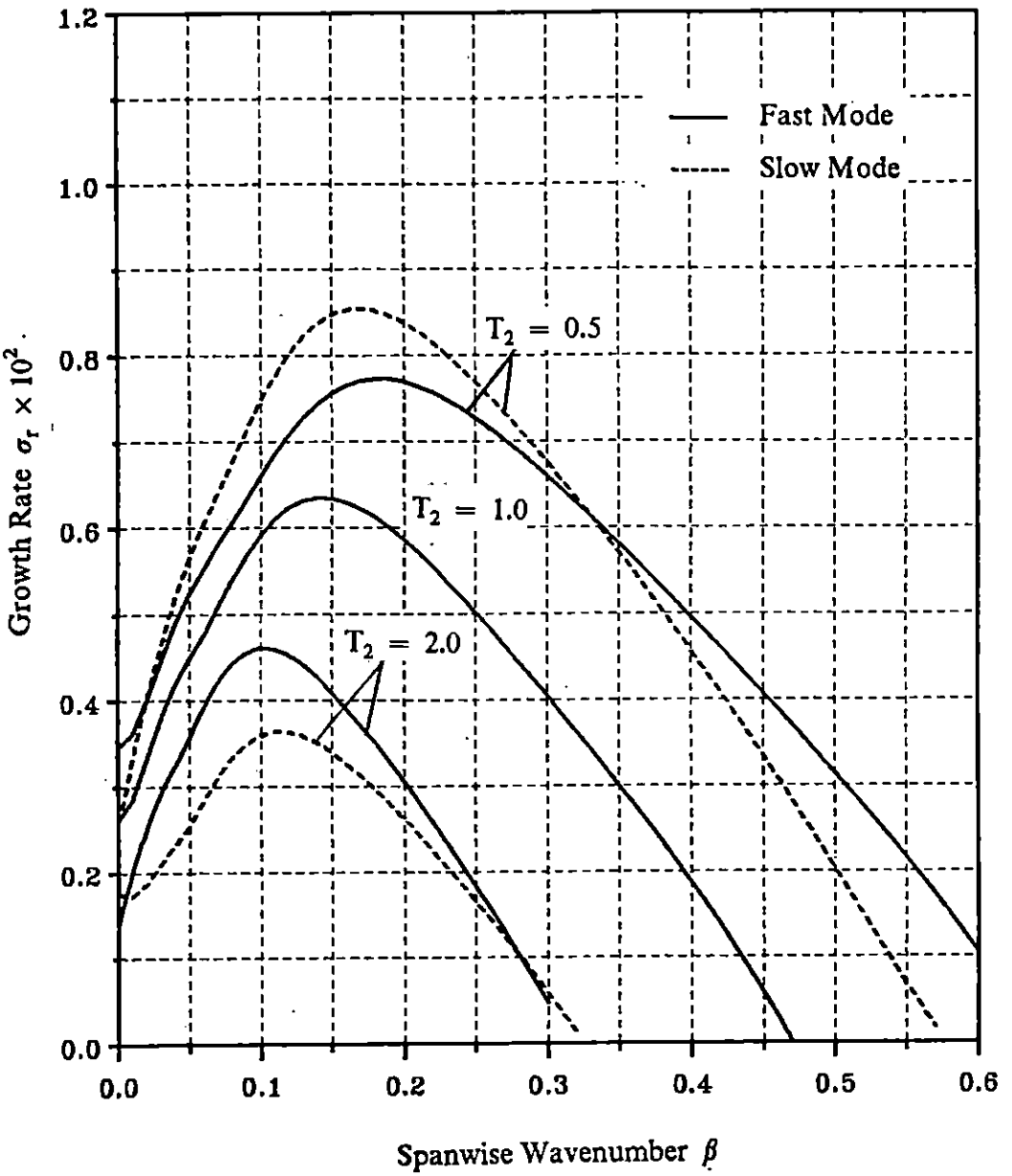

Figure 7.37 The growth rates σ_r of 3D subharmonic synchronized mode vs. spanwise wavenumber β for various T_2 with A_{rms} = 0.06. TANH Profile, R = 500, M_1 = 2.5, U_2 = 0.0.

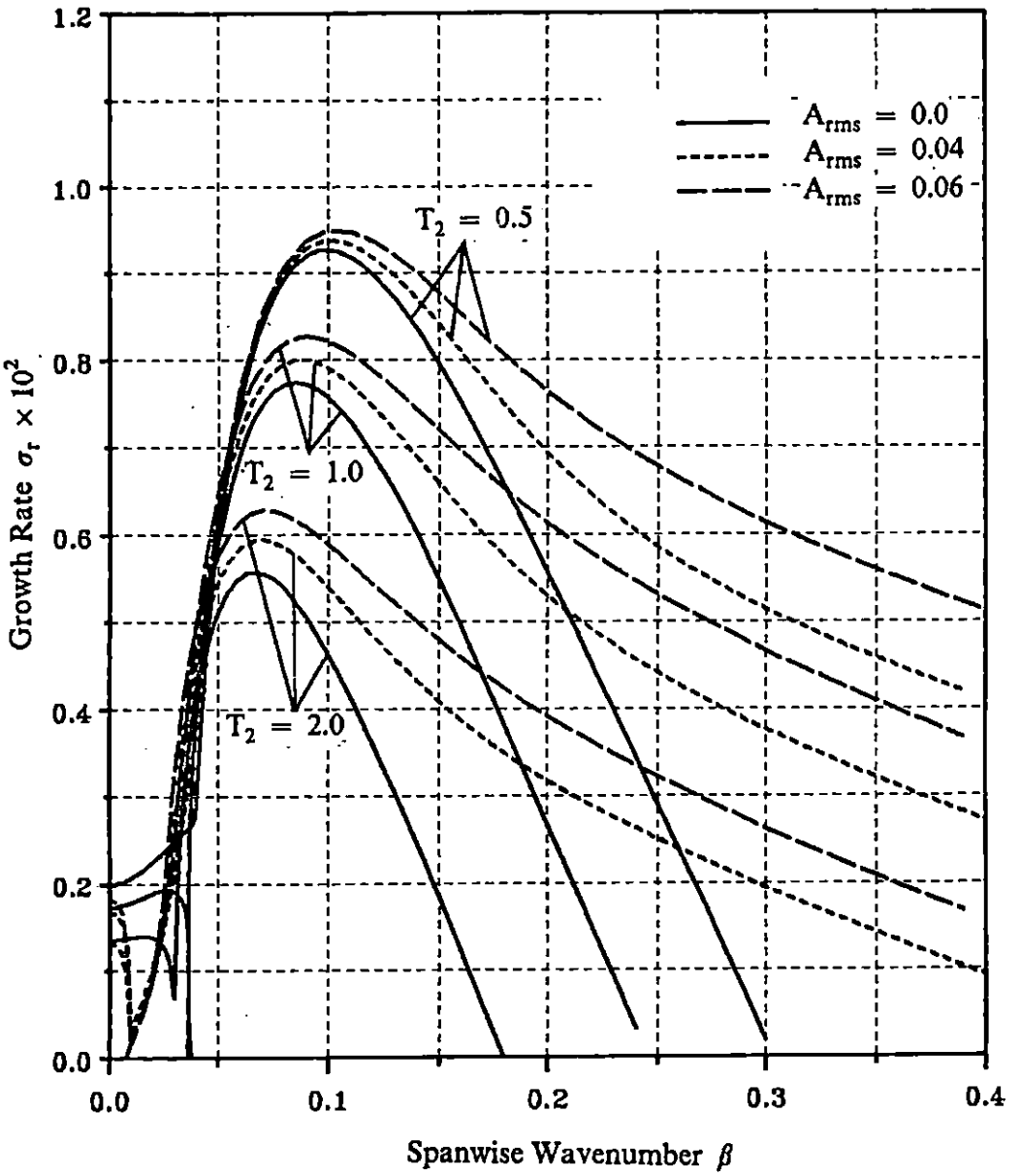

Figure 7.38 The growth rates σ_r of 3D subharmonic detuned mode vs. spanwise wavenumber β for various T_2 and A_{rms}. (Fast Primary Mode). TANH Profile, R = 500, M_1 = 2:5, U_2 = 0.0.

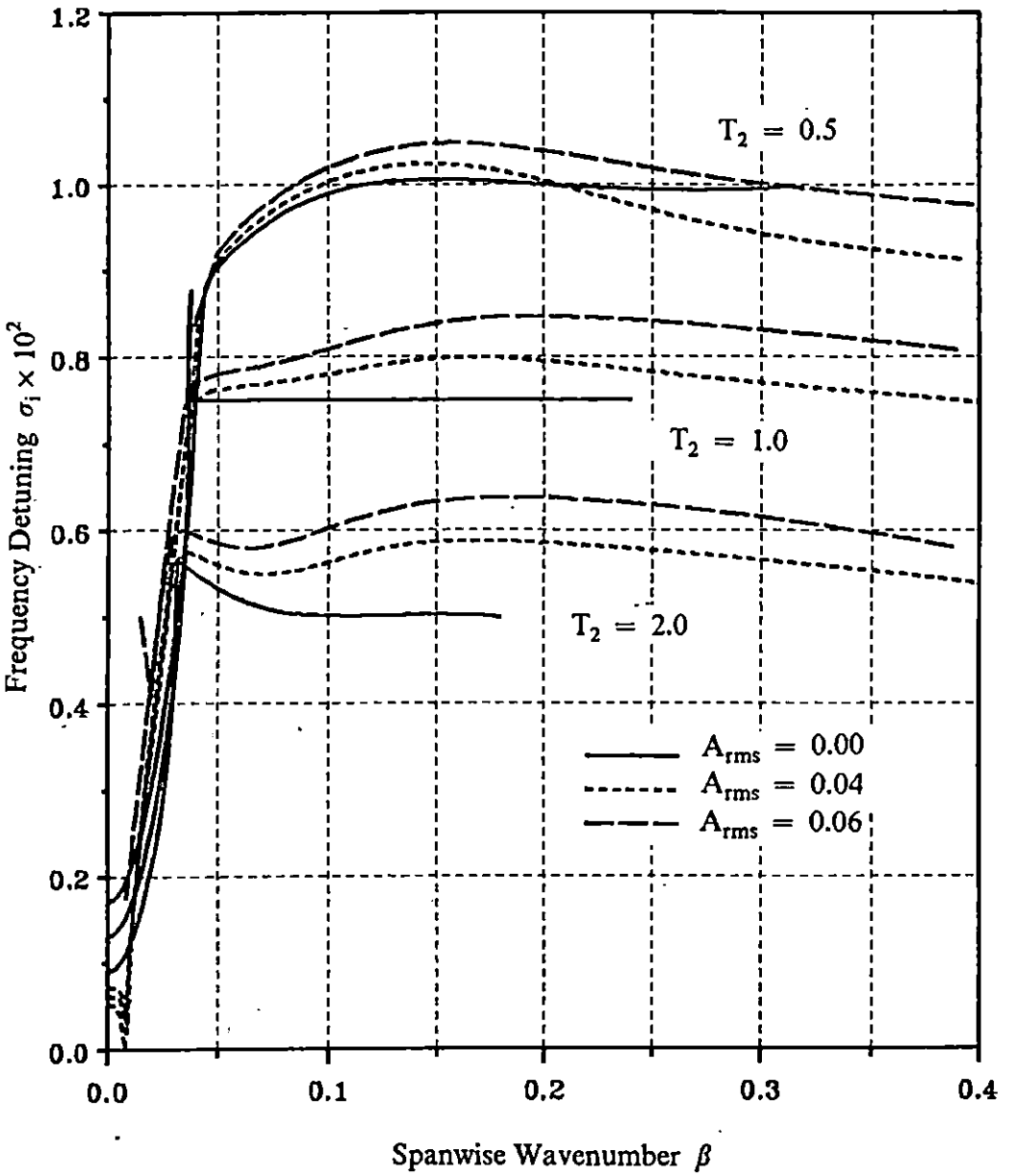

Figure 7.39 The detuned frequency σ_i of 3D subharmonic detuned mode vs. spanwise wavenumber β for various T_2 . TANH Profile, R = 500, M_1 = 2.5, U_2 = 0.0 and T_2 = 1.0 (Fast Primary Mode).

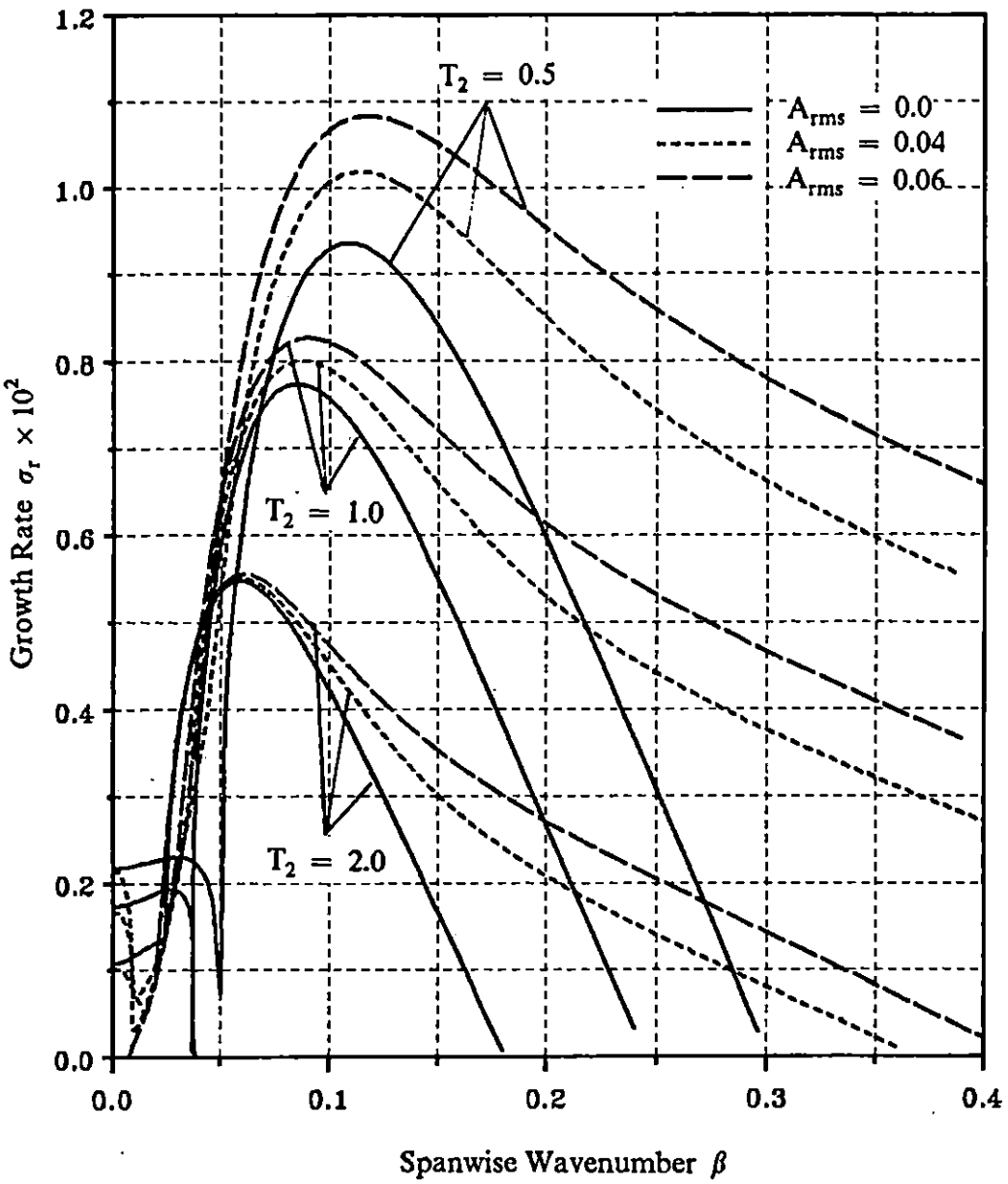

Figure 7.40 The growth rates σ_r of 3D subharmonic detuned mode vs. spanwise wavenumber β for various T_2 and A_{rms}. (Slow Primary Mode). TANH Profile, R = 500, M_1 = 2.5, U_2 = 0.0.

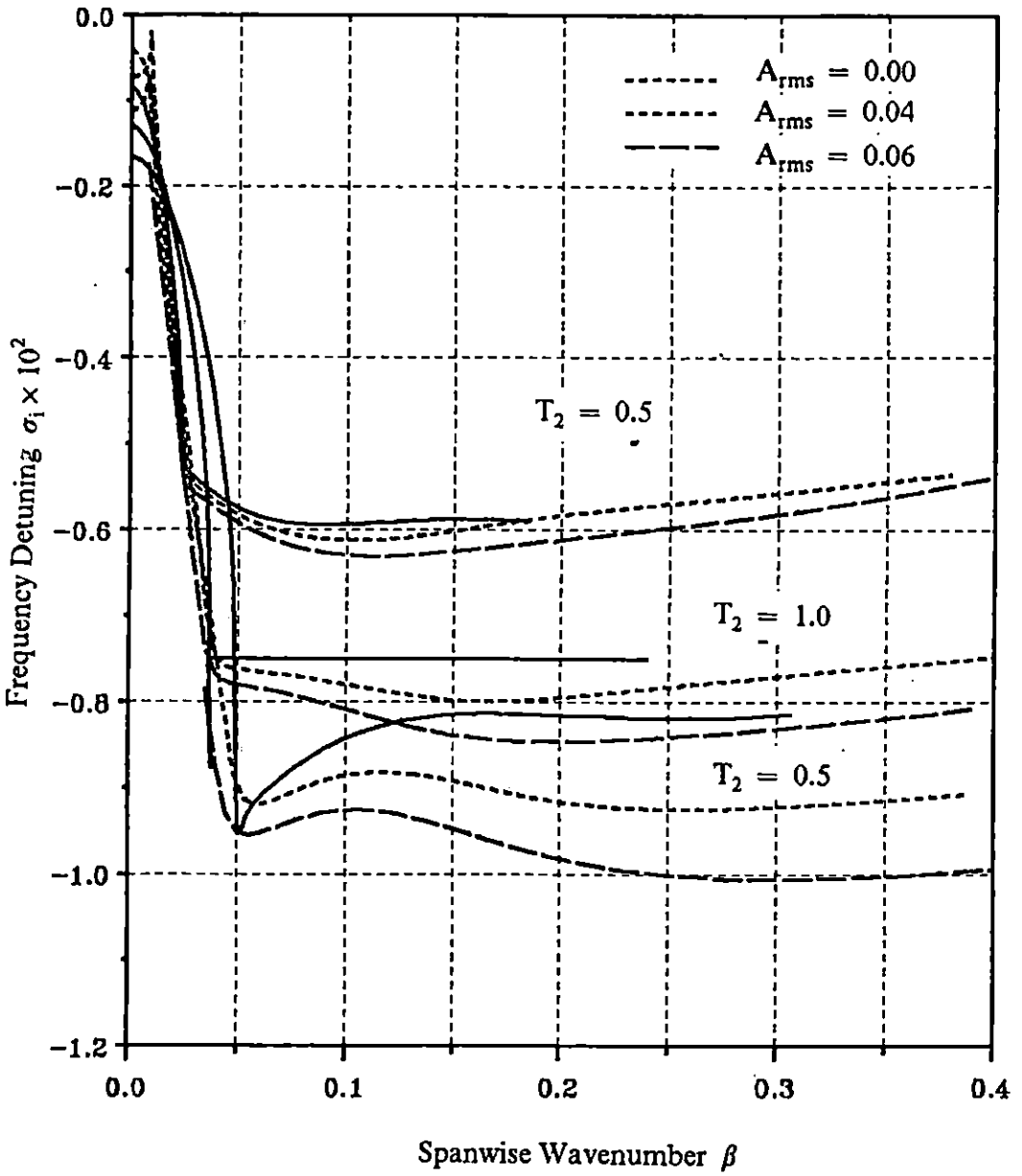

Figure 7.41 The detuned frequency σ_1 of 3D subharmonic detuned mode vs. spanwise wavenumber β for various T_2 . TANH Profile, R = 500, M_1 = 2.5, U_2 = 0.0 and T_2 = 1.0 (Slow Primary Mode).

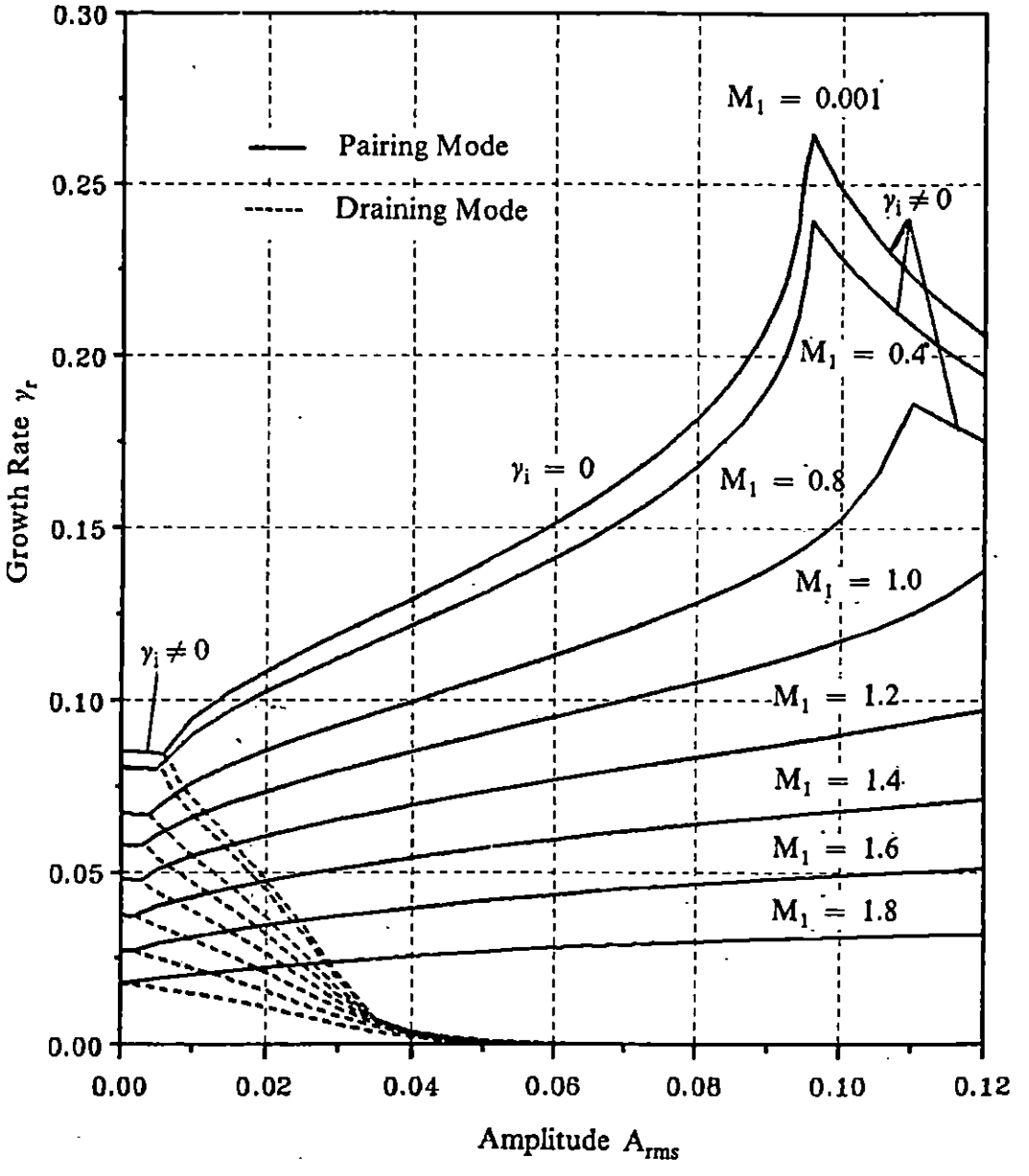

Figure 7.42 The spatial growth rates γ_r of 2D subharmonic mode vs. r.m.s. amplitude A_{rms} for various Mach number M_1. TANH Profile, R = 500.0, $U_2 = 0.0$, $T_2 = 1.0$.

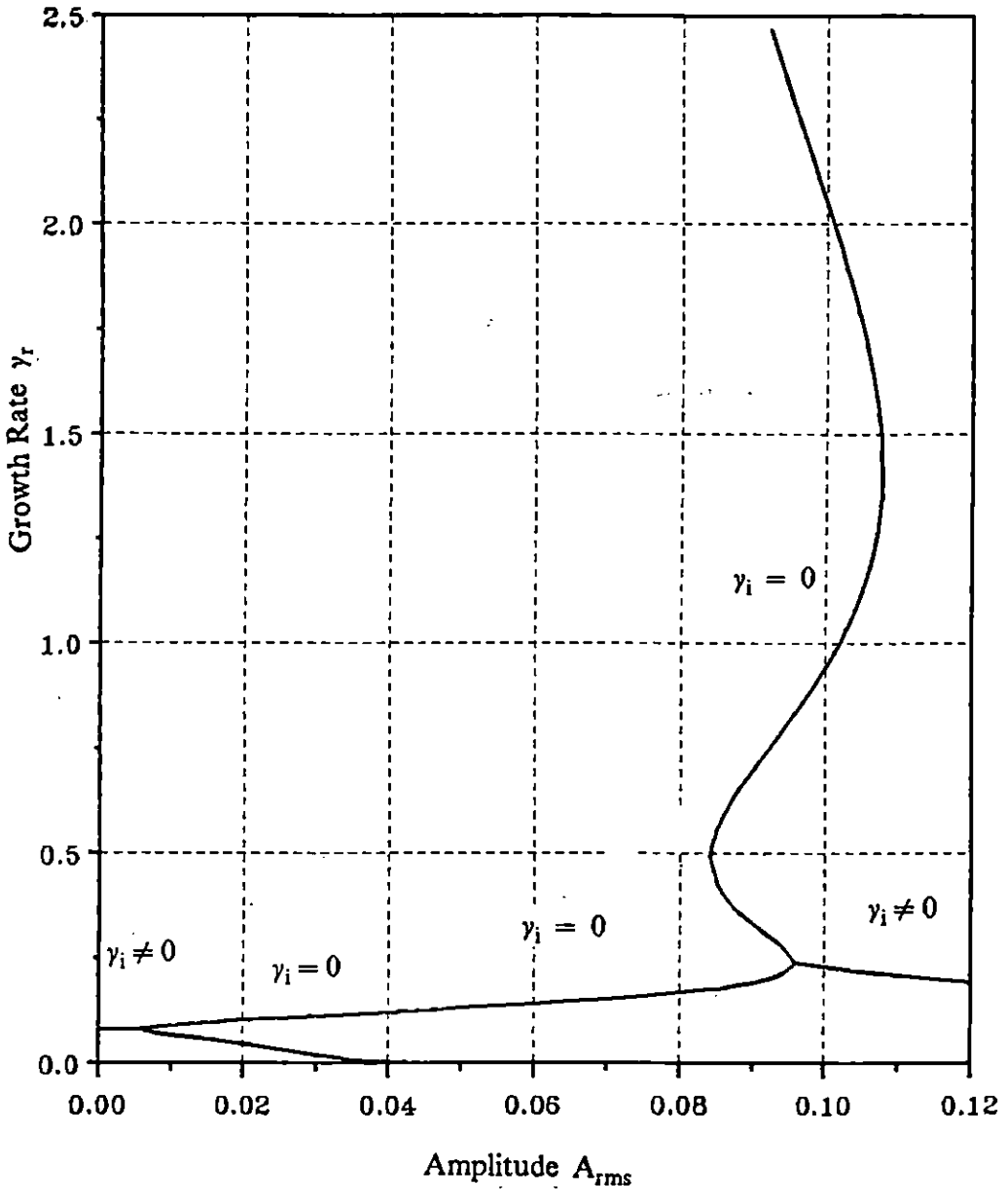

Figure 7.43 The spatial growth rates γ_r of 2D subharmonic mode vs. r.m.s. amplitude A_{rms} for the Mach number $M_1 = 0.4$. TANH Profile, $R = 500.0$, $U_2 = 0.0$, $T_2 = 1.0$.

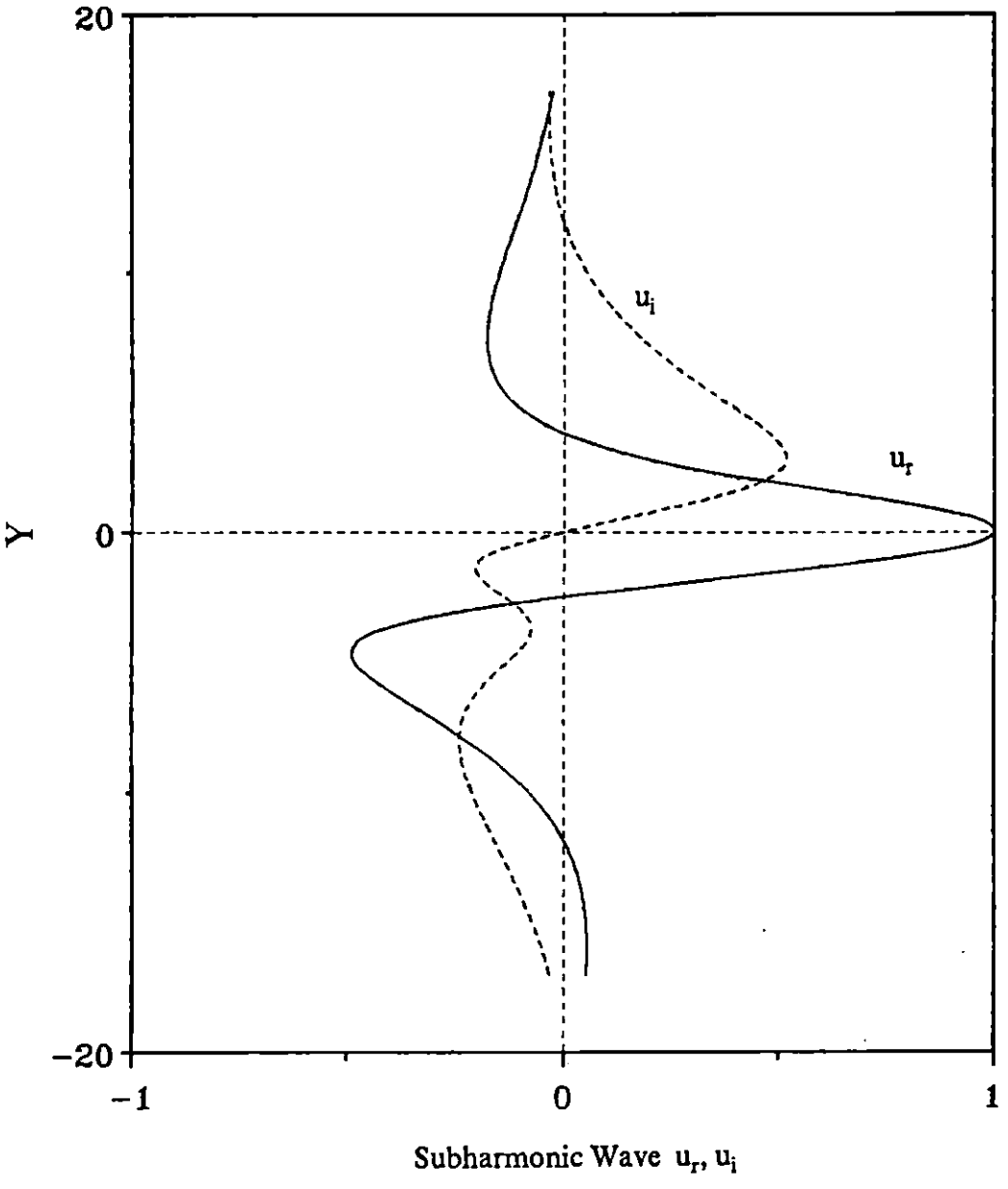

Figure 7.44 The real and imaginary parts of a 2D subharmonic wave eigenfunction with the spatial growth rate $\gamma_r = 0.192$ at $M_1 = 0.4$ and $A_{rms} = 0.09$. TANH Profile, $R = 500.0$, $U_2 = 0.0$, $T_2 = 1.0$.

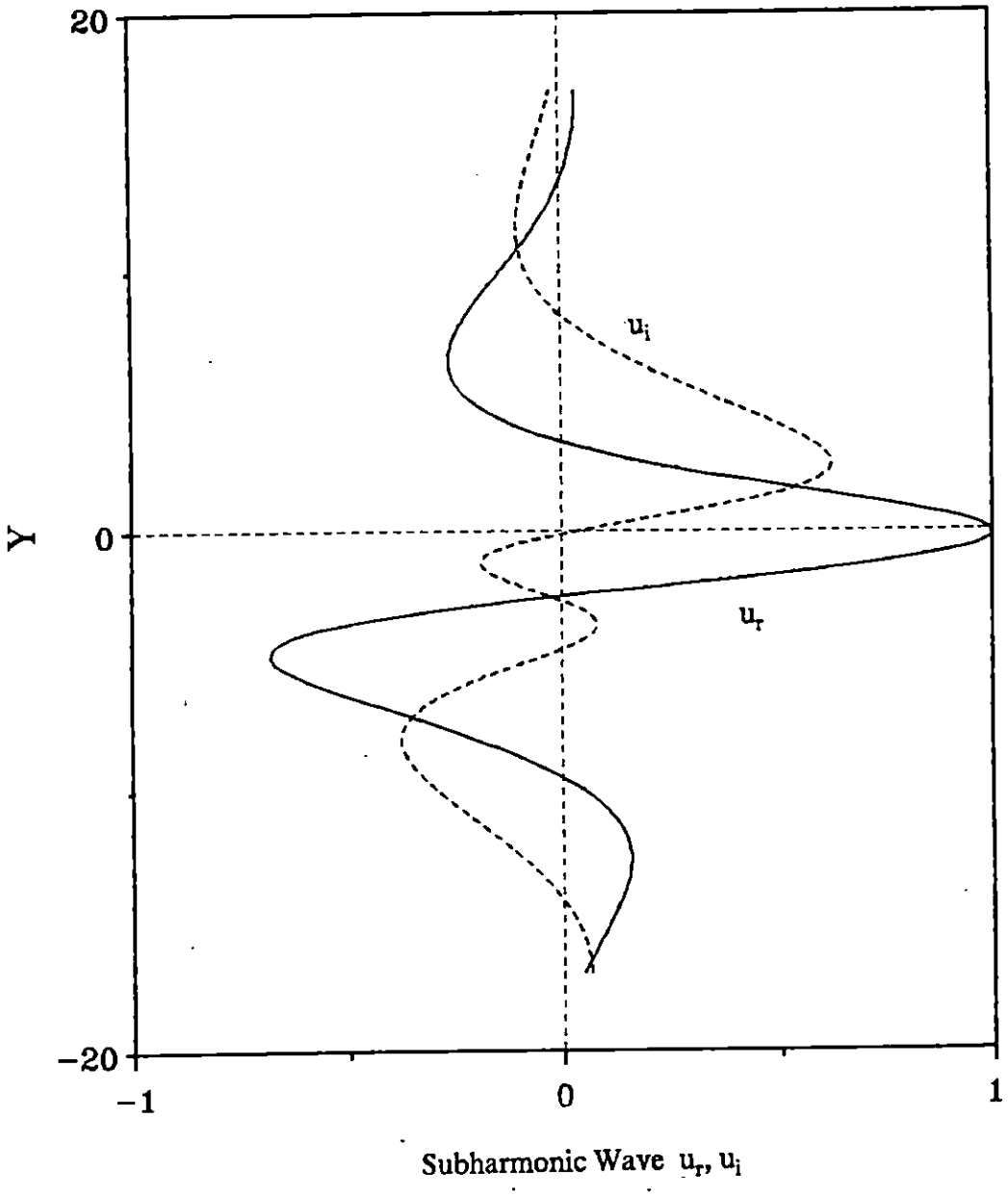

Figure 7.45 The real and imaginary parts of a 2D subharmonic wave eigenfunction with the spatial growth rate $\gamma_r = 0.331$ at $M_1 = 0.4$ and $A_{rms} = 0.09$. TANH Profile, $R = 500.0$, $U_2 = 0.0$, $T_2 = 1.0$.

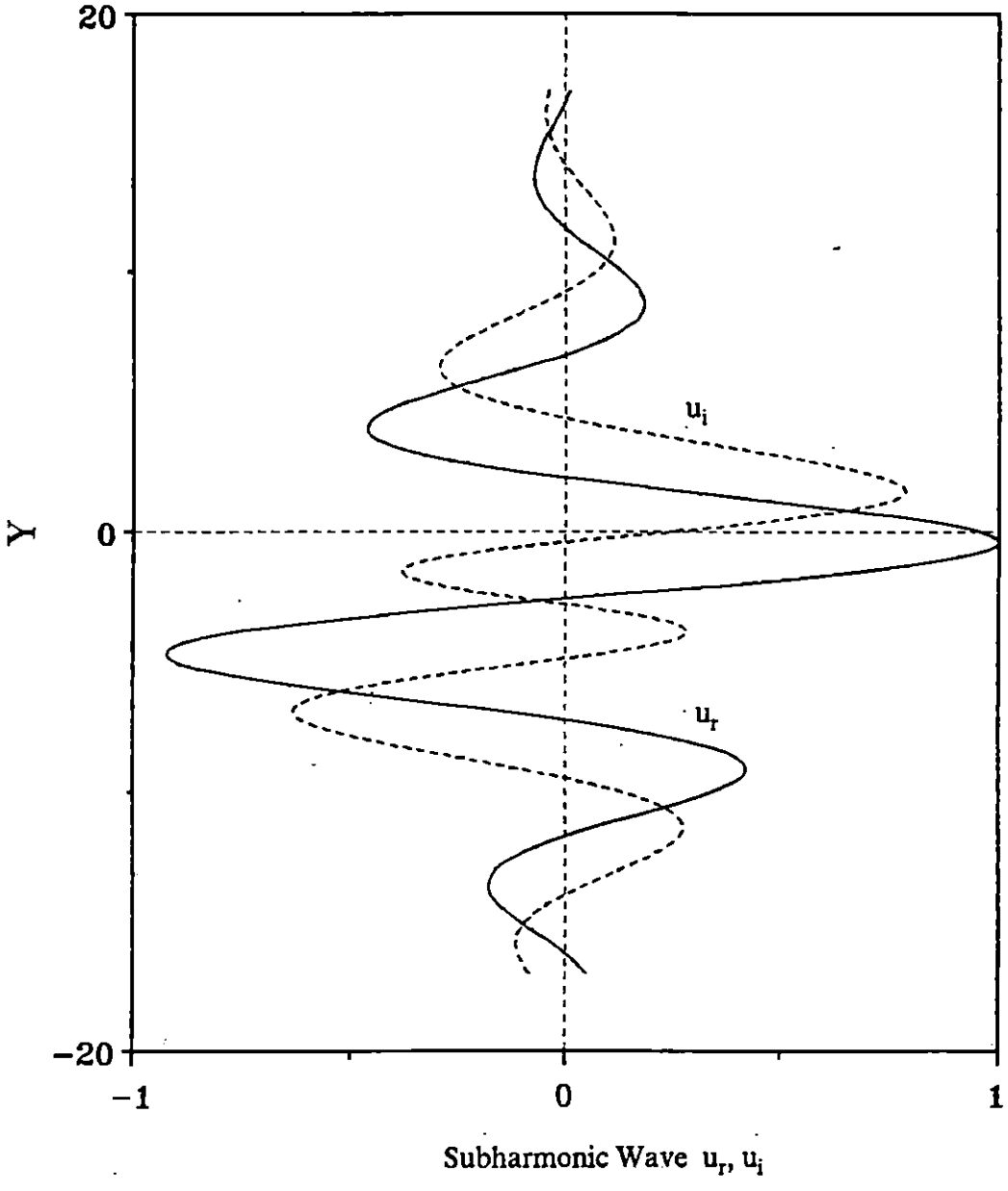

Figure 7.46 The real and imaginary parts of a 2D subharmonic wave eigenfunction with the spatial growth rate $\gamma_r = 0.701$ at $M_1 = 0.4$ and $A_{rms} = 0.09$. TANH Profile, $R = 500.0$, $U_2 = 0.0$, $T_2 = 1.0$.

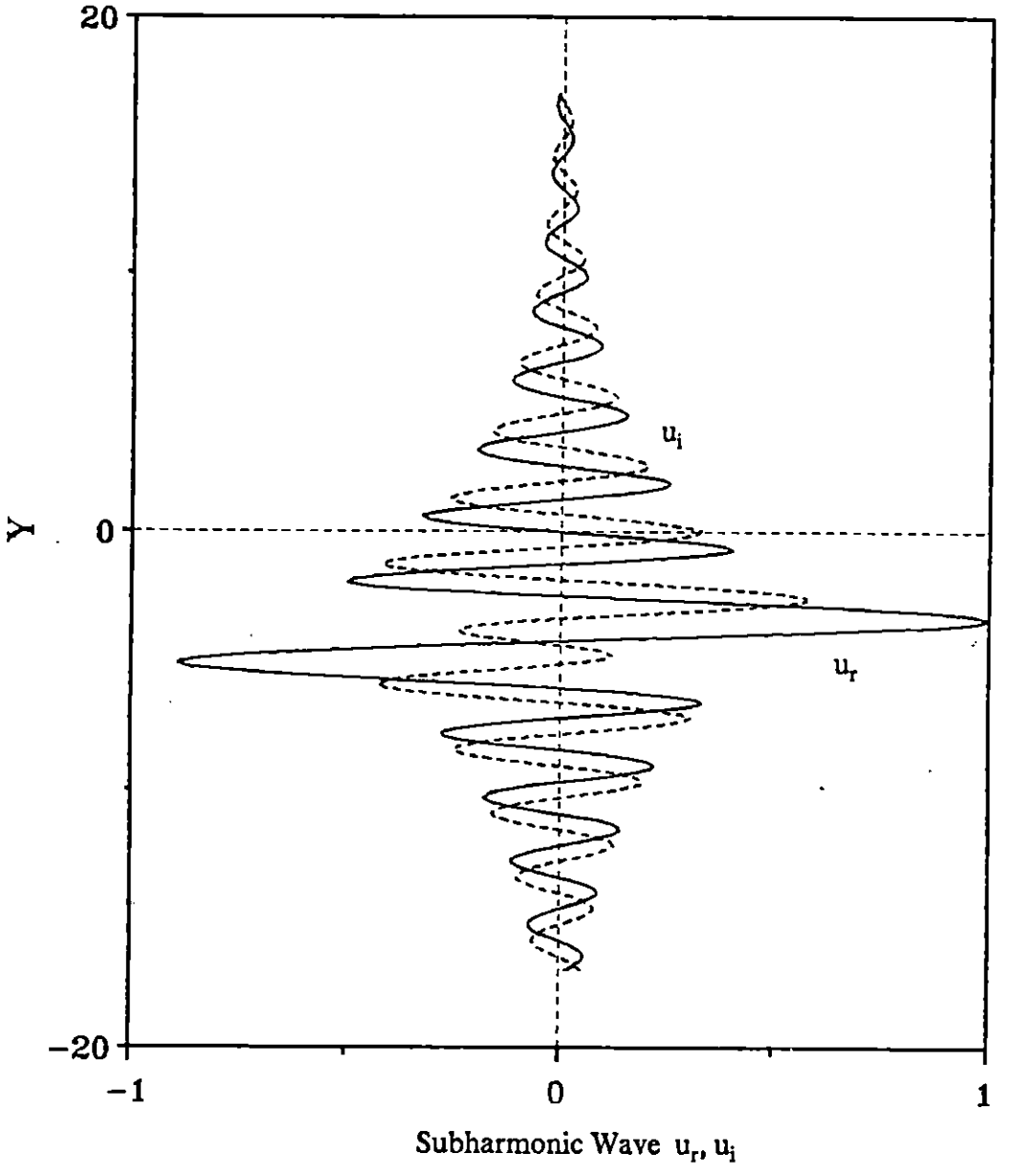

Figure 7.47 The real and imaginary parts of a 2D subharmonic wave eigenfunction with the spatial growth rate $\gamma_r = 2.579$ at $M_1 = 0.4$ and $A_{rms} = 0.09$. TANH Profile, $R = 500.0$, $U_2 = 0.0$, $T_2 = 1.0$.

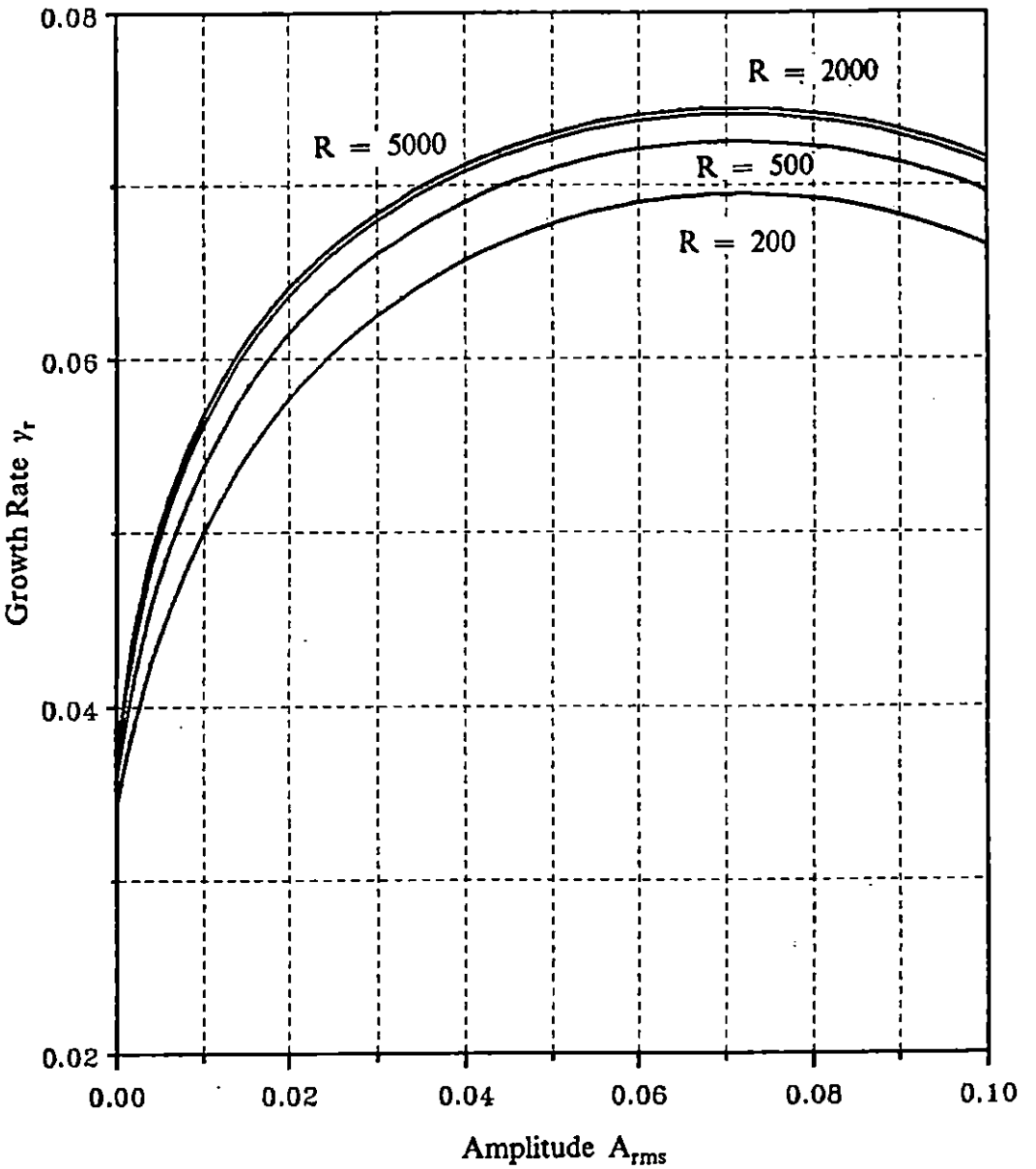

Figure 7.48 The spatial growth rates γ_r of 3D subharmonic mode vs. r.m.s. amplitude A_{rms} for various R. TANH Profile, $M_1 = 1.4$, $U_2 = 0.0$, $T_2 = 1.0$, $\beta = 0.12$.

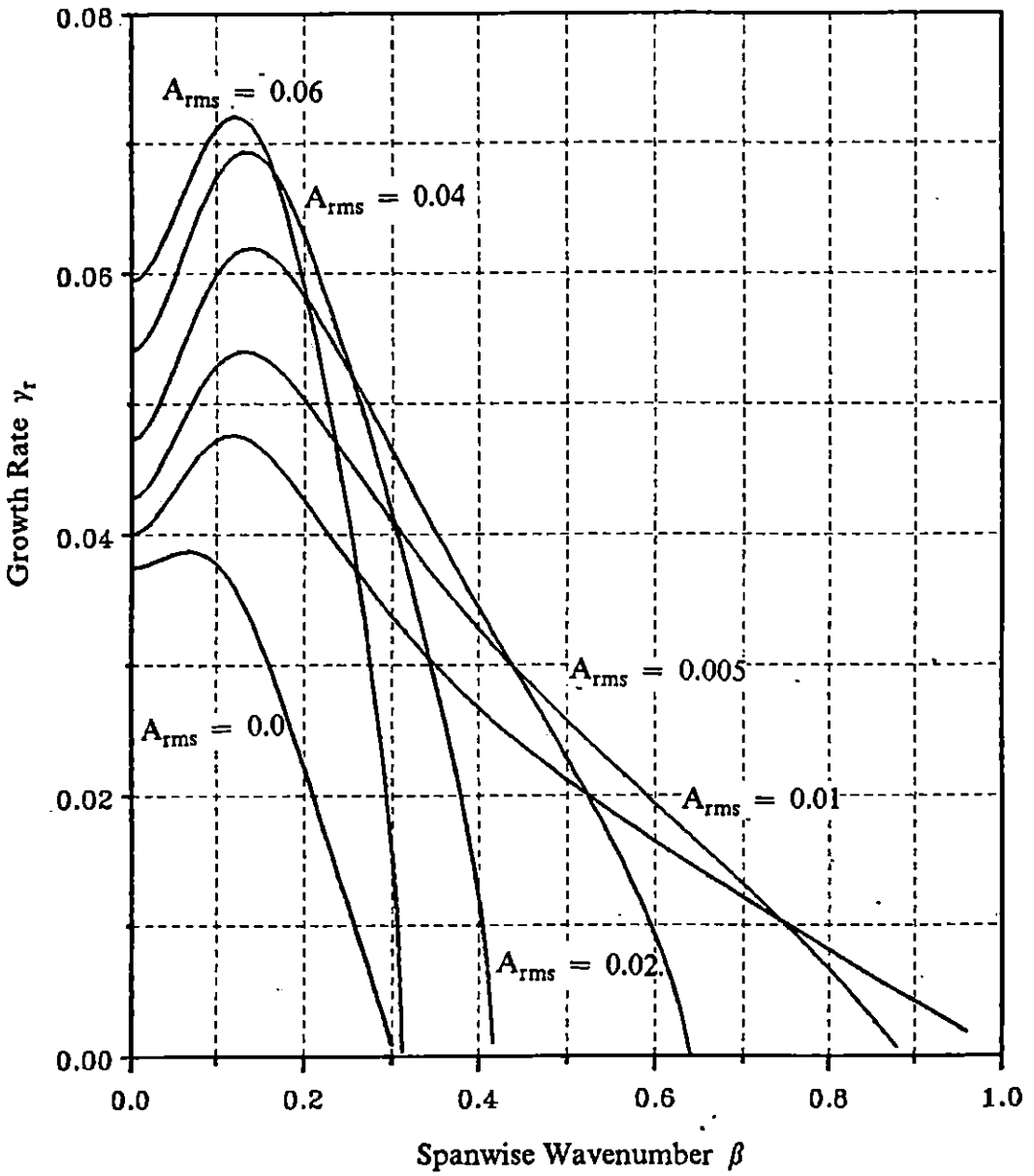

Figure 7.49 The spatial growth rates γ_r of 2D subharmonic mode vs. spanwise wavenumber β for various A_{rms}. TANH Profile, R = 500.0, $M_1 = 1.4$, $U_2 = 0.0$, $T_2 = 1.0$.

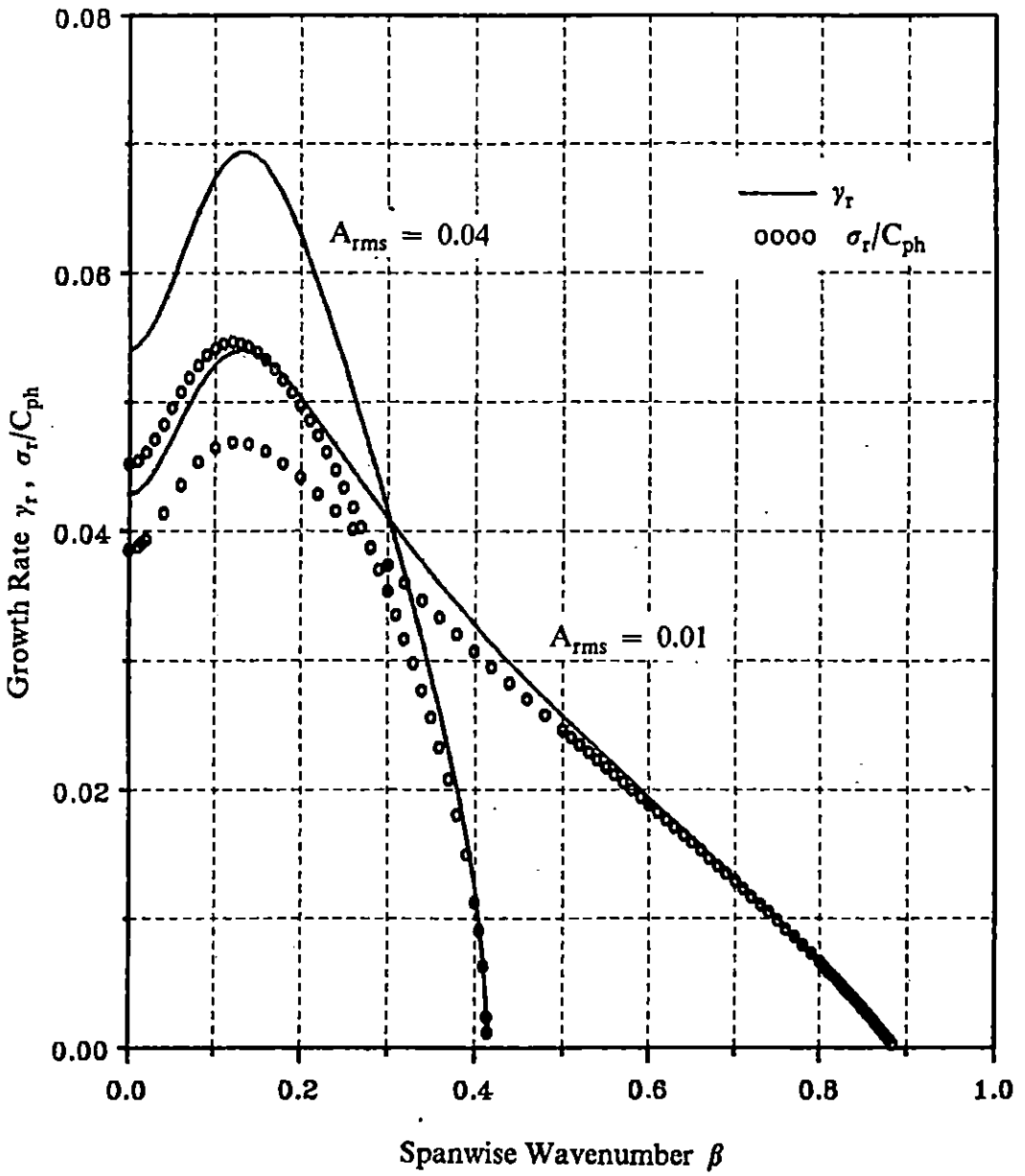

Figure 7.50 The comparisons between σ_r/C_{ph} and the spatial growth rates γ_r of 2D subharmonic mode, $C_{ph} = 0.5$. TANH Profile, R=500.0, $M_1 = 1.4$, $U_2 = 0.0$, $T_2 = 1.0$.

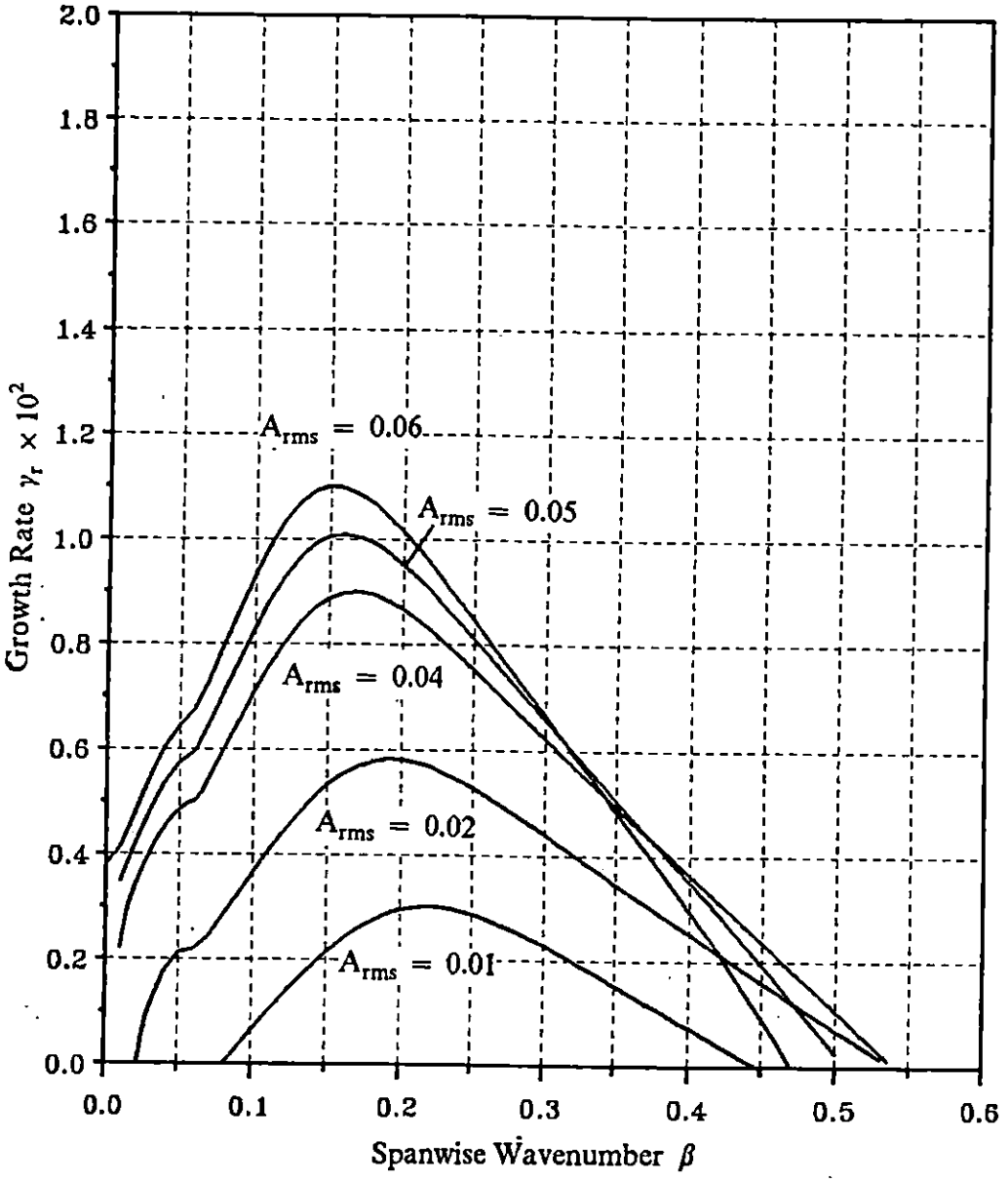

Figure 7.51 The growth rates γ_r of 3D subharmonic synchronized mode vs. spanwise wavenumber β for various A_{rms}. TANH Profile, R = 500, $M_1 = 2.5$, $U_2 = 0.0$, $T_2 = 1.0$. The Wavenumber and frequency of the periodic wave are $\alpha_r = 0.09$, $\omega_r = 0.06$

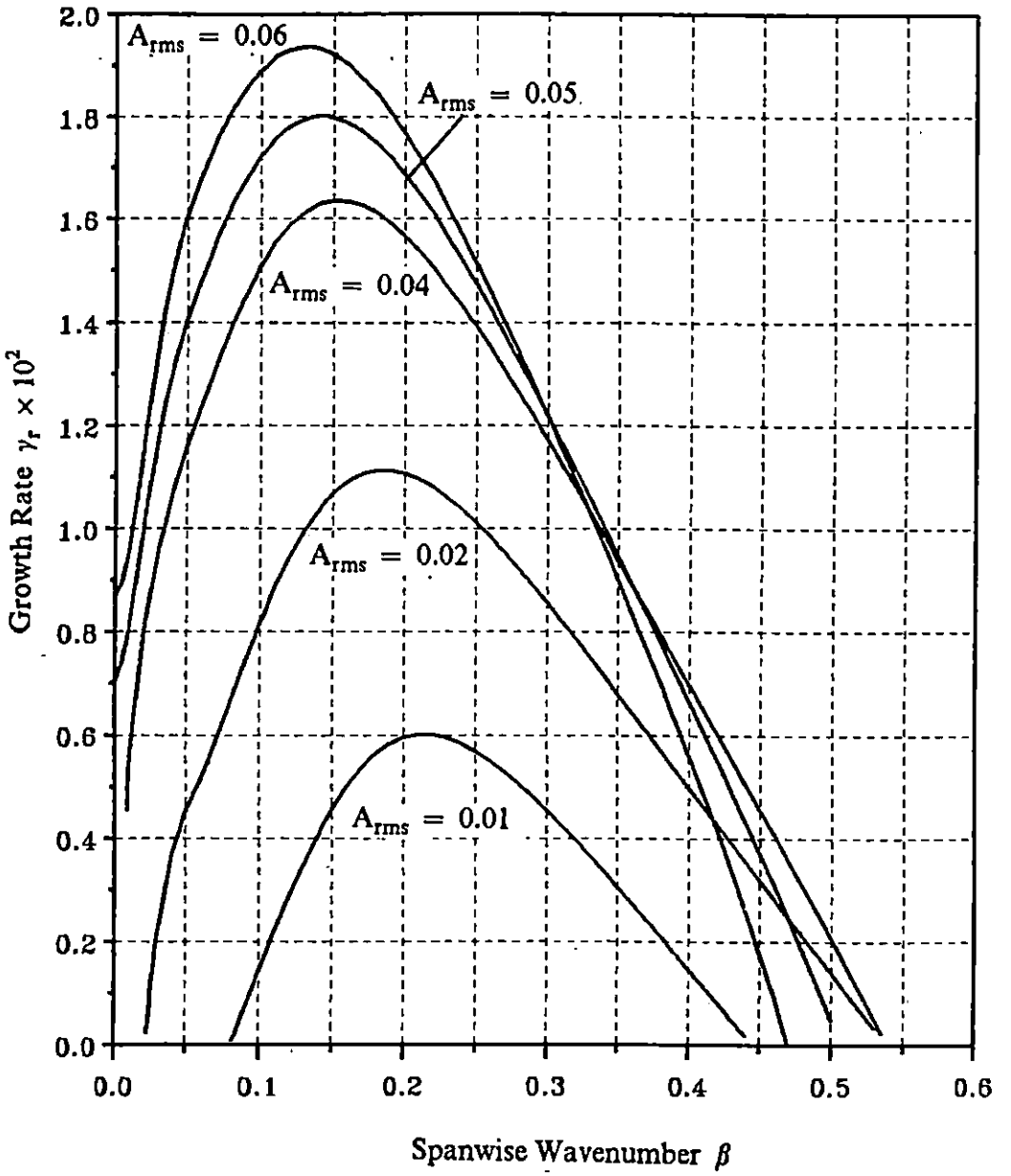

Figure 7.52 The growth rates γ_r of 3D subharmonic synchronized mode vs. spanwise wavenumber β for various A_{rms}. TANH Profile, R = 500, $M_1 = 2.5$, $U_2 = 0.0$, $T_2 = 1.0$. The Wavenumber and frequency of the periodic wave are $\alpha_r = 0.09$, $\omega_r = 0.03$

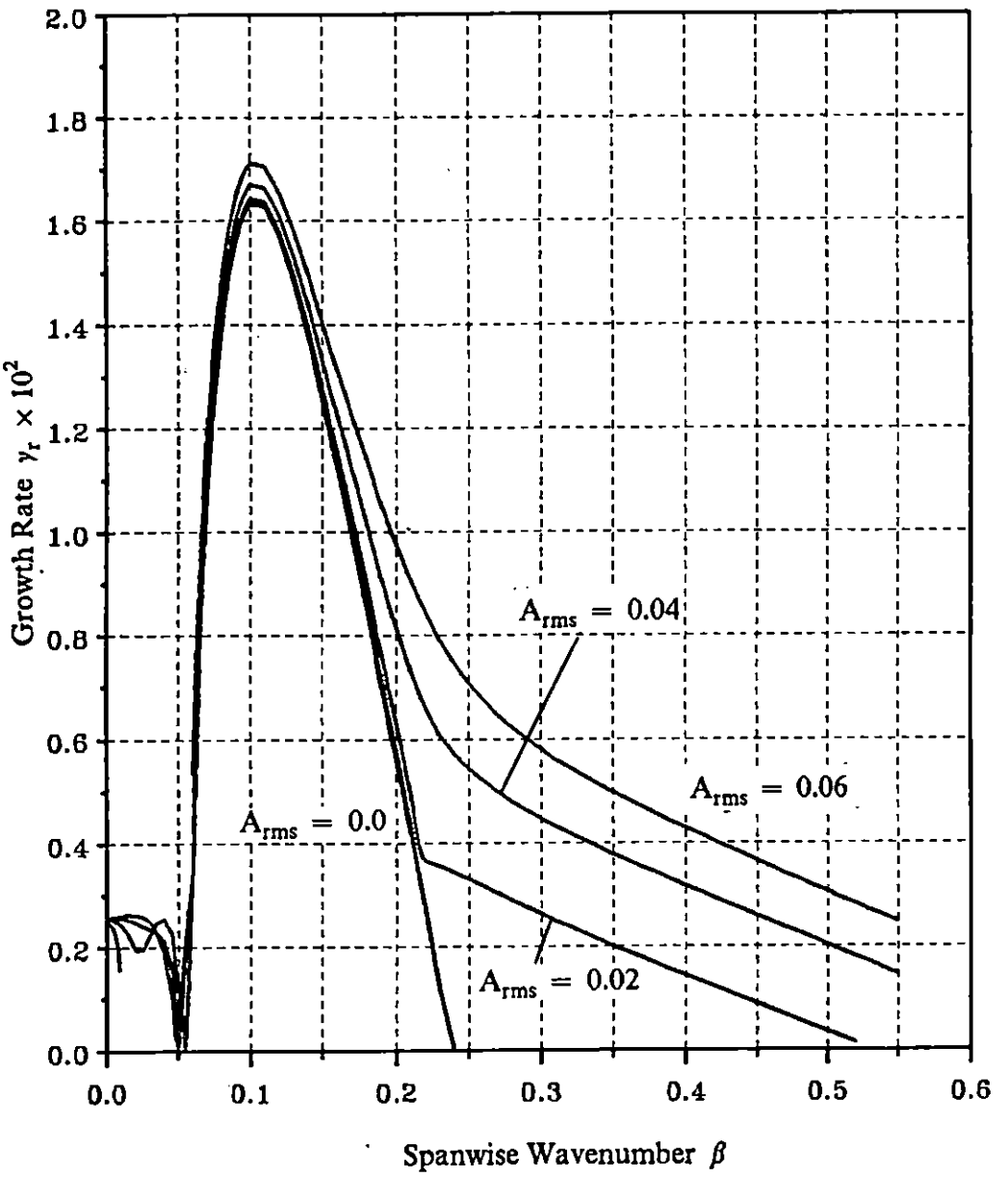

Figure 7.53 The growth rates γ_r of 3D subharmonic detuned mode vs. spanwise wavenumber β for various A_{rms}. TANH Profile, R = 500, $M_1 = 2.5, U_2 = 0.0, T_2 = 1.0$. The Wavenumber and frequency of the periodic wave are $\alpha_r = 0.09, \omega_r = 0.06$

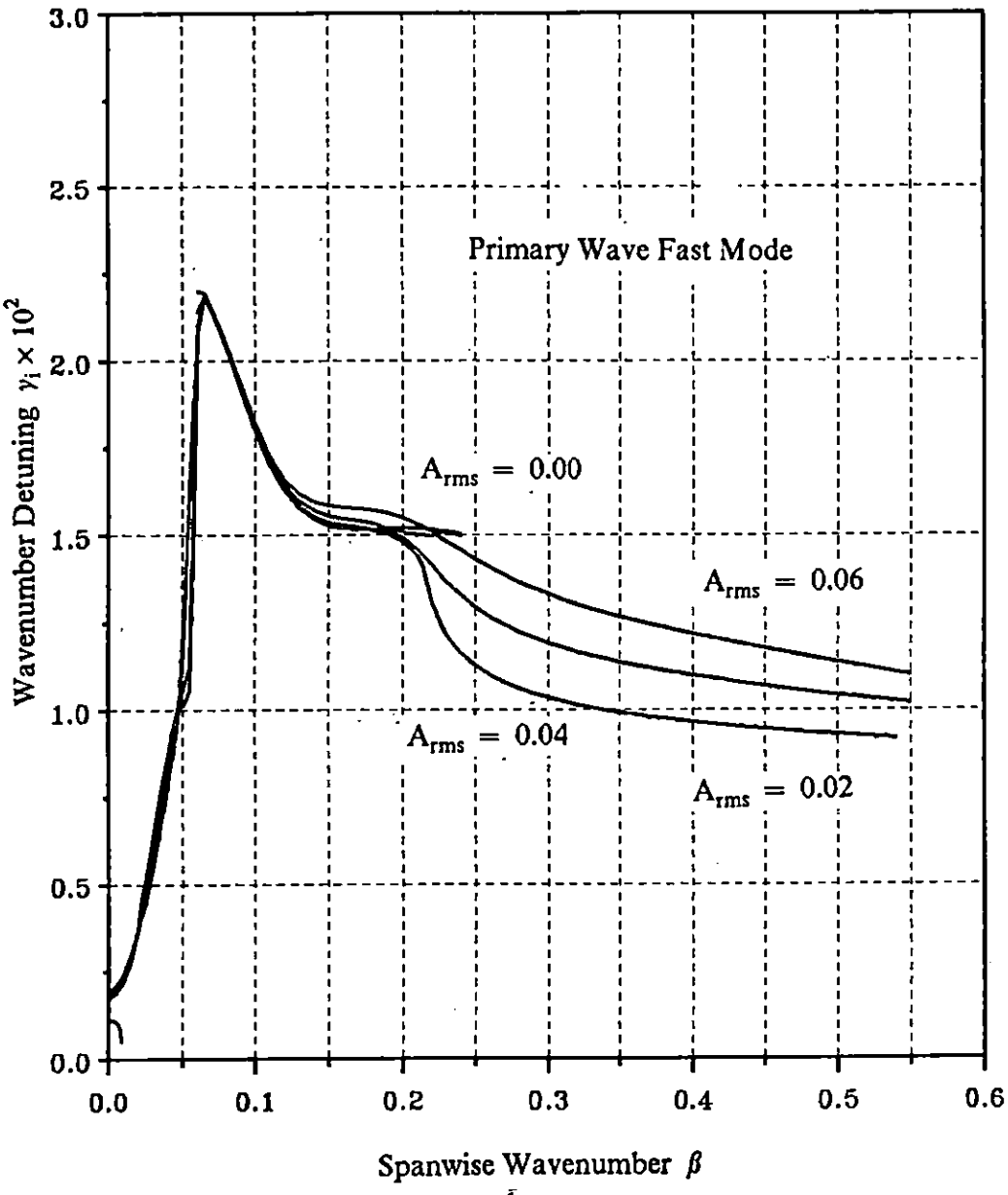

Figure 7.54 The detuned wavenumber γ_i of 3D subharmonic detuned mode vs. spanwise wavenumber β for various A_{rms}. TANH Profile, R = 500, $M_1 = 2.5$, $U_2 = 0.0$, $T_2 = 1.0$. The Wavenumber and frequency of the periodic wave are $\alpha_r = 0.09$, $\omega_r = 0.06$

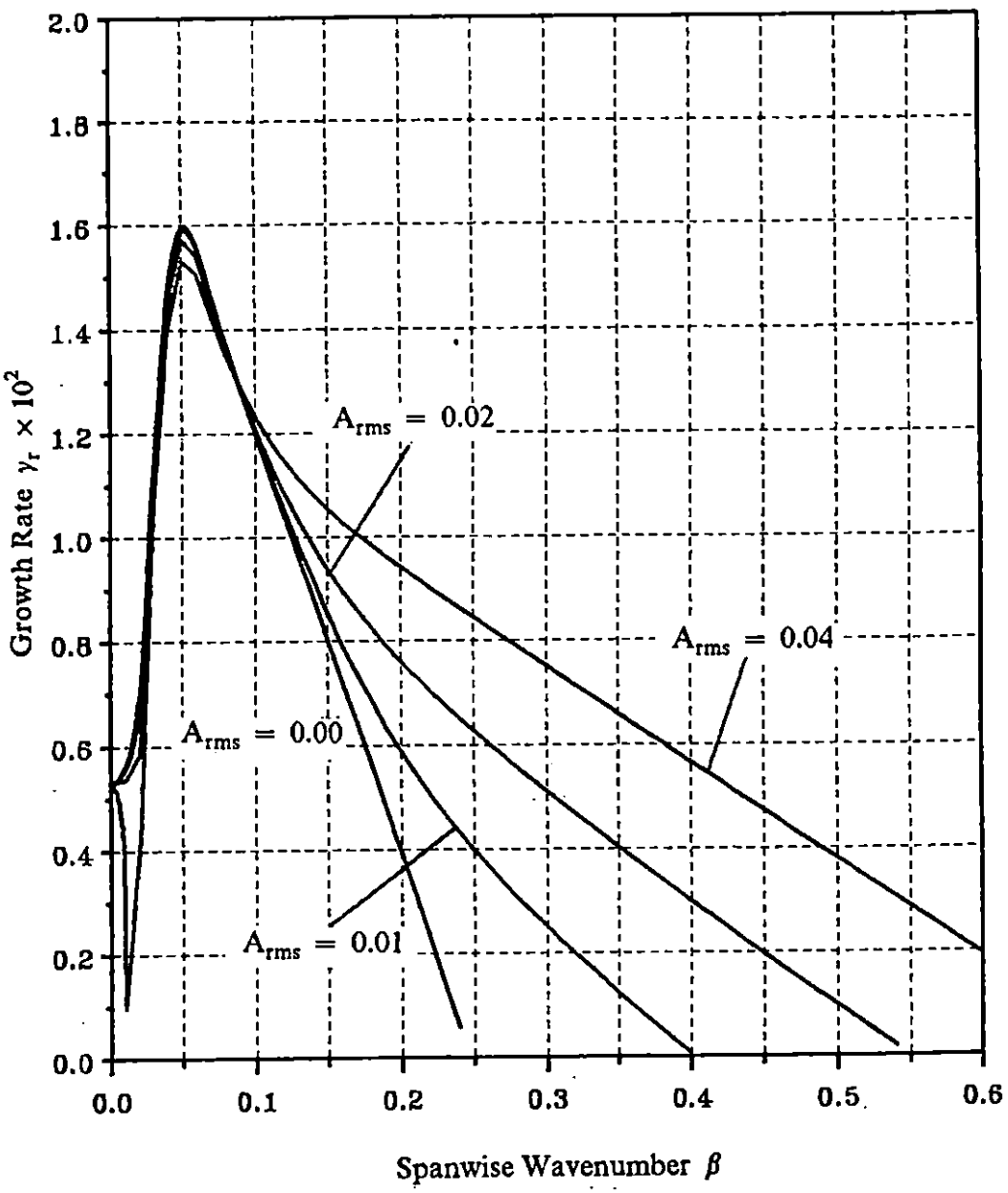

Figure 7.55 The growth rates γ_r of 3D subharmonic detuned mode vs. spanwise wavenumber β for various A_{rms}. TANH Profile, R = 500, $M_1 = 2.5$, $U_2 = 0.0$, $T_2 = 1.0$. The Wavenumber and frequency of the periodic wave are $\alpha_r = 0.09$, $\omega_r = 0.03$

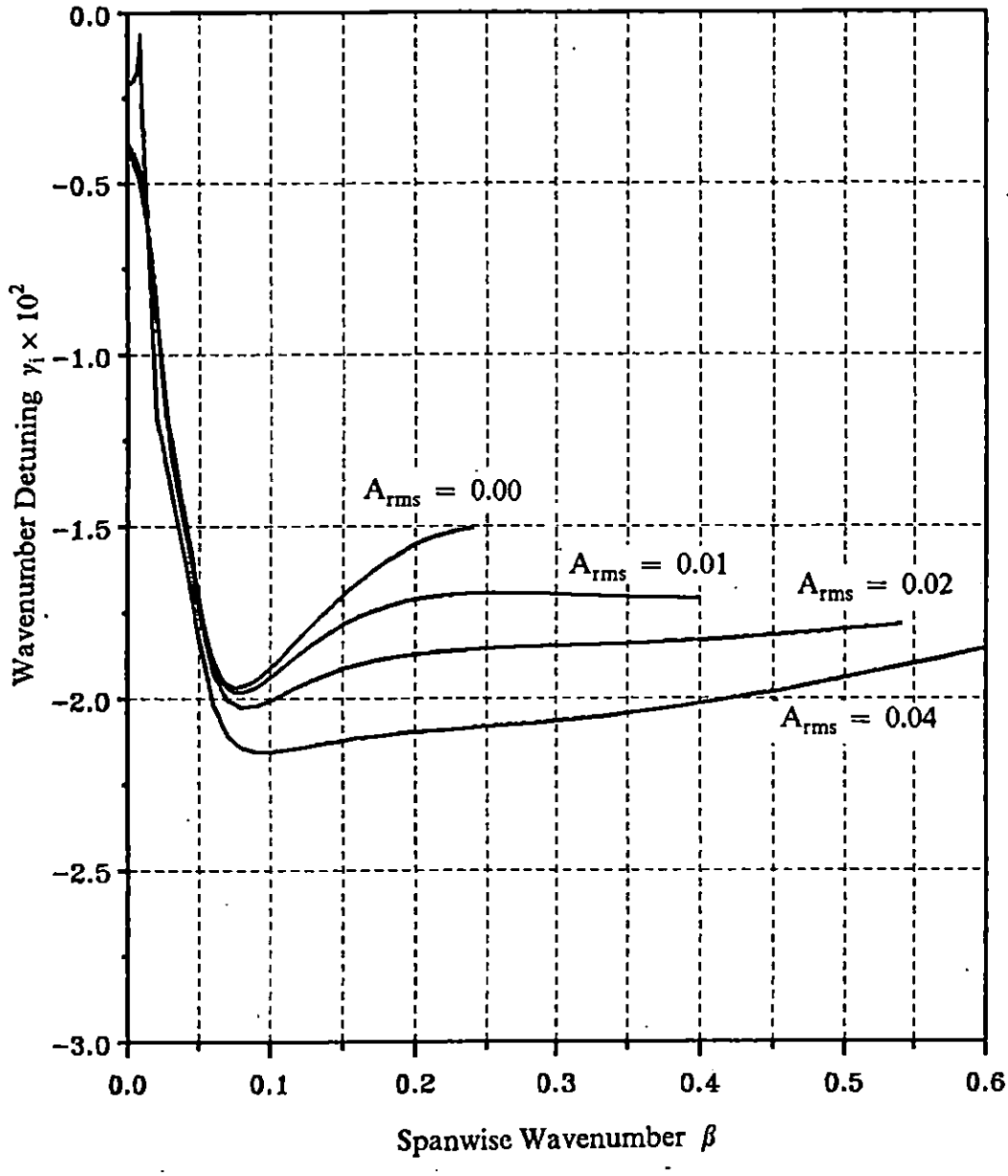

Figure 7.56 The detuned wavenumber γ_i of 3D subharmonic detuned mode vs. spanwise wavenumber β for various A_{rms}. TANH Profile, R = 500, M_1 = 2.5, U_2 = 0.0, T_2 = 1.0. The Wavenumber and frequency of the periodic wave are α_r = 0.09, ω_r = 0.03

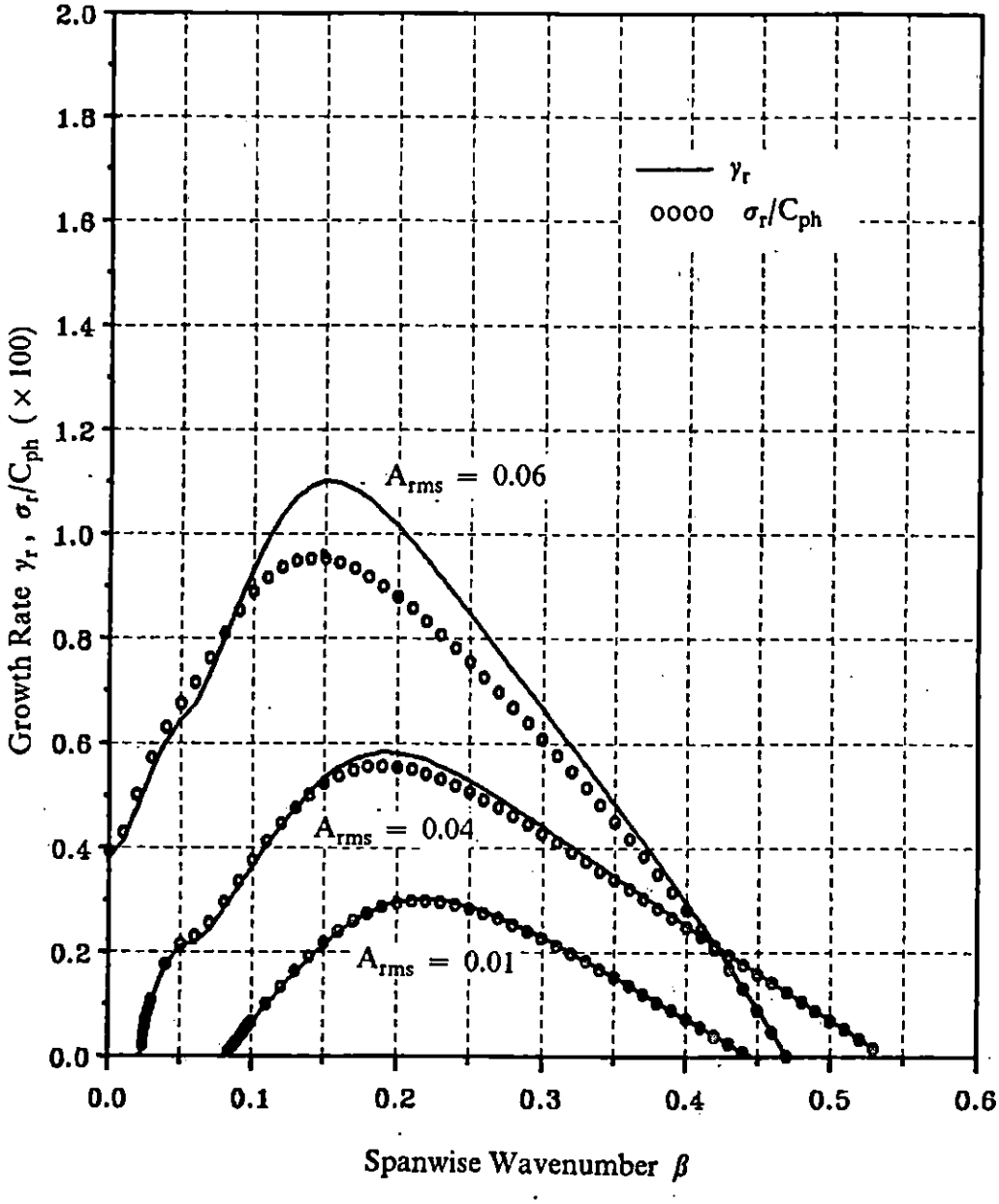

Figure 7.57 The comparisons between σ_r/C_{ph} and the spatial growth rates γ_r of 2D subharmonic mode, $C_{ph} = 2/3$. TANH Profile, R = 500.0, $M_1 = 2.5, U_2 = 0.0, T_2 = 1.0$.

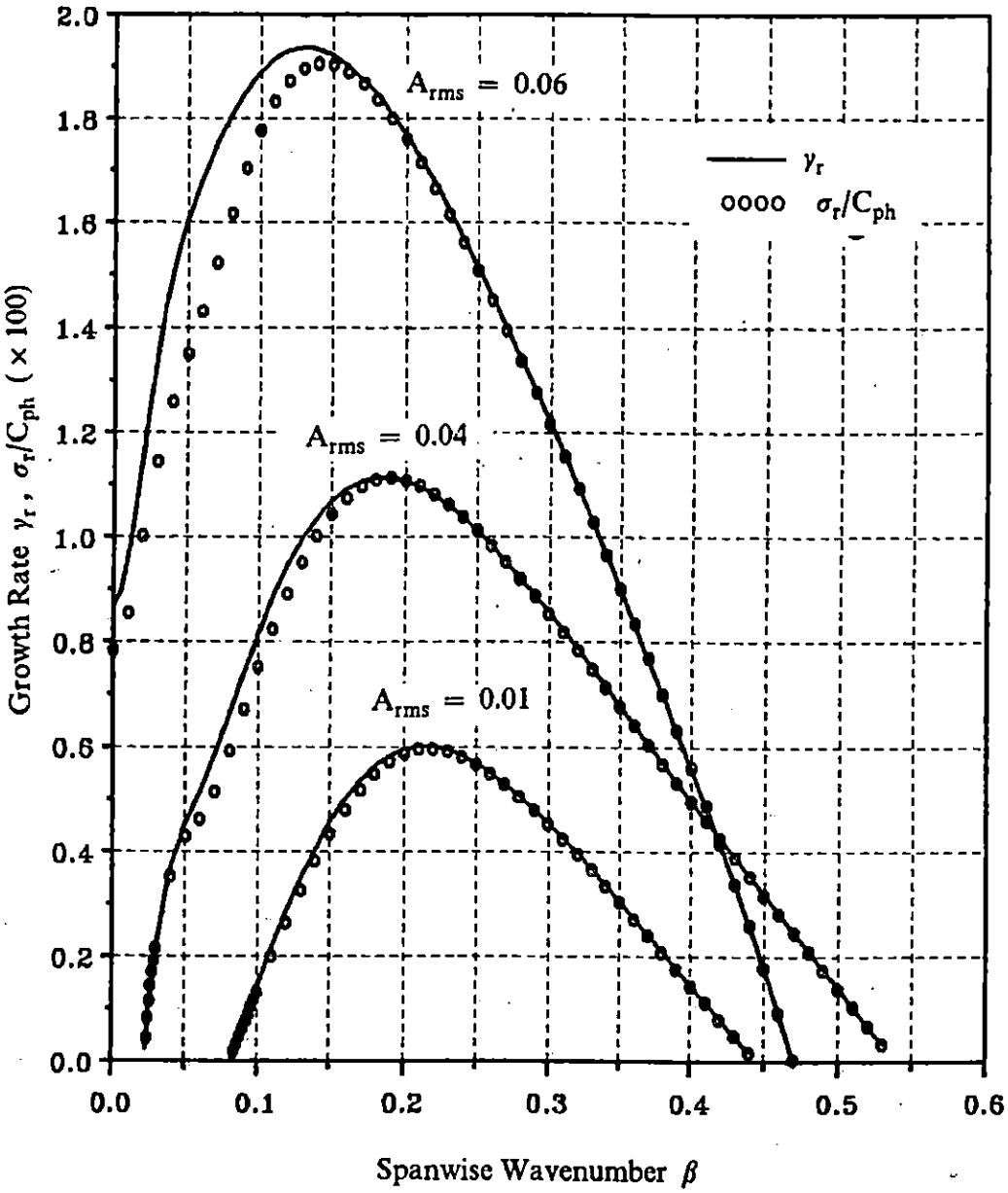

Figure 7.58 The comparisons between σ_r/C_{ph} and the spatial growth rates γ_r of 2D subharmonic mode, C_{ph} = 1/3. TANH Profile, R = 500.0, M_1 = 2.5, U_2 = 0.0, T_2 = 1.0.

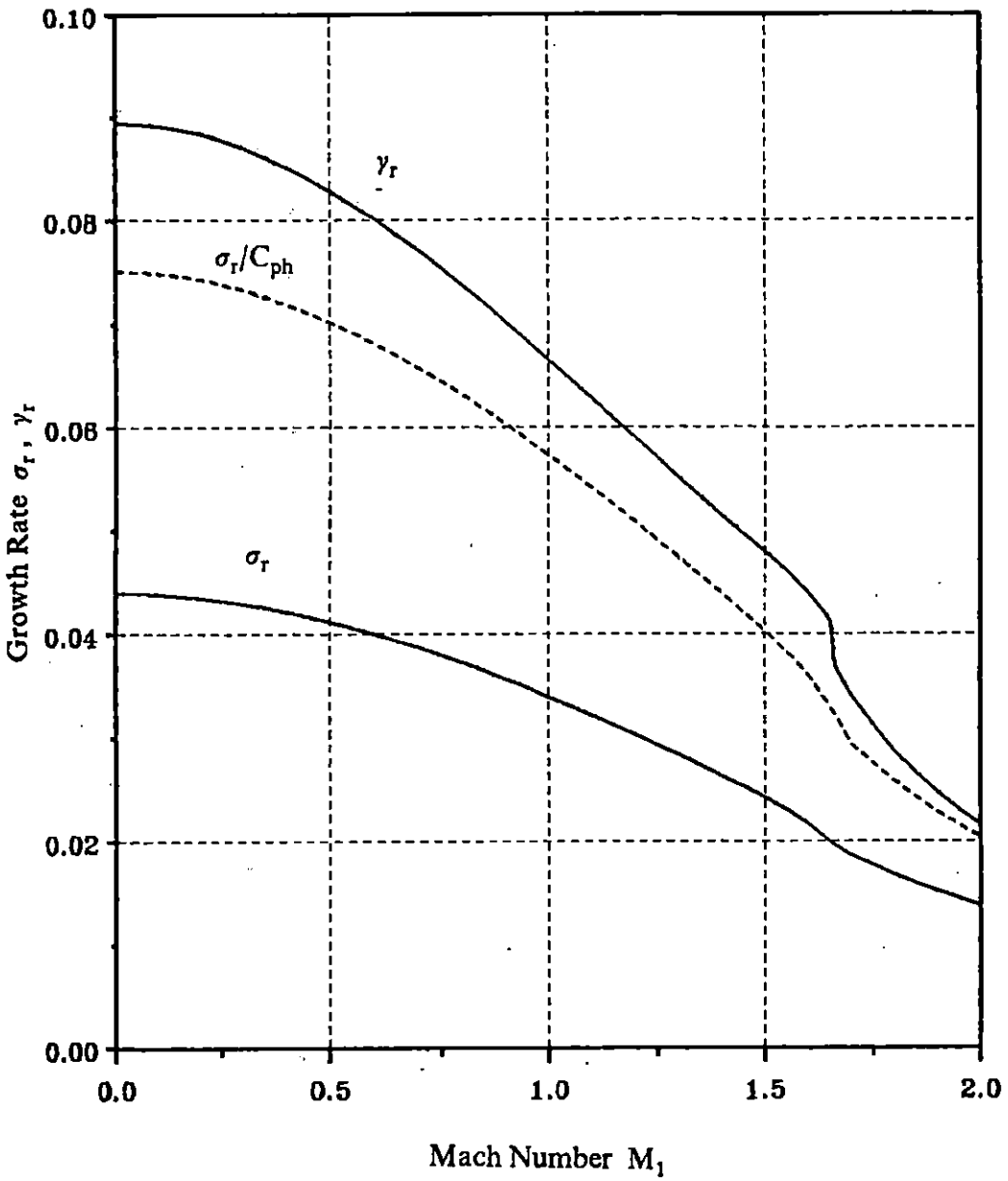

Figure 7.59 The temporal and the spatial growth rates of subharmonic modes vs. Mach number M_1 at $\beta = 0.12$ with $A_{rms} = 0.04$. SHEAR Profile, $R = 500.0$, $U_2 = 0.0$, $T_2 = 1.0$.

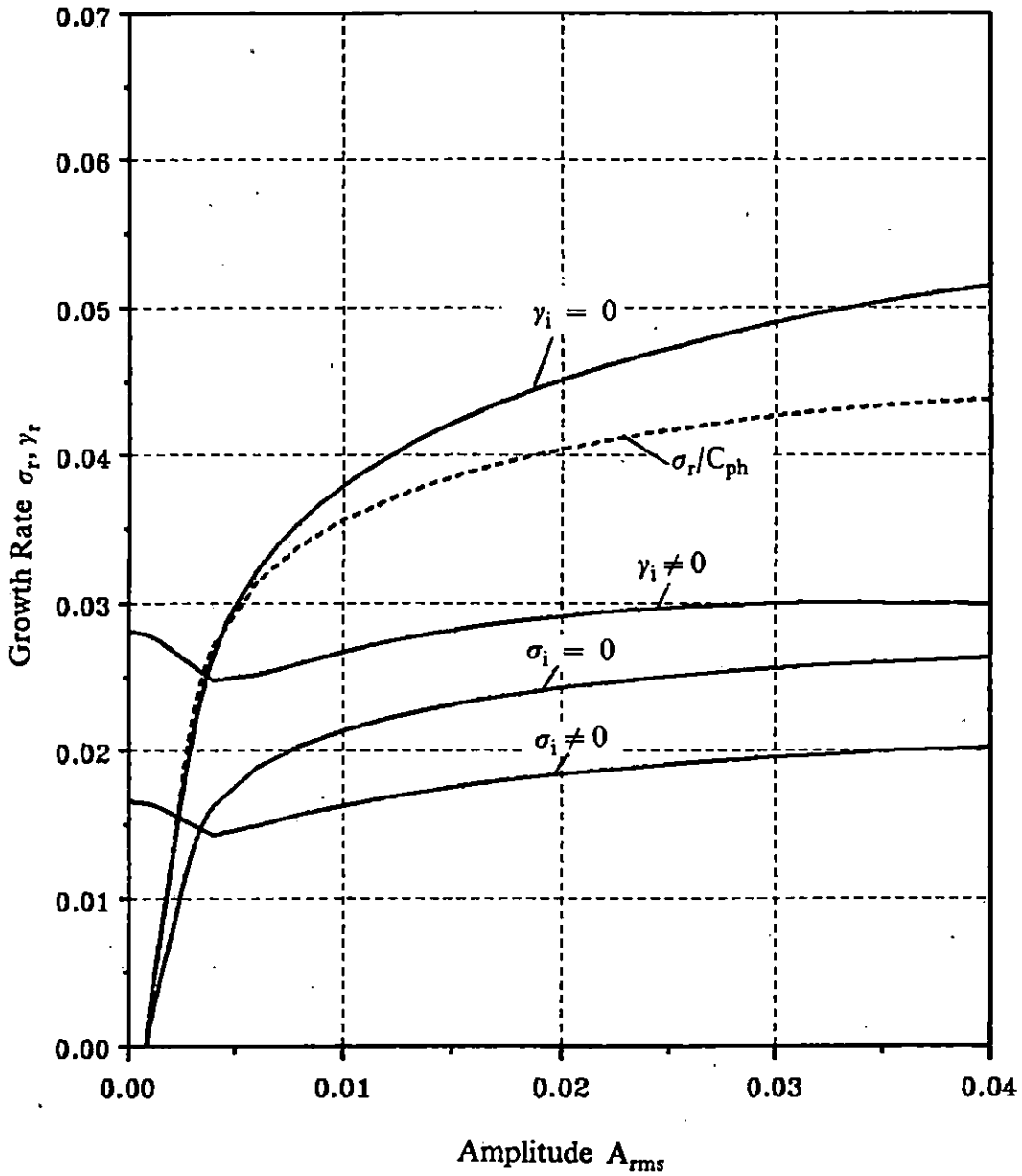

Figure 7.60 The temporal and the spatial growth rates of subharmonic modes vs. A_{rms} at $\beta = 0.12$ with $M_1 = 1.4$. SHEAR Profile, R = 500.0, $U_2 = 0.0$, $T_2 = 1.0$.

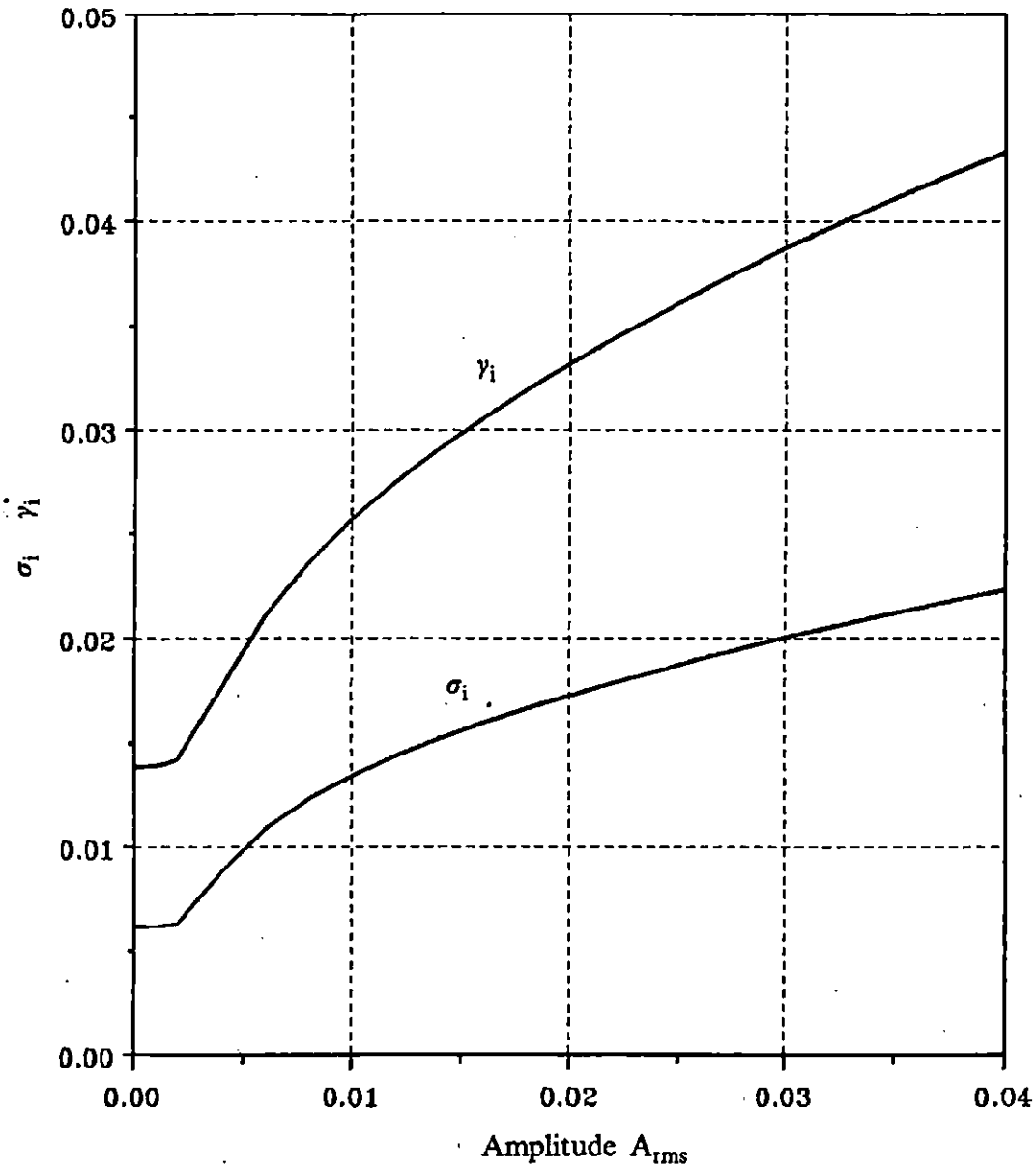

Figure 7.61 The frequency and the wavenumber detuning of subharmonic modes vs. A_{rms} at $\beta = 0.12$ with $M_1 = 1.4$. SHEAR Profile, $R = 500.0$, $U_2 = 0.0$, $T_2 = 1.0$.

The vita has been removed from the scanned document